Drug delivery across the blood-brain barrier using short-pulse focused ultrasound and microbubbles for the treatment of diffuse intrinsic pontine glioma

Dani Chattenton

A thesis submitted for the degree of Doctor of Philosophy from the University of London

CRUK CONVERGENCE SCIENCE CENTRE
DEPARTMENT OF RADIOTHERAPY AND IMAGING, THE INSTITUTE OF CANCER RESEARCH
DEPARTMENT OF BIOENGINEERING, IMPERIAL COLLEGE LONDON

MARCH 2023

Declaration

I hereby declare that this thesis reports my own original work and any contribution made to this research by others is explicitly acknowledged.

Dani Chattenton

Abstract

Patients with diffuse intrinsic pontine glioma (DIPG; a type of diffuse midline glioma), have a 9-month median survival, with the tumour spreading throughout the pons. The pons is a critical anatomic location, responsible for basic functions such as breathing and swallowing. Currently, the only available treatment is palliative radiotherapy. DIPG has a largely intact blood-brain barrier (BBB), which prevents drugs from reaching the cancer cells and is a major reason for drugs failing in clinical trials. Thus, there is a strong unmet need for improved drug delivery to DIPG. The use of focused ultrasound (FUS) and intravenous microbubbles enables temporary increases in BBB permeability, allowing therapeutics to enter the targeted brain region. In recent pre-clinical studies, applying a short pulse (<5 μs) ultrasound sequence to the hippocampus provided drug delivery and safety benefits over traditionally used long pulses (10 ms). This thesis reports studies that evaluated whether short-pulse ultrasound (developed at Imperial College London (ICL)) can be used to produce a similar safety and drug delivery profile in the pons of non-tumour bearing mice and in a syngeneic DIPG mouse model (examined at the Institute of Cancer Research (ICR)).

First, the benefits of short pulse ultrasound and microbubbles were investigated in the pons at 300 kHz, a frequency suitable for transcranial transmission. BBB disruption (BBBD) was feasible but variable and so ultrasound emitted at a frequency of 1.05 MHz was examined in the next chapter. At this frequency a pressure window for BBBD was established and these parameters used to test the efficacy and safety of a newly assembled sonication setup at the ICR. Lastly, the ability of short pulse ultrasound to increase the concentration of a promising DIPG drug (panobinostat) was assessed. FUS, in combination with microbubbles, increased panobinostat concentration by 10% in a syngeneic DIPG mouse model compared to the control not exposed to ultrasound, but this level was not statistically significant (p>0.05).

Overall, the work described in this thesis has shown that FUS-mediated drug delivery is feasible in a DIPG mouse model providing a platform for expanding treatment options.

Contents

Acknowledgements **10**

Publications **11**

List of figures **13**

List of tables **17**

Abbreviations **18**

1 Introduction **23**

1.1 Motivation 23

1.2 The blood-brain barrier and blood tumour barrier 24

1.3 Diffuse intrinsic pontine glioma (DIPG) 26

1.3.1 DIPG tumour biology 27

1.3.2 Therapeutic targets 31

1.3.3 Clinical trials for DIPG 32

1.3.4 Panobinostat 32

1.4 Methods of overcoming the blood-brain barrier and brain blood tumour barrier 38

1.5 Blood-brain barrier disruption using focused ultrasound and microbubbles 38

1.5.1 Focused ultrasound 39

1.5.2 Microbubbles 40

1.5.3 Mechanism of blood-brain barrier disruption with focused ultrasound and microbubbles 44

1.5.4 Ultrasound sequence 44

1.5.5 Applications of focused ultrasound mediated drug delivery in the brain 47

1.5.6 Targeting 48

1.5.7 Acoustic pressure 49

1.5.8 Blood-brain barrier closing time 49

1.5.9 Size of therapeutic agent 50

1.6 Tissue effects 50

1.6.1 Transient immune response 51

1.6.2 Tissue effects in non-human primates 51

1.6.3 Microbubble dose 52

1.7 Monitoring blood-brain barrier disruption 52

1.8 Translation to the clinic 54

1.8.1 Considerations for clinical translation 55

1.8.2 Ultrasound parameters 55

1.8.3 Clinical systems 56

1.8.4 Other benefits beyond drug delivery 59

1.9 Blood-brain barrier disruption in the pons for DIPG 59

1.9.1 Preclinical studies 59

1.9.2 Clinical trials for DIPG 61

1.10 Thesis aims 64

2 Common methods **65**

2.1 Animals 65

2.2 Preparation for sonication 66

2.3 ICL methodology 66

2.3.1 Ultrasound setup 66

2.3.2 Targeting 70

2.4 ICR methodology 72

2.4.1 Ultrasound setup 72

2.2.2. Development of the ICR targeting system 74

2.5 Microbubbles and model drugs 78

2.6 Brain tissue processing 79

2.7 Haematoxylin and Eosin (H&E) staining 80

2.8 Microscopy of dextran and biotin 81

2.9 Fluorescence pixel intensity quantification 81

2.10 Acoustic emissions analysis (ICL) 82

2.11 Conclusion 82

3 Blood-brain barrier disruption using a rapid short-pulse sequence at 300 kHz 83

3.1 Background 83

3.1.1 Transcranial transmission 84

3.1.2 Microbubble dynamics at 250-300 kHz 84

3.1.3 Ultrasound parameters and protocols that may have an important role in the reproducibility of brain drug delivery 85

3.1.4 Burst length 85

3.1.5 Peak-rarefactional pressure (PRP) 86

3.1.6 Microbubbles (MB) 86

3.1.7 Acoustic emissions to predict treatment outcomes 87

3.2 Aims and objectives 88

3.3 Materials and methods 89

3.3.1 Effect of burst length on blood-brain barrier disruption 89

3.3.2 Targeting the pons 90

3.3.3 Peak-rarefactional pressure 90

3.3.4 Microbubble comparison 91

3.3.5 Statistical analysis 92

3.4 Results 93

3.4.1 Burst length in the hippocampus 93

3.4.2 Blood-brain barrier disruption in the pons 101

3.4.3 Peak-rarefactional pressure 102

3.4.4 Microbubble comparison 106

3.5 Discussion 109

3.5.1 Burst length 109

3.5.2 Drug delivery to the pons 111

3.5.3 Acoustic pressure 112

3.5.4 Microbubble type 112

3.5.5 Clinical relevance 114

3.5.6 Limitations and future work 115

3.6 Conclusion 120

4 Blood-brain barrier disruption in the pons at 1.00 and 1.05 MHz 121

4.1 Background 121

4.1.1 Centre frequency 121

4.1.2 Beam size change and targeting 121

4.1.3 Acoustic pressure 122

4.1.4 Tissue effects 122

4.1.5 ICR sonication system 123

4.2 Aims and objectives 124

4.3 Materials and methods 125

4.3.1 Pons sonications at ICL 125

4.3.2 Targeting the pons 125

4.3.3 Acoustic pressure optimisation 126

4.3.4 Sonications with the novel system at the ICR 127

4.4 Results 130

4.4.1 Targeting the pons at 1.05 MHz (ICL) 130

4.4.2 Acoustic pressure optimisation 131

4.4.3 Targeting the pons at 1 MHz (ICR) 139

4.5 Discussion 143

4.5.1 Targeting the pons (ICL) 143

4.5.2 Pressure window for blood-brain barrier disruption (ICL) 143

4.5.3 Histological assessment of tissue damage (ICL) 144

4.5.4 Efficacy of the ICR BBBD system 145

4.5.5 Histological assessment at ICR 146

4.5.6 Limitations and future work 146

4.6 Conclusion 149

5 Assessment of ultrasound-mediated panobinostat delivery to the pons 150

5.1 Background 150

5.1.1 Panobinostat *in vitro* 150

5.1.2 Panobinostat *in vivo* 151

5.1.3 Panobinostat in the clinic 151

5.1.4 Panobinostat delivery using focused ultrasound 151

5.1.5 Study design 152

5.2 Aims and objectives 153

5.3 Materials and methods 154

5.3.1 Cell culture 154

5.3.2 *In vitro* panobinostat cytotoxicity assay 155

5.3.3 Pharmacokinetic study 157

5.3.4 Plasma and brain tissue collection for LC-MS/MS 157

5.3.5 Tolerability and assessment of panobinostat delivery 158

5.3.6 Tumour model selection 161

5.3.7 Tumour inoculation 161

5.3.8 Monitoring tumour growth 163

5.3.9 Focused ultrasound treatment tolerability in tumour-bearing mice 163

5.3.10 Panobinostat delivery in tumour-bearing mice 165

5.3.11 Statistical analysis 165

5.4 Results 167

5.4.1 *In vitro* efficacy of panobinostat 167

5.4.2 Pharmacokinetic study of panobinostat 169

5.4.3 Tolerability and efficacy of panobinostat delivered across the blood-brain barrier using focused ultrasound in non-tumour bearing mice 170

5.4.4 Tolerability, safety, and efficacy of blood-brain barrier disruption in a DIPG mouse model 177

5.4.5 Delivery of panobinostat across the blood-brain barrier using focused ultrasound in a DIPG mouse model 182

5.5 Discussion 187

5.5.1 *In vitro* cytotoxicity and pharmacokinetics of panobinostat 187

5.5.2 Panobinostat delivery in non-tumour bearing mice 187

5.5.3 Blood-brain barrier disruption in a DIPG mouse model 189

5.5.4 Panobinostat delivery in a DIPG mouse model 190

5.5.5 Vascular differences between mice 191

5.5.6 Blood-brain barrier closing time and drug diffusion 191

5.5.7 Variation and sample size 192

5.5.8 Future prospects 193

5.5.9 Clinical relevance 196

5.6 Conclusion 197

6 Thesis conclusions 198

7 Appendix 200

8 References 203

Acknowledgements

I am deeply indebted to a multitude of individuals whose collective expertise and unwavering support have enabled this project to flourish.

First, I'd like to thank my supervisory team: Prof. Gail ter Haar; Dr. James Choi; Dr. Ian Rivens, Dr. Jessica Boult; Prof. Simon Robinson; and Prof. Chris Jones for their unwavering support and advice throughout this project.

I'd like to also thank the past and present members of the Noninvasive Surgery & Biopsy Laboratory at Imperial College London (ICL) and the dedicated teams at the Institute of Cancer Research (ICR), including the Therapeutic Ultrasound, Preclinical MRI, and Glioma teams. Special mention is due to Dr. Matthew Copping and Dr. Gerard Hernández-Mir for imparting their *in vivo* protocol expertise; Dr. Krit Sujarittam, Dr. Zheng Jiang, and Jiho Kim for their invaluable assistance with acoustic emissions analysis; Dr. Ian Rivens, whose tireless efforts led to the assembly of the ultrasound system at ICR, enabling the completion of my drug studies; Dr. Jessica Boult, for her guidance on MRI and mouse model intricacies; and the Glioma team, particularly Dr. Diana Carvalho for her support with *in vitro* and *in vivo* DIPG experiments, and Valeria Molinari for her insightful histology guidance.

I extend my profound thanks to my diligent proof-readers: Krit Sujarittam, Dr. Zheng Jiang, Shusei Kawara, William Lim Kee Chang, Afraa Alzoubi, and Dr. Sophie Morse. Your meticulous attention to detail has been an invaluable asset.

Thank you also to our collaborators for their assistance with this work: the Facility for Imaging by Light Microscopy (FILM) at ICL for microscopy advice; Dr Claire Higgins (ICL) for allowing me access to her cryostat; Craig Cummings in the ICR mechanical workshop; Richard Symonds-Taylor (ICR) for help with electronics and GUI amendments; Ruth Ruddle and Dr Florence Raynaud for LC-MS/MS analysis (ICR); Oren Becher group for providing cells; and Louise Howell for support at the Light Microscopy Facility (ICR).

Lastly, to my friends and family. To Alex for being my second brain and sharing the life rollercoaster. Lara, my partner in crime and continuously showing we can do hard things. Helene for #teamDelene antics, alongside Flat 11 and Rosie for endless culinary delights, and Kyle for his unwavering support. The Laps squad, Clapham Chasers swimmers and other

training partners who have been a beacon of sanity throughout. Finally, to my sister Kira, who will forever be my biggest cheerleader.

Publications

Conference presentations based on this doctoral thesis:

CHATTENTON, D. Drug delivery across the blood-brain barrier using acoustic wavelets and microbubbles for the treatment of diffuse intrinsic pontine glioma. *The Institute of Cancer Research Annual Conference, 2020, Online.* Oral presentation.

CHATTENTON, D. Drug delivery to the pons using short-pulse ultrasound and microbubbles. *The Institute of Cancer Research Annual Conference, 2021, Online.* Oral presentation.

CHATTENTON, D., COPPING, M., HERNANDEZ MIR, RIVENS, I., BOULT, J., JONES, C., ROBINSON, S., TER HAAR, G. & CHOI, J. Drug delivery across the blood-brain barrier using acoustic wavelets and microbubbles for the treatment of diffuse intrinsic pontine glioma. *OxCD3 Oncological Drug Delivery Conference, 2019, Oxford, United Kingdom.* Oral and poster presentation.

CHATTENTON, D., JIANG, Z., RIVENS, I., KRIT, BOULT, J., JONES, C., ROBINSON, S., TER HAAR, G. & CHOI, J. Establishing Drug Delivery to the Pons Using Short-pulse Ultrasound and Microbubbles. *The 20th International Society for Therapeutic Ultrasound, 2021, Online.* Poster presentation.

CHATTENTON, D., JIANG, Z., RIVENS, I., KRIT, BOULT, J., JONES, C., ROBINSON, S., TER HAAR, G. & CHOI, J. Establishing Drug Delivery to the Pons Using Short-pulse Ultrasound and Microbubbles. *53rd Annual Scientific Meeting of the British Medical Ultrasound Society, 2021, Online.* Oral presentation.

CHATTENTON, D., RIVENS, I., RUTH R., JIANG, Z., CARVALHO, D., SUJARITTAM, K., BOULT, J., JONES, C., ROBINSON, S., TER HAAR, G. & CHOI, J. Drug Delivery to a Diffuse Midline Glioma

Model Using Short-pulse Focused Ultrasound and Microbubble Exposure. *8th International Symposium on Focused Ultrasound, 2022, Bethesda, USA (online participant).* Oral presentation.

CHATTENTON, D., RIVENS, I., JIANG, Z., CARVALHO, D., SUJARITTAM, K., BOULT, J., JONES, C., ROBINSON, S., TER HAAR, G. & CHOI, J. Drug Delivery to the Pons Using Short-pulse Focused Ultrasound and Microbubble exposure for the Treatment of Diffuse Midline Glioma. *20th International Symposium on Paediatric Neuro-Oncology, 2022, Hamburg, Germany.* Oral presentation.

CHATTENTON, D., RIVENS, I., RUDDLE, R., JIANG, Z., CARVALHO, D., SUJARITTAM, K., BOULT, J., JONES, C., ROBINSON, S., TER HAAR, G. & CHOI, J. Drug Delivery to a Diffuse Midline Glioma Model Using Short-pulse Focused Ultrasound and Microbubble Exposure. *Cancer Research UK Brain Tumour Conference, 2022, London, UK.* Awarded oral presentation in the Future Leaders session.

CHATTENTON, D., RIVENS, I., RUDDLE, R., JIANG, Z., CARVALHO, D., SUJARITTAM, K., BOULT, J., JONES, C., ROBINSON, S., TER HAAR, G. & CHOI, J. Drug Delivery to a Diffuse Midline Glioma Model Using Short-pulse Focused Ultrasound and Microbubble Exposure. *Cancer Research UK Convergence Science Centre Symposium, 2022, London, UK.* Oral presentation

List of figures

Chapter 1:

Figure 1.2.1 The blood-brain barrier. 24
Figure 1.2.2 Transport across the blood-brain barrier. 25
Figure 1.2.3 The blood-tumour barrier. 26
Figure 1.3.1 MRI of DIPG tumours. 28
Figure 1.3.2 Genome organisation. 29
Figure 1.3.3 Histone modifications in diffuse intrinsic pontine glioma (DIPG). 30
Figure 1.3.4 Panobinostat in DIPG. 34
Figure 1.5.1 Ultrasound wave parameters. 39
Figure 1.5.2 Microbubble behaviour in the presence of ultrasound. 41
Figure 1.5.3 Ultrasound sequences. 45
Figure 1.9.1 Sagittal view of the mouse brain. 60

Chapter 2:

Figure 2.1 Experimental workflow. 65
Figure 2.3.1 ICL experimental setup. 68
Figure 2.3.2 ICL transducer, PCD and webcam on the 3D positioning mount. 69
Figure 2.3.3 Brain targeting using the ICL system. 71
Figure 2.4.1 ICR experimental setup. 72
Figure 2.4.2 ICR degassing system. 73
Figure 2.4.3 ICR mouse bed. 75
Figure 2.4.4 Adjustments to the ICR ultrasound setup. 77

Chapter 3:

Figure 3.3.1 Burst length study protocol. 89
Figure 3.3.2 Peak-rarefactional pressure study protocol. 91
Figure 3.3.3 Microbubble comparison protocol. 92
Figure 3.4.1 Burst length dependence for blood-brain barrier disruption (BBBD). 93
Figure 3.4.2 Fluorescent images of coronal brain slices from mice exposed to ultrasound and intravenous microbubbles of different burst lengths. 95
Figure 3.4.3 Fluorescence pixel intensity for four burst lengths. 96

Figure 3.4.4 Example energy heat maps for acoustic emissions recorded during ultrasound exposure resulting in blood brain barrier disruption (BBBD). 97
Figure 3.4.5 Mean energy for each burst recorded during ultrasound exposure indicating microbubble lifetime. 99
Figure 3.4.6 Fluorescence pixel intensity compared to total acoustic energy in mice exposed to ultrasound. 100
Figure 3.4.7 Blood-brain barrier disruption in mice exposed to ultrasound. 101
Figure 3.4.8 Pressure dependence for blood-brain barrier disruption (BBBD). 102
Figure 3.4.9 Energy heat maps of acoustic emissions recorded during ultrasound exposure where blood brain barrier disruption (BBBD) occurred. 104
Figure 3.4.10 Total acoustic energy at two acoustic pressures and the corresponding fluorescence pixel intensity. 105
Figure 3.4.11 Evans Blue extravasation indicating blood-brain barrier disruption after ultrasound exposure. 106
Figure 3.4.12 Microbubble influence on blood-brain barrier disruption as assessed by Evans Blue extravasation. 107
Figure 3.4.13 Examples of energy heat map calculated from acoustic emissions recorded during ultrasound exposure. 108
Chapter 4:
Figure 4.3.1 Schematic and photographs of height study. 126
Figure 4.3.2 ICR system targeting assessment. 129
Figure 4.4.1 Blood-brain barrier disruption in the pons at 1.05 MHz. 130
Figure 4.4.2 Targeting the pons at 1.05 MHz. 131
Figure 4.4.3 Drug delivery at three acoustic pressures and sham control. 132
Figure 4.4.4 Pressure dependence for blood-brain barrier disruption. 133
Figure 4.4.5 Quantification of tissue effects observed using H&E staining. 134
Figure 4.4.6 Histological assessment of brain slices from mice exposed to ultrasound with peak rarefactional pressure of 0 MPa (sham control) and 0.2 MPa. 135
Figure 4.4.7 The pons region of H&E-stained brain slices from mice exposed to ultrasound at peak rarefactional pressure of 0.4 MPa. 135

Figure 4.4.8 Gross histological damage seen in brains of two mice exposed to ultrasound at peak rarefactional pressure of 0.6 MPa. 136
Figure 4.4.9 Histological assessment of brain slices from mice exposed to ultrasound at peak rarefactional pressure of 0.6 MPa, pons region shown. 137
Figure 4.4.10 Total acoustic emission energy as a function of acoustic pressure and the corresponding fluorescence pixel intensity. 138
Figure 4.4.11 ICR system Evans Blue tests. 139
Figure 4.4.12 ICR system dextran delivery. 140
Figure 4.4.13 ICR targeting assessment: comparison of model drug (dextran) extravasation in non-tumour-bearing mice with tumour growth in a mouse model. 141
Figure 4.4.14 Co-localisation of tumour growth and dextran extravasation. 141
Figure 4.4.15 Histological assessment after ultrasound exposure (peak rarefactional pressure: 0.4 MPa) on the ICR system. 142

Chapter 5:

Figure 5.3.1 In vitro panobinostat cytotoxicity assay. 156
Figure 5.3.2 Pharmacokinetic study of panobinostat (LBH-589) in C57BL/6J mice. 157
Figure 5.3.3 Tolerability and assessment of panobinostat delivered across the blood-brain barrier via focused ultrasound and microbubbles in non-tumour bearing mice. 158
Figure 5.3.4 Tolerability and assessment of panobinostat delivered across the blood-brain barrier via focused ultrasound and microbubbles in non-tumour bearing mice: revised protocol. 160
Figure 5.3.5 Tumour inoculation. 162
Figure 5.3.6 Tolerability and efficacy of ultrasound and microbubble mediated blood-brain barrier disruption in a DIPG tumour model. 164
Figure 5.3.7 Assessment of panobinostat delivery across the blood-brain barrier using focused ultrasound and microbubbles in a DIPG mouse model. 166
Figure 5.4.1 In vitro cytotoxicity of panobinostat. 168
Figure 5.4.2 Pharmacokinetic study of panobinostat (LBH-589) in C57BL/J mice. 169
Figure 5.4.3 Tolerability and efficacy of panobinostat delivered across the blood-brain barrier via focused ultrasound in non-tumour bearing mice: study one. 171

Figure 5.4.4 Tolerability and efficacy of panobinostat delivered across the blood-brain barrier via focused ultrasound in non-tumour bearing mice: study one. 172
Figure 5.4.5 Tolerability and efficacy of panobinostat delivered across the blood-brain barrier via focused ultrasound in non-tumour bearing mice: study two. 173
Figure 5.4.6 Tolerability and efficacy of panobinostat delivered across the blood-brain barrier via focused ultrasound in non-tumour bearing mice: study two. 174
Figure 5.4.7 Tolerability of panobinostat delivered across the blood-brain barrier using focused ultrasound in non-tumour bearing mice. 176
Figure 5.4.8 T2-weighted MRI of tumour growth of a DIPG cell line. C57BL/6J mice were implanted with a murine DIPG cell line in the pons region. 177
Figure 5.4.9 Tolerability of blood-brain barrier disruption in a DIPG mouse model. 178
Figure 5.4.10 Blood-brain barrier disruption in a DIPG mouse model. 179
Figure 5.4.11 Blood-brain barrier disruption in a DIPG mouse model, despite a fluid-filled region. 180
Figure 5.4.12 Tissue effects of blood-brain barrier disruption in a DIPG mouse model. 181
Figure 5.4.13 Ultrasound-mediated panobinostat delivery in a DIPG tumour model. 182
Figure 5.4.14 Ultrasound-mediated panobinostat delivery in a DIPG tumour model. 183
Figure 5.4.15 Ultrasound-mediated panobinostat delivery in a DIPG tumour model. 185
Figure 5.4.16 Ultrasound-mediated panobinostat delivery in tumour bearing (TB) and non-tumour bearing (NTB) mice. 186

Chapter 7

Figure 7.1 Beam profiles at 300 kHz (ICL). 200
Figure 7.6.1.1 Beam profiles at 1.05 MHz (ICL). 201
Figure 7.6.1.2 Beam profiles at a centre frequency of 1 MHz (ICR). 202

List of tables

Chapter 1:

Table 1.1 Clinical trials involving panobinostat for the treatment of DIPG. 37

Table 1.2 Commercially available microbubbles used in combination with focused ultrasound for blood-brain barrier disruption. 43

Table 1.3 Clinical trials involving brain tumours using focused ultrasound and microbubbles. 57

Table 1.4 In vivo studies using FUS and microbubbles for drug delivery to the pons. 62

Table 2.1 Ultrasound exposure parameters. 67

Chapter 2:

Table 2.2 Microbubbles, and their properties, use in the studies described in this thesis. 78

Table 2.3 Model drugs used in the studies described in this thesis. 79

Chapter 5:

Table 5.1 The cell lines tested in vitro. p. refers to the location of the mutation. 155

Table 5.2 Seeding density for in vitro panobinostat cytotoxicity assay. 156

Table 5.4 The GI_{50} of LBH-589 (panobinostat) in four diffuse intrinsic pontine glioma (DIPG) cell lines. 167

Abbreviations

ANOVA	Analysis of variance
ATP	Adenosine triphosphate
BBB	Blood-brain barrier
BBBD	Blood-brain barrier disruption
BMECs	Brain microvascular endothelial cells
BRF	Burst repetition frequency
BTB	Blood tumour barrier
CAR	Chimeric antigen receptor
CED	Convection enhanced delivery
CNS	Central nervous system
CSF	Cerebrospinal fluid
CT	Computed tomography
CTG	CellTiter-Glo®
DC	Direct current
DIPG	Diffuse intrinsic pontine glioma
DMEM	Dulbecco's modified eagle medium
DMSO	Dimethyl sulfoxide
DPPA	Dipalmitoylphosphatidic acid
DPPC	Dipalmitoylphosphatidylcholine
DPPE	Dipalmitolyphosphatidylethanolamine
DPPG.Na	Dipalmitoylphosphatidylglycerol sodium
DSCP	Distearoyl-phosphatidylcholine
EEG	Electroencephalogram
EGF	Epidermal growth factor
FDA	Food and Drug Administration
FGF	Fibroblast growth factor
FITC	Fluorescein isothiocyanate
FOV	Field of view

FUS	Focused ultrasound
FWHM	Full width at half maximum
GBM	Glioblastoma
GUI	Graphical user interface
H&E	Haematoxylin & eosin
HDAC	Histone deacetylase
Hz	Hertz
ICL	Imperial College London
ICR	Institute of Cancer Research
IHP	In-house prepared
IP	Intraperitoneal
IV	Intravenous
JAM	Junctional adhesion molecule
LC-MS/MS	Liquid chromatography triple quadrupole mass spectrometry
MALDI	Matrix-assisted laser desorption ionization
MB	Microbubble
MRI	Magnetic resonance imaging
MS	Mass spectrometry
mTOR	Mammalian target of rapamycin
NF-kB	Nuclear factor kappa B
NHP	Non-human primates
NICE	National Institute for Heath and Care Excellence
NSB	Non-invasive surgery and biopsy
NTB	Non-tumour bearing
OCT	Optimum cutting compound
OS	Overall survival
Pa	Pascal
PARP	Poly-ADP ribose polymerase
PBS	Phosphate buffered saline

PCD	Passive cavitation detector
PDGF	Platelet derived growth factor
PEG	Poly(ethylene glycol)
PET	Position emission tomography
PFS	Progression-free survival
PIL	Personal licence
PPL	Project licence
PRF	Pulse repetition frequency
PRP	Peak-rarefactional pressure
PVDF	Polyvinylidene difluoride
rAAV	Recombinant adeno-associated virus
RARE	Rapid acquisition with refocused echoes
RF	Radio frequency
ROI	Region of interest
ROUT	Robust regression followed by outlier elimination
RPM	Revolutions per minute
SSEP	Somatosensory evoked potentials
sTRAIL	Secreted form of necrosis factor-related apoptosis-inducing ligand
SWI	Susceptibility weighted imaging
TB	Tumour bearing
TEeff	Effective echo time
TR	Repetition time
UK	United Kingdom
USA	United States of America
WHO	World Health Organisation

1 Introduction

1.1 Motivation

The prevalence of brain diseases is increasing (Raggi and Leonardi, 2020). These include brain tumours e.g. glioblastoma (GBM), neurodegenerative diseases e.g. Alzheimer's and Parkinson's, and autoimmune diseases e.g. multiple sclerosis. With improved diagnostic and therapeutic capabilities, cancer mortality rates are expected to fall. Yet over the last decade, brain, other central nervous system (CNS) and intracranial tumour (malignant and non-malignant) mortality rates have remained stable in the United Kingdom (UK) and are projected to fall by less than 1% by 2040 (CRUK).

Therapeutic options for brain tumours are rarely curative, and result in many undesired toxic effects (Huang et al., 2023). The classical therapeutic regimen for brain cancer includes surgical resection followed by chemotherapy and/or radiotherapy (Davis, 2016). Temozolomide is an example of a standard adjuvant chemotherapy for high grade GBM. However, the chances of relapse for malignant brain tumours are very high (Gill et al., 2014, Qi et al., 2022). New therapies have struggled with specificity, low efficacy, and toxic side effects (Zhao et al., 2023).

Poor therapeutic outcomes are largely attributed to the inability of drugs to cross the brain blood vessel walls, known as the blood-brain barrier (BBB), to reach the brain extravascular tissue (McDannold et al., 2011). In general, it is accepted that bioavailability and distribution of drugs in CNS tumours is poor compared to non-CNS tumours (Quader et al., 2022). Methods of overcoming the BBB are being explored to expand treatment options for brain tumours including diffuse intrinsic pontine glioma (DIPG).

DIPG, a lethal paediatric brain cancer, is highly resistant to standard therapies (Himes et al., 2022, Zhou et al., 2017). Radiotherapy is the current standard of care and is only able to achieve a palliative effect, surgical resection is not viable and chemotherapy trials have had poor results (Himes et al., 2022). There is a lack of contrast enhancement on magnetic resonance imaging (MRI), suggesting that these tumours have an intact BBB which may impede the penetration of therapeutic agents into the tumour tissue. There is therefore strong motivation for improved drug delivery for this disease.

1.2 The blood-brain barrier and blood tumour barrier

The BBB is a physical and chemical barrier that prevents large (>400 Da) and hydrophilic drugs from entering the brain, thus inhibiting the treatment of neurological conditions such as brain cancer (Zlokovic, 2008). Even when these agents can enter the brain, they are often exported by active transport mechanisms. Overall, the BBB precludes drug development for ~95% of molecules (Dong, 2018).

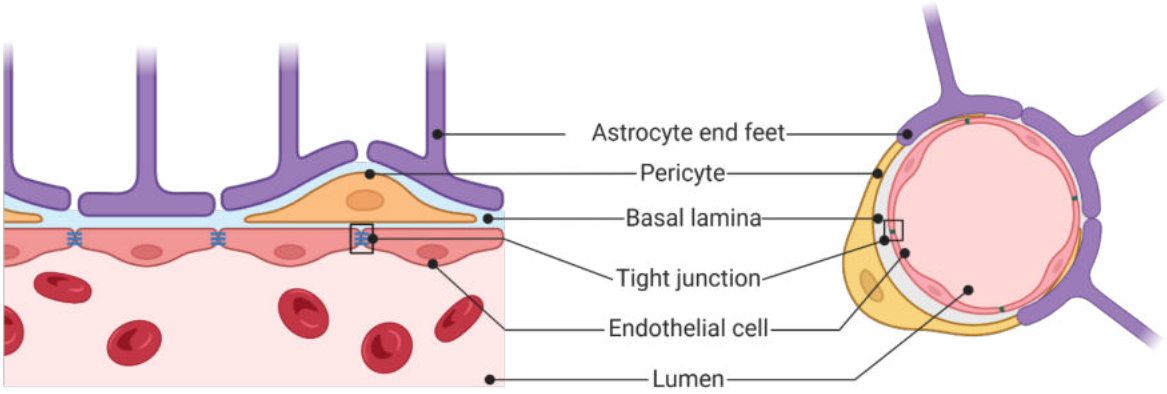

Figure 1.2.1 The blood-brain barrier. *The blood-brain barrier is a semi-permeable barrier that prevents large and hydrophilic substances from entering the brain parenchyma. Endothelial cells and basal lamina are surrounded by astrocyte end feet and pericytes to form the neurovascular unit. Tight junctions join adjacent endothelial cells together. Figure created using Biorender.com using information from Bernardo-Castro et al. (2020).*

The BBB consists of brain microvascular endothelial cells (BMECs), and a basal lamina surrounded by pericytes and astrocytic end-feet which form a neurovascular unit (**figure 1.2.1**) (Knox et al., 2022). Adjacent endothelial cells are connected by tight junctions, not present in blood vessels elsewhere in the body, forming a physical barrier (Stamatovic et al., 2016). Tight junctions consist of transmembrane proteins: junctional adhesion molecules (JAMs), claudin and occludin (**figure 1.2.2**). Claudin is the primary sealing protein, and occludin regulates paracellular permeability. Together, claudin and occludin determine the barrier and functionalities of tight junctions. These tight junction proteins are anchored in place by zonula occludins, present in the cytoskeleton of endothelial cells.

The BBB is a highly selective filter which allows passage of selected molecules through controlled routes (Zaragoza, 2020). Transport across the BBB can be transcellular (across cells) or paracellular (between cells; **figure 1.2.2**). Transcellular pathways across the BBB include

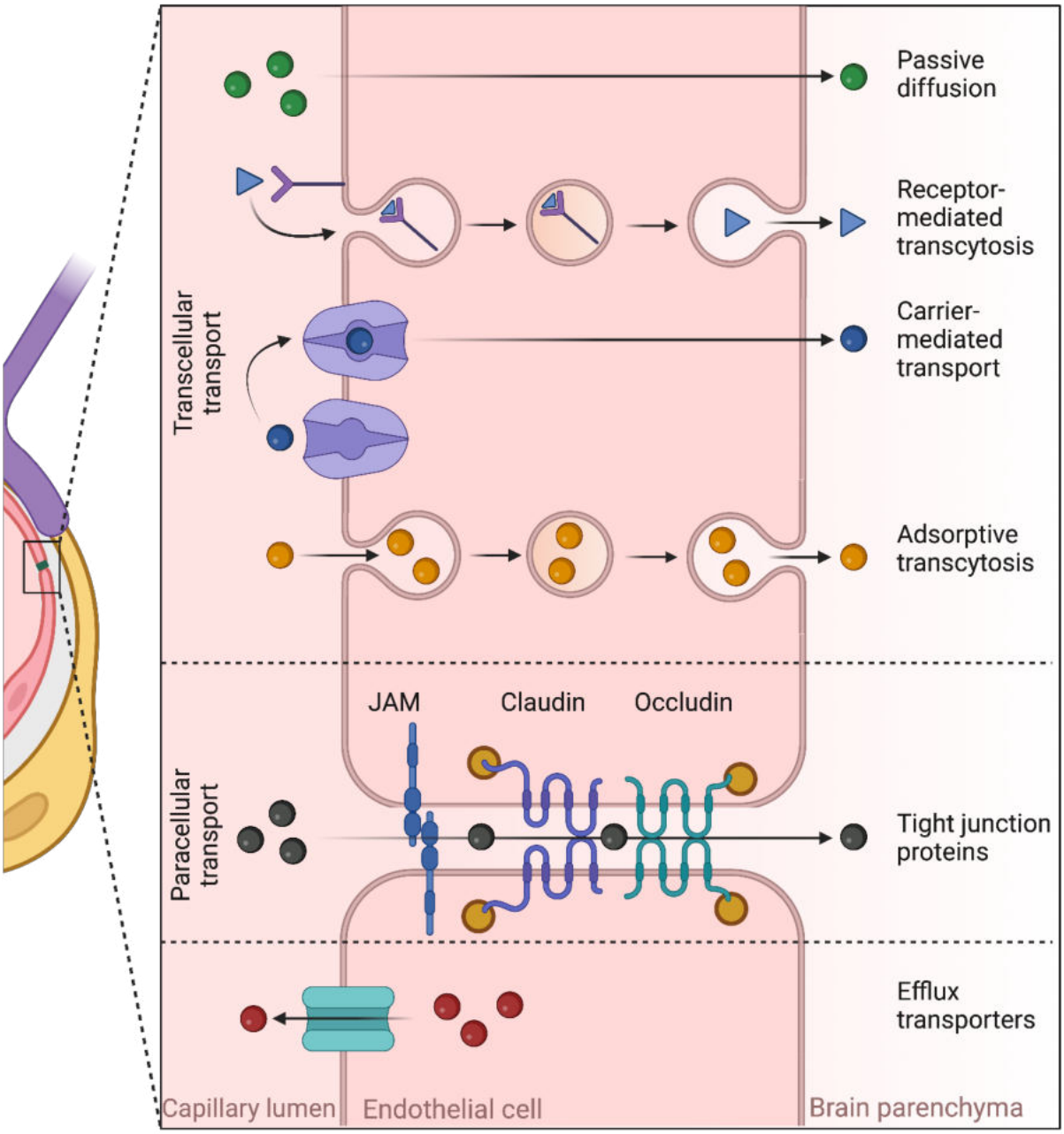

Figure 1.2.2 Transport across the blood-brain barrier. *Substances can cross the blood-brain barrier through transcellular routes including passive diffusion, receptor-mediated transcytosis, carrier-mediated transport, and adsorptive transcytosis. Paracellular transport occurs through tight junctions which are composed of junction adhesion molecules (JAM), claudin and occludin proteins. Efflux transporters are responsible for the removal of substances from endothelial cells and brain parenchyma, into the blood stream. Figure created using Biorender.com using information from Bernardo-Castro et al. (2020).*

passive diffusion, receptor-mediated transcytosis, carrier-mediated transport, and adsorptive transcytosis (Bernardo-Castro et al., 2020). To achieve paracellular transport, molecules pass passively through tight junction proteins, as described above. Efflux transporters are also present in endothelial cells. These are responsible for removing substances from the brain parenchyma.

Neurological diseases often affect the function and permeability of the BBB. In brain cancers, the BBB/ blood tumour barrier (BTB), is typically heterogenous with highly variable permeability within different areas of the same tumour (Zaki Ghali et al., 2019). In some cancers such as GBM, the BTB tends to be more permeable in the tumour core and intact at its periphery. Whilst some level of therapeutics might be able to reach the tumour, the BTB is thought to be a critical factor in GBM recurrence. Other brain tumours have a near impenetrable BTB; the BTB in diffuse DIPG has been deemed to be a 'super BBB' with almost no penetration of molecules (Warren, 2018).

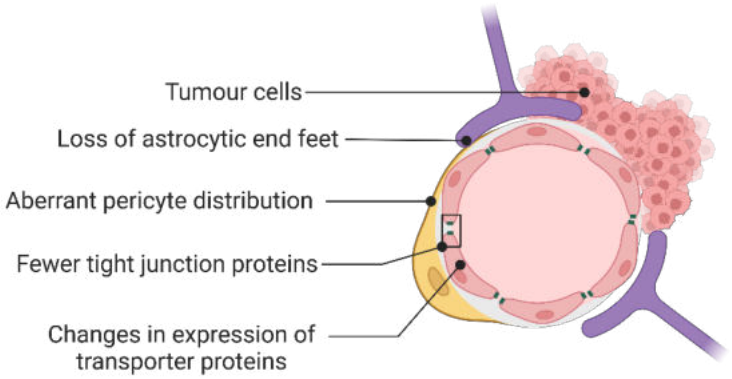

Figure 1.2.3 The blood-tumour barrier. *The presence of a tumour affects the permeability of the blood-brain barrier. This often includes the loss of astrocytic end feet, aberrant pericyte distribution, fewer tight junction proteins and changes in expression of transporter proteins. Figure created using Biorender.com using information from (Allen and Limoli, 2022, Steeg, 2021).*

1.3 Diffuse intrinsic pontine glioma (DIPG)

DIPG represents 10-15% of all childhood brain tumours and is the leading cause of brain tumour related death in children (Jones et al., 2017, Vanan and Eisenstat, 2015). Its poor prognosis is attributed to the critical location and growth pattern of the tumour which

originates in the pons and spreads diffusely (Aziz-Bose and Monje, 2019, Qin et al., 2017, Caretti et al., 2014). The pons is a critical brain stem structure which controls several basic functions including breathing and swallowing. It is therefore essential to remove or kill tumour cells selectively without causing significant damage to the normal tissue.

1.3.1 DIPG tumour biology

DIPG tumours are usually diagnosed using MRI which shows hypointensity on a T1-weighted scan with indiscrete margin and hyperintensity on T2-weighted images without contrast enhancement (**figure 1.3.1**)(Williams et al., 2020). The tumour core is generally located in the pons, encasing the basilar artery, the main artery that supplies blood to the back portion of the brain. Beyond the tumour core, the tumours infiltrate along fibre tracts to the thalamus and cerebellum (Kluiver et al., 2020).

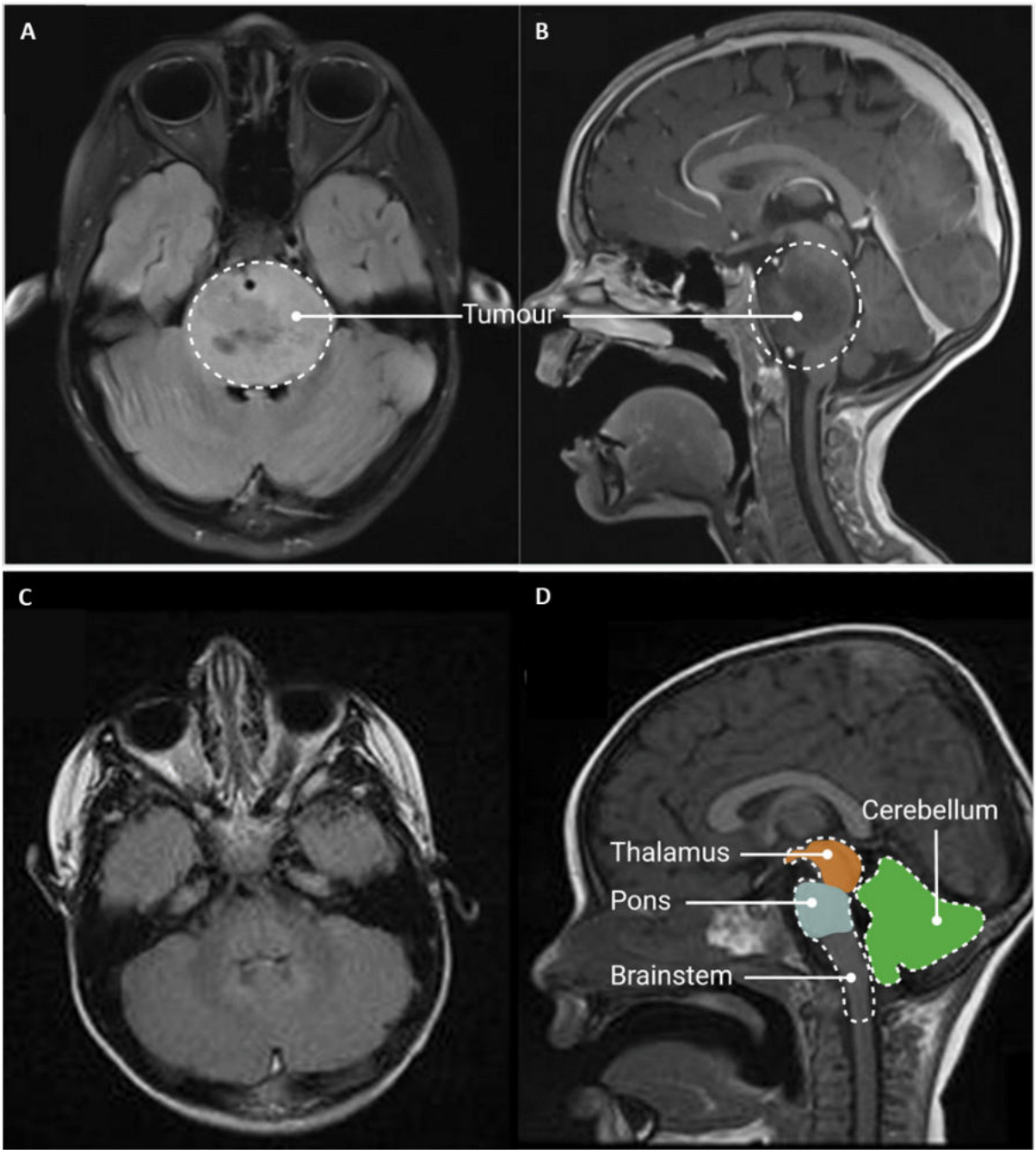

Figure 1.3.1 MRI of DIPG tumours. *MRI images of a radiographically classic DIPG including (A) axial T2 fluid attenuated inversion recovery (FLAIR) and (B) sagittal T1 post-contrast images, with the tumour indicated by the dashed circle. Compared to corresponding scans without a tumour in the (C) axial and sagittal planes. DIPG arises in the pons (blue) which is located in the brainstem (dashed white line) and often grows infiltratively along fibre tracts to the thalamus (orange) and cerebellum (green). A&B from Vitanza and Monje (2021) and C&D from Casey et al., (2017).*

Due to the delicate nature of the brain stem, needle biopsies have only been used to confirm diagnosis in Europe since 2003 (Roujeau et al., 2007). This has led to a rapid improvement in the understanding of the disease and identification of therapeutic targets. Importantly these tumours are molecularly distinct from adult high-grade gliomas (Schroeder et al., 2014). The improved molecular and genomic insights have identified key epigenetic modifications present in DIPG tumours (Srikanthan et al., 2021).

Epigenetics relates to DNA changes affecting gene expression without altering the DNA sequence (Weinhold, 2006). Eight histone proteins join to form a histone octamer that DNA wraps around to form a nucleosome, like beads on a string (**figure 1.3.2**). Nucleosomes condense together to form chromatin that forms chromosomes. When nucleosomes are packed tightly together, DNA becomes inaccessible to transcription factors and gene expression does not occur (Bednar et al., 1998). The histone proteins have 'tails' to which

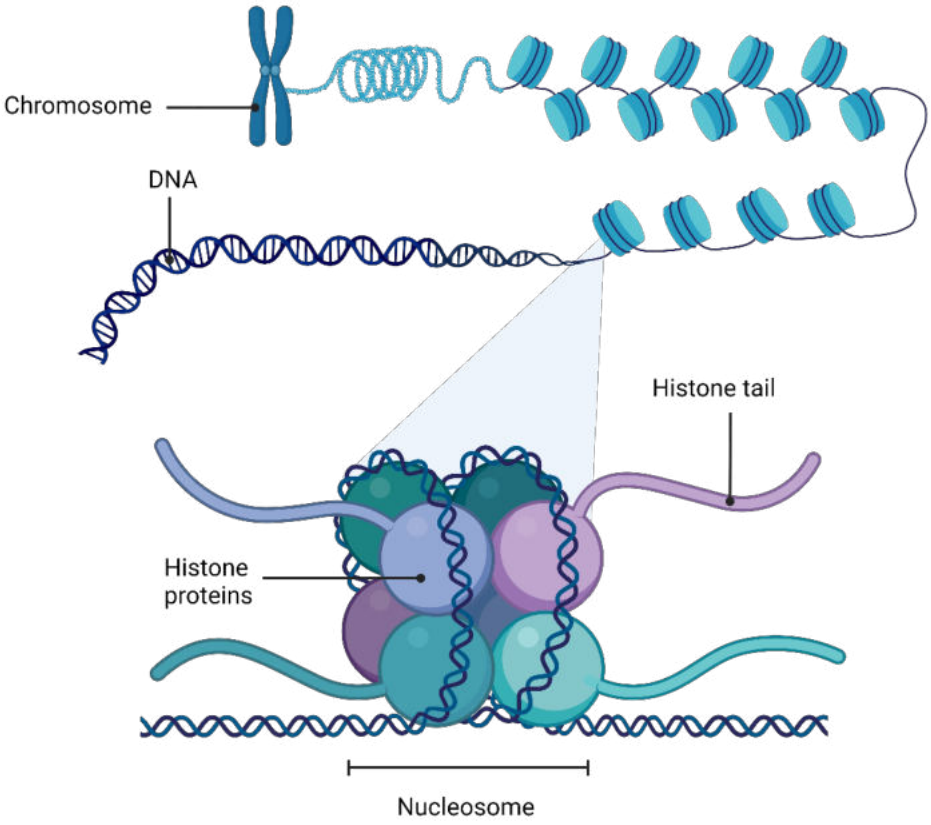

Figure 1.3.2 Genome organisation. *The DNA double helix wraps around a complex of histone proteins to form a nucleosome. Nucleosomes are condensed to form chromosomes. Modifications of histone tails affect gene expression. Figure created using Biorender.com.*

epigenetic modifiers bind to alter nucleosome interactions and therefore gene expression. Epigenetic modifications include acetylation which increases gene expression, and methylation which reduces gene expression (**figure 1.3.3A**).

The increase in molecular knowledge about DIPG obtained from needle biopsies has led to the identification of histone gene mutations, genetic drivers, and methylation changes (Srikanthan et al., 2021). It has been learnt that 80% of DIPGs have lysine-to-methionine substitutions at position 27 in Histone 3 (**figure 1.3.3B**). These epigenetic changes affect the

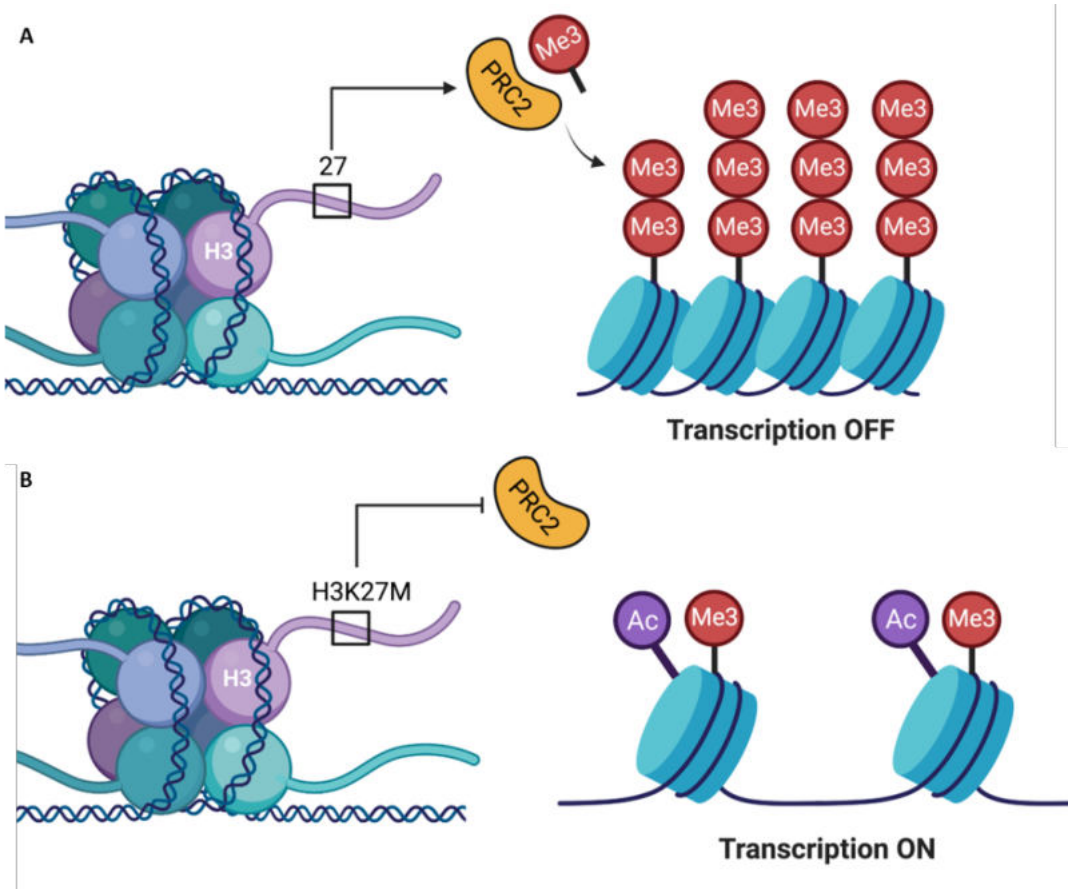

Figure 1.3.3 Histone modifications in diffuse intrinsic pontine glioma (DIPG). *Epigenetic modifiers bind to histone tails altering gene expression. (A) Position 27 on histone tail H3 promotes methylation through the polycomb repressive complex 2 (PRC2) resulting in transcriptional repression of genes e.g. oncogenes. (B) Approximately 80% of DIPGs harbour a lysine-to-methionine substitution at position 27 on histone H3 resulting in suppression of PRC2, leading to loss of methylation and enabling transcription of oncogenes. Figure created using Biorender.com.*

genes encoding H3.3 (*H3F3A*) and H3.1 (*HIST1H3B*) - H3K27M. As a result, the world health organisation (WHO) classification changed in 2016 to include 'diffuse midline glioma H3 K27M-mutant' as a new tumour entity which includes DIPGs with the K27 mutation (Louis et al., 2016). There was a further WHO classification change in 2021 to include the subset of DIPGs lacking the H3K27M mutation but which exhibited global loss of tri-methylation (Kurokawa et al., 2022). Intra- and inter-tumoral heterogeneity has been documented (Hoffman et al., 2016). Immunohistological staining may be used for diagnosis and the H3 status/ isoform is likely to give a prognostic indication. Histologically, DIPG tumours present with high-grade astrocytic histology with increased mitotic activity, microvascular proliferation and/or necrosis (Yoshimura et al., 2003).

1.3.2 Therapeutic targets

Unveiling information about the molecular profile of the disease has enabled the identification of therapeutic targets. Mounting evidence from *in vitro* drug screens suggests that many available cancer drugs could be repurposed for DIPG (Grasso et al., 2015b). Such targets include the tumour microenvironment (Ross et al., 2021, Lin et al., 2016), tumour metabolism (Chung et al., 2020, Tsoli et al., 2018, Khan et al., 2021), and epigenetic landscape (Chan et al., 2013, Ehteda et al., 2021, Gasparian et al., 2011, Taylor et al., 2015, Lovén et al., 2013, Piunti et al., 2017, Grasso et al., 2015a, HasHizume, 2017, Knudsen and Witkiewicz, 2017, Mohammad et al., 2017). H3K27M drives DIPG growth suggesting its role as a key promoter of tumorigenesis through global reduction in the repressive epigenetic mark H3K27me3 (enabling expression of oncogenes) (Harutyunyan et al., 2019). There is also evidence of a link between DIPG cell metabolism and the underlying activation status of key epigenetic markers in DIPGs (Hayden et al., 2021). Research efforts have been focused on the development of pharmacological inhibitors designed to regulate these epigenetic mechanisms, targeting epigenetic modifiers.

As the H3K27M mutation is present in approximately 80% of DIPGs with a single point mutation, the histone modification could be a simple therapeutic target. Histone deacetylase (HDAC) inhibitors (e.g. panobinostat) and demethylase inhibitors (e.g. GSK-J1/4) have shown

promise *in vitro* and *in vivo* (Grasso et al., 2015b, Bagcchi, 2015, HasHizume, 2017, Katagi et al., 2019).

Immunotherapy stimulates the body's immune system to attack cancer cells with effects that can include complete remission (Abdelhakam et al., 2020). The DIPG tumour microenvironment has been reported as non-inflammatory (lack of immune cells) but there is conflicting evidence regarding the presence of tumour-associated macrophages or the lack of inflammatory cytokine secretion (Lin et al., 2018). It is generally accepted that there is no T-cell infiltration into DIPG tumours, and so immunotherapy should be focused on recruitment or introduction of immune cells into the tumour. Initial results with anti-GD2 chimeric antigen receptor (CAR) T-cell therapy have provided early promise in *in vivo* DMG xenografts (Mount et al., 2018).

1.3.3 Clinical trials for DIPG

Approximately 250 clinical trials have been initiated for DIPG treatment, but monotherapies and combination chemotherapies have so far shown no benefit (Vanan and Eisenstat, 2015, Long et al., 2017, Frazier et al., 2009, Grimm and Chamberlain, 2013). Poor treatment outcomes have mostly been attributed to the lack of effective drug delivery across the BBB, which can also explain why successful therapeutics against other gliomas have been ineffective in DIPG (Veringa et al., 2013). Drug doses have been increased to overcome low BBB penetration, but the doses required for a therapeutic effect cause toxicity elsewhere. In order to circumvent the BBB, attempts have been made to modify drugs to increase their solubility and reduce cytotoxicity, but overall, there is poor progress in the development of DIPG treatments (Dalle Ore et al., 2023).

1.3.4 Panobinostat

Panobinostat, a HDAC inhibitor, is currently used in the clinic for the treatment of multiple myeloma (a bone marrow cancer)(Moore, 2016). The drug is involved in the deacetylation of histone and non-histone cellular proteins as well as in interfering with cell cycle control genes (**figure 1.3.4**). Panobinostat has shown a broad range of potency in different DIPG subgroups,

whilst drugs used to treat other brain tumours e.g. temozolomide for GBM, have had no effect (Bailey et al., 2013).

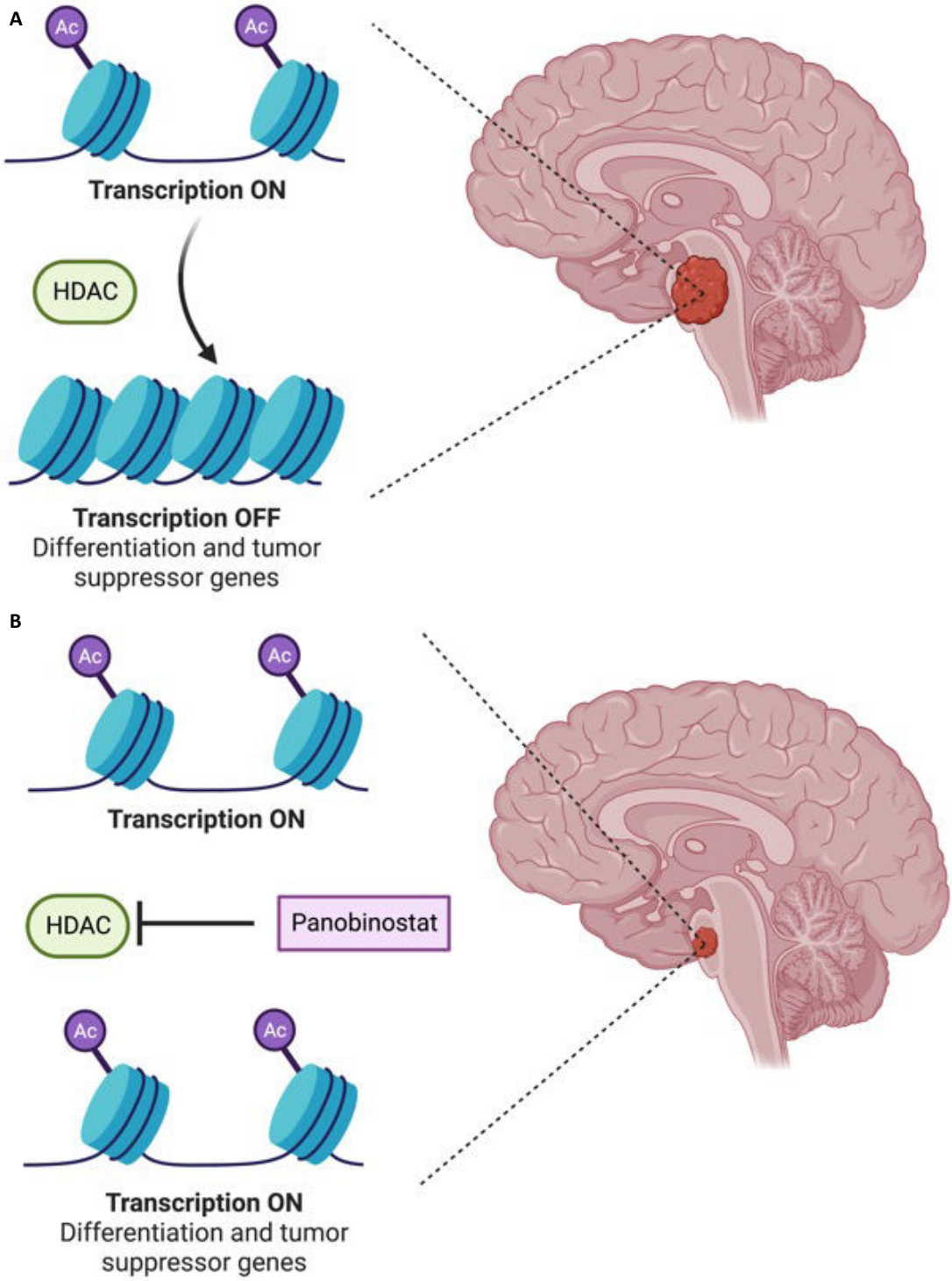

Figure 1.3.4 Panobinostat in DIPG. *(A) Histone deacetylases (HDACs) remove acetyl epigenetic modifications resulting in reduced gene expression e.g. differentiation and tumour suppressor genes, in DIPG. (B) Panobinostat is a HDAC inhibitor, restoring gene expression resulting in a therapeutic effect. Figure made using Biorender.com.*

Panobinostat has shown promise against DIPG cell lines *in vitro* but few studies have achieved a therapeutic effect at non-toxic/tolerated doses *in vivo* (Grasso et al., 2015b, Hennika et al., 2017). Despite its small size (349 Da), it appears that panobinostat is unable to cross the BBB. Alongside difficulty in crossing the BBB, panobinostat is also a substrate for the P-glycoprotein (P-gp) efflux pump, meaning it is likely to be removed promptly from the brain parenchyma (Homan et al., 2021). Methods for improving drug delivery across the BBB are required for true assessment of this drug against DIPGs.

There are six clinical trials that are either completed, active or have been withdrawn and involve panobinostat for DIPG patients: three in combination with another therapeutic agent (marizomib, everolimus or ONC201), one investigating the side effects and the optimal dose of Panobinostat, and two investigating methods of improving panobinostat concentrations in the brain (focused ultrasound and convection enhanced delivery; **table 1.1**).

Marizomib is the only known BBB permeable proteasome inhibitor which blocks normal cell protein recycling (Di et al., 2016). Panobinostat and marizomib showed potent anti-tumour efficacy in patient-derived xenograft models, leading to a greater increase in median survival when given in combination than individually (Lin et al., 2019). Moreover, there was no difference in markers of neurotoxicity (assessed by immunohistochemistry of cleaved caspase-3) between the treated and control groups. Everolimus is a mammalian target of rapamycin (mTOR) inhibitor and has been shown to increase tumour-infiltrating lymphocytes, normalise tumour blood vessels and improve adaptive cell transfer therapy (Kirchner et al., 2004). Moreover, everolimus can inhibit the efflux pump P-gp, for which panobinostat is a substrate, providing a synergistic effect. ONC201 is a small molecule that can induce the cellular integrated stress response pathway, resulting in tumour cell death (Ralff et al., 2017).

If a method of improved drug delivery to DIPG tumours can be established, there is hope for patients with this life-limiting disease.

Table 1.1 Clinical trials involving panobinostat for the treatment of DIPG.

ClinicalTrials.gov identifier	Phase and aim	Therapeutic Agent	Status
NCT04341311	I/II: Safety, tolerability, and preliminary efficacy	Marizomib and panobinostat	Active, not recruiting
NCT02717455	I: Side effects and best dose	Panobinostat	Active, not recruiting
NCT03632317	II: Activity of drugs	Panobinostat and Everolimus	Withdrawn
NCT03566199	I/II: Safety and tolerability of drug via convection enhanced delivery	Soluble form of panobinostat (MTX110)	Completed
NCT04804709	I: Safety and tolerability of drug with ultrasound treatment	Panobinostat	Active, not recruiting
NCT05009992	II: Effectiveness of drug combinations	ONC201 with panobinostat or paxalisib	Recruiting

1.4 Methods of overcoming the blood-brain barrier and brain blood tumour barrier

i. Osmotic agents

Intravenous administration of osmotic agents such as mannitol increases the universal permeability of the BBB but lacks specific targeting that is important for cancer, to avoid off-target effects. Osmotic agents have resulted in undesirable side effects including neurological deficits, syndromes similar to stroke, possible migration of tumour cells, seizures, and new tumour-nodule formation at distant brain locations (Doolittle et al., 2000, Marchi et al., 2007).

ii. Convection enhanced delivery

Convection enhanced delivery (CED) is a more targeted approach and involves direct injection of the drug into the tumour through surgically implanted catheters (Stine and Munson, 2019). However, this invasive technique comes with the risks of any neurosurgical intervention. Moreover, there is a recovery period necessary between implantation of the catheters and treatment initiation, which is undesirable for cancer patients.

iii. Focused ultrasound and microbubbles

The use of focused ultrasound (FUS) and microbubbles (MBs) is a non-invasive drug delivery technique that temporarily and reversibly disrupts the BBB, overcomes invasive safety concerns, and provides precise targeting (Hynynen et al., 2001). This method enables the delivery of a wide range of imaging and therapeutic agents into the brain parenchyma and is discussed in more detail in the following section, as it is the main technique being investigated in this thesis work.

1.5 Blood-brain barrier disruption using focused ultrasound and microbubbles

FUS exposures in the presence of microbubbles can deliver drugs across the BBB to deep subcortical structures. The technique was first presented in publication in 2001 then, advanced to a non-invasive and localised procedure (Hynynen et al., 2001, Choi et al., 2007b, McDannold et al., 2005, Hynynen et al., 2005). In this technique, pre-formed, gas-filled microbubbles are administered systemically into the bloodstream. When exposed to ultrasound, the microbubbles oscillate volumetrically (Apfel, 1997). Microbubble activity in blood vessels can result in an increase in permeability of the BBB, allowing therapeutics in the bloodstream to enter the brain parenchyma.

1.5.1 Focused ultrasound

Ultrasound is a pressure wave operating above the human audible frequency range (>20 kHz). In the medical world, it is most known for imaging, but has considerable therapeutic applications (Miller et al., 2012). Sound waves are generated by applying an electrical current to a piezoelectric crystal, mounted in a transducer head. The voltage applied to a piezoelectric crystal causes it to expand and contract, generating sound waves that radiate from the transducer (Hunt et al., 1983). Sound propagates through a medium as regions of high (compression) and low (rarefaction) pressure (**figure 1.5.1**).

Ultrasound waves can be characterised by several parameters (**figure 1.5.1**). Frequency is the number of wave cycles per second and measured in Hertz (Hz). Therapeutic ultrasound typically uses a frequency lower than 3 MHz (Morishita et al., 2014) . The period (s) is the length of time required for a complete cycle, whilst the wavelength (m) is the distance between two adjacent wave peaks. Frequency (Hz) is inversely related to period and

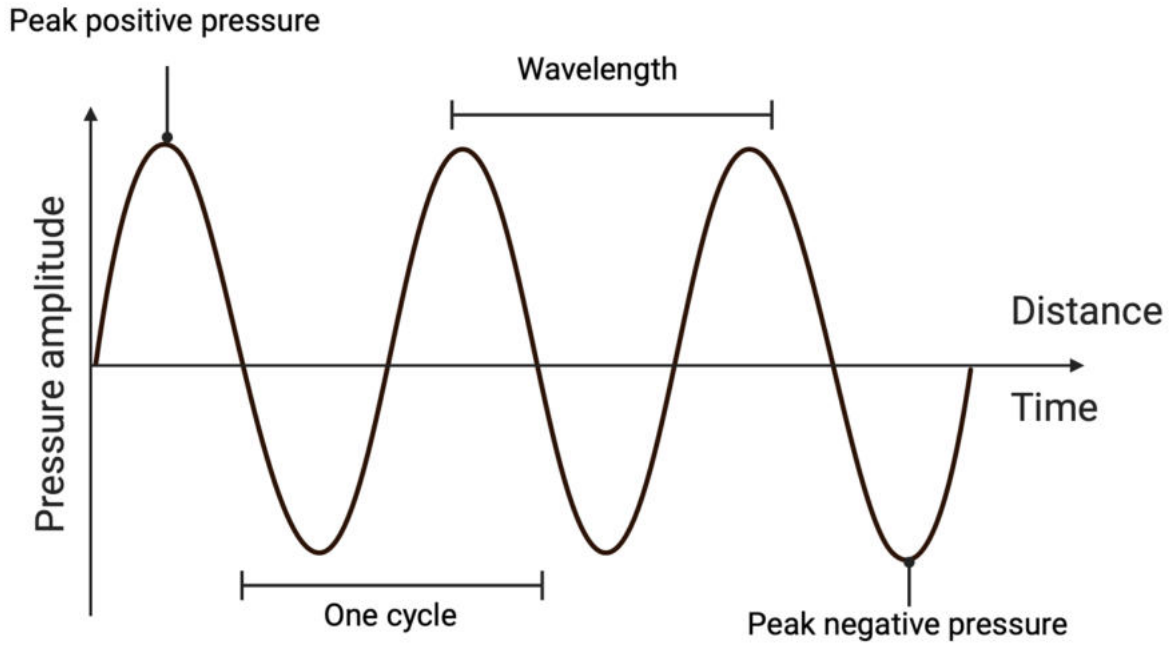

Figure 1.5.1 Ultrasound wave parameters. *Ultrasound can be characterised by the maximum peak positive and peak negative pressure amplitudes. Wavelength is the distance between two adjacent wave peaks and is inversely proportional to the frequency. Figure made using Biorender.com.*

wavelength so that the shorter the wavelength, the higher the frequency. The ultrasound pressure is reported in terms of the amplitude of the wave measured in Pascals (Pa). The speed of the ultrasound is the rate at which waves pass through a medium and depends on the characteristics of the medium.

As ultrasound travels through tissue, the acoustic energy is attenuated. Sound waves can be reflected and refracted at interfaces of different tissue. Within the tissue, the ultrasound energy is converted to heat (absorption) and scattered (when ultrasound meets structures smaller than its wavelength) (Shriki, 2014). Morse (2020) reported an 11% decrease in peak-rarefactional pressure (centre frequency: 1 MHz, short-pulse sequence) due to attenuation by the mouse skull.

1.5.2 Microbubbles

The microbubbles used for FUS-mediated BBBD are gas-filled and micron-sized with a lipid or protein shell (**figure 1.5.2A**) (Lindner, 2004). Their size and behaviour within the vasculature is similar to red blood cells and they are routinely used as medical imaging contrast agents (Sirsi and Borden, 2009). The gas core scatters ultrasound for imaging purposes and can enhance drug delivery due to volumetric oscillations (Nolsøe et al., 2016). The shell stabilises the gas core and, commonly used Definity® and SonoVue® microbubbles have poly(ethylene glycol) (PEG) brushes attached to prevent coalescence and increase *in vivo* half-life (Ferrara et al., 2009).

When exposed to an ultrasound field in liquid, microbubbles are driven into radial oscillations by the rarefactional and compressional phases of the sound wave; a behaviour known as acoustic cavitation (**figure 1.5.2B**) (Apfel, 1997, Leighton and Apfel, 1994). The radial oscillations are determined by the ultrasound pressure, inertia of the surrounding liquid and internal gas pressure (Flynn, 1975, Morse, 2020). At low acoustic pressures, microbubbles oscillate stably around a mean radius, in a behaviour described as stable or non-inertial cavitation. The magnitude of the radial oscillation increase with pressure until a threshold is reached where the inertia of the surrounding fluid becomes the dominant driving force

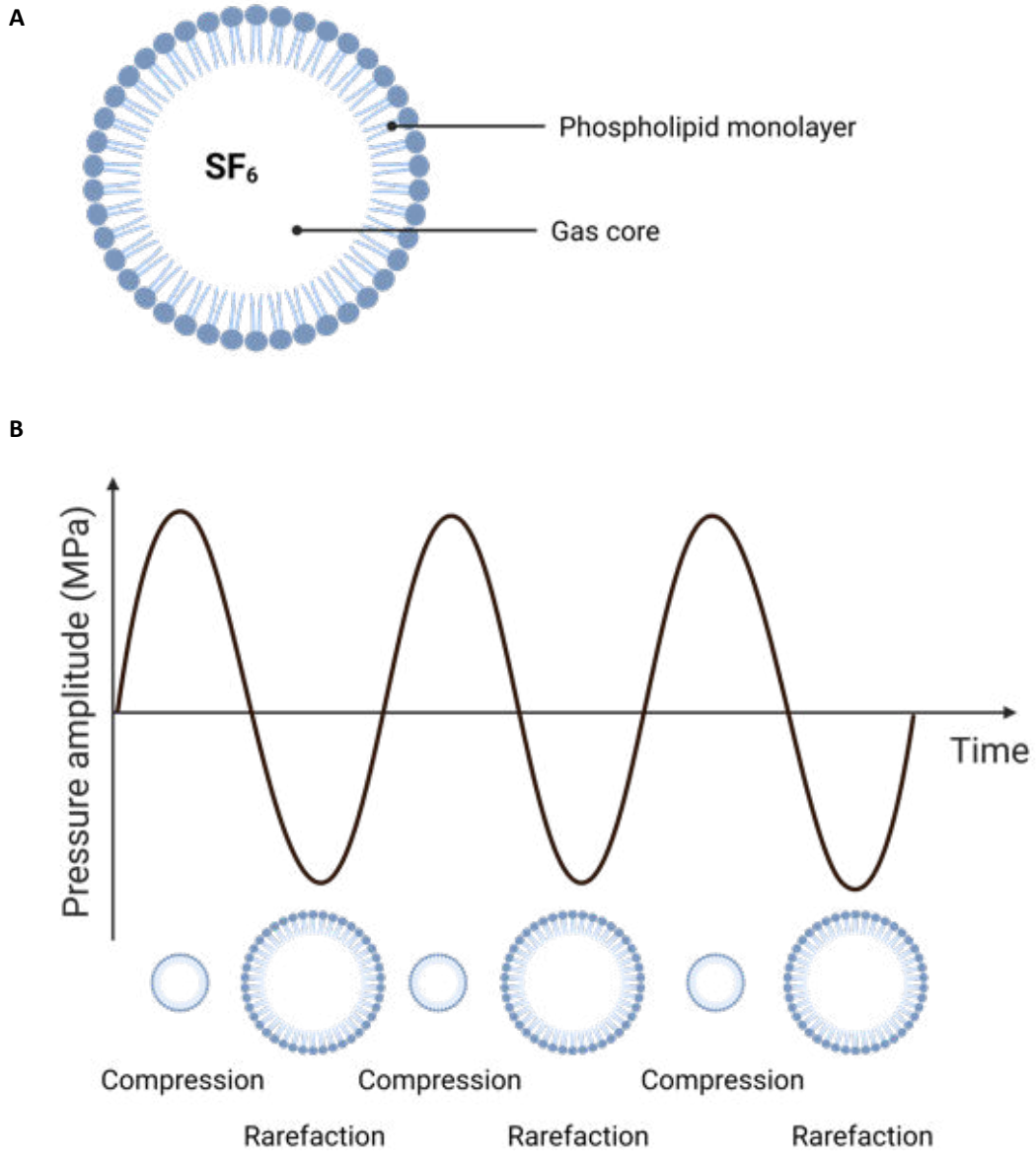

Figure 1.5.2 Microbubble behaviour in the presence of ultrasound. *Microbubbles in the presence of ultrasound can be used to increase the permeability of the blood-brain barrier. Such microbubbles are composed of a gas core surrounded by a lipid or protein shell. (A) SonoVue® microbubbles are typically used for this technique and possess a phospholipid monolayer surrounding a sulfur hexafluoride gas core. (B) When exposed to an ultrasound field, microbubbles are driven into volumetric oscillations by the rarefactional and compressional phases of the sound wave. Figure created using Biorender.com.*

(Leighton and Apfel, 1994). Above this threshold, microbubble behaviour is described as inertial cavitation; the microbubble diameter at least doubles then rapidly collapses (Church

and Carstensen, 2001, Coussios and Roy, 2008). The microbubble collapse is driven by the inertia of the surrounding liquid and can result in production of shockwaves, high temperatures, microstreaming, and fluid jets (Leighton and Apfel, 1994). Inertial cavitation can be stable, lasting over several cycles (stable inertial cavitation) or temporary (non-stable inertial cavitation) (Chomas et al., 2001a).

A microbubbles resonant frequency is related to its diameter. At this frequency, the microbubble will most strongly experience the amplitude of the ultrasound wave. The resultant amplitude of the microbubble's oscillation, at resonance frequency, is at maximum for a fixed acoustic pressure compared to non- resonant frequencies (Halliday, 2013).

Three types of commercial microbubbles are available and used for BBB disruption in combination with FUS (**table 1.2**). Optison™ (GE Healthcare, WI, USA), Definity® (Lantheus Medical Imaging, MA, USA), and SonoVue® (Bracco, Milano, Italy), are all clinically approved for diagnostic purposes by the U.S. food and drug association (FDA). Under identical concentrations, SonoVue® and Definity® microbubbles induce similar and equivalent BBBD effect (Wu et al., 2017). However, persistence was dependent on the degradation dynamics of each microbubble type. At the lowest acoustic pressure investigated, SonoVue® microbubbles had a relatively superior BBBD performance. This was attributed to a greater amount of stable cavitation.

Phospholipids (used in Definity® and SonoVue®) form a thinner and more flexible coating resulting in a lower cavitation threshold and stronger dynamic response than protein coating (used in Optison™)(Wu et al., 2015). Moreover, phospholipid coated microbubbles sustain cavitation behaviour for longer, extending the period for which microbubbles can act for BBBD (Borden et al., 2005). The impact of the gas core is less significant than other microbubble parameters, but some have suggested that perfluorocarbon gas-filled microbubbles are more effective than sulphur hexafluoride microbubbles (Omata et al., 2019).

The commercially available microbubbles discussed above are all polydisperse in size. Microbubble size affects its interaction with ultrasound and impacts BBBD, particularly at low peak negative acoustic pressures where stable cavitation is occurring (Wang et al., 2014, Choi et al., 2010a). In preclinical studies, microbubbles with diameters of 4-8 μm have resulted in

significantly greater BBBD than those with diameters of 1-2 µm but the smaller microbubbles resulted in a faster BBB return to pre-sonication permeability levels (Vlachos et al., 2011, Samiotaki et al., 2012, Song et al., 2017). The optimal microbubble size depends on the exposure conditions (Kovacs et al., 2018, Choi et al., 2010a).

Table 1.2 Commercially available microbubbles used in combination with focused ultrasound for blood-brain barrier disruption.

Microbubble	Concentration	Coating	Core	Size
SonoVue®	1.5-5.6 x10^8 MBs/mL	Lipids	Sulphur hexafluoride	1.5-2.5 µm
Definity®	1.2 x10^{10} MBs/mL	Lipids	Octafluoropropane	1.1-3.3 µm
Optison™	5.0-8.0 x10^8 MBs/mL	Protein	Octafluoropropane	3.0-4.5 µm

Vascular parameters such as blood flow and pressure and vessel dilation/ constriction may have an impact on interactions between the microbubbles and vessel walls (Caskey et al., 2006, Zheng et al., 2007). Simulation studies have suggested that the diameter and elastic properties of small vessels influence the resonant frequency of the microbubble oscillation, and that the diameter of the vessels influences the inertial cavitation threshold (Sassaroli and Hynynen, 2005, Martynov et al., 2009). These factors in turn impact the local bubble concentration, change vessel compliance, and increase or decrease the distance between the microbubbles and the blood vessel walls (McDannold et al., 2011). These vessel factors will vary between brain structures and thus the microbubble interaction with the ultrasound field, and so the biological outcome may differ.

After administration, microbubbles are cleared within 2-4 minutes via three main mechanisms. Microbubbles will gradually dissolve as they circulate in the blood stream, releasing the gas core which is exhaled through the respiratory system. As the microbubbles pass through the capillary network, they can be mechanically disrupted by the shear stress exerted by the blood flow. This leads to the fragmentation and destruction of the microbubbles into smaller particles. Some of the smaller microbubble remnants or particles

are recognised and removed by the body's reticuloendothelial system. This system consists of cells, such as macrophages, which are responsible for engulfing and eliminating foreign particles or debris from the blood (Cerroni et al., 2018).

1.5.3 Mechanism of blood-brain barrier disruption with focused ultrasound and microbubbles

The mechanisms underlying FUS-mediated BBBD is not well defined, but studies suggest the involvement of both the transcellular and paracellular transport pathways (described in **§1.2**) (Sheikov et al., 2004). Reorganisation of tight junction proteins have been observed up to four hours after FUS exposure (Sheikov et al., 2004, Baseri et al., 2010). The increase in transcellular transport is linked to the increase in channel formation, and vesicular transport via caveolae and cytoplasmic vacuoles (Sheikov et al., 2006, Sheikov et al., 2004, Hynynen et al., 2005). Notably, an observed increase in active vesicular transport in arterioles over capillaries and venules indicates that BBBD occurs in multiple vessel types (Sheikov et al., 2006). Vasoconstriction has been observed during BBBD, this can increase transcytosis (Cipolla et al., 2004). Reduced expression of P-gp efflux pumps has also been reported. This could aid the maintenance of drug concentrations within the brain parenchyma after FUS exposure (Choi et al., 2019, Cho et al., 2016, Aryal et al., 2017).

It is hypothesised that the mechanism of BBBD is related to the type of cavitation and associated microbubbles behaviour. Stable cavitation is sufficient for BBBD and is linked to the microstreaming and acoustic radiation force which can lead to an activation of mechanosensitive ion channels, or to endothelial deformation (McDannold et al., 2006b, Hamill, 2006, Cipolla et al., 2004).

1.5.4 Ultrasound sequence

The choice of ultrasound parameters will influence microbubble behaviour and vessel effects (Cheng et al., 2019). For BBBD, microbubbles are generally stimulated by repetitive periods of ultrasound (burst) followed a rest period, emitted at a certain frequency (burst repetition frequency). During repeated ultrasound exposures, microbubbles may cease to oscillate due to them dissolving, being destroyed, or modified and thus become

therapeutically ineffective (Apfel, 1997, Chomas et al., 2001b, Borden et al., 2005, Samuel et al., 2009). The rest periods between bursts allow a population of fresh microbubbles to flow into the beam focus.

Most BBBD studies, including all clinical trials, use long pulses (1,000 to 10,000 cycles) of ultrasound emitted in a slow sequence [burst repetition frequency (BRF) 0.5 Hz] (**figure 1.5.3A**)(Carpentier et al., 2016, McDannold et al., 2006a, Downs et al., 2015b). The long ultrasound pulse stimulates the microbubbles circulating in the brain capillaries, inducing blood-brain barrier permeability change. These pulses are applied in a slow emission sequence to provide a long ultrasound off time to allow the vasculature to be replenished

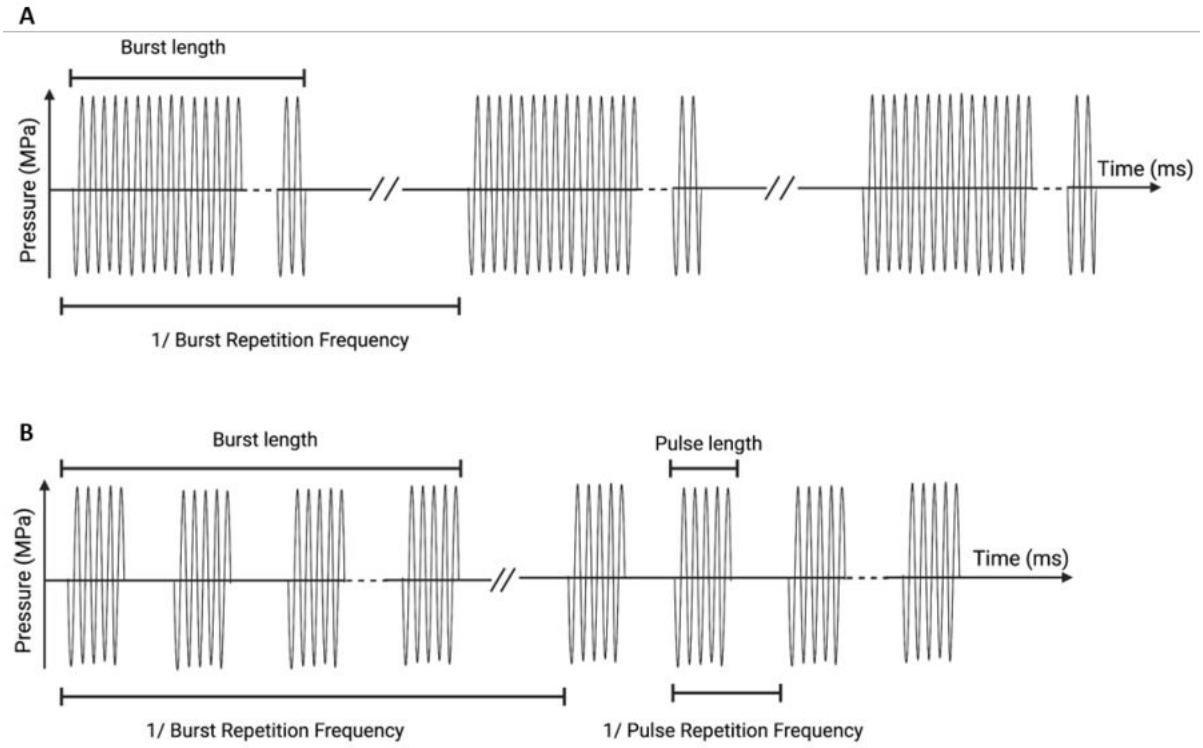

Figure 1.5.3 Ultrasound sequences. *(A) Most studies use ultrasound in long bursts (1,000-10,000 cycles) emitted in a slow sequence (burst repetition frequency 0.5 Hz). (B) Research has shown that dividing long pulses into short (5 cycle) pulses emitted in a rapid sequence (pulse repetition frequency 1.25 kHz) in a slow burst sequence may provide an advantageous drug delivery and safety profile (Choi et al., 2011a, Morse et al., 2019). Figure created using Biorender.com.*

with new microbubbles as the long pulses of ultrasound destroy, dissolve, and modify them (Borden et al., 2005, Chomas et al., 2001b, Apfel, 1997, Choi et al., 2011a).

However, research has shown that dividing these high-energy long pulses into short low-energy pulses (5 cycles) emitted at a rapid rate [pulse repetition frequency (PRF) 1.25 kHz] in a slow burst sequence (BRF 0.5 Hz) could be advantageous (**figure 1.5.3B**)(Choi et al., 2011b).

The rapid short pulse sequence was designed to gently stimulate the microbubbles, thereby reducing the likelihood of microbubble destruction, prolonging their lifetime in the vasculature, and allowing them to act at multiple locations (Pouliopoulos et al., 2014, Pouliopoulos et al., 2016). This would allow microbubbles to gradually stimulate the blood vessel walls homogenously, resulting in uniform BBBD and drug delivery. The sequence design was based on extensive *in vitro* and *in vivo* work, consisting of an ultrasound burst emitted at a slow rate (Pouliopoulos et al., 2014, Pouliopoulos et al., 2016). The burst is composed of a series of short-duration pulses emitted at a high pulse repetition frequency. The short off time between pulses allowed microbubbles to flow down the vessels and thereby distribute their activity as observed *in vitro* vessels; microbubbles moved more during an ultrasound burst than during a long pulse. Moreover, fewer, and smaller microbubble clusters formed with short pulses than with long pulses of ultrasound, suggesting that microbubbles are more dispersed throughout the vasculature and may lead to more uniform drug delivery in the targeted volume. The time off between bursts allowed for new microbubbles to enter the vasculature in the target volume.

Published work by a member of the non-invasive surgery and biopsy (NSB) lab at Imperial College London (ICL) has demonstrated advantages of such ultrasound sequences over traditional long pulses (Morse et al., 2019). When targeting the left hippocampus of mice *in vivo*, the following benefits were shown: a more homogenous drug distribution, shorter BBB closing time (less than 10 minutes), and a lack of detectable damage using histological staining. High- speed microscopy *in vitro* showed that this could be due to the pulse-off time allowing microbubble mobility, and the improved spatial distribution of cavitation (Pouliopoulos et al., 2014, Pouliopoulos et al., 2016).

Short-pulse ultrasound has successfully disrupted the BBB in non-human primates (NHPs), as shown by signal enhancement on MRI (Zhou et al., 2021). Zhou et al. (2021) showed that short pulses (frequency: 300 kHz, pulse length: 30 or 60 μs) did not result in oedema or

haemorrhage, whereas haemorrhage was observed with long pulses (frequency: 300 kHz, pulse length: 10 ms). Energy deposition with short-pulses was 6% of that with long-pulses. However, compared with short pulses, McMahon et al. (2021) observed greater tracer delivery, less erythrocyte extravasation and no difference in BBB closing time with long-pulses. Different microbubble types and doses were used by McMahon et al. (2021) and Morse et al. (2019) which may explain the observed differences in BBB disruption.

DIPG arises in the pons, located near the skull base in mice which could reflect the ultrasound, increasing the acoustic intensity experienced by the microbubbles, causing tissue damage (McDannold et al., 2012, Ishida et al., 2021). Pelekanos et al. (2018) suggested that reducing pulse lengths to less than 1 ms could alleviate tissue damage concerns by reducing standing waves.

1.5.5 Applications of focused ultrasound mediated drug delivery in the brain

To date, small and large molecule drugs have been delivered successfully across the BBB using ultrasound *in vivo* (Tran et al., 2020, Schoen et al., 2022). Phase I/II clinical trials have been ongoing since 2015 for a range of pathologies including Alzheimer's disease, GBM, and diffuse midline glioma (specifically DIPG) (Lipsman et al., 2018, Carpentier et al., 2016, clinical trial: NCT04804709). FUS and microbubble mediated BBBD have resulted in an increased concentration in the tumours of anticancer agents including chemotherapies, antibodies, nanoparticle drug-, magnetic nanoparticle-, microbubble- conjugates, and viruses (Schoen et al., 2022).

Chemotherapeutic agents are small (194-690 Da; < 1 nm) yet struggle to cross the BBB at therapeutic levels. *In vivo* studies in a range of brain tumour models have shown a 3.9-fold higher drug concentration and 30% increase in median survival duration with the use of FUS and microbubbles compared to drug alone (Schoen et al., 2022). Interestingly, larger chemotherapies (>400 Da) performed better, probably because it is more difficult to efflux such drugs. The pharmacokinetics of chemotherapies means that they are rapidly cleared from circulation, reducing the exposure time to cancer cells.

The potency and low toxicity of antibodies are desirable therapeutic characteristics for cancer therapy (Drago et al., 2021, Mullard, 2021). On average FUS has been shown to

increase the antibody concentration in the brain 2.7-fold with a 32% increase in median survival (Schoen et al., 2022). Antibodies and other protein based drugs delivered with FUS and microbubbles for murine brain tumour models are: trastuzumab (herceptin & emtansine) (Park et al., 2012, Arvanitis et al., 2018), pertuzumab (Kobus et al., 2016), interleukin-12 (Chen et al., 2015), bevacizumab (Liu et al., 2016), IgG2a (Brighi et al., 2020), anti-mCD47 (Sheybani et al., 2021) and anti-PD-1 (Sabbagh et al., 2021). A well-publicised antibody success story is the improved delivery of trastuzumab emtansine for HER2+ breast cancer metastases in the brain (Meng et al., 2021).

Concentrations of drugs conjugated with nanoparticles, magnetic nanoparticles and microbubbles have all increased in the brain with FUS exposure. The mean interstitial flow velocity magnitude doubled *in vivo* with FUS and was attributed to the large increase in nanoparticle concentration and brain penetration after FUS exposure (Curley et al., 2020, Arvanitis et al., 2018). Microbubble drug conjugates combine BBBD with triggered drug release into a tumour. Loading chemotherapeutic drugs into nanoparticles can slow their release into the tumour and overcome rapid efflux issues. However, there are concerns that fast microbubble kinetics may result in incomplete cargo release (Schoen et al., 2022).

Using FUS and microbubbles for delivery of viruses into the brain may expand treatment options for brain cancer by allowing viruses e.g. recombinant adeno-associated virus (rAAV) vectors to penetrate the BBB in a more localised manner, reducing off-target effects (Noroozian et al., 2019).

1.5.6 Targeting

Besides selecting the most appropriate parameters, the correct location must be targeted for optimal therapeutic response. Many FUS drug delivery systems use MRI for targeting but these methods are lengthy, require access to appropriate scanners, and increase costs (McMahon et al., 2020, McMahon and Hynynen, 2017, Kovacs et al., 2017). Alternative targeting systems include an implantable device and creation of a cranial window – both of which require surgery (Carpentier et al., 2016, Idbaih et al., 2019). Another method uses a metal grid, aligned with anatomical landmarks, visualised with B-mode imaging to align the focal region (Ye et al., 2018). Other preclinical systems include a closed-loop feedback

controller system (Chien et al., 2022). These latter methods require the least amount of specialist equipment and skills, but there remains room for a faster, and cheaper, bench top system.

1.5.7 Acoustic pressure

The impact of peak negative acoustic pressure on microbubble behaviour and BBBD has been widely studied. Safe and effective BBBD has been achieved in preclinical studies at acoustic pressures from 0.2 to 0.5 MPa (Gandhi et al., 2022). There is a pressure threshold at any given frequency at which BBBD occurs (Chen and Konofagou, 2014, Sierra et al., 2017), after which there is a correlation between increased pressure and drug delivery (Shin et al., 2018b, McDannold et al., 2007, Liu et al., 2008b, Hynynen et al., 2005). However, an increased acoustic pressure can result in tissue damage with microbubbles undergoing unstable inertial cavitation resulting in rapid microbubble expansion and violent collapse (Fan et al., 2014a). Microbubble collapse exerts up to four times higher stress than stable bubble expansion, resulting in tissue damage including cell necrosis and erythrocyte extravasation (Baseri et al., 2010, Hynynen et al., 2001, Hosseinkhah et al., 2013). Tsai et al. (2018) used optical coherence tomography to observe increased vascular effects with increased acoustic pressure, yet temporary effects could be recovered in several hours when a low exposure was applied. Acoustic pressure is also associated with the time taken for the BBB permeability to return to pre-exposure levels and the size of therapeutic agent that can be delivered.

1.5.8 Blood-brain barrier closing time

Whilst BBBD is desired for improved drug delivery, the BBB must return to its pre-disruption state to reduce the likelihood of unwanted substances entering the brain, and to avoid transcranial infection. The time taken for the BBB to return to its normal state has been reported as being between 10 minutes and 4 days (Morse et al., 2019, Marquet et al., 2014). The closing time has been shown to be dependent on the acoustic pressure (Liu et al., 2009, Samiotaki et al., 2012) and ultrasound sequence design (Morse et al., 2019) but is independent of opening volume (O'Reilly et al., 2017a, Marquet et al., 2014).

1.5.9 Size of therapeutic agent

Many research teams have reported a size threshold for drug delivery, whereby the larger the agent the lower the dose delivered (Choi et al., 2011a, Batts et al., 2023, Choi et al., 2010b, Marty et al., 2012, Chen and Konofagou, 2014, Valdez et al., 2020, Pandit et al., 2020, Nhan et al., 2013, Shen et al., 2016, Arsiwala et al., 2022). If extravasated, larger agents have a more heterogenous distribution than smaller ones which correlates with the pressure differential across the beam (Choi et al., 2011a, Choi et al., 2010b, Chen and Konofagou, 2014, Valdez et al., 2020, Shen et al., 2016, Arsiwala et al., 2022). Model drugs up to, and including 500 kDa have been successfully delivered across the BBB with long pulses of ultrasound at an acoustic pressure of 0.6 MPa (Pandit et al., 2020). A recent study with short pulse ultrasound reported a smaller size threshold of 70 kDa with an acoustic pressure of 0.35 MPa (Chang et al., 2023). Higher acoustic pressures are required for the extravasation of larger agents, but these are also associated with adverse tissue effects and so there becomes a safety/ efficacy trade-off (Morse et al., 2022).

1.6 Tissue effects

One of the most important things to consider when translating this technique into the clinic is the safety of the procedure. This is especially important when treating children with DIPG, where long-term neurological deficits must especially be avoided. As discussed above in **§1.5.2**, microbubbles undergoing inertial cavitation can rapidly collapse resulting in liquid jets with high levels of energy that cause mechanical damage to the tissue. Early studies were concerned with safety. For example, McDannold et al. (2005) reported that BBBD is possible in rabbits without inducing substantial vascular damage that would result in ischemic or apoptotic death to neurons. Variable neuronal and glial cell damage can occur as a function of amplitude and duration of pressure, yet under a specific set of sonication parameters, neuronal damage could be prevented (Hynynen et al., 2005, Alonso et al., 2010, Baseri et al., 2010).

Tissue damage is typically analysed using histological staining at experiment termination and MRI scans whilst the animal remains alive. Haematoxylin and eosin (H&E) are the most common form of histological assessment, with staining of tissue slices allowing the

identification of different types of cells and tissues. H&E staining after FUS treatment is often used to identify extravasated erythrocytes and other morphological tissue changes e.g. microvacuolations (Baseri et al., 2010). Position emission tomography (PET) scans, electroencephalogram (EEG), Somatosensory Evoked Potentials (SSEP) monitoring and behavioural scales for potential toxicity have also been used (Horodyckid et al., 2017). When assessing long term effects of FUS mediated BBBD, MRI scans (to identify haemorrhage and oedema) in combination with behavioural studies provide a multi-faceted approach (Downs et al., 2015b).

1.6.1 Transient immune response

Tissue damage can last for various time periods. Activation of the nuclear factor kappa B (NF-kB) pathway leads to sterile inflammation to a level comparable with ischemia or mild-traumatic brain injury (Kovacs et al., 2017). Significant elevations in this pathway as well as in other proinflammatory, anti-inflammatory and trophic factors associated with an innate immune response have been observed but returned to baseline levels after 24 h. The same study identified infiltration of immune cells (CD68+ macrophages) 6 days post sonication – consistent with an innate immune response. The stimulation of these immune cells results in a transition from their resting to activated state, coordinating the immune system's response. It has been suggested that the immune response is a result of standing waves from microbubble cavitation stimulating microglia, astrocytes, and neurons beyond the vasculature.

Stavarache et al. (2018) followed rats from several hours to 15 months after a single sonication. The animals had transient inflammation for the first few days and no inflammation from two weeks to six months, with no evidence of substantial toxicity, tissue injury or neuronal loss long-term. Overall, this suggests that FUS and microbubble induced BBBD can stimulate a short-term immune response that returns to pre-BBBD levels.

1.6.2 Tissue effects in non-human primates

Studies involving NHPs have assessed safety using behavioural studies during and post-treatment, and post-treatment MRI scans and histological staining after experiment

termination. No behavioural effects or changes in visual acuity were reported after repeated BBBD in non-human primates, suggesting there was no functional damage (McDannold et al., 2012). However, histological analysis revealed two locations of significant erythrocyte extravasations that were not detected on MRI. Similar results have been observed by others: Tsai et al. (2018a) reported minor and short-term behavioural changes, despite significant tissue damage being identified on histology.

On a longer time scale, non-human primates repeatedly exposed to ultrasound over 4-20 months had no long-term effects on their general physiology, on the structure of the brain regions targeted or on decision making and motor function (Downs et al., 2015b). However, some hyperintense spots were seen on T2-weighted MRI scans indicating haemorrhage or oedema. These signals were not present after a week, suggesting they were cleared by the brain. O'Reilly et al. (2017b) investigated the safety of BBBD in an Alzheimer's disease dog model. A single adverse event (bloody urine and vomiting) was observed, which was cleared in 24 hrs. Further histological analysis showed comparable microhaemorrhage in treated and control hemispheres two weeks after sonication, but no evidence of chronic microglial activation.

1.6.3 Microbubble dose

There is a relationship between increasing microbubble dose and adverse bioeffects. McMahon and Hynynen (2017) reported that acute inflammatory response and cellular apoptosis are dependent on microbubble dose, with a dose roughly equivalent to 1.2×10^9 MBs/kg associated with NF-kB pathway activation, inflammatory response, and apoptosis. Others found cellular apoptosis (Tsai et al., 2018a, Yang and Lee, 2012) and the level of tissue damage positively correlated with microbubble dose administered to the mouse (Tsai et al., 2018b, Yang and Lee, 2012, Lapin et al., 2020).

1.7 Monitoring blood-brain barrier disruption

As mentioned above, many FUS drug delivery systems use MRI for targeting before FUS treatment and to detect BBBD after treatment. MRI contrast agents that cannot cross the BBB are often administered, and will be seen in the brain parenchyma on T1-weighted scans if

BBBD is successful (Downs et al., 2015a). As well as detecting BBBD, post-sonication MRI can be used for detecting adverse events such as haemorrhage or oedema. These can be seen with T2-weighted scans and susceptibility weighted imaging (SWI) sequences (Downs et al., 2015b). McMahon and Hynynen (2017) suggested that post-FUS gadolinium enhancement could be predictive of the magnitude of inflammatory response. However, others have reported significant erythrocyte extravasation upon histological assessment that were not detected on MRI, indicating that the technique can render false negatives (McDannold et al., 2012). This is undesirable when considering clinical translation as problems in patients must be detected immediately.

It has been shown that MRI dampens FUS-mediated BBBD, decreasing the BBBD volume up to 11.6-fold compared to outside the MR field (Yang et al., 2021). It was established that as the magnetic field increased, stable cavitation decreased, generating lower mechanical forces on the vessel wall and reduced BBBD. This is an important consideration for clinical translation as most clinical studies use an FUS system (e.g. the ExAblate®, Insightec system) within an MRI scanner.

MRI assessment of BBBD can only occur after treatment. Acoustic emissions returned from microbubbles can be recorded using a passive cavitation detector (PCD) and monitored in real-time. Microbubbles undergoing stable and unstable inertial cavitation have distinct acoustical signatures that can be detected using real-time feedback. Stable cavitation and low magnitude inertial cavitation have been associated with subharmonic and ultra-harmonic emissions (O'Reilly et al., 2017a). Unstable inertial cavitation and microbubble collapse have been associated with broadband emissions, leading to cell damage, erythrocyte extravasation and tissue damage (Liu et al., 2008b, Bing et al., 2018, Tu et al., 2006, Hwang et al., 2006). The aim is to drive the transducer at a level to maintain stable cavitation to prolong microbubble behaviour and drug delivery whilst avoiding microbubble behaviour that can cause unwanted tissue damage. Acoustic emissions have been used successfully to predict BBBD and damage in mice and rhesus macaques (McDannold et al., 2012).

If weak microbubble oscillation is detected, indicating lack of BBBD, the procedure can be stopped, or adjusted to fully exploit the allocated treatment session. Some have argued that

the lack of MRI will reduce targeting accuracy, but clinical systems have emerged that employ neuro-navigation for successful BBBD (**§1.8.3**) (Pouliopoulos et al., 2020).

Combined MRI and PCD monitoring provides the benefits of both systems: highly precise targeting using the MRI pre-sonication, establishing stable cavitation during sonication and BBBD assessment post-sonication. (Kamimura et al., 2018) used an MR-guided system with PCD real-time feedback control as a tool for better controlling the BBBD. This system is designed to provide high-resolution anatomical images and to follow the diffusion of a contrast agent with improved temporal and spatial resolution, allowing comparison between FUS exposures within and between animals. However, the lengthy MRI time remains, and procedures can take three hours. This is undesirable when treating children with DIPG as they are likely to need sedation for such long treatments.

1.8 Translation to the clinic

With a large body of promising preclinical work demonstrating efficacy, FUS and microbubbles to increase drug delivery have been in human clinical trials since 2015 (Carpentier et al., 2016). FUS and microbubbles for BBBD is attractive as drugs with poor pharmacokinetic, pharmacodynamic and brain penetration already approved by the FDA such as panobinostat for the treatment of DIPG, can be repurposed. Clinical trials have investigated the delivery of chemotherapeutics e.g. carboplatin and temozolomide, nanoparticles e.g. albumin-bound paclitaxel for brain tumours and cerezyme for Parkinson's disease. Current clinical trials are in phase I/II and have demonstrated that FUS can transiently disrupt the BBB in a well-tolerated manner (Idbaih et al., 2019).

A study in non-human primates has shown that the procedure can be performed safely whilst patients are awake. Subjects performed a behavioural task whilst receiving FUS treatment. They had a 28% larger BBBD region and no damage markers (oedema and microhaemorrhage) compared to previous FUS exposure when they had been anaesthetised (Downs et al., 2015a). No physiological effects (heart rate, motor evoked potentials) were observed during any of the procedures. This is beneficial for translation to the clinic where repeated treatments are likely. Repeat general anaesthesia has been linked to cognitive and

mental health decline, especially in children and so it would be beneficial to avoid sedation for BBBD treatments (Kirby et al., 2020).

1.8.1 Considerations for clinical translation

Many preclinical trials with FUS and microbubbles for improved drug delivery have been successful. Most have been conducted in mice or rats due to the accessibility of appropriate disease models. The technique has been investigated in larger animal models such as pigs, sheep, dogs, and non-human primates. Whilst the larger animal models are more likely to represent patient geometries, there are challenges to be addressed. The improvement in retention and penetration of therapeutics in the brain may be difficult to scale up and to reach deep cortical tumours. The diffusion of contrast agents in NHPs after BBBD has not followed the same uniform pattern as in mice and differences in the acoustic pressure required for BBBD have been seen between two NHPs in the same study (Samiotaki et al., 2017). This highlights the individuality in treatment outcomes and the question as to whether therapeutically relevant levels of the drugs can be maintained after crossing the BBB (Marquet et al., 2014).

1.8.2 Ultrasound parameters

The same ultrasound parameters are often used when sonicating small animals in a study but must be dynamically determined in the clinic. Ultrasound is attenuated by the skull as it passes through to the brain tissue. The skull thickness and bone-to-marrow composition differ between species and so the *in-situ* pressure experienced by the microbubbles, and the resultant bioeffects will differ between patients. Moreover, the human skull is irregularly shaped, meaning that there will be differences in phase aberrations and absorption depending on the targeted region (Fry, 1977, McDannold et al., 2012). As a result, skull heterogeneity will result in challenges to reproducibility of acoustic parameters *in situ* (Kamimura et al., 2018).

Reported studies have sonicated non-human primates with FUS parameters appropriate for their body weight (Downs et al., 2015b). One study in non-human primates attributed variation in BBBD to pressure amplitude loss due to the skull, and uncertainty in estimating *in*

vivo exposure levels (McDannold et al., 2012). Patients in the clinic will vary in skull thickness, and it is therefore necessary to personalise ultrasound parameters.

As well as skull differences there are size differences between small animals and patients. This means that multiple exposures are likely to be needed to cover the full tumour volume in patients. Dogs were sonicated multiple times to cover the entire hemisphere with up to 13 sonications and with no reported adverse effects, indicating that it is possible to sonicate multiple locations safely in the brain (O'Reilly et al., 2017b).

Repeat sonications are likely to be needed for a full therapeutic response. Tsai et al. (2018a) found no behavioural or histological changes from BBBD in rats after sonication every two days for a total of three sonications. The first trial of repeated exposures in patients showed hypointense spots on T2*-weighted MR scans post-sonication (Park et al., 2020). These spots were not present in the scan one month later suggesting that they indicated venule dilation. Temporary cerebral vessel dilation was observed *in vivo* too when investigating FUS on brain microstructure and microcirculation in mice (Tsai et al., 2018c). GBM patients received BBBD adjacent to tumour resection margin targets for six cycles of the standard temozolomide treatment protocol (Park et al., 2020). No clinical adverse effects were reported, and a longer follow-up is awaited.

1.8.3 Clinical systems

Clinical systems for drug delivery in the brain can be divided into three categories: MRI-guided, implantable or neuronavigation (**table 1.5**). In the MRgFUS system e.g. ExAblate Neuro® (INSIGHTEC Inc.) uses a fixed stereotactic frame on the patient's head. The patient is placed in an MR scanner for pre-treatment planning scans and BBBD is confirmed by MRI immediately after treatment (Barzegar-Fallah et al., 2022).

The implantable device, SonoCloud® (CarThera Inc.) involves the insertion of a transducer directly into the skull (Lipsman et al., 2018). Patients with Alzheimer's disease had repeatable BBBD with no clinically severe adverse events nor clinically significant worsening in cognitive performance three months after BBBD. Another clinical trial involving patients with recurrent GBM showed repeat treatments to be well tolerated and can increase survival with carboplatin (Idbaih et al., 2019). Three clinical trials are currently recruiting investigating the

SonoCloud® device in patients with melanoma brain metastases (NCT04021420), malignant brain tumours in children (NCT05293197) and recurrent GBM (NCT04528680). The ultrasound is unfocused, meaning that only one specific brain region can be targeted, and that it is thus unsuitable for more diffuse neurodegenerative diseases and pathological targets where sonications at multiple locations are necessary.

Neuronavigation systems e.g. NaviFUS® (NaviFUS Inc.), involve an external device that does not require MRI and instead uses neuronavigation to guide the FUS procedure (Chen et al., 2021). Pre-treatment simulations are used to steer the ultrasound beam intraoperatively to the targeted region. A dose escalating pilot trial in patients with recurrent GBM showed a dose-dependent opening effect with no immunological response.

There are advantages and disadvantages to each system and the preferred system is likely to depend on the location and size of the therapeutic target. Clinical trials involving brain tumours, to date, are listed in **table 1.3**.

Table 1.3 Clinical trials involving brain tumours using focused ultrasound and microbubbles.
GBM: glioblastoma, DIPG: diffuse intrinsic pontine glioma, DMG: diffuse midline glioma.

ClinicalTrials.gov identifier	Condition	Device	Drug	Status
NCT03626896	GBM	NaviFUS	-	Completed
NCT03551249	GBM	ExAblate, Insightec	-	Active, not recruiting
NCT05879120	Recurrent GBM	ExAblate, Insightec	Pembrolizumab	Not yet recruiting
NCT02343991	Brain tumour	ExAblate, Insightec	-	Active, not recruiting
NCT04446416	GBM	ExAblate, Insightec	Bevacizumab	Recruiting
NCT04804709	DIPG	Neuro-navigator-	Panobinostat	Active, not recruiting

		controlled sonication		
NCT05630209	DIPG	ExAblate, Insightec	-	Recruiting
NCT01698437	Malignant brain tumours	ExAblate, Insightec	-	Completed
NCT03714243	Breast cancer brain metastases	ExAblate, Insightec	-	Recruiting
NCT04998864	GBM	ExAblate, Insightec	-	Recruiting
NCT04417088	Recurrent GBM	ExAblate, Insightec	Carboplatin	Recruiting
NCT05762419	DMG	Neuro-navigator-controlled sonication	Etoposide	Recruiting
NCT05383872	GBM	ExAblate, Insightec	-	Recruiting
NCT05733312	Brain tumour	ExAblate, Insightec	-	Recruiting
NCT04440358	Recurrent GBM	ExAblate, Insightec	-	Active, not recruiting
NCT05317858	Brain tumour	ExAblate, Insightec	Pembrolizumab	Recruiting
NCT05615623	Brain tumour	ExAblate, Insightec	Doxorubicin	Recruiting
NCT03616860	GBM	ExAblate, Insightec	-	Active, not recruiting

1.8.4 Other benefits beyond drug delivery

FUS mediated BBBD can provide multi-faceted benefits beyond drug delivery. Radiosensitisers can be attached to therapeutics and delivered into tumours and FUS-mediated BBBD can radiosensitise tumours directly by inducing the formation of ceramide which is involved in radiation-induced cell death (Czarnota et al., 2012). DIPG tumours can also be radioresistant, therefore the effects of FUS increased radiosensitivity may be beneficial (Werbrouck et al., 2019).

Similarly, there is evidence for immunostimulatory effects of FUS treatment. Brain tumours are notoriously immunologically 'cold', but FUS can promote the recruitment of immune cells (Chen et al., 2021). Sim et al. (2022) suggested that poly-ADP ribose polymerase (PARP) inhibitors could potentiate the cytotoxic effects of radiotherapy and chemotherapy, priming the tumour microenvironment for immunotherapy. Microbubbles can also be loaded with drug for a multipurpose effect: BBBD and drug delivery.

As well as synergistic effects with other treatment modalities, FUS-mediated BBBD can improve drug convection and provide diagnostic information. Arvanitis et al. (2018) suggested that FUS enhances convective transport of therapeutics post-BBBD by increasing interstitial hydraulic conductivity. BBBD can release tumour biomarkers into the blood which can be used as a non-invasive diagnostic method, tumour monitoring and clinical trial patient stratification (Rincon-Torroella et al., 2022).

1.9 Blood-brain barrier disruption in the pons for DIPG

DIPG arises in the pons and despite its multitude of therapeutic targets (**§1.3.2**), a therapeutic drug concentration cannot currently be reached in the brain, as discussed above. DIPG is thus an ideal candidate for FUS and microbubble treatment as the BBB is the main limiting factor for curative therapy. To date most preclinical FUS studies have focused on drug delivery to the hippocampus.

1.9.1 Preclinical studies

Six pre-clinical studies have investigated BBBD in the pons with the first published in 2018 (**table 1.4**). Three have investigated the use of FUS to increase the level of a chemotherapeutic

agent (doxorubicin) two with radiolabelled nanoclusters and the last with model drugs and an MRI contrast agent (gadolinium). Of these six studies, four involved FUS induced BBBD in a DIPG mouse model and the other two in non-tumour-bearing mice (Englander et al., 2021, Zhang et al., 2020, Ishida et al., 2021, Alli et al., 2018, Haumann et al., 2022, Ye et al., 2018).

Ye et al. (2018) saw the same signal emitted from radiolabelled nanoclusters 24- and 48-hours post sonication, suggesting closure of the BBB after a few hours, yet diffusion volume increased in this time. This supports the idea that FUS can increase interstitial fluid flow and improve drug distribution in the tumour. Others have reported that bolus injection of microbubbles followed by sonication at recurring locations resulted in the best spatial homogeneity (Englander et al., 2021, Alli et al., 2018). Overall, BBBD is repeatable and safe in the pons and promising for development of drug delivery for DIPG patients.

There are some challenges associated with targeting the pons, especially in the smaller animal models. DIPG originates in the pons which lies more posteriorly in the brain than the previously targeted hippocampus (**figure 1.9.1**). The skull has an increased thickness and curvature in this region, so ultrasound attenuation is expected to be higher (Alli et al., 2018). Moreover, the pons is located near the skull base which can reflect ultrasound, resulting in standing waves and causing tissue damage (McDannold et al., 2012, Ishida et al., 2021).

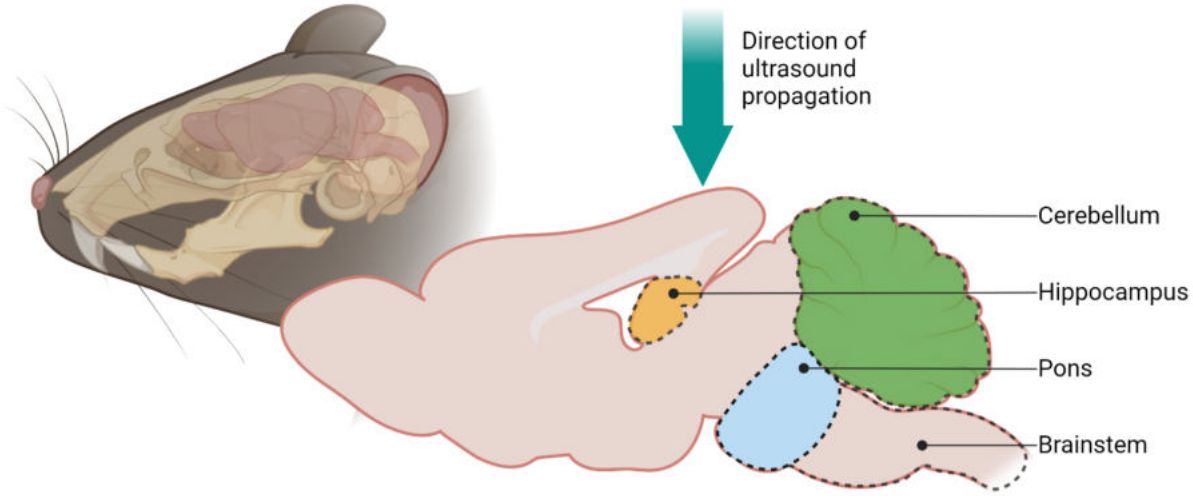

Figure 1.9.1 Sagittal view of the mouse brain. *Schematic showing the location of the cerebellum, hippocampus, pons, and brainstem. Ultrasound is propagated through the top of the head. Figure created using BioRender.com*

1.9.2 Clinical trials for DIPG

One clinical trial involving the use of FUS for improving drug delivery in DIPG is underway. This clinical trial employs a neuro-navigator controlled system to examine the feasibility and safety of FUS BBBD with panobinostat (Clinical trials identifier: NCT04804709). Patient's tumours are sonicated in one, two or three locations with a 30-minute total treatment time during which the patients are awake. Three patients have been enrolled for the first phase of this trial.

Table 1.4 In vivo studies using FUS and microbubbles for drug delivery to the pons.

Authors	Aim	Tumour model	Frequency (MHz)	Pressure (MPa)	Pulse length (ms)	Microbubble type and dose	Outcome level and significance
Zhang et al. (2020)	Delivery of radiolabelled copper nanoclusters (^{64}Cu-CuNCs)	Yes	1.5	0.61	6.7	In-house prepared with mean diameter 4-5 um, concentration $8x10^8$ MBs/ml	FUS resulted in significant tumour uptake, dynamic distribution, and prolonged retention within DIPG tumours delivery and time-dependent diffusion
Alli et al. (2018)	Delivery of doxorubicin to brainstem	No	1.68	0.71	10	Definity microbubbles 0.02mL/kg	Doxorubicin was significantly higher in mice receiving FUS and microbubbles than drug alone
Englander et al. (2021)	Safe and repeatable BBBD	Yes	1.5	0.70	10	SonoVue, Bracco, Milan, Italy or Definity, Lantheus Medical Imaging, Norther Billerica, MA, USA 100 µl of microbubbles	FUS increased intra-tumoral etoposide concentration by more than fivefold

Ye et al. (2018)	Delivery of radiolabelled nanoclusters (^{64}Cu-CuNCs)	No	1.5	0.56	0.67	In-house prepared with mean diameter 4-5 um, concentration 8x10^{8} MBs/ml	FUS significantly enhanced the delivery of ^{64}Cu-AuNCs to the pons compared to nanocluster only group
Haumann et al. (2022)	Delivery of doxorubicin-free or liposome treatment	Yes	1.5	0.40		120 uL of SonoVue microbubbles	No treatment effect after a single dose of free doxorubicin or the liposomal formulations: 2B3-101 or Caelyx®, in combination with FUS
Ishida et al. (2021)	Delivery of doxorubicin	Yes	1.78	-	10	0.02 ml/kg; Definity; Lantheus Medical Imaging	FUS increased doxorubicin concentration in the tumours fourfold and decreased tumour growth

1.10 Thesis aims

The overall aim of the work described in this doctoral thesis is to improve drug delivery to the pons using ultrasound and microbubbles for the treatment of DIPG. Recently published work has indicated that short pulses of ultrasound have a preferable drug delivery and safety profile over traditionally used long pulses of ultrasound. This recent work has been focused on drug delivery to the hippocampus for the treatment of Alzheimer's disease. The first objective was therefore to establish repeatable and safe BBBD in the pons, where DIPG arises. This was first assessed using ultrasound emitted at a centre frequency of 300 kHz, and then at 1.05 MHz (at ICL). A model drug was used to assess BBBD and histological staining for tissue damage. In parallel, an ultrasound system similar to that at ICL but with some modifications was assembled and tested for safe and repeatable BBBD at the Institute of Cancer Research (ICR) using ultrasound emitted at a frequency of 1 MHz. The second objective was to assess drug delivery, first in non-tumour bearing mice, and then in a DIPG mouse model. Overall, the research presented here aims to establish a drug delivery system that is capable of expanding treatment options for DIPG.

2 Common methods

This chapter describes methodologies used for the studies described in further chapters of this thesis. To reduce variability, one mouse strain, of the same gender and approximate age, was used throughout the studies described here. A standardised experimental workflow was followed for all ultrasound exposures (**figure 2.1**). The ultrasound setup, calibration, and targeting at Imperial College London (ICL) and the Institute of Cancer Research (ICR) are described individually as is system design and assembly at the ICR. The microbubbles and model drugs used, tissue processing protocols and analysis used at both institutions are then described.

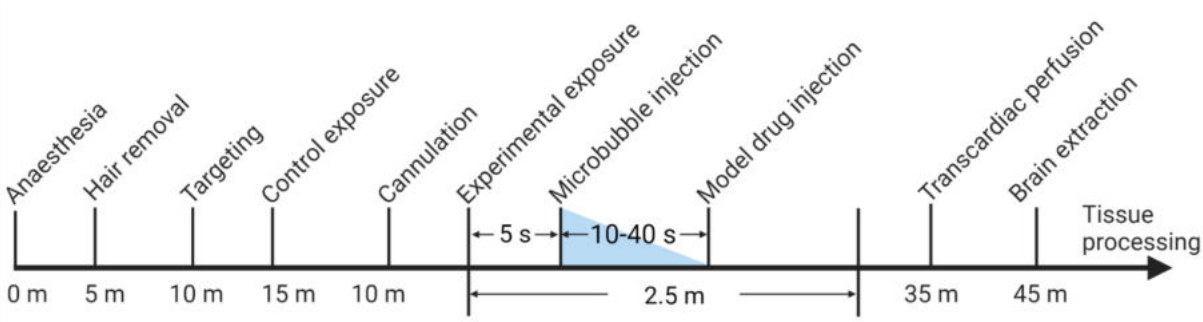

Figure 2.1 Experimental workflow. *Mice were anaesthetised and hair removed. The correct position within the brain was identified, and a control exposure performed (**§2.10**). A cannula, through which microbubbles were injected over a period of 10-40 s as soon as the experimental exposure started, was inserted into the tail vein. Where used, model drug was injected through the same cannula once the microbubble infusion was complete. Experimental sonication lasted for 2.5 min, after which mice were perfused transcardially to remove blood from the circulation system and fix the brain, if necessary. The brain was extracted, and tissue processed for histological assessment. Figure created with BioRender.com.*

2.1 Animals

Female C57Bl/6 wild-type mice (Envigo (ICL) and Charles River (ICL & ICR) depending on availability, UK), aged 8-10 weeks on arrival, mass: 20 ± 2 g (at experiment start) were used for the experiments described in this thesis. All experiments conformed to the UK Home Office Animals (Scientific Procedures) Act 1986 and were approved by the ICL's or the ICR's animal facility committee as appropriate. Experiments were performed under the project

licences (PPLs) PBDB8AA12 (ICL), P1A014C38 (ICR), and PEBBE4BAF (ICR) and personal licence (PIL) ICE5CC54E.

2.2 Preparation for sonication

Prior to sonication mice were anaesthetised with 1.5-2.0% vaporised isoflurane (Zoetis, UK) carried in oxygen (0.8 L/min) using an anaesthesia vaporizer (Harvard Apparatus, UK). Whilst anaesthetised, the mice were kept on a heat mat to maintain their body temperature. The fur from the top of their head was removed using hair clippers and depilatory cream (Nair), and the eyes protected with Viscotears (Bausch + Lomb, Canada).

2.3 ICL methodology

2.3.1 Ultrasound setup

Ultrasound at a centre frequency of 300 kHz or 1.05 MHz was used. Exposure parameters used are shown in **table 2.3.1**. The ultrasound source was a transducer (H-117 Sonic Concepts, WA, USA) with fundamental frequency of 300 kHz. A cone filled with deionised and degassed water, was mounted on the transducer front face 37.3 mm in height and 20 mm diameter (referred to as coupling cone; **figure 2.3.1**). The opening of the coupling cone was sealed with an acoustically transparent membrane (polyethylene plastic wrap, Thermo Fisher Scientific, MA, USA), without trapping bubbles.

Table 2.1 Ultrasound exposure parameters.

Parameter	**ICL**		**ICR**
Centre frequency	300 kHz	1.05 MHz	1 MHz
Peak negative pressure (MPa)	0.25 ± 3.70 x10^{-4} 0.3 ± 2.3 x10^{-3}	0.2 ± 4.2 x10^{-3} 0.4 ± 3.7 x10^{-3} 0.6 ± 3.7 x10^{-3}	0.4
Input voltage amplitude (mV)	37.5 45	24.5 51.1 78.3	55.3
Pulse length (cycles)	1	5	5
Phase (degrees)	335	340	60
Pulse repetition frequency (kHz)	1.25	1.25	1.25
Burst length (ms)	6/ 10 / 20 / 30	30	30
Pulses per burst	8 / 13 / 25 / 38	38	38
Burst repetition frequency (Hz)	0.5	0.5	0.5
Number of bursts	125	125	125
Total time (s)	250	250	250

Two function generators (33500B Series; Agilent Technologies, CA, USA) were used to create the complex ultrasound output: one to create an ultrasound pulse of 1 or 5 cycles emitted at a pulse repetition frequency of 1.25 kHz, and the second to emit 6-30 ms pulses (for 8-38 pulses), in bursts, every 2s for a total of 125 bursts. The sequence was sent through a 50-dB radio frequency (RF) power amplifier (2100L 100W; Electronic & Innovation, NY, USA) to the transducer. The transducer was driven at its 300 kHz fundamental for *in vivo* exposures described in chapter 3, and then at 1.05 MHz for *in vivo* exposures described in chapter 4.

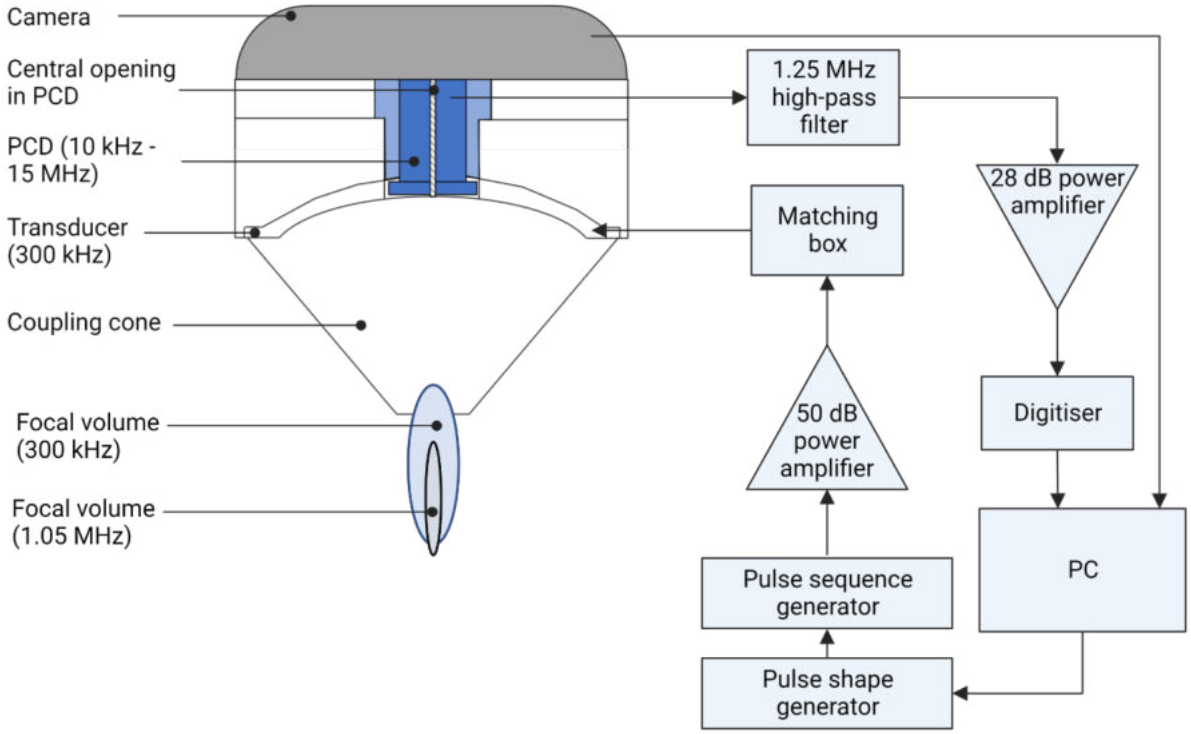

Figure 2.3.1 ICL experimental setup. *Ultrasound sequences were generated by two function generators, one the pulse shape generator, and the second the pulse sequence generator. The sequence was sent through a 50 dB power amplifier and matching box and then was converted to an ultrasound pressure wave by the H117 focused ultrasound transducer (fundamental frequency 300 kHz). A PCD mounted centrally in the FUS transducer was used to capture acoustic emissions from the ultrasound-stimulated microbubbles. These were high pass filtered, amplified (28 dB) and then digitised at 100 MHz. PCD = passive cavitation detector, PC = personal computer. Figure created with BioRender.com, transducer and cone to scale.*

The beam profiles of the transducer were established using a 0.2 mm polyvinylidene difluoride (PVDF) needle hydrophone (Precision Acoustics, Dorchester, UK) in deionised and degassed water tank by another member of the ICL lab (Dr Zheng Jiang; **appendix 7.1 and 7.2**). At a centre frequency of 300 kHz, results defined the pressure full width half maximum (FWHM) to have a 5 mm elevational and lateral diameter and 18 mm axial length (the focal volume overlapped with the opening of coupling cone as seen in **figure 2.3.1**). At a centre frequency of 1.05 MHz, the FWHM was 1.8 mm elevational and lateral diameter and 12.8 mm axial length; the focal volume was located past the opening of the coupling cone (**figure 2.3.1**).

The transducer had a central aperture (20-mm diameter) into which a single element passive cavitation detector (PCD; Y107, Sonic Concepts, WA, USA) with bandwidth 10 kHz – 15 MHz was inserted. This allowed detection of acoustic emissions during the sonication. Captured emissions were filtered (high-pass filter, 1.25 MHz; Mini Circuits, NY, USA), amplified using a 28-dB preamplifier (Stanford Research Systems, CA, USA), and digitised with a GageApplied 14-bit digitiser at 100 million samples a second (**figure 2.3.1**). A polished glass rod was inserted through a central aperture in the PCD (0.99-mm diameter). An optical

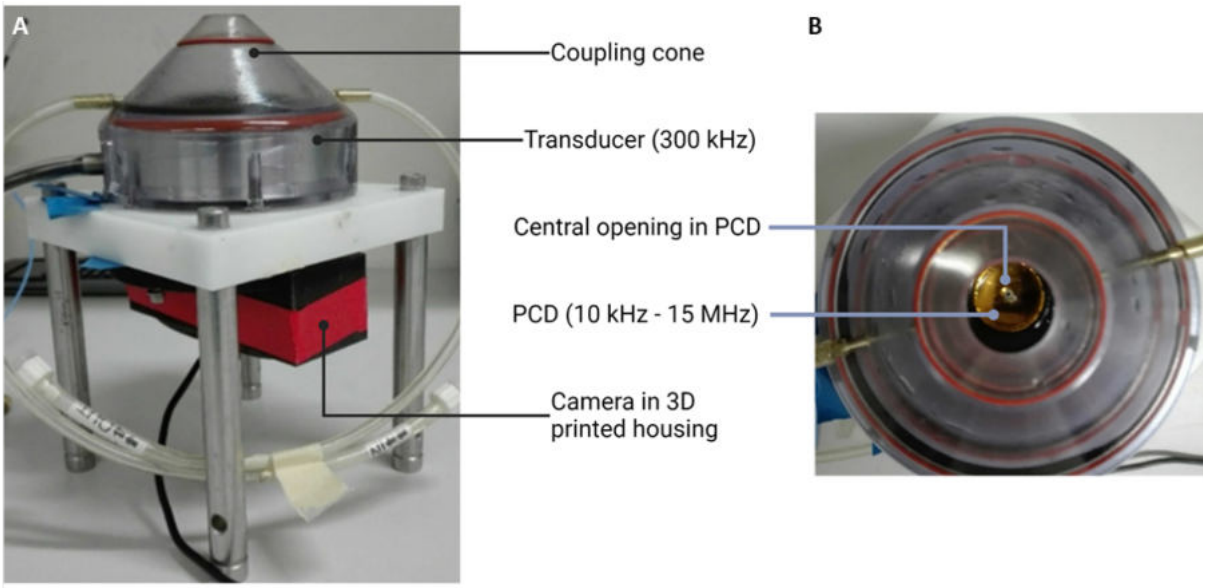

Figure 2.3.2 ICL transducer, PCD and webcam on the 3D positioning mount. *(A) Side view showing the coupling cone, H-117 transducer and camera in a 3D printed housing. (B) Top view showing the passive cavitation detector (PCD) inserted into the centre of the transducer and the central opening in the transducer. Photos obtained from Dr Matthew Copping.*

camera (resolution: 15 MP, 30 frames per second, USB connectivity, model: Logitech C9C0) was mounted on the back of the transducer in a 3D-printed housing. The centre of the camera field of view (FOV) was confirmed to align with the transducer focus using a 0.2 mm needle hydrophone (Precision Acoustics, UK). The transducer, PCD and camera were assembled into a rigid body (**figure 2.3.2**) that was suspended above the mouse on a 3D positioning system (Velmex, Bloomfield, NY, USA), pointing vertically downwards.

2.3.2 Targeting

For *in vivo* exposures at ICL, the hippocampus or the pons of the mouse brain was targeted with ultrasound using a camera-based targeting system (**figure 2.3.3**). Mice were prepared for sonication (shown in **§2.2**) and placed on a stereotactic frame (World Precision Instruments, FL, USA). Body temperature was monitored using a rectal probe connected to a heat pad as part of a homeothermic monitoring system (Harvard Apparatus, MA, USA). Anaesthesia was maintained through a nose cone held in place with a bite bar and ear bars; the ear bars were angled to stretch the skin on the scalp to visualise the sutures on the skull. A pen mark was used to indicate the intersection of the lambdoidal and sagittal suture (lambda; **figure 2.3.3A**) on the overlying skin (**figure 2.3.3B**). The pen mark on the mouse skin was centred in the camera FOV (**figure 2.3.3C**) by moving the transducer using a three-dimensional positioning system (0.1 mm precision, Velmex) controlled by a graphical user interface (GUI). The GUI was written by Dr Pouliopoulos and modified by Dr Copping from the NSB laboratory at ICL. To target the hippocampus, the transducer was moved 1.5 mm distal, and 3 mm left of lambda, and to target the pons, 0.8 mm proximal and 1 mm left (schematic shown in **figure 2.3.3A**).

Once the correct transducer position had been established in a horizontal plane, the transducer was lowered so that the membrane covering the opening of the coupling cone was in contact with the mouse scalp on visual inspection (**figure 2.3.3D**). The transducer was then raised 50 mm, degassed (by centrifugation) ultrasound gel added to the mouse head to achieve acoustic coupling, and the transducer lowered 50 mm to return to the desired sonication position (**figure 2.3.3E**).

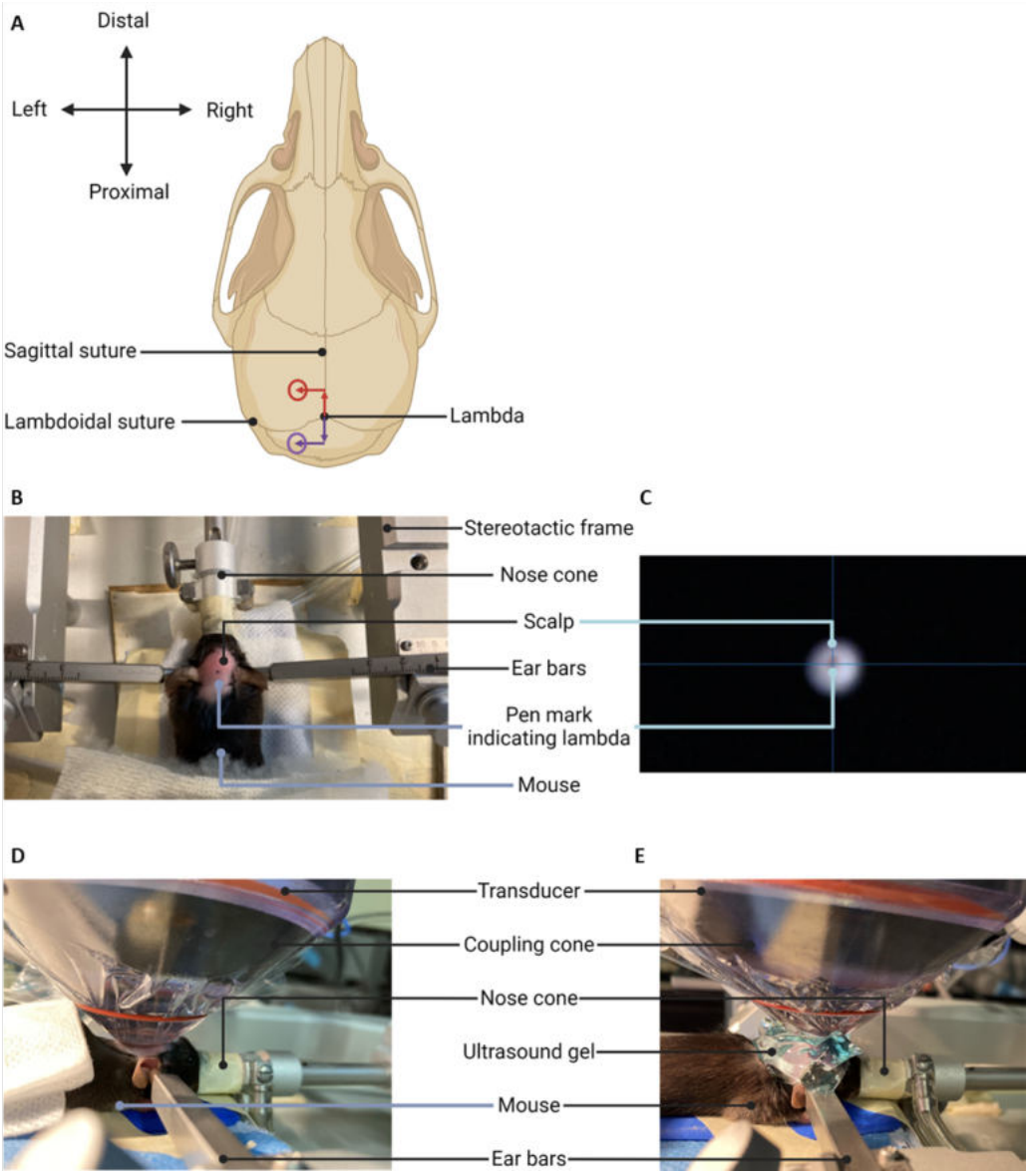

Figure 2.3.3 Brain targeting using the ICL system. *(A) Schematic showing the sagittal and lambdoidal sutures, their intersection, lambda, and the targeting adjustments for the hippocampus (red) and pons (purple). (B) Mice were prepared for sonication and placed on a stereotactic frame. The head was secured with ear bars and mouse kept anaesthetised through the nose cone. A pen mark on the overlying skin was used to indicate lambda. (C) The camera fixed to the back of the transducer housing was used to line the centre of the transducer with the pen mark using a 3D-positioning system. The transducer was moved 1.5 mm distal, and 3 mm left to target the hippocampus or 0.8 mm proximal, and 1 mm left to target the pons. (D) The transducer was lowered so the membrane covering the opening of the coupling cone was visually in contact with the mouse scalp. (E) Ultrasound gel was added to acoustically couple the transducer and mouse head. Figure created with BioRender.com.*

2.4 ICR methodology

To exploit their expertise in rodent cancer models, oncological therapeutics, and magnetic resonance imaging (MRI) a similar ultrasound system was assembled at the ICR to reach the PhD aim of improving drug delivery to the pons for treatment options for DIPG. The system was designed and built, in collaboration with a member of the therapeutic ultrasound team (Dr Ian Rivens). Whilst the ultrasound setup and exposure conditions were similar, a different targeting system was developed.

2.4.1 Ultrasound setup

A similar transducer (H-117, Sonic Concepts), PCD (Y107, Sonic Concepts) and coupling cone were purchased and assembled as for the ICL system (**figure 2.4.1**). For sonication's at

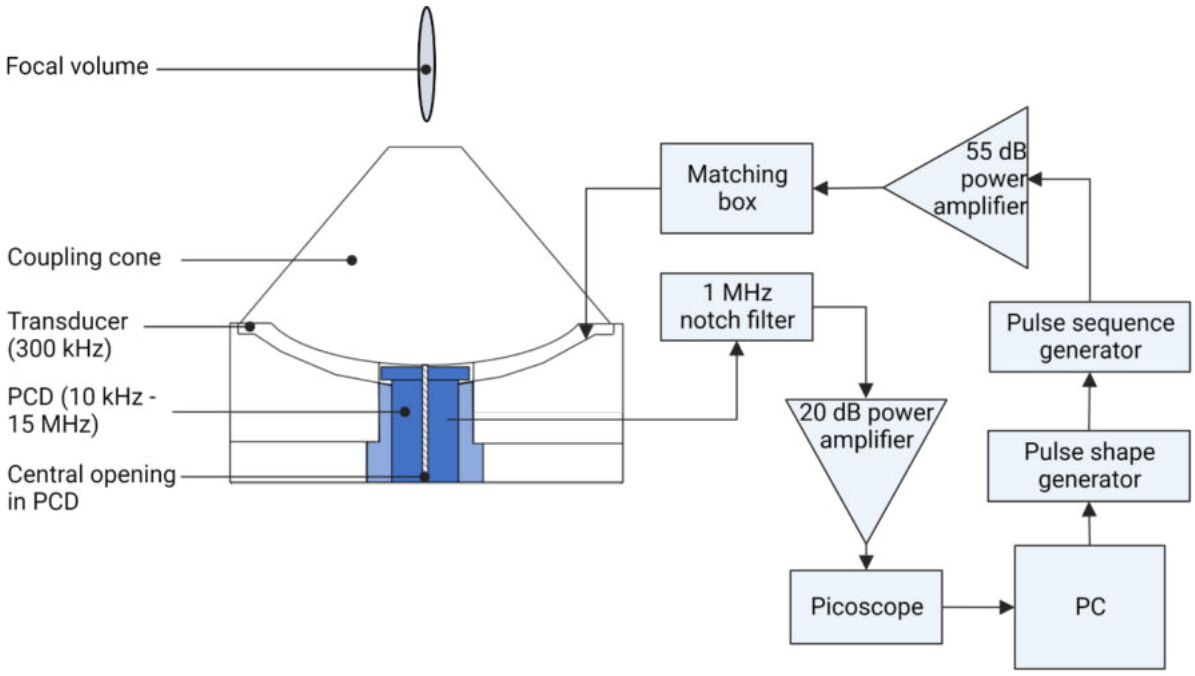

Figure 2.4.1 ICR experimental setup. *Ultrasound sequences were generated using two function generators, passed through a 55 dB power amplifier and matching box thence to the transducer. The PCD captured acoustic emissions from the microbubbles, which were filtered by a 1 MHz notch filter, amplified by a 20 dB amplifier, and captured with a picoscope. The focal volume was located beyond the opening of the coupling cone. PCD = passive cavitation detector, PC = personal computer. Figure created with BioRender.com. Figure created with BioRender.com.*

the ICR, the ultrasound was emitted with centre frequency of 1 MHz, and the transducer was driven using the same components as used at ICL (described in **§2.3.1**) except for the power amplifier which was a 55-dB power amplifier (A300 E&I, NY, USA). During sonication, the PCD captured acoustic emissions which were filtered (notch filter, 1.0 MHz; built in house), amplified using a 20-dB preamplifier (P0.1-30/20VD, Advanced Receiver Research, CT, USA), and recorded using a picoscope (544D, Pico Technology, UK).

The ICR system had a continuous flow of degassed water through the coupling cone. The degassing system consisted of a pump to keep the water circulating, a Liqui-Cel™ (G541 MM series, 3M, Germany) to filter the water and a vacuum pump (VACUUBRAND VP 100 C, VWR, PA, USA) to assist the filter (**figure 2.4.2**). At the start of each experimental day, the coupling cone and water pump were filled with partially degassed, deionised water taken from a beam plotting tank at room temperature and the system started.

Another member of the ICR lab (Dr Ian Rivens) calibrated the transducer using an HNA-0400 needle hydrophone (ONDA Corp., USA, CA) in a degassed, deionised water tank before the commencement of *in vivo* exposures. The FWHM had a lateral and elevational dimension of 2.0 mm, and 14.5 mm axial length (**appendix 7.3**).

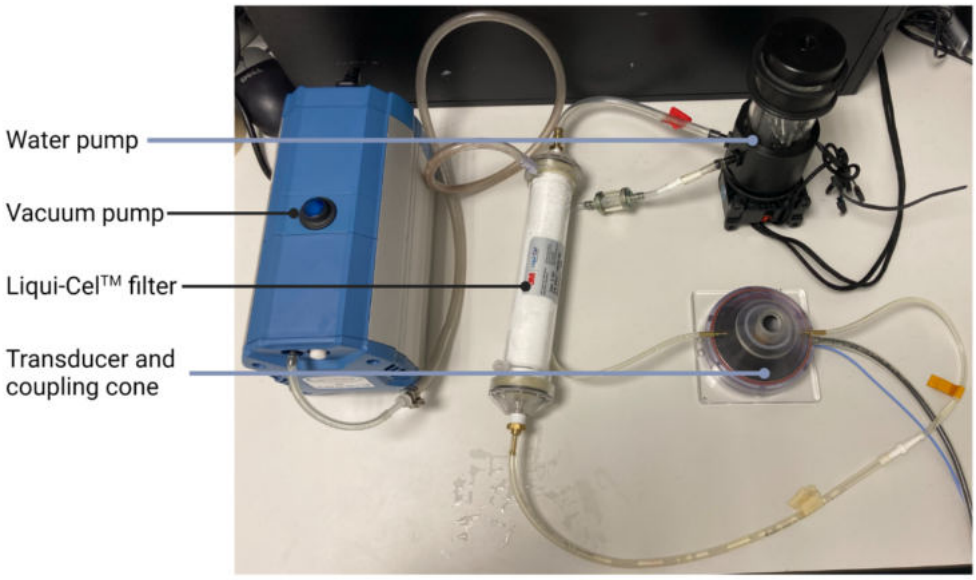

Figure 2.4.2 ICR degassing system. *A water pump kept partially degassed, deionised water circulating into the transducer coupling cone through a Liqui-Cel™ filter assisted by a vacuum pump. Figure created with BioRender.com.*

2.2.2. Development of the ICR targeting system

The ICR sonication system (transducer and drive chain) was kept similar to the ICL system to reduce the number of adjustments required for successful blood-brain barrier disruption (BBBD). The only difference being the amplifier and similar but different transducer/impedance matcher. A different targeting system was developed so that a large, automated 3D positioning system, and ultrasound gel for acoustic coupling were no longer needed.

The ICL system (**§2.3.1**) suspended the H117 transducer above the mouse using the 3D positioning system, with the mouse mounted prone on a stereotactic frame on the bench and coupled the mouse head to the transducer's coupling cone with ultrasound gel. When a centre frequency of 1.05 MHz was used, the ultrasound focus was 5 mm further away from the coupling cone than at a centre frequency of 300 kHz. To maintain the focal depth of the beam within the brain, the transducer was suspended (vertically) further away from the mouse head and so more ultrasound gel was needed to achieve acoustic coupling. The ultrasound gel could be a source of variation for BBBD. Whilst the gel was centrifuged and observable bubbles removed, microscopic bubbles in the gel may have remained, attenuating the ultrasound as it passed through the gel. The attenuation will vary between exposures, depending on the number of bubbles present in the gel, consequently varying the acoustic pressure experienced by the microbubbles between exposures. Overall, this could reduce the reproducibility of drug delivery.

The ICR system was designed so that the transducer was located below the mouse (which was supine) and that the top of its head was immersed in the circulating degassed water in the coupling cone. This decreased the number of interfaces the ultrasound passed through before reaching the brain and negated the need for ultrasound gel coupling, hopefully reducing variation of *in situ* acoustic pressure (and resultant microbubble behaviour) to yield more repeatable BBBD.

The position of the transducer under the mouse also meant that no large 3D positioning system was required to suspend the transducer. Instead, the bed which held the mouse was attached to a 3D micrometre positioning stage so that the mouse could be moved in 3D (± 5 mm) relative to the transducer. The smaller positioning system made the ICR sonication setup more portable than the ICL system, expanding its possible uses.

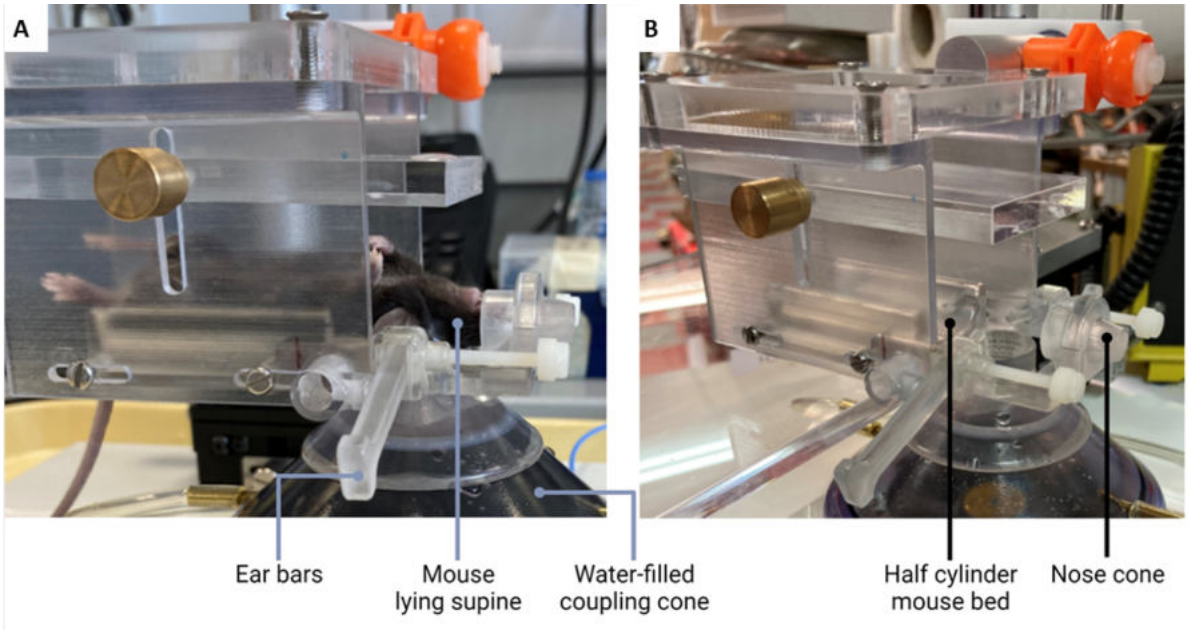

Figure 2.4.3 ICR mouse bed. *The mouse bed was 3D printed. The side view is shown (A) with and (B) without a mouse. The mouse was held in position using ear bars which could be angled to stretch the skin on the mouse head. A nose cone allowed the delivery of inhaled anaesthetic during experiments. The bed was curved to support the mouse lying supine and the hole between the nose cone and bed allowed the scalp to sit in the water-filled coupling cone.*

The bed to hold the mouse was 3D printed at the ICR (**figure 2.4.3**). The bed was a half cylinder to accommodate the mouse lying supine with a nose cone that was attached to an anaesthetic delivery system for FUS exposures with a flexible arm (not pictured). A gap was present in the bed, allowing the scalp to sit in the water in the coupling cone. Ear bars were 3D printed to immobilise the head. Several ear bars were designed and trialled so that they were in the correct position in relation to the mouse ears, could be angled to stretch the skin on the scalp, and be at the correct height to suspend the mouse skull at the opening on the coupling cone.

The first iteration of the targeting system involved aligning a cross hair (representing the transducer focus in the horizontal plane) with a pen mark on the mouse scalp indicating the lambda suture). This method was too complicated and involved rotating the mouse after targeting alignment which was prone to mouse movement.

Although this targeting system was viable it could be improved, and so some adjustments were made (**figure 2.4.4**). Instead of using the cross hair and magnifier to represent the ultrasound focus, a pointer was designed and built. The pointer slotted into the base of the frame where the transducer fitted (**figure 2.4.4A**). The mouse was inserted supine, and its head was secured with ear bars, ensuring the skin on the scalp was taut and that the mouse was visually determined to be central and straight on the bed. A mirror surrounding the pointer allowed the alignment of lambda with the pointer/ transducer focus using the 3D positioning system attached to the mouse bed (**figure 2.4.4B**). Once the desired targeting position was achieved, the pointer was removed and replaced with the transducer (**figure 2.4.4C**). Markers were added to the base, pointer, and transducer to ensure the pointer and transducer were always inserted into the base in the correct orientation.

A platform independent of the mouse bed and attached to the mouse holder base was added to support the heat mat used to warm the mouse during FUS exposure (**2.4.4B**) and the syringe whilst inserting the cannula into the mouse tail vein (**figure 2.4.4C**).

In the final sonication protocol, the targeting position was achieved as described above. Acoustic coupling with the mouse head was ensured by maintaining the water level of the degassed water in the coupling cone. Lastly, the cannula was inserted ready to start the sonication.

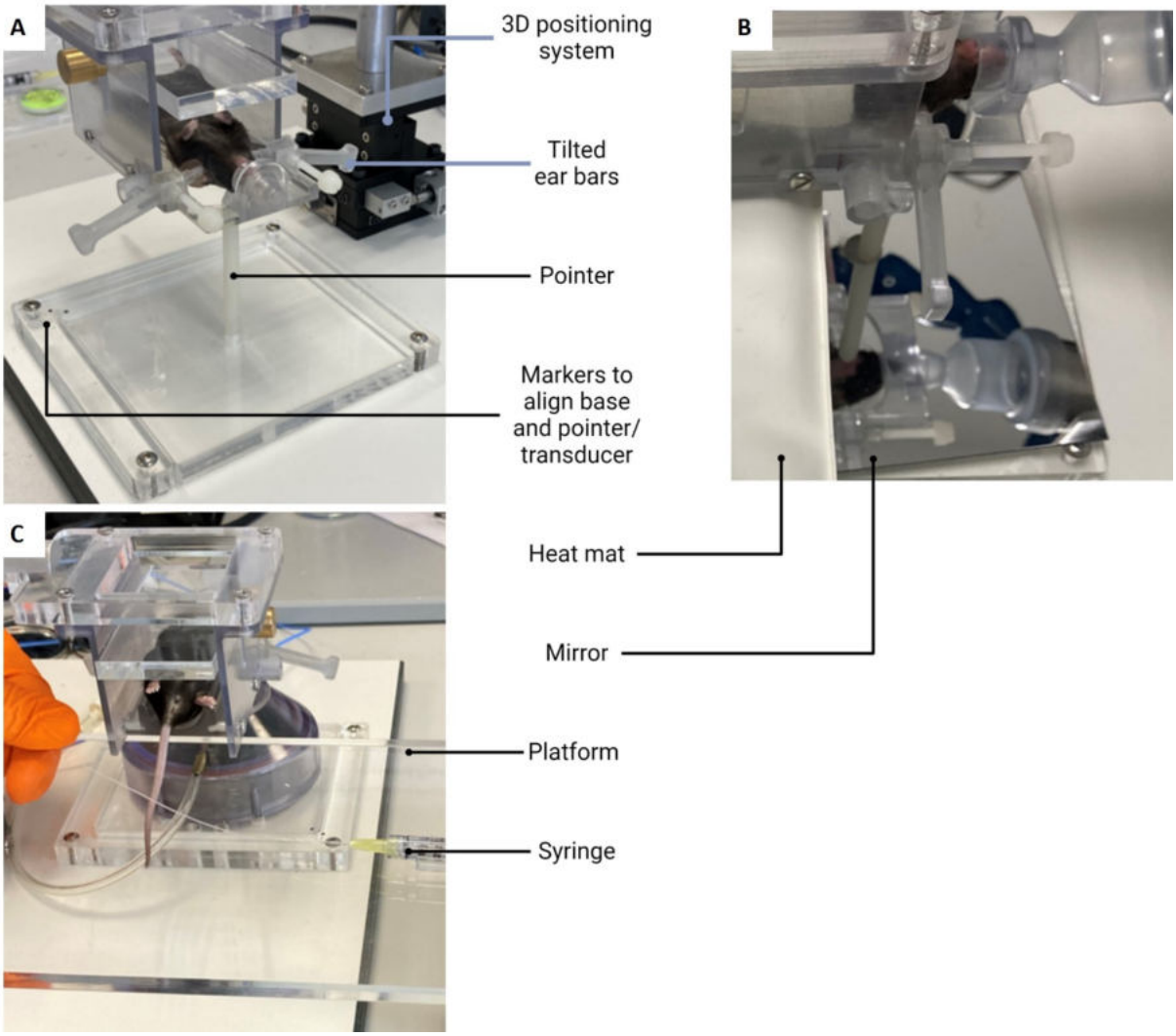

Figure 2.4.4 Adjustments to the ICR ultrasound setup. *(A) The first targeting method used a cross hair and magnifier which was complicated and prone to movement as the mouse was rotated after alignment. This was replaced with a pointer indicating the transducer focus and the mouse remained supine throughout the procedure. Markers on the base and pointer ensured correct orientation of the pointer. Ear bars were used to stretch the skin covering the skull. (B) A mirror surrounding the pointer base was used to align the pointer with lambda by moving the mouse bed attached to a 3D positioning system (± 5 mm). A heat mat which rested on a platform (C) warmed the mouse during exposures. The platform also held the cannula through which the microbubbles and model drug were injected during FUS exposure.*

2.5 Microbubbles and model drugs

During ultrasound exposure, a 100 μL injection of microbubbles over 10-40 seconds was administered into the tail vein using a home-made 30-gauge cannula, approximately 6 cm in length. Either SonoVue® (Bracco, Italy) diagnostic imaging contrast agent, or in-house manufactured microbubbles, were used in this thesis work (**table 2.2**).

Table 2.2 Microbubbles, and their properties, use in the studies described in this thesis. *DPPC: dipalmitoylphosphatidylcholine, DPPA: dipalmitoylphosphatidic acid, DPPE-PEG5000: dipalmitolyphosphatidylethanolamine–PEG5000, DSCP: distearoyl-phosphatidylcholine, DPPG.Na: dipalmitoylphosphatidylglycerol sodium, PA: palmitic acid. Values are mean ± standard deviation. IHP data obtained from (Pouliopoulos et al., 2014). SonoVue® data obtained from (Wu et al., 2017).*

Microbubble	Concentration	Coating	Gas core	Mean diameter
In-house prepared (IHP)	$7.3 \pm 4x10^{9}$ MBs/ml	Lipids: DPPC-82%, DPPA-8%, DPPE–PEG5000-10%	Perfluorobutane	1.62 ± 0.87μm
SonoVue®	$2\ x10^{8}$ MBs/ml	Lipids: DSCP 45%, DPPG.Na 45%, PA 10%	Sulfur hexafluoride	2.5 μm

In-house manufactured microbubbles were prepared as described in detail by (Pouliopoulos et al., 2014). Solutions of three phospholipids (Avanti Polar Lipids Inc, AL, USA) dipalmitoylphosphatidylcholine (DPPC-82%), dipalmitoylphosphatidic acid (DPPA-8%), and dipalmitolyphosphatidylethanolamine–PEG5000 (DPPE–PEG5000-10%) mixed and diluted with saline and glycerol, were prepared by another member of the NSB laboratory at stored at 4°C. Immediately prior to sonication, perfluorobutane (FluoroMed L.P., Texas, USA) was

added and the mixture amalgamated with a Vialmix dental shaker (Lantheus Medical Imaging, MA, USA) for 45 s.

The model drugs used in this thesis work to assess BBBD were chosen on the basis that they could not pass through the blood-brain barrier (BBB), and were the fluorescently tagged tracers dextran and biotin, and the dye Evans Blue (**table 2.3**). Evans Blue was used when an immediate assessment of BBBD was required as this dye can be seen on brain extraction. In contrast, the fluorescent tracers, biotin, and dextran, require approximately one week of tissue processing, and were used to assess distribution (as detailed in chapters 3-5). The model drug(s) were injected through the tail vein cannula approximately 5 s after the end of the microbubble infusion.

Table 2.3 Model drugs used in the studies described in this thesis.

Model drug	Size (kDa)	Concentration (w/v)	Volume injected
Dextran- Texas Red conjugate (Invitrogen)	3.00	0.012 mg/µL	50 µL
Biotin- Fluorescein conjugate (Invitrogen)	0.65	0.0125 mg/µL	50 µL
Evans Blue (Merck Life Sciences)	0.96	1% or 2%	1%: 50 µL 2%: 50 or 100 µL

2.6 Brain tissue processing

Mice were euthanised by overdose of pentobarbital administered intraperitoneally (0.1 mL) then perfused transcardially with 15 mL of heparin [0.05 mg/ml (w/v) in PBS; Merck, UK] to remove the blood from vessels. The perfusion rate was controlled by a peristaltic pump (mini-peristaltic-pump II, Harvard Apparatus).

Where a model drug was used to assess BBBD, following heparin mice were perfused with 15 mL paraformaldehyde (4% v/v; Sigma Aldrich, UK), to fix the brain tissue. Brains were extracted and fixed in paraformaldehyde (4 % v/v; Sigma Aldrich, UK) stored at 4^{o}C overnight, in the dark.

For the model drug Evans Blue, brains were sectioned (1 mm thickness, coronal plane) using an acrylic brain matrix (RBMA-200C, World Precision Instruments, FL, USA) using a razor blade. Photographs were taken of the sections using a smartphone.

Where biotin and/or dextran were used as model drugs, brains were transferred to 30% sucrose (w/v) to cryoprotect the tissue and stored at 4^{o}C overnight, in the dark. For cryosectioning, brains were embedded in optimum cutting compound (OCT; Agar Scientific, Stansted, UK) and sectioned into 30 µm thick coronal (hippocampus targeting) or sagittal (pons targeting) slices. Brain slices were collected on positively charged microscope slides (Superfrost^{TM} Ultra Plus Adhesion Slides, Thermo Fisher).

Fixed and cryoprotected (as described above) brain tissue for haematoxylin and eosin (H&E) staining was embedded in either OCT (Agar Scientific, UK) or paraffin. Brains embedded in OCT were cryosectioned into 5 and 7 µm thick sagittal sections collected on positively charged microscope slides (Superfrost^{TM} Ultra Plus Adhesion Slides, Thermo Fisher). Those embedded in paraffin were sectioned into 4 µm thick sagittal sections with a microtome and collected on positively charged microscope slides (X-tra adhesive, Leica Biosystems, Germany).

2.7 Haematoxylin and Eosin (H&E) staining

H&E staining was used to assess damage to brain tissue after ultrasound exposure. Slides with sectioned brain tissue were dewaxed with xylene, dehydrated in absolute ethanol, stained pink with Haematoxylin, differentiated in acid alcohol, blued in Scotts tap water substitute, stained with Eosin, dehydrated with ethanol, cleared with xylene and cover slipped.

2.8 Microscopy of dextran and biotin

Cryosectioned brain slices were imaged using fluorescence microscopy. At ICL, images were obtained using a widefield microscope (10 X; Zeiss Axio Observer, Oberkochen, Germany). Texas Red (conjugated to dextran) was excited at 592 nm with emissions filtered at 604- 644 nm and fluorescein isothiocyanate (FITC; conjugated to biotin) was excited at 495 nm with emissions filtered at 500- 550 nm. At the ICR, brain slices were imaged using a slide scanner (20X or 40X; Zeiss Axio Scan.Z1, Oberkochen). Texas Red (dextran conjugate) was excited at 592 nm with emissions filtered at 618- 675 nm. After H&E staining, brain slices were imaged using Zeiss Axio Scan.Z1 (10 X) at the ICR.

2.9 Fluorescence pixel intensity quantification

Fluorescence pixel intensity was quantified to represent the total amount of model drug present in the brain after BBBD. Fluorescence in imaged brain slices (**§2.8**) was quantified using a custom MATLAB R2016b script created by another member of the NSB laboratory (Dr Matthew Copping) and modified for sagittally sectioned brain slices. Five brain slices per mouse in the targeted region, with minimal artefacts were selected, to obtain the most representative measure of model drug delivery. A line based on anatomical landmarks indicating the midline of the brain slice, was drawn. Artefacts, which are common in cryosectioned brain slices (from tissue folds or tears) were traced by hand and digitally removed. A region of interest (ROI) from the right hemisphere (for hippocampus targeting) or distal portion (for pons targeting) of the brain slice was selected to represent background fluorescence and used to calculate the average background pixel intensity. These were untargeted regions, contained no artefacts and showed homogenous intensity within the ROI (visually defined). The background intensity was subtracted from the image. The pixel intensities above the mean plus three standard deviations of background fluorescence were summed in the remaining brain slice on either side of the mid-line. The summed pixel intensity from the right hemisphere (for hippocampus targeting) or distal half (for pons targeting) of the brain slice was subtracted from the contralateral hemisphere/ half of the brain to determine the ‘dose’ delivered in the targeted region.

2.10 Acoustic emissions analysis (ICL)

Acoustic emissions recorded during ultrasound exposures were analysed using MATLAB R2018b (Mathworks) with the assistance of Jiho Kim, a member of NSB group at ICL. Acoustic signals recorded on the passive cavitation detector (PCD) carried a direct current (DC) offset, which naturally exists in all electrical systems, along with background reflection from the driving pulse and high-frequency noise components. The DC offset was calculated by averaging the amplitude for each pulse in every burst and then subtracted from the original pulse amplitude.

A constant time window was applied to minimize interference from high-frequency noise components in the acoustic cavitation signals. This ensured only the signal within a specific time range relevant to acoustic cavitation was extracted for each pulse in every burst. The fixed range of the time window was empirically defined after reviewing the time series of recorded signals, and this definition remained consistent for all recorded bursts throughout the experiment.

The amplitude of the time-windowed signal was then squared and integrated within the time-window size range, resulting in a single value analogous to acoustic energy for the individual pulse, measured in units of mV^2. To eliminate background reflection, the energy of each pulse in the sequence for the first burst was subtracted from the pulse energy of the other bursts. Consequently, the pulse energy exclusively resulted from acoustic cavitation.

The energy of each burst was tabulated by summing all the obtained single pulse energies within a single burst. The cumulative energy was computed by adding the burst energy from all the bursts in the single exposure.

Due to use of short pulses (1-5 cycles), the harmonic components of the acoustic signal cannot be distinguished from the background frequency content as the peaks overlap considerably (Copping, 2020).

2.11 Conclusion

This chapter has described the sonication setups and protocol performed at both ICL and the ICR in the chapters 3, 4 and 5 of this thesis. In the next chapter, blood-brain barrier disruption at 300 kHz at ICL is examined.

3 Blood-brain barrier disruption using a rapid short-pulse sequence at 300 kHz

3.1 Background

This purpose of the work described in this thesis is to improve treatment options for diffuse intrinsic pontine glioma (DIPG), a paediatric brain cancer, in which an intact blood-brain barrier (BBB) results in ineffective drug doses reaching tumour cells (Warren, 2018, Veringa et al., 2013). The use of focused ultrasound (FUS) and intravenous microbubbles can transiently and noninvasively disrupt the permeability of the BBB allowing drugs to enter the brain parenchyma (Hynynen et al., 2001, Choi et al., 2007b, McDannold et al., 2005, Hynynen et al., 2005).

Current clinical systems use long pulses (~10 ms) of ultrasound emitted in a slow sequence (e.g. 0.5 to 10 Hz) (**§1.5.4**). Long pulses have been associated with undesirable characteristics including a non-uniform drug distribution within the beam (Nhan et al., 2013, Choi et al., 2011b, Choi et al., 2007a, Choi et al., 2011a, Stieger et al., 2007), unwanted biological responses (Kinoshita et al., 2006a, Baseri et al., 2010, Shin et al., 2018b) and the BBB remaining disrupted for up to 48 h (Sheikov et al., 2008, Hynynen et al., 2005, Samiotaki and Konofagou, 2013, Zhao et al., 2018). In a recent clinical trial, hypointense signals on T2-weighted magnetic resonance imaging (MRI) indicated microhaemorrhages after BBBD with long pulse ultrasound (Lipsman et al., 2018).

Recent studies have shown that short pulses of ultrasound emitted in a rapid sequence confer efficacy and safety benefits not seen with long-pulse ultrasound. The short-pulse ultrasound sequence was designed by the non-invasive surgery and biopsy (NSB) laboratory at Imperial College London (ICL). In a direct comparison with long pulses of ultrasound, Morse et al. (2019) reported an equivalent drug dose with a more homogenous distribution throughout the focal volume, reduced tissue damage and BBB was altered for a shorter time. Whilst promising for advancing DIPG treatment options, these ultrasound exposures were performed at a frequency of 1 MHz which is not optimal for human skull transmission (Hynynen et al., 2005).

The studies reported in this chapter investigate whether the benefits of rapid short pulse ultrasound at 1 MHz can be achieved at a lower centre frequency of 300 kHz, suitable for transcranial transmission (Yin and Hynynen, 2005).

3.1.1 Transcranial transmission

(Hynynen and Jolesz, 1998) demonstrated the potential for transcranial transmission at centre frequency of 1 MHz, but the skull attenuated and distorted the ultrasound field. In patients it would be difficult to predict the *in-situ* pressure field due to considerable inter- and intra- patient variability in skull transmission efficiency and standing wave formation within the skull (Kamimura et al., 2018). If a centre frequency of 1 MHz were to be used in the clinic, patient-specific aberration correction would be necessary, increasing time and expertise required for the ultrasound procedure. Alternatively, simulation of transcranial ultrasound using computed tomography (CT) image data has shown that transcranial transmission is possible at 250 kHz with reduced distortion and attenuation compared to higher frequencies (Yin and Hynynen, 2005). The lower frequency can also allow beam steering by reducing grating lobes, increasing the potential brain targets that can be treated using a single sonication device (Ilovitsh et al., 2018).

A centre frequency of ~220 kHz is used by clinical BBBD devices such as ExAblate® (Insightec Inc.) (**§1.8.3**), but few small animal studies have used these low frequencies. The initial work comparing short and long pulses of ultrasound was performed with ultrasound emitted at a centre frequency of 1 MHz. Investigations using a low centre frequency that can traverse the human skull for preclinical assessments may lead to easier translation into the clinic, minimising the need for some of the sophisticated refocusing techniques necessary for higher frequencies.

3.1.2 Microbubble dynamics at 250-300 kHz

The ultrasound induced microbubble dynamics seen at centre frequencies below 250-300 kHz are very different from those at 1 MHz and above. 250-300 kHz is approximately an order of magnitude lower than the resonance frequencies of most contrast agent bubbles (properties described in **§1.5.2**). At these frequencies, microbubble oscillations become

highly non-linear, resembling a quasi-static process rather than one of linear resonators (Yasui et al., 2008). Large microbubbles are unstable under static negative pressures and expand to very large sizes during the rarefactional phase of the driving ultrasound, before collapsing rapidly during the following compressional phase. For example, it has been shown *in vitro* that when a bubble was exposed to 250-kHz ultrasound at an acoustic pressure of 400 kPa, it expanded 30 fold, yet a similar bubble expanded only 1.6-fold when the ultrasound frequency increased to 1-MHz (Ilovitsh et al., 2018). Implications of the larger expansion – in terms of brain treatment consistency, efficacy, or safety – are still unclear. A greater microbubble expansion could result in increased blood-brain barrier disruption (BBBD) and drug delivery but could also lead to tissue damage during the rapid bubble collapse (Church and Miller, 2016).

3.1.3 Ultrasound parameters and protocols that may have an important role in the reproducibility of brain drug delivery

It is well documented that the ultrasound parameters (including frequency) largely dictate microbubble behaviour and resultant drug delivery (Cheng et al., 2019). Stimulating microbubbles at 300 kHz will produce different microbubble dynamics than at 1 MHz. Therefore, it is probable that the ultrasound parameters may need to be adjusted for optimal BBBD. Two key parameters that could influence the drug delivery pattern are burst length and peak-rarefactional pressure (PRP)(Gandhi et al., 2022). FUS-mediated BBBD is also dependent on the microbubble type and distribution (Wang et al., 2014) and so the effect of all three on BBBD are assessed here.

3.1.4 Burst length

There is a positive correlation between burst length (using long pulses of ultrasound) and drug delivery (Liu et al., 2010, Shin et al., 2018a). Initially, a burst length of 38 pulses per burst was used in the studies described in this chapter to maximise the chance of drug delivery by exploiting microbubble stimulation in each burst. However, a plateauing effect has been reported, where longer burst lengths conferred no drug delivery benefits and increased tissue damage (Choi et al., 2011a, Hynynen et al., 2001). A shorter burst length would reduce the

acoustic energy deposited in the brain, decreasing the likelihood of tissue damage, and extending the microbubble lifetime by reducing the amount of time for which they are stimulated (Morse, 2020). There is a risk that reducing the burst length will reduce the probability of BBBD and extent of drug delivery. The effect of reducing the burst length on drug delivery has been assessed in this thesis work.

3.1.5 Peak-rarefactional pressure (PRP)

Acoustic PRP will affect the magnitude of microbubble oscillation and resultant effect on vasculature and BBBD (Baseri et al., 2010, Chen and Konofagou, 2014, Cheng et al., 2019, Yang and Lee, 2012, Hynynen et al., 2003a, Aryal et al., 2017, Shin et al., 2018a, Kinoshita et al., 2006a, Tsai et al., 2018b, Fan et al., 2014a). There is a PRP threshold for BBBD (also dependent on centre frequency), above which there is a positive correlation with drug dose delivered (Chen and Konofagou, 2014, Sierra et al., 2017). Baseri et al. (2010) found a BBBD threshold of 0.15- 0.3 MPa (frequency: 1.525 MHz) using long pulses of ultrasound. Increases in PRP have been associated with increase in volume of BBBD shown with MRI contrast agents (Vlachos et al., 2011, Samiotaki et al., 2012, Choi et al., 2010b), the model drug dextran (Chen and Konofagou, 2014) and cancer drugs such as herceptin (Kinoshita et al., 2006a). This trend correlates positively with PRP up to a second threshold above which tissue damage occurs (Liu et al., 2009, Choi et al., 2010b, Baseri et al., 2010). Baseri et al. (2010) reported an increase in tissue effects from 0.3 – 0.75 MPa and large-scale detectable haemorrhage at 0.98 MPa.

3.1.6 Microbubbles (MB)

Microbubble type, dose, size, and distribution can influence biological effects from ultrasound exposure (Kovacs et al., 2018). Commercially available microbubbles that are commonly used for BBB studies are Definity®, Optison™ and SonoVue®. These microbubbles all differ in size, dispersity, and concentration, all of which influence their BBBD efficacy and tissue effects (**§1.5.2**). Moreover, the difference in BBBD ability between microbubble types can change with acoustic pressure and centre frequency. (Wang et al., 2014) compared Definity® and their in-house prepared (IHP) microbubbles and found no difference in permeability and volume of opening at 0.45 MPa and 0.6 MPa but did so at 0.3 MPa. Previous

work with rapid short pulse ultrasound has used SonoVue® microbubbles at concentrations of 1.5-5.6 $x10^8$ MBs ml^{-1} and mean diameter 1.5-2.5 µm (Morse et al., 2019). Other microbubbles, such as the IHP agents described by (Pouliopoulos et al., 2014) may give better drug delivery and safety profile with rapid short pulse ultrasound at 300 kHz. These microbubbles were used at a concentration of 7.3 ± 4 $x10^9$ MBs ml^{-1} and mean diameter 1.62 ± 0.87 µm. The difference in size, concentration, coating composition and gas core may affect their BBBD and drug delivery profile and so these are compared here with SonoVue® bubbles.

3.1.7 Acoustic emissions to predict treatment outcomes

Many preclinical and clinical ultrasound systems use magnetic resonance imaging (MRI) to confirm BBBD. Whilst this method is effective, the requirement of an MRI scanner increases costs, requires specialist staff, depends on scanner availability, and increases treatment time for the patient. Children are likely to require general anaesthesia which increases the number of resources and staff required. Acoustic emissions from the microbubbles recorded during sonication could be used to provide real-time treatment feedback and as an alternative for treatment assessment (**§1.7**).

3.2 Aims and objectives

The aim of this chapter is to describe work designed to achieve BBBD in the pons of mice at a centre frequency that is suitable for human transcranial transmission. This is the first study to investigate BBBD in the pons with rapid short pulse ultrasound, and at a frequency of 300 kHz. Microbubble activity differs at the lower frequency of 300 kHz, than at the 1 MHz previously used, and so the optimal parameters for BBBD are likely to change.

First the effect of burst length on the probability of BBBD and resultant drug delivery in the hippocampus was examined. The correlation between recorded acoustic emissions and model drug delivery during these treatments was assessed.

Next, the ability of rapid short pulses of ultrasound to disrupt the BBB in the pons was established. To optimise drug delivery to the pons, the effect of acoustic pressure and microbubble type on BBBD were examined.

3.3 Materials and methods

For this study, mice were exposed to ultrasound emitted in a rapid short-pulse sequence using the parameters shown in **table 2.3.1** (centre frequency: 300 kHz, PRP: 0.3 MPa, pulse length: 1 cycle, pulse repetition frequency: 1.25 kHz, burst length: 38 pulses, burst repetition frequency: 0.5 Hz, number of bursts: 125, total time: 250s). The effect of (i) burst length, (ii) the ability to target the pons, (iii) PRP, and (iv) microbubble type on BBBD were assessed.

3.3.1 Effect of burst length on blood-brain barrier disruption

The effect of burst length on BBBD was assessed as described in **figure 3.3.1**. Mice (strain, gender, weight are described in **§2.1**) were prepared for sonication as described in **§2.2**, and the left hippocampus targeted (**§2.3.2**). Once targeting position was established, mice were

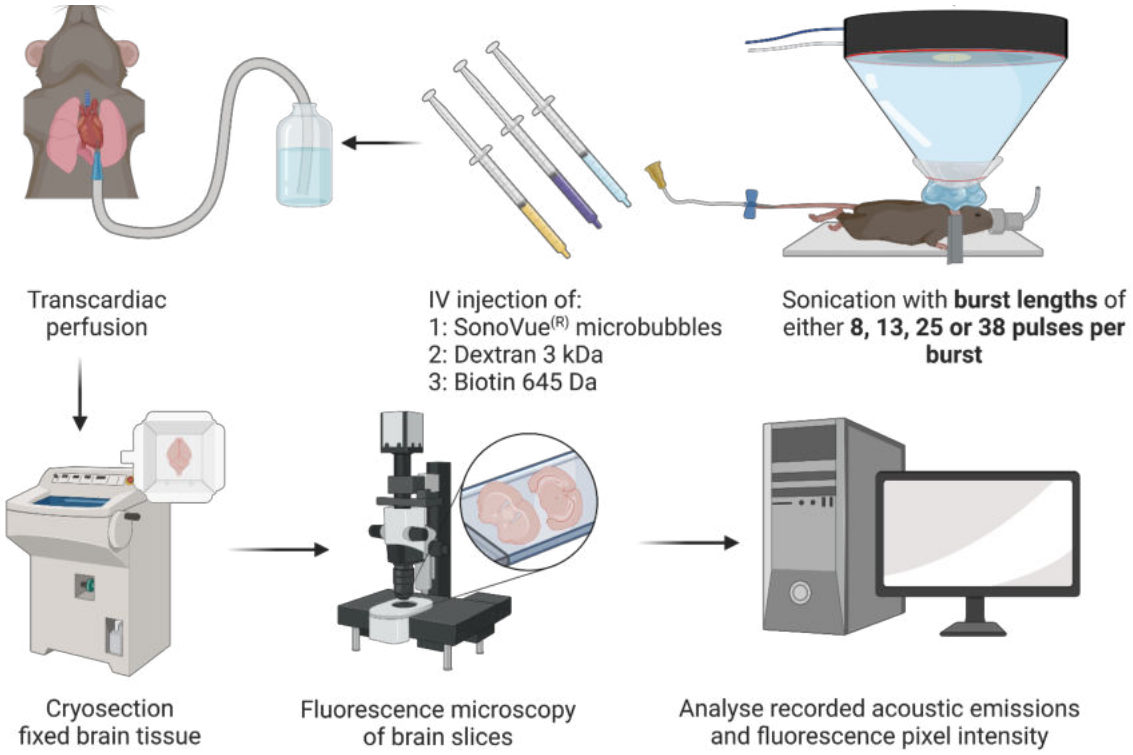

Figure 3.3.1 Burst length study protocol. *C57BL/6J mice were prepared for sonication and the transducer aligned to target the left hippocampus. A cannula was inserted into the mouse tail vein through which microbubbles and two model drugs (Dextran 3 kDa and Biotin 645 Da) were injected. Sonication was started at the same time as the injection, and mice were exposed to ultrasound with burst lengths containing 8, 13, 25 or 38 pulses. After sonication, mice were perfused transcardially, brains fixed, cryosectioned and imaged using fluorescence microscopy.*

exposed to ultrasound (parameters **§3.3**) with burst lengths of either 8, 13, 25 or 38 pulses per burst (n=5 each burst length). During ultrasound exposure, mice received an intravenous injection of SonoVue® microbubbles, and the model drugs dextran and biotin (**§2.5**). Immediately after sonication, mice were perfused transcardially (**§2.6**), the brain was extracted and cryosectioned into coronal slices and imaged (**§2.8**). BBBD in sonicated mice was compared to sham controls that underwent the same procedures but were not exposed to ultrasound (n=3). Fluorescence pixel intensity was quantified in five sections per brain (**§2.9**) and the acoustic signal recorded from each exposure processed (**§2.10**).

3.3.2 Targeting the pons

The work described in this thesis focused on improving drug delivery to the pons, therefore, BBBD in this region of the brain was assessed. To first assess drug delivery to the pons, mice were exposed to ultrasound as described in **§3.3.1** with ultrasound targeted at the pons as described in **§2.3.2**. Dextran was used as the model drug.

3.3.3 Peak-rarefactional pressure

The effect of PRP on BBBD in the pons was assessed by exposing mice to ultrasound at acoustic pressures of either $0.25 \pm 3.70 \times 10^{-4}$ MPa or $0.3 \pm 2.3 \times 10^{-3}$ MPa (n=8 each pressure) and comparing results to those from controls not exposed to ultrasound (n=3). The protocol described above for initial targeting of the pons was followed. Fluorescence pixel intensity was quantified (**§2.9**) in five sagittal brain slices per mouse, as were the acoustic signals (**§2.10**) from each exposure.

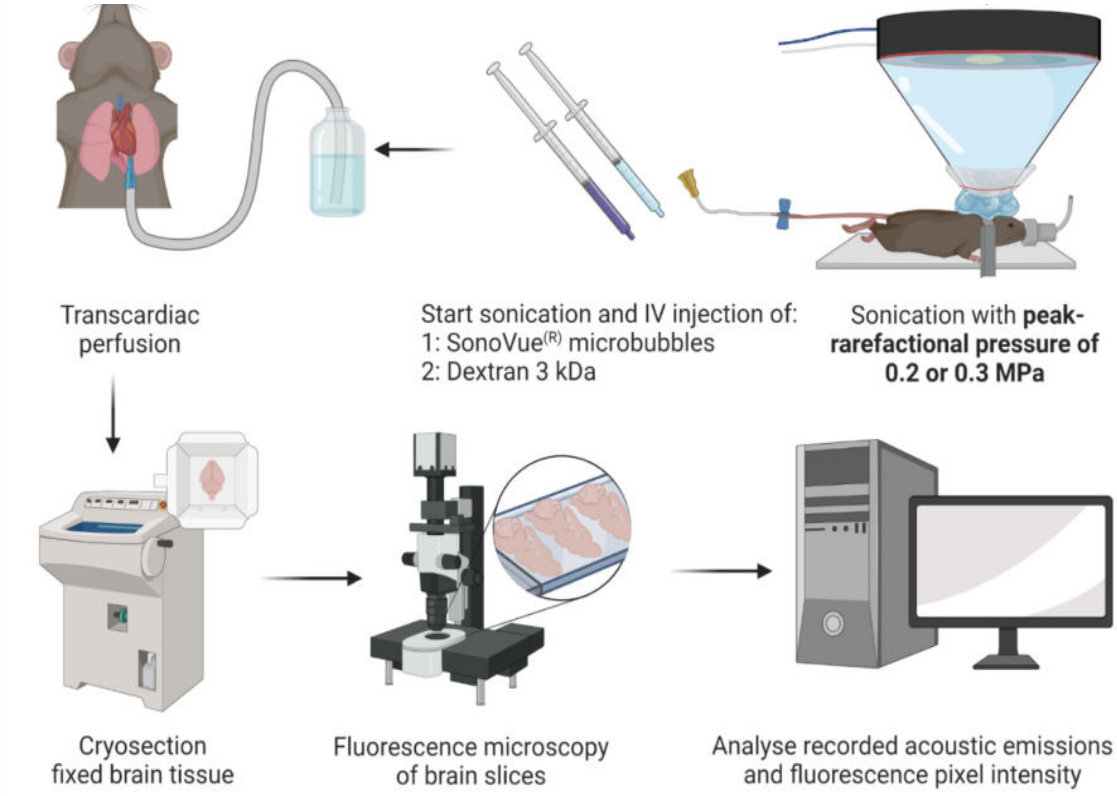

Figure 3.3.2 Peak-rarefactional pressure study protocol. *C57BL/6J mice were prepared for sonication, and the transducer focus aligned with the pons. A cannula was inserted into the mouse tail vein through which microbubbles and the model drug dextran were sequentially injected. Sonication was started at the same time as the injection, with mice being exposed to peak-rarefactional pressures of either 0.25 or 0.3 MPa. After sonication, mice were perfused transcardially, brains fixed, cryosectioned, and imaged using fluorescence microscopy. Recorded acoustic emissions and fluorescence pixel intensity were analysed.*

3.3.4 Microbubble comparison

Two microbubble types and their effect on BBBD in the pons were compared. Ultrasound exposure was performed as described in **§3.3.2**. During the exposure, mice were given either SonoVue® or IHP microbubbles (n=5 each bubble type), and Evans Blue (2%) acting as a model drug, through a tail vein cannula (**§2.5**). Mice were allowed to recover from anaesthesia then perfused transcardially 30 minutes after sonication ended (**§2.6**), and the brain tissue processed. Evans Blue extravasation was compared to sham control mice that had not received a microbubble injection (n=3). Acoustic emissions recorded during ultrasound exposures were also analysed (**§2.10**).

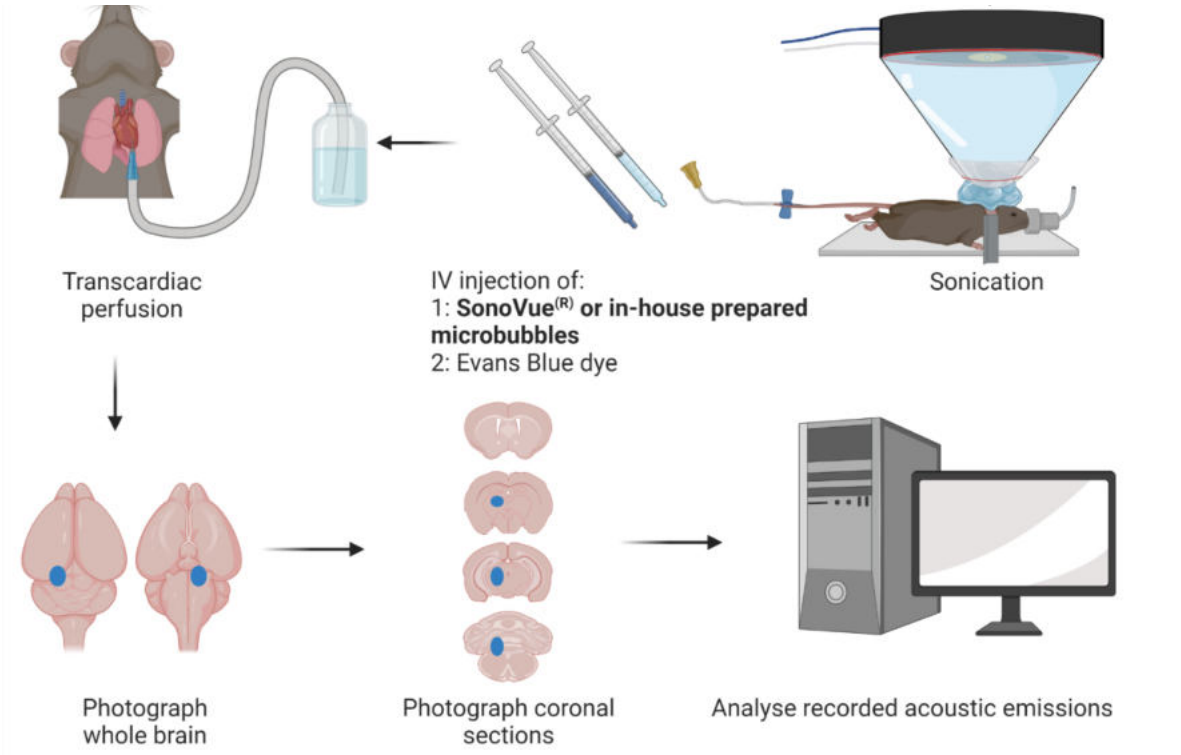

Figure 3.3.3 Microbubble comparison protocol. *C57BL/6J mice were prepared for sonication and the transducer focus aligned with the pons. A cannula was inserted into the mouse tail vein through which either SonoVue® or in-house prepared microbubbles and Evans Blue dye were injected. Sonication was started at the same time as the injection. After sonication, mice were perfused transcardially, brains fixed, sectioned into coronal slices and photographs taken.*

3.3.5 Statistical analysis

GraphPad Prism v7.01 was used for all statistical analysis. A two-way ANOVA was performed to examine the interaction between burst length and PRP on the fluorescence pixel intensity. A post-hoc Tukey's multiple comparison test was performed on any significant interaction. Linear regression analysis was performed to assess correlation between the fluorescence pixel intensity and total energy from the recorded acoustic emissions. An unpaired t-test assessed the difference in total acoustic energy between SonoVue® and IHP microbubble types. Outliers were assessed using the robust regression followed by outlier elimination (ROUT) method.

3.4 Results

The aim of study described in this chapter was to establish repeatable BBBD in the pons region when ultrasound is emitted in a rapid short pulse sequence with a centre frequency of 300 kHz. BBBD was assessed from the extravasation of two model drugs in the targeted region compared to that in a control that received no ultrasound. The effect of two ultrasound parameters and microbubble types on BBBD were assessed.

3.4.1 Burst length in the hippocampus

The first FUS parameter to be assessed was the burst length. Previous work by the ICL lab has shown successful drug delivery using a burst length of 38 pulses per burst (unpublished). Here, the effect of reducing the length to 8, 13 or 25 pulses per burst on the delivery of two model drugs- biotin and dextran- to the left hippocampus of mice was assessed.

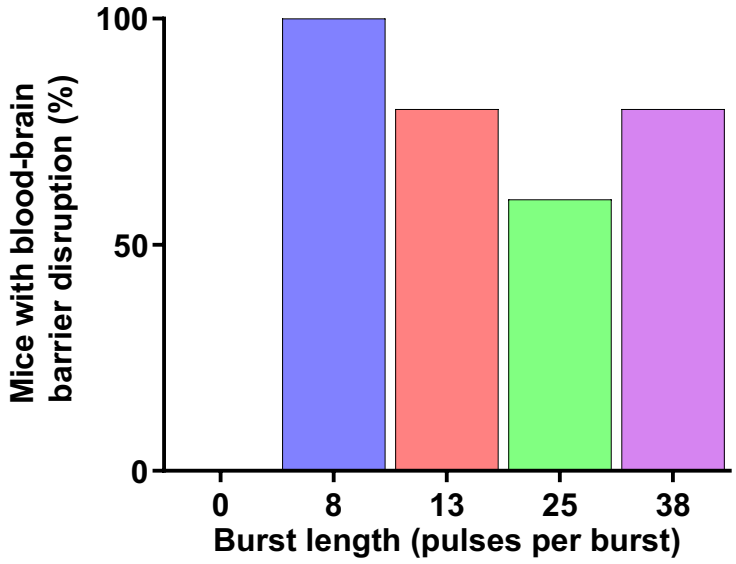

Figure 3.4.1 Burst length dependence for blood-brain barrier disruption (BBBD). *Mice were exposed to ultrasound emitted in a rapid short pulse sequence targeted on the hippocampus. During ultrasound exposure, mice were given two fluorescently tagged tracers (biotin 645 Da and dextran 3 kDa) intravenously to assess blood-brain barrier disruption at four burst lengths (n=5 each) compared to a sham control that received no ultrasound (n=3). BBBD was defined as visible extravasation of fluorescently tagged tracer.*

3.4.1.1 Model drug delivery

Qualitative increased in fluorescence was observed in the targeted region at all burst lengths evaluated (8, 13, 25, and 38 pulses per burst) for both fluorescent tracers, biotin (645 Da) and dextran (3 kDa). No visual increase in fluorescence occurred in any of the control (no FUS) mice. The percent of animals with drug delivery was not always 100% (**figure 3.4.1**). The greatest percentage of BBBD occurred in the shortest burst length (8 pulses) with biotin and dextran observed in all mice of this burst length. BBBD was determined by observing fluorescence tracers present in the targeted region compared to the untargeted region. This occurred in four out of five mice receiving 13 & 38 pulses per burst and three out of five mice receiving 25 pulses per burst.

3.4.1.2 Model drug delivery distribution and quantification

The location and overall area of the brain slice containing biotin and dextran was similar for both model drugs, but the distribution within these regions differed (**figure 3.4.2**). Overall, the distribution of biotin was more homogenous than dextran, which was in more of a spot-like pattern. At 8, 13 and 25 pulses per burst, biotin and dextran extended through half the height of the brain slice (**figure 3.4.2.B-D**). The delivery of both tracers with 38 pulses per burst appeared to cover a larger brain region than was seen for the shorter burst lengths. Overlaying images showed that the delivery of both tracers had a similar localisation.

These observations were confirmed by quantifying the fluorescence pixel intensity in five brain slices per mouse (**figure 3.4.3**). For biotin, the fluorescence pixel intensity in those brains without successful BBBD was similar to that in the control (marked with an X in **figure 3.4.3A**). In those mice with successful BBBD, all burst lengths had one value higher than the others and the remaining values clustered together. The greatest mean fluorescence pixel intensity occurred at 38 pulses per burst ($2x10^{10} \pm 1x10^{10}$ A.U.; ± is SD) and was more than double the mean fluorescence pixel intensity of the shorter burst lengths (8: $7x10^{9} \pm 6x10^{9}$ A.U., 13: $9x10^{9} \pm 6x10^{9}$ A.U., 25: $6x10^{9} \pm 7x10^{9}$ A.U.).

BBBD occurred in four mice exposed to 38 pulses per burst and the fluorescence pixel intensity for these mice is greater than the fluorescence pixel intensity at the shorter burst lengths. Ordinary one-way ANOVA and Tukey post-hoc analysis revealed a significant

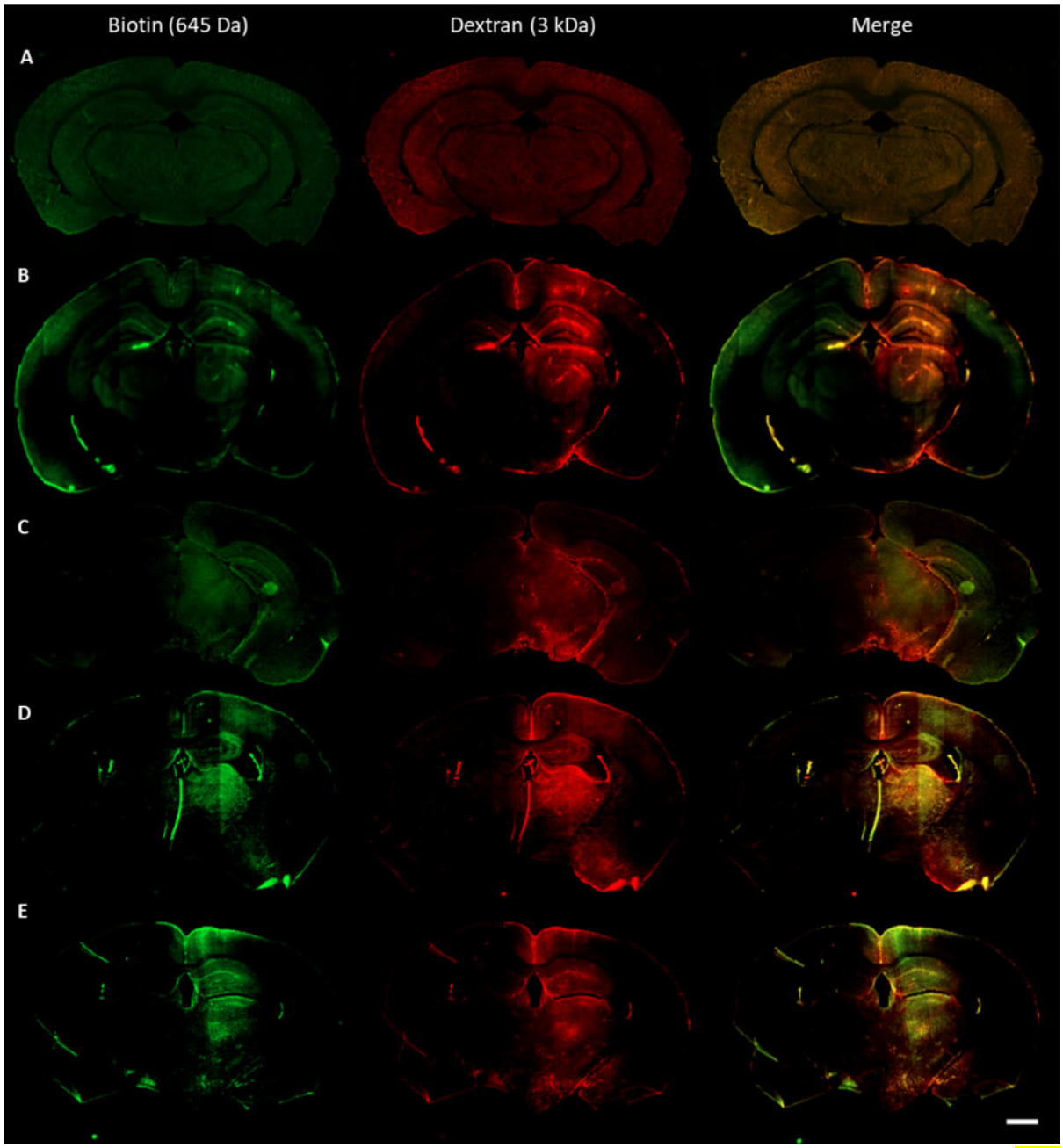

Figure 3.4.2 Fluorescent images of coronal brain slices from mice exposed to ultrasound and intravenous microbubbles of different burst lengths. *The left hemisphere of the hippocampus was exposed to ultrasound emitted in rapid short bursts of either 8 (B), 13 (C), 25 (D) or 38 (E) pulses (n=5 each) and compared to a sham control (A; dosed with microbubbles, no FUS; n=3). The contralateral hemisphere also acted as an internal control for each mouse. Mice were dosed with the fluorescently tagged tracers biotin (645 Da) and dextran (3 kDa) which acted as model drugs to assess blood-brain barrier disruption. Representative examples from each burst length are shown as the biotin and dextran individually and as an overlay. Scale bar represents 1 mm.*

difference between the fluorescence pixel intensity in the control and 38 pulses per burst ($p > 0.05$). Variation (SD) between mice was similar at 8, 13 and 25 pulses per burst and greatest at 38 pulses per burst.

For dextran, the mice with no observable extravasation had fluorescence pixel intensity values similar to the control (marked with an X in **figure 3.4.3B**). The mean value of fluorescence pixel intensity was greater at 13 pulses per burst ($2x10^{10} \pm 2x10^{10}$ A.U.) than for the other burst lengths (8: $8x10^{9} \pm 2x10^{9}$ A.U., 25: $8x10^{9} \pm 7x10^{9}$ A.U., 38: $1x10^{10} \pm 8x10^{9}$ A.U.). One mouse subjected to 13 pulses per burst returned fluorescence pixel intensity greater than the rest, but this was not deemed statistically to be an outlier. The mean fluorescence pixel intensities at 8, 25 and 38 pulses per burst are similar, and there was no significant

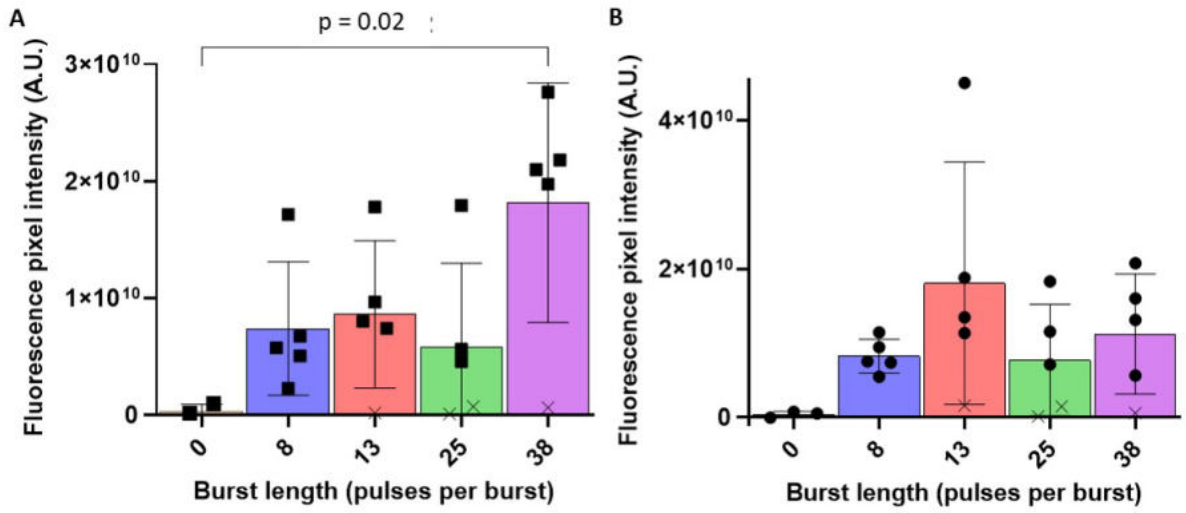

Figure 3.4.3 Fluorescence pixel intensity for four burst lengths. *Mice were exposed to ultrasound emitted in a rapid short pulse sequence at four burst lengths (n=5) and results were compared to sham controls (with microbubbles, no ultrasound; n=3). The fluorescently tagged tracers biotin (645 Da) and dextran (3 kDa) were used to assess blood-brain barrier disruption. The sum of fluorescence pixel intensity was quantified in the targeted left hippocampus and compared to the right hippocampus for (A) biotin and (B) dextran, with the data plotted representing the difference between the treated and untreated regions. Data shows the mean, and error bars represent the standard deviation. A two-way ANOVA and post-hoc Tukey multiple comparison test was performed with the only significant difference being between 38 pulses per burst and the control for biotin ($p = 0.02$), all other values were non-significant ($p > 0.05$).*

difference between the mean fluorescence pixel intensity of each burst length assessed by ANOVA and Tukey post-hoc analysis ($p > 0.05$).

3.4.1.3 Acoustic emission analysis

Acoustic emissions were recorded during sonication and were analysed. Across all burst lengths, there was a peak in acoustic energy that coincides with microbubble injection, lasting until approximately burst 40 (**figure 3.4.4**). After the initial peak, the acoustic energy plateaus

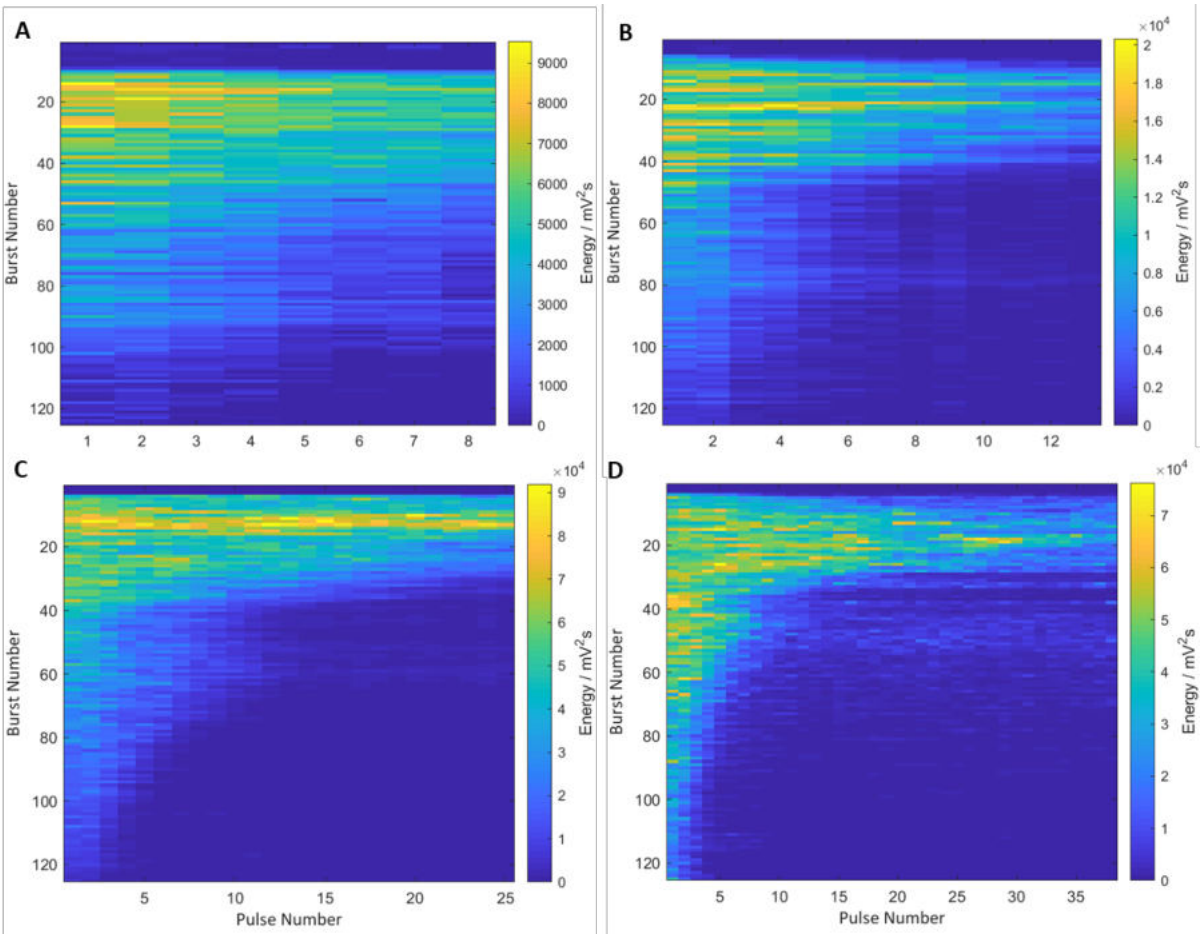

Figure 3.4.4 Example energy heat maps for acoustic emissions recorded during ultrasound exposure resulting in blood brain barrier disruption (BBBD). *Mice were exposed to ultrasound in the presence of microbubbles with burst lengths of either (A) 8, (B) 13, (C) 25 or (D) 38 pulses for 125 bursts. Successful BBBD was assessed by the presence of biotin and dextran (two fluorescent markers) that do not normally cross the blood brain barrier. Figure created using MATLAB v.2018b.*

for the remaining bursts. Whilst the trend was similar for all burst lengths, the magnitude of the energy peak increased with burst length.

When the duration of microbubble activity was further investigated, it was confirmed that the maximum burst energy (t_{100}) occurred at bursts 14-19 and the magnitude increases with burst length (**figure 3.4.5**). The burst at which t_{50} occurs is inversely correlated with burst length: the t_{50} is greatest at 8 pulses per burst (burst 64 ± 23), lower at 13 pulses per burst (43 ± 14) and decreases further at 25 pulses per burst (burst ± 7). The t_{50} at 38 pulses per burst (burst 32 + 2) is similar to 25. The mean t_{25} follows the same trend as t_{50}: the mean t_{25} occurs at a later burst for the shorter burst lengths (8: 91, 13: 43, 25: 42) and is similar for 25 and 38 (40) pulses per burst.

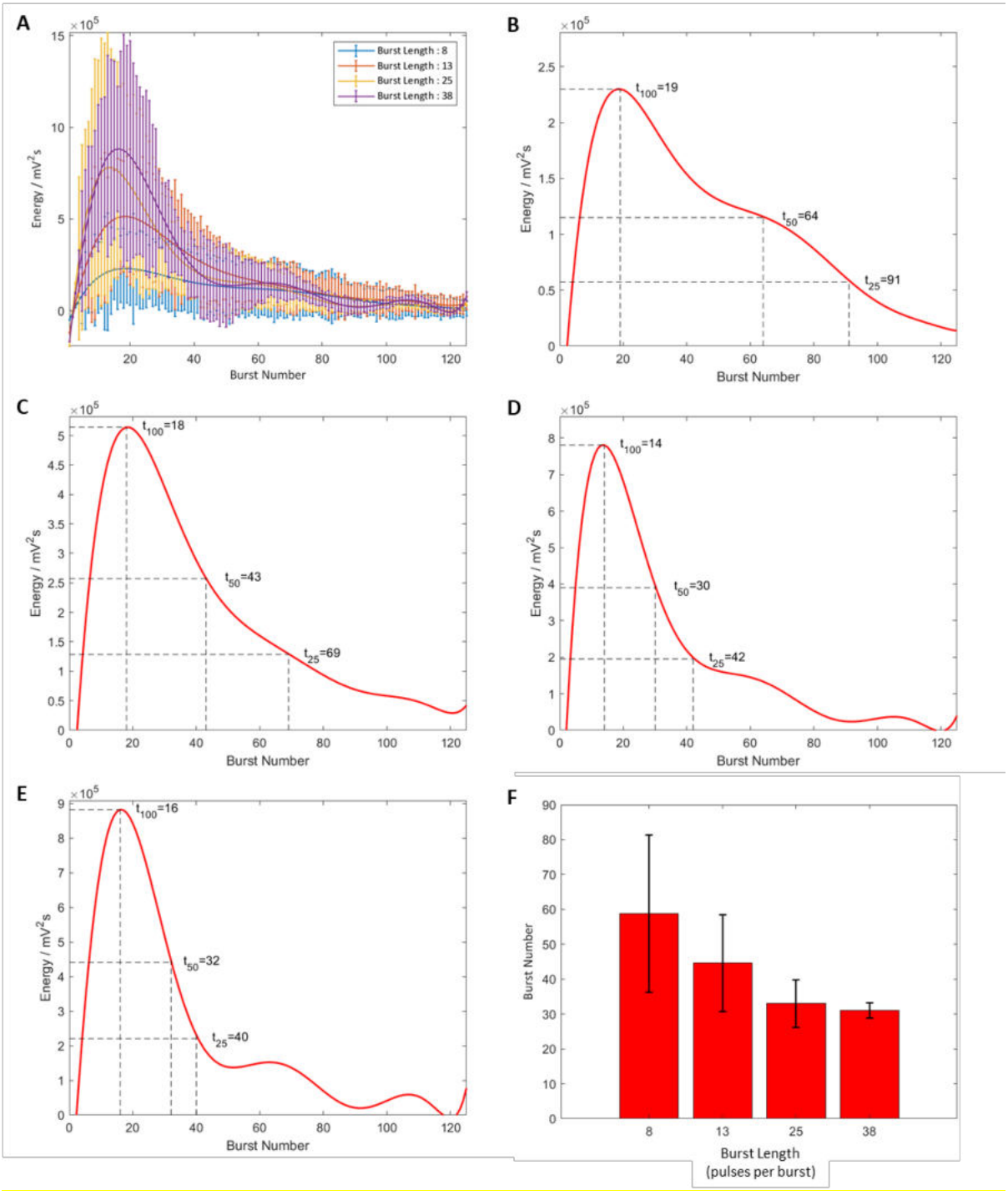

Figure 3.4.5 Mean energy for each burst recorded during ultrasound exposure indicating microbubble lifetime. *Acoustic emissions were recorded during sonication of four different burst lengths shown (A) together and (B-E) separately (8, 13, 25 & 38 pulses per burst, respectively). The burst number at which maximum energy (t100), then 50% (t50) and 25% (t25) of maximum are calculated to indicate microbubble lifetime. Error bars are standard deviation. Figure created using MATLAB v2018b and the fitted curve is 8th order polynomial function.*

The calculated acoustic emissions were summed to give a value for total acoustic cavitation energy (mV^2) for each mouse. Total acoustic energy showed an upward trend with burst length (**figure 3.4.6A**). Overall, there was no significant difference between total acoustic energy between burst lengths, assessed by one-way ANOVA ($p > 0.05$).

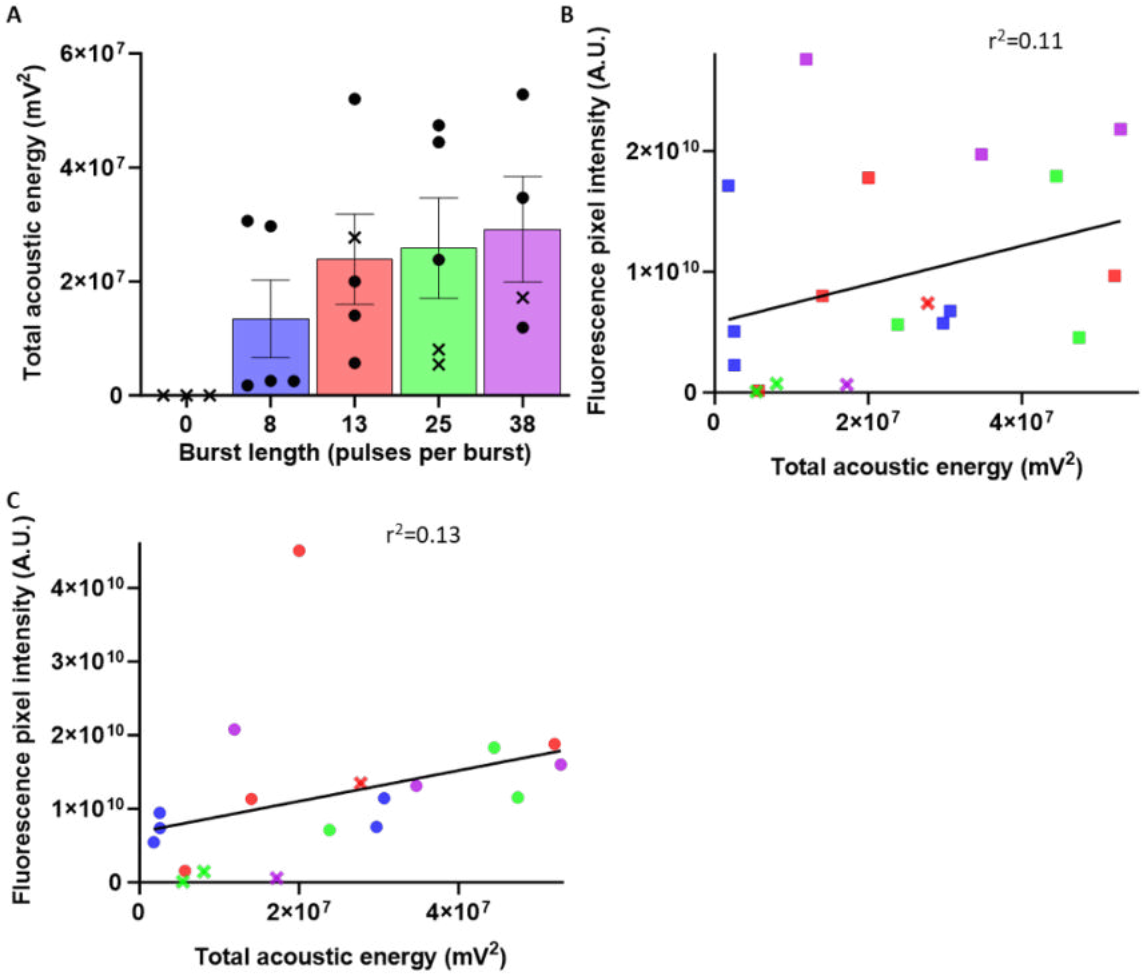

Figure 3.4.6 Fluorescence pixel intensity compared to total acoustic energy in mice exposed to ultrasound. *(A) Acoustic emissions were recorded during sonication and analysed to give total energy for each burst length (n=5 each burst length, error bars represent standard deviation). The sum of fluorescence pixel intensity in the left hemisphere minus the right hemisphere plotted against total acoustic energy for (B) biotin, and (C) dextran. A linear regression was fitted, and correlation assessed; biotin $r^2 = 0.11$, dextran $r^2 = 0.13$. Those mice without observable blood brain barrier disruption (BBBD) are noted by an 'X' symbol.*

Next, the correlation between total acoustic energy and fluorescence pixel intensity was investigated to assess whether acoustic emissions correlated with BBBD success and drug delivery (**figure 3.4.6B&C**). There was a trend of increasing fluorescence pixel intensity with increasing total acoustic energy (**figure 3.4.6&C**) but the correlation was weak (biotin: r^2: 0.11, dextran: r^2: 0.13).

3.4.2 Blood-brain barrier disruption in the pons

DIPG arises in the pons, therefore, all further work focused on improving drug delivery to this brain region. As the above study did not suggest that a shorter burst length was beneficial, the baseline parameters (PRP: 0.400 ± 0.004 MPa; pulse length: 5 cycles; pulse repetition frequency (PRF): 1.25 kHz; burst length: 38 pulses; burst repetition frequency (BRF): 0.5 Hz; number of bursts: 125; total time: 250s; shown in **table 2.3.1**) were used for BBBD in the pons.

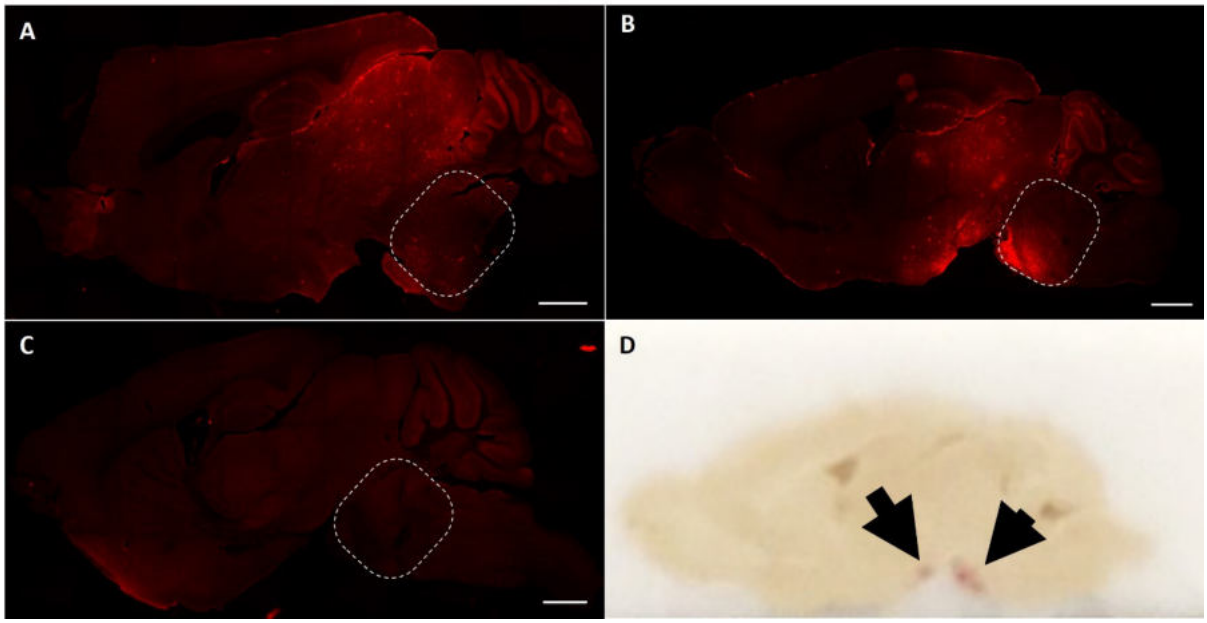

Figure 3.4.7 Blood-brain barrier disruption in mice exposed to ultrasound. *Mice were exposed to ultrasound emitted in a rapid short pulse sequence at peak negative pressures of (A) 0.25 MPa or (B) 0.3 MPa compared to (C) a sham control (dosed with microbubbles, no ultrasound). Successful blood-brain barrier disruption was assessed by an increase in fluorescence of the fluorescently tagged tracer dextran (3 kDa) compared to the control. In mice exposed to acoustic pressure of 0.3 MPa, some haemorrhage was observed when the brain was sectioned, indicated by the arrows (D). Scale bar represents 1 mm the pons region is defined by the dotted line.*

The pons region was successfully targeted, and fluorescence increase was seen throughout the height of the brain (**figure 3.4.7**). The distribution of dextran was mostly homogenous throughout this region with some greater intensity around morphology similar to blood vessels. Haemorrhage was seen at brain extraction around the skull base in two mice out of eight sonicated (**figure 3.4.7D**).

3.4.3 Peak-rarefactional pressure

To overcome the haemorrhage observed at an acoustic pressure of 0.3 MPa, BBBD and resultant drug delivery at a lower PRP of 0.25 MPa was compared to 0.3 MPa. The increase in fluorescence of dextran after exposure to ultrasound with PRPs of 0.25 and 0.3 MPa (n=8 each

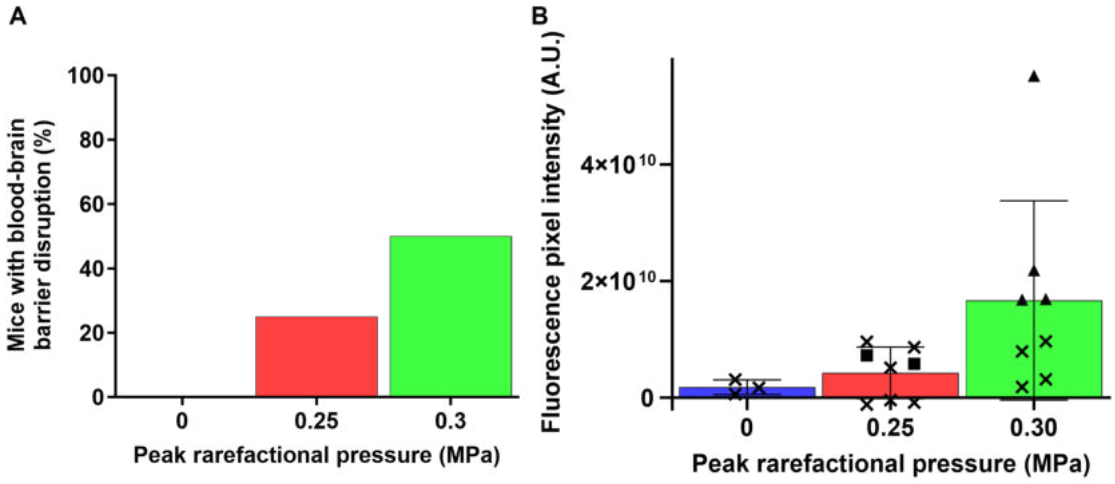

***Figure 3.4.8* Pressure dependence for blood-brain barrier disruption (BBBD).** *Mice were exposed to ultrasound at peak-rarefactional pressures of 0.25 or 0.3 MPa (n=8 each pressure) and assessed for increase in the fluorescently tagged tracer dextran (3 kDa) compared to a sham control (received microbubble and tracer injection but no ultrasound exposure). (A) The percentage of mice with BBBD determined by observable dextran delivery was 0% in the control, 20% at 0.25 MPa and 50% at 0.3 MPa. (B) Quantification of fluorescence pixel intensity, a proxy for dose delivered, of five slices from each mouse brain. Each symbol represents the mean of five slices from one mouse brain and the 'X' symbol represents no observable BBBD. A two-way ANOVA and post-hoc Tukey analysis revealed no significant difference between the fluorescence pixel intensity at each acoustic pressure ($p > 0.05$). Error bars represent standard deviation.*

pressure) were compared to sham controls (n=3) that were dosed with microbubbles but not exposed to ultrasound (**figure 3.4.8**). The observable fluorescence at 0.25 MPa is less than at 0.3 MPa. At 0.3 MPa the dextran is distributed homogenously throughout the targeted region, whereas the distribution is more heterogeneous at 0.25 MPa. No dextran fluorescence was observed in the control mice. Of the eight mice exposed to 0.25 MPa of ultrasound, two had observable dextran increase (**figure 3.4.8A**). At 0.3 MPa, 50% of the eight mice had observable dextran delivery.

The fluorescence pixel intensity was quantified in all mice as a proxy for drug dose present in the brain parenchyma (**figure 3.4.8B**). The fluorescent pixel intensity was similar for all mice exposed to 0.25 MPa. The two mice in which BBBD was observed have lower fluorescence pixel intensity than two mice without observable BBBD. Overall, the mean fluorescence pixel intensity was greater at 0.3 MPa ($2x10^{10} \pm 2x10^{10}$ A.U.) than at 0.25 MPa ($4x10^{9} \pm 4x10^{9}$ A.U.) and both higher than the control ($2x10^{9} \pm 1x10^{9}$ A.U.) with greatest variation at 0.3 MPa, although there was no significant difference between the fluorescence pixel intensity by one-way ANOVA (p=0.08).

The acoustic emissions recorded during sonication were analysed. A similar distribution of energy was seen in all mice with BBBD whilst the magnitude of such energy differs (**figure 3.4.9**). There is a sharp increase in energy, during bursts 5-60, followed by a rapid decrease and plateau. The magnitude of peak energy is greater for 0.3 MPa than for 0.25 MPa, except for one mouse where the recorded peak energy at 0.3 MPa was lower than 0.25 MPa (**figure 3.4.9F**).

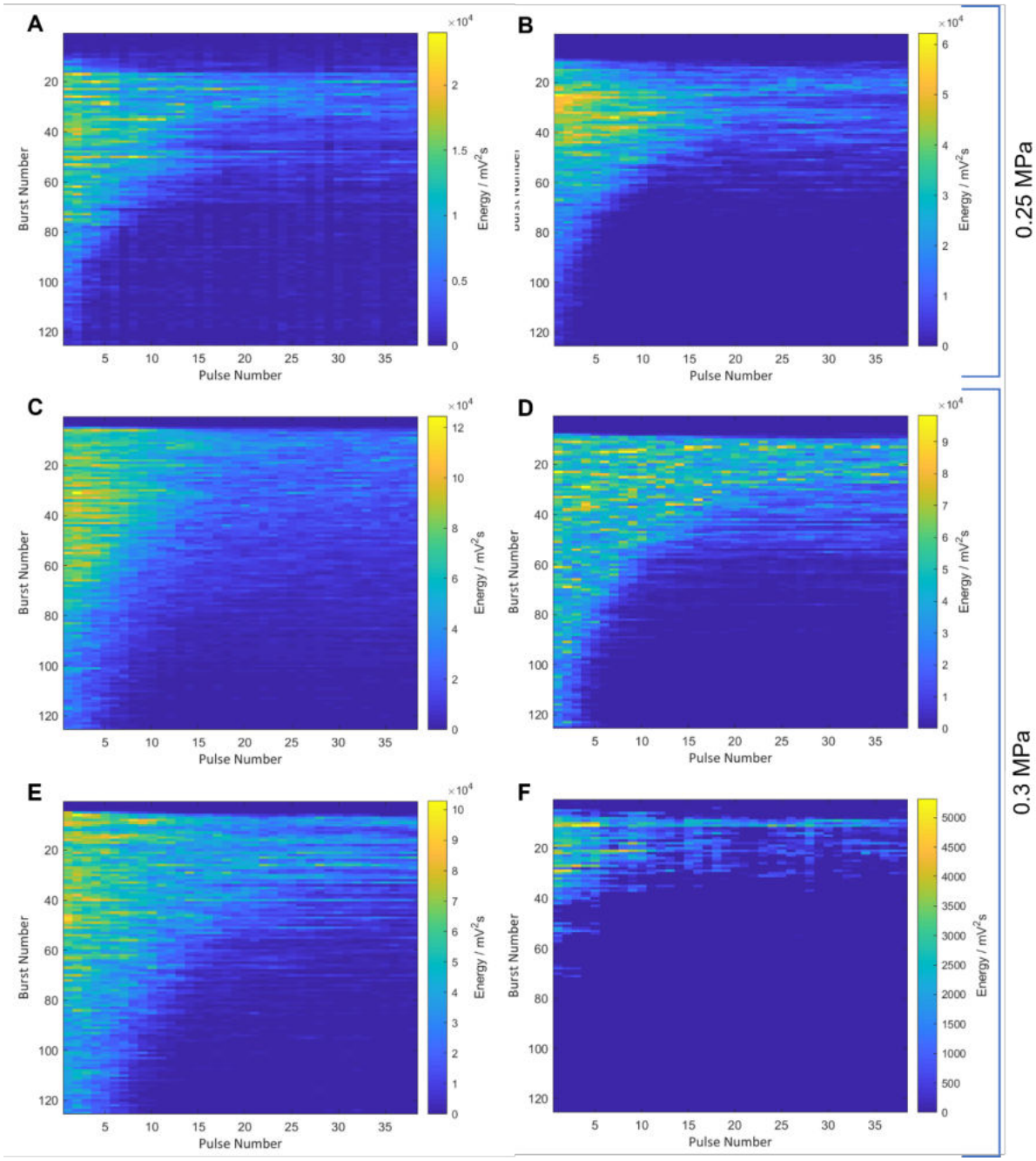

Figure 3.4.9 Energy heat maps of acoustic emissions recorded during ultrasound exposure where blood brain barrier disruption (BBBD) occurred. *Mice were exposed to ultrasound in the presence of SonoVue® microbubbles at an acoustic peak-negative pressure of either (A&B) 0.25 MPa or (C-F) 0.30 MPa. BBBD was determined by extravasation of a fluorescently tagged tracer (3 kDa) in the targeted pons region. Figure created with MATLAB v2018b.*

The total acoustic energy was calculated from acoustic emissions recorded during ultrasound exposures (**figure 3.4.10A**). At 0.25 MPa the total energy was similar, with one outlier where BBBD did not occur. At 0.3 MPa, the total energy recorded in five mice were similar and three greater. The mean acoustic energy at 0.3 MPa ($3.1 \times 10^7 \pm 4.6 \times 10^7$ mV^2) was higher than at 0.25 MPa ($1.3 \times 10^7 \pm 2.0 \times 10^7$ mV^2) with greater variation (standard deviation) between mice at 0.3 MPa, but the difference was not significant (p=0.14) on an unpaired t-test.

The correlation between total acoustic energy and fluorescence pixel intensity was investigated (**figure 3.4.10B**). The mice with no observable fluorescence increase, cluster near the origin, and have a lower acoustic energy than those with BBBD (indicted by an X in **figure 3.4.10B**). One data point from 0.3 MPa does not fit within this window and has acoustic energy similar to those with no BBBD despite the presence of observable dextran. The

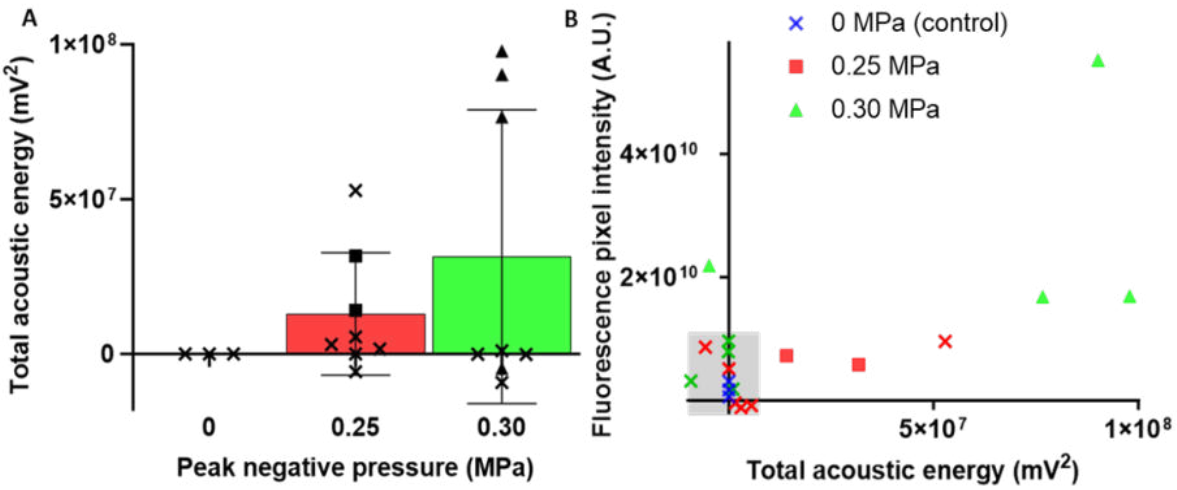

Figure 3.4.10 Total acoustic energy at two acoustic pressures and the corresponding fluorescence pixel intensity. *Mice were exposed to ultrasound emitted in a rapid short pulse sequence, targeted at the pons, at peak negative pressure of either 0.25 or 0.30 MPa. (A) During sonication, acoustic emissions were recorded and processed to give total acoustic energy. There was no significant difference between total acoustic energy by unpaired t-test (p=0.1433). Error bars represent standard deviation. (B) The fluorescence of the model drug, dextran (3 kDa) given during sonication, was quantified, and compared to the total acoustic energy for each sonication. Mice with no observable dextran extravasation are 'X' symbols.*

correlation between acoustic energy and fluorescence pixel intensity was weak for both acoustic pressure (0.25 MPa: r^2= 0.23, p=0.22, 0.3 MPa: r^2= 0.40, p=0.09).

3.4.4 Microbubble comparison

In a bid to achieve the aim of consistent BBBD in the pons, two different microbubble types were investigated. SonoVue® microbubbles, used thus far, were compared to IHP

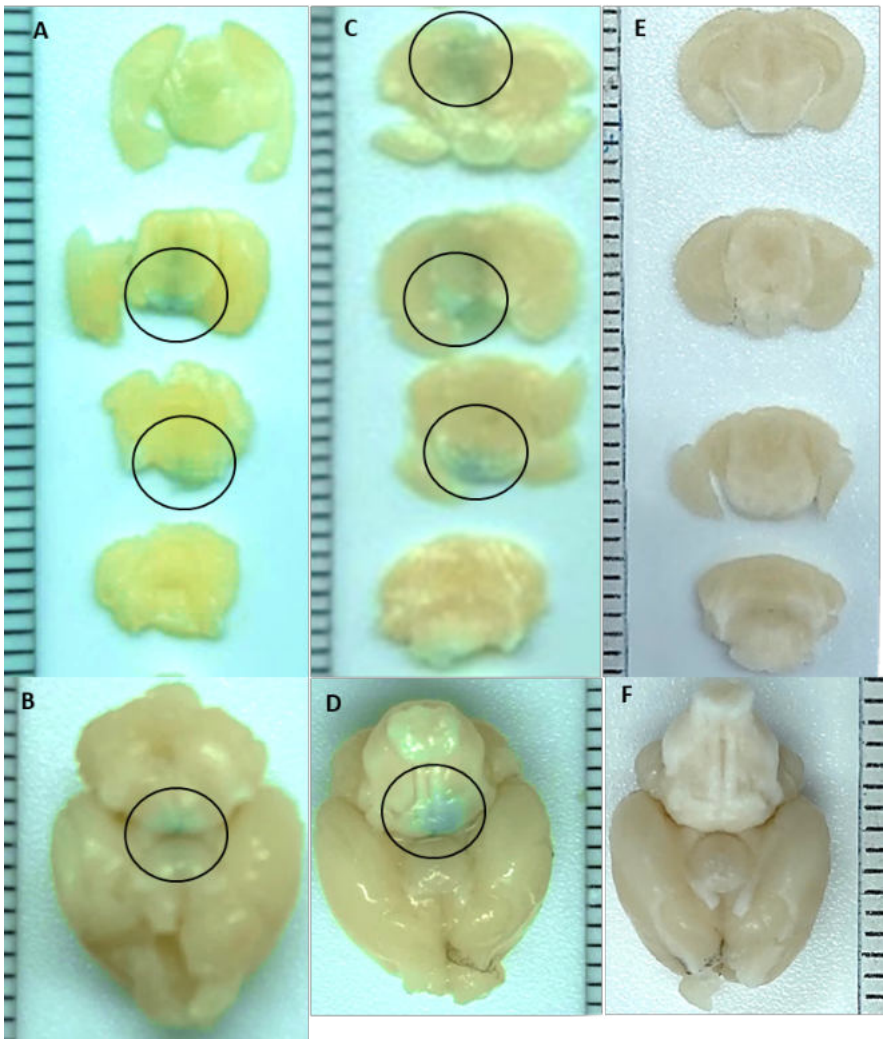

Figure 3.4.11 Evans Blue extravasation indicating blood-brain barrier disruption after ultrasound exposure. *Mice were exposed to ultrasound emitted in a rapid short pulse sequence in the presence of either (A&B) SonoVue® or (C&D) in-house prepared microbubbles (n=5 each) and compared to a sham control that received no microbubbles (E & F). Evans Blue extravasation can be seen in the ventral view of the whole brain (B & D) and 1 mm coronal slices (A & C) indicated by the oval. Ruler marks indicate 1 mm. Brain slices and whole brain*

microbubbles at a PRP of 0.3 MPa and burst length of 38 pulses. BBBD was confirmed by Evans Blue extravasation in whole brains and in 1 mm coronal slices compared to the control which showed no Evans Blue extravasation (**figure 3.4.11E&F**). The observable region of extravasation was larger with the IHP microbubbles than with the SonoVue® microbubbles (**figure 3.4.11A-D**). Overall, only one mouse (20%) with SonoVue® microbubbles had Evans Blue extravasation whilst all five (100%) with IHP microbubbles had BBBD (**figure 3.4.12**).

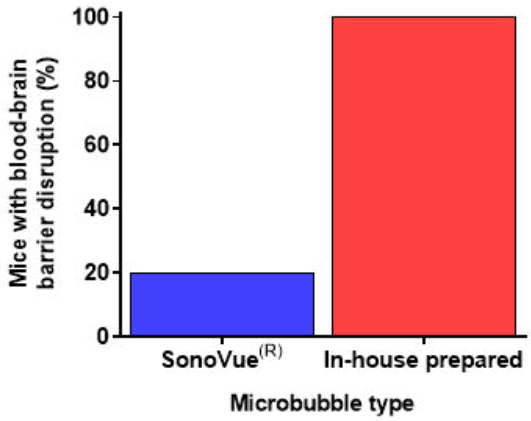

Figure 3.4.12 Microbubble influence on blood-brain barrier disruption as assessed by Evans Blue extravasation. *Mice were exposed to ultrasound emitted in a rapid short pulse sequence (peak rarefactional pressure of 0.4 MPa) in the presence of either SonoVue® or in-house prepared (IHP) microbubbles (n=5 each). The percentage of mice with blood-brain barrier disruption, indicated by Evans Blue extravasation, with SonoVue® and IHP microbubbles.*

Higher energy was sustained for longer in IHP microbubbles compared to SonoVue® microbubbles (**figure 3.4.13**). In the example shown, the energy drops off at approximately burst 40 for SonoVue® but appears to be present throughout all 125 bursts for IHP microbubbles. The magnitude of energy is similar between both microbubble types. When BBBD did not occur, the distribution of energy is similar to when BBBD occurred but at a smaller magnitude of energy. The total acoustic energy was similar for the SonoVue® and IHP microbubbles (**figure 3.4.13D**). The mean total acoustic energy with the SonoVue® microbubbles ($7.6 \times 10^6 \pm 1.1 \times 10^7$ mV^2) is lower than with IHP microbubbles ($2.4 \times 10^7 \pm 2.0 \times 10^7$ mV^2), but the range and variation (standard deviation) between mice are similar. The difference was confirmed as non-significant by an unpaired t-test (p=0.32).

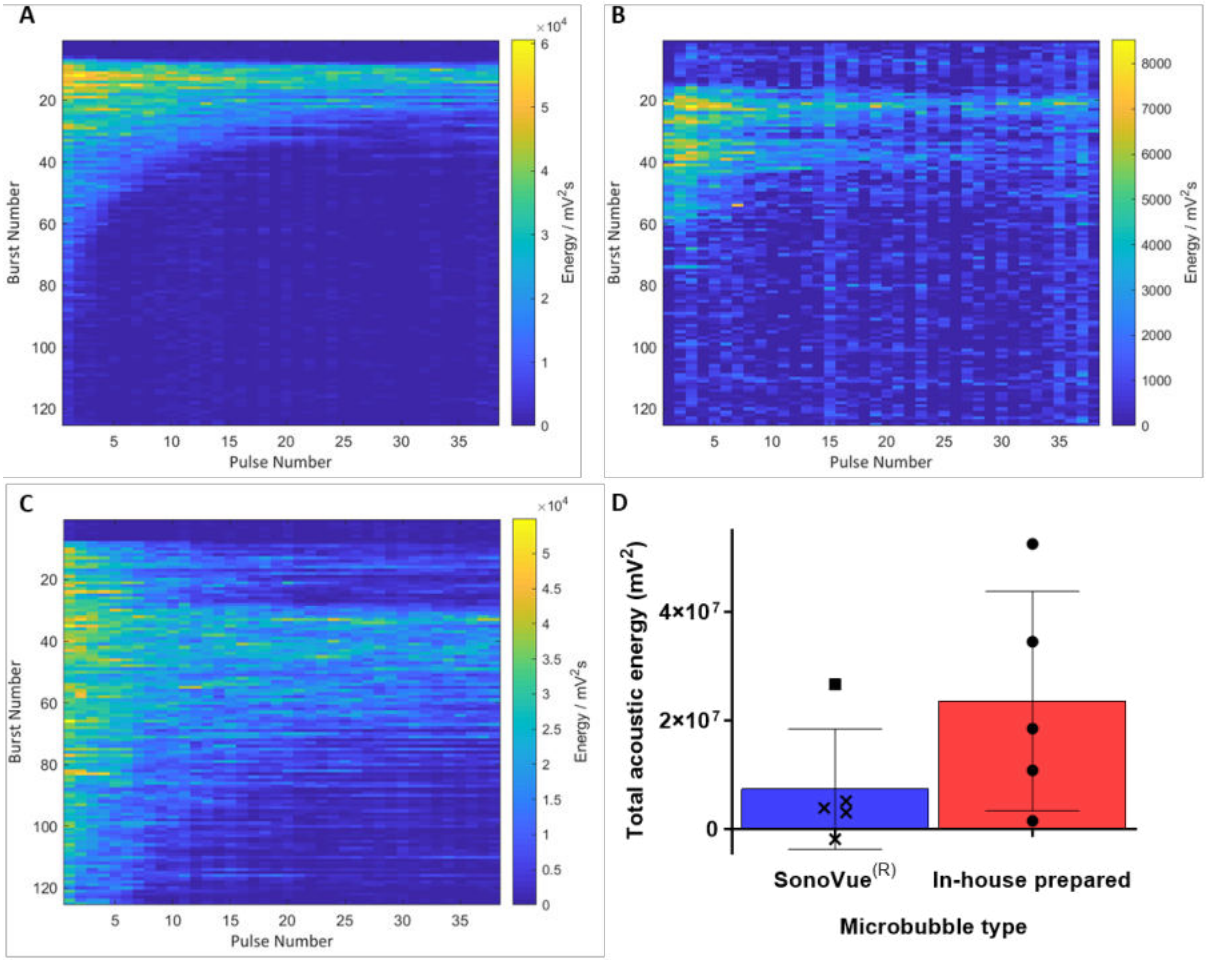

Figure 3.4.13 Examples of energy heat map calculated from acoustic emissions recorded during ultrasound exposure. *Mice were exposed to ultrasound in the presence of either (A&B) SonoVue® or (C) in-house prepared (IHP) microbubbles at an acoustic pressure of 0.25 MPa. Blood brain barrier disruption was assessed by the extravasation of Evans Blue dye with (A&C) resulting in BBBD, and (B) no BBBD. (D) The energy was summed to produce total acoustic energy for each microbubble type. There was no difference between the total acoustic energy for each microbubble type which was confirmed by an unpaired t-test ($p < 0.05$). Error bars represent standard deviation and 'X' symbols indicate those mice without BBBD.*

3.5 Discussion

Previous work assessing drug delivery with ultrasound emitted in a rapid short pulse sequence has focused on drug delivery to the hippocampus for the treatment of conditions such as Alzheimer's disease and glioblastoma. Moreover, this previous work was conducted at a centre frequency of 1 MHz which complicates human transcranial transmission. The advantages of low frequencies include enhanced penetration depth, enlarged focal region to reduce treatment time for larger targets, reduced distortion, and attenuation (Yin and Hynynen, 2005). Here, it has been shown that rapid short pulses of ultrasound can be used to achieve drug delivery in the pons, where DIPG arises, at a centre frequency of 300 kHz. Whilst BBBD was achieved, it was variable. Two ultrasound parameters – burst length and PRP – and microbubble type were investigated for achieving reliable BBBD in the pons.

3.5.1 Burst length

Firstly, the effect of burst length on BBBD and drug delivery was investigated. Three burst lengths shorter than the baseline parameters previously established by the NSB lab at ICL were assessed. The burst length did not influence the likelihood of BBBD, and the results here suggest that eight pulses per burst is sufficient for BBBD (**figure 3.4.1**). Eight pulses per burst was the shortest burst length examined here, so the number of pulses required for BBBD could be reduced, and this warrants further investigation.

A positive correlation between burst length and drug delivery has been found with long pulse ultrasound (Liu et al., 2010, Shin et al., 2018a). Here, to assess the dose delivered by each burst, the fluorescent pixel intensity was quantified for each model drug, which acted as a proxy for dose delivered. For biotin, 38 pulses per burst resulted in a significantly higher dose than the shorter burst lengths, suggesting that the bubble stimulation occurring during pulses 26-38 caused the physical effect that allowed more fluorescent tracer into the brain parenchyma (**figure 3.4.3**).

For dextran, the greatest dose was delivered with 13 pulses per burst, but the mean value was distorted by a high data point. Whilst this was not statistically determined to be an outlier, if it were to be neglected, the dose delivered would be similar at 13 and 38 pulses per

burst (**figure 3.4.3**). An increase in sample size would indicate whether this high value is an outlier.

It is widely accepted there is threshold for the size of model drug/ drug that can enter the brain because of FUS-mediated BBBD. The threshold is determined by the ultrasound parameters, with the largest molecule reported as 500 kDa dextran at PRP of 0.6 MPa and with long pulses of ultrasound (Chen and Konofagou, 2014, Shen et al., 2016). Interestingly, here the smaller model drug (biotin) had the greatest concentration at the longest burst length, whilst there was no difference in delivery between burst lengths for the larger model drug (dextran). This may be due to the microbubble dynamics with short pulse ultrasound at low centre frequencies.

Overall, the highest dose delivered into the brain parenchyma was achieved for 38 pulses per burst with biotin. This is seen in the example images where both biotin and dextran delivery cover a larger area of the brain (not quantified; **figure 3.4.2**), and in the quantification of model drug delivery (**figure 3.4.3**). Larger areas of drug delivery are important when treating DIPG as this disease spreads diffusely throughout the brain. It is important to treat all cancer cells to prevent recurrence. Therefore, since a larger area of drug delivery is beneficial, 38 pulses per burst were used for further work.

Analysis of the acoustic emissions recorded during ultrasound exposure suggests that the duration of microbubble activity is increased at shorter burst lengths. This suggests that stimulating the microbubbles for shorter periods can prolong their lifetime. At the longer burst lengths the microbubbles are driven into greater oscillations, indicated by the higher energy recorded, this could mean that the microbubbles are becoming destroyed or non-functional in terms of BBBD but evidence is required to support this hypothesis. There was no significant difference in the fluorescence pixel intensity (representing the amount of model drug delivered) between burst lengths so here the microbubble strength and durability does not seem to impact drug delivery. This may change with therapeutics depending on their properties e.g. size, charge, and lipophilicity.

3.5.2 Drug delivery to the pons

It has been shown here that short pulses of ultrasound emitted in a rapid sequence are able to deliver fluorescent tracers across the BBB at parameters suitable for use in the clinic (**figure 3.4.8**). The first study presented in this chapter with short pulses of ultrasound targeted the hippocampus to allow comparison with previous studies. However, DIPG originates in the pons, and it was therefore important to assess the ability of the short pulse sequence for delivering drugs to this region. BBBD, indicated by an increase in fluorescence, was successful with a homogenous dextran delivery profile that extended beyond the pons, similar to that demonstrated by (Morse et al., 2019).

Whilst drug delivery was successful, some haemorrhage was observed on the dorsal side of the brain near the skull base (**figure 3.4.5**). This could be due to an elevated local pressure in this region caused by reflection of ultrasound from the skull base. The focal volume at 300 kHz is 7 mm long axially (defined by the full width at half maximum), while the height of mouse brain is approximately 5 mm and so approximately 2 mm of the focus is outside the brain. The portion of the beam reaching the skull base could be reflected, and interfere constructively with the incoming ultrasound, resulting in an elevated local acoustic pressure near the skull base experienced by nearby microbubbles (O'Reilly et al., 2010, Fan et al., 2015). This increased amplitude could drive the bubbles into the unstable inertial cavitation regime, which is associated with mechanical damage to tissue and haemorrhage (Baseri et al., 2010, Hynynen et al., 2001, Hosseinkhah et al., 2013). In line with the results above, (Ilovitsh et al., 2018) also observed inertial cavitation-induced mechanical lesions and haemorrhage near the skull base at a PRP of 0.19-0.25 MPa and centre frequency of 250 kHz, although they performed their study with long pulse ultrasound.

The potentially high local pressure caused by reflection may be a major concern that needs to be addressed in future studies. A major artery network, the Circle of Willis, is located near the pons in both mice and humans. Specifically, DIPG encases the basilar artery (Williams et al., 2020). Rupturing a major artery could cause major physiological damage. This needs to be avoided to maintain the high level of safety needed for DIPG treatments in children.

3.5.3 Acoustic pressure

It is reported that at lower frequencies a lower PRP is required to achieve BBBD (McDannold et al., 2006, Shin et al., 2018, Fan et al., 2014, Fan et al., 2015, McDannold et al., 2008). In the results presented here, at a PRP of 0.25 MPa, BBBD occurred, suggesting the threshold for BBBD in the mice pons at 300 kHz is below 0.25 MPa. At this PRP, BBBD could be achieved but only in the minority of cases. Increasing the PRP resulted in an increase in the probability of delivery, but also of tissue damage.

This finding agrees with the well documented trade-off between safety and efficacy with BBB opening (Tsai et al., 2018a). At higher pressures, microbubbles exert mechanical force on the blood vessels. This often results in greater penetration of agents into the brain parenchyma, which could be due to either an increase in BBB permeability or to damage to the blood vessels. The results seen here confirm findings from Ilovitsh et al. (2018), that there is a narrow window between safe BBBD and tissue damage at a centre frequency of 250-300kHz. Whilst no haemorrhage was observed at 0.25 MPa, only 20% of mice had BBBD which is unacceptable for the clinic. At the slightly higher PRP of 0.3 MPa, BBBD was more consistent, but damage was also observed. In attempts to improve the safety profile, other methods of overcoming haemorrhage and optimising drug delivery to the pons were explored.

The acoustic emissions analysis revealed a similar trend of microbubble durability at both 0.25 and 0.3 MPa. There was a greater probability of BBBD and greater fluorescence pixel intensity (indicating dose delivered) at 0.3 MPa than 0.25 MPa indicating that there is a threshold of acoustic energy required for BBBD, regardless of duration of microbubble activity.

3.5.4 Microbubble type

Attempts to optimise BBBD and drug delivery at a centre frequency of 300 kHz by altering ultrasound parameters were unsuccessful. Next, microbubble type was explored, comparing SonoVue® described both previously in this thesis, and by Morse et al. (2019) with IHP microbubbles, with BBBD being assessed using Evans Blue dye extravasation. The IHP

microbubbles outperformed the SonoVue® bubbles, resulting in BBBD and Evans Blue extravasation in 100% of mice.

The difference in BBBD could be explained by the disparity in size and concentration of the microbubbles. The concentration of IHP microbubbles (7.3 ± 4 x10^9/ml) is greater than SonoVue® microbubbles (2 x10^8/ml). (McMahon and Hynynen, 2017) showed that the extent of BBBD – measured by MRI contrast enhancement – depended on microbubble dose. It would be instructive to compare BBBD with the same concentration of IHP and SonoVue® microbubbles to eliminate concentration differences as a variable.

Microbubble oscillations will be greatest at its resonant frequency (**§1.5.2**), which changes with microbubble diameter. Therefore, microbubble diameters are better BBBD agents at a given centre frequency (Wang et al., 2014, Choi et al., 2010a, Vlachos et al., 2011, Samiotaki et al., 2012, Song et al., 2017). The mean diameter of SonoVue® microbubbles is 2.5 µm and IHP microbubble mean diameter is 1.62 ± 0.87 µm (Pouliopoulos et al., 2014). At 300 kHz with rapid short pulses of ultrasound, the IHP microbubbles may be closer to resonance than SonoVue® microbubbles diameter. This finding opposes those seen by (Wang et al., 2014), who reported that the microbubbles with a larger diameter provided greater agent extravasation because of BBBD. However, in this study, the effect of the microbubble diameter is likely to be offset by the difference in concentration between the two microbubble types.

Here it has been shown that microbubble type has an important effect on BBBD. This was also seen by Wang et al. (2014) when they compared Definity® with their IHP microbubbles. They also observed that the effects were more significant at lower acoustic pressures (PRP: 0.3 MPa, frequency 1.5 MHz), where IHP outperformed Definity® microbubbles. Wang et al. (2014) suggested that this was due to a greater degree of variability of the strength of stable cavitation occurring at this pressure, as opposed to those of inertial cavitation occurring at higher pressures. This could be relevant to rapid short pulse ultrasound as the sequence is designed to promote stable cavitation (Choi et al., 2011b, Pouliopoulos et al., 2014, Pouliopoulos et al., 2016). Thus, microbubble type may be especially crucial when short pulses are used, inducing stable cavitation.

Both SonoVue® and IHP microbubbles are polydisperse. Microbubbles with different sizes will respond differently to a given centre frequency and acoustic pressure depending on how

close the microbubbles are to resonance (Halliday, 2013). Therefore, for a given set of ultrasound parameters not all microbubbles will be instrumental in causing safe BBBD. Thus, it might be more appropriate to use mono-sized microbubbles as their induced behaviours might be more predictable and uniform. Thus, a future study may consider using mono-sized bubbles in determining appropriate sonication parameters for a given target in the brain. Nevertheless, the optimal bubble size may be target-specific because local blood vessel size and vasculature will still affect microbubble behaviour. For each target, a different combination of optimal bubble size, acoustic pressure and centre frequency combination may have to be separately determined.

Analysis of acoustic emissions recorded during ultrasound exposures revealed that the microbubble activity of IHP microbubbles was sustained for longer than the SonoVue® microbubbles. This is likely due to the greater concentration of IHP microbubbles. Additionally, the mean total energy recorded from the IHP microbubbles was greater than SonoVue® microbubbles which correlates with the percentage of observed BBBD.

Here, IHP microbubbles were investigated to overcome the issues seen with variability. Whilst the IHP microbubbles performed better than SonoVue® microbubbles, in terms of the consistency of treatment outcome, the concentration of IHP microbubbles used is unlikely to be approved for clinical use as it is so high. Other commercially available microbubbles such as Definity® or Optison™ might be more suited to BBBD at 300 kHz than SonoVue® and could be examined. For future studies described in this thesis SonoVue® microbubbles were used whilst other methods to overcome the variability in BBBD were explored.

3.5.5 Clinical relevance

The *in vivo* work here has been designed to closely follow the probable clinical setting. SonoVue® microbubbles are currently used in the clinic as contrast imaging agents and are more likely to be approved for BBBD than microbubbles that are not currently used in the clinic. All ultrasound exposures were performed at a centre frequency of 300 kHz which is suitable for transcranial transmission. As microbubble behaviour and dynamics will change

with frequency, establishing a set of optimal ultrasound parameters pre-clinically could inform clinical exposures.

This chapter has shown that 300kHz ultrasound emitted in a rapid short pulse sequence can disrupt the BBB in two brain regions with the same ultrasound parameters. This is promising for the clinic as tumour location will differ between patients. An ultrasound system that can treat the most patients is more cost effective than one that can only target a specific region and therefore more likely to be used. Moreover, it is likely that patients will require multiple sonications per treatment to cover the tumour area, meaning that accurate steering enabled by the lower frequency of the ultrasound used here will be imperative for full tumour treatment.

This chapter has also demonstrated that FUS-mediated BBBD could simultaneously increase the fluorescence of two model drugs in the brain parenchyma during a single sonication. This is promising when considering that clinical translation using a combination of agents is often required for cancer treatment. As well as multiple therapeutic agents, imaging contrast agents may need to be delivered simultaneously to monitor the extent of therapeutic delivery. On the other hand, delivery of contrast agents prior to treatment could also be useful to establish the extent of permeability of the BBB, giving an indication of treatment volume, and establishing the correct targeting region for each patient before injection of therapeutic agents. Whilst a study of the specific combination of therapies/ imaging agents is necessary to confirm co-delivery, this initial work provides promise for future exploration.

3.5.6 Limitations and future work

The overall aim of the work described in this chapter was to establish BBBD in the pons of mice with ultrasound emitted in a rapid short pulse sequence, at a centre frequency of 300 kHz. Whilst BBBD was achieved, shown by increase in fluorescence of model drugs in the targeted brain region, there was a lot of variation in the extent of BBBD achieved. Future studies may aim to study the influence of different factors causing the variation, to establish a protocol that could more consistently safely disrupt the BBB. These factors include the

centre frequency and resultant size of the ultrasound focal region, anatomical differences between mice, the ultrasound protocol, sample size and fluorescence quantification method.

The variation within and between studies is greater than for previous work at 1 MHz, even when controlled for mouse type, most equipment, sonication protocol, and most sonication parameters, suggesting that the difference in frequency is a probable explanation (Morse et al., 2019). Ilovitsh et al. (2018) showed that at 250 kHz there is a very small window for successful BBBD. The slight variations in skull thickness, body shape and size between mice, and targeting location may be amplified at 300 kHz resulting in the inconsistency seen here.

The skull attenuates ultrasound as it passes through to the brain, therefore differences in skull thickness will affect the resultant *in situ* ultrasound pressure experienced by the microbubbles in the brain tissue (Guo et al., 2021). The difference in skull thickness in the beam path leading to the pons and hippocampus may be enough to affect the opportunity for successful BBBD. There could be a larger variation in skull thickness between mice in the skull covering the pons, than for the hippocampus, and explain the variation in BBBD seen between mice when the pons is targeted. Moreover, differences in the angles the skull bone makes with the incident beam may also affect how much transmission and reflection occur.

Alongside skull thickness, there are vascular differences between the pons and hippocampus. Differences in vascular density, vessel diameter and blood flow will affect the distribution of microbubbles within the beam focal volume and their interaction with the ultrasound field which could affect resultant BBBD (Bazzoni and Dejana 2004; Greene et al., 2018).

At 300 kHz, the focal region of the beam is longer than the mouse brain and this could be responsible for some of the variation seen. As mentioned, approximately 2 mm of the focal region (defined by FWHM) is likely to lie beyond the brain. This can result in the ultrasound beam reflecting off the skull base, re-penetrating the brain tissue and interfering with the incoming ultrasound beam. This can also explain the observed tissue damage (Fan et al., 2015). Larger animal models may be more suitable for assessing BBBD at 300 kHz, where the focal volume is contained within the skull. Other studies have examined 500 kHz in rats (Shin et al., 2018b), 260 kHz in rabbits (Hynynen et al., 2006, McDannold et al., 2006a), and 500 kHz and 286 kHz in sheep (Pelekanos et al., 2018).

Other sources of variation could be the sonication procedure such as the coupling method and efficacy of the cannula. Ultrasound gel is used to acoustically couple the mouse head with the transducer and air bubbles in the gel could distort the ultrasound beam. To overcome this, the ultrasound gel is centrifuged to remove air bubbles and observable bubbles are removed before sonication. Some bubbles may remain, and the amount and distribution could vary between mice, affecting the ultrasound field experienced by the microbubbles within the vasculature. Future development of the ultrasound system will explore other acoustic coupling methods to remove ultrasound gel from the setup.

Microbubbles are given intravenously through a tail vein cannula which could be incomplete, meaning that the microbubbles and/or model drug leak into the parenchyma of the tail rather than entering the blood stream. Tail vein cannulation in C57BL/6J mice is well known to be difficult and the cannula can move as syringes are exchanged for bubble and drug injection. When using dyes such as Evans Blue, the presence of the dye in the vein or tail parenchyma can be observed immediately. This is not the case with the model drugs biotin and dextran used here and so it cannot be ascertained whether the lack of BBBD was due to the ultrasound sonication or to a failed cannulation.

It would be beneficial to have a feedback method to assess cannulation and IV injection. One option would be to establish real-time feedback of microbubble signal recorded by the PCD. The GUI used to operate the ultrasound system displays this information but no correlation between the displayed signal and BBBD has been achieved.

Another source of variation could be the small sample size. This study is exploratory and relatively small sample sizes (the smallest group is n=3) were used to test many parameters. Therefore, the results are subjected to a large uncertainty associated with statistical variations. A future study should use larger sample sizes to gain more statistical confidence in the results.

The main limitation of the above method lies in the way BBBD was evaluated. It uses fluorescence intensity quantification, which compares total fluorescence of the targeted and un-targeted hemispheres. This allows the concentration of tracer molecules present in the brain to be quantified. However, the distribution of these tracers and the targeting accuracy

could not be evaluated using this measurement. These are important factors when considering drug delivery for therapeutic treatment, including DIPG, as the drug must reach all tumour cells for maximum chance of treatment success. Therefore, it would be useful to quantify the area of model drug in future studies.

Moreover, there is still a need for a new method that could assess the amount of tracer delivered into the pons. The fluorescence intensity method was initially developed for assessing increase in fluorescence in the hippocampus and may not be best suited to the pons region. Those brains where the hippocampus was targeted were sectioned along the coronal axis, allowing comparison of fluorescence in the two hemispheres. When the pons was targeted, brains were sectioned along the sagittal axis (**figure 3.4.5**) to assess the accuracy of targeting and retain structural integrity of brain slices. As a result, dorsal and posterior regions of the brain were compared for quantification, instead of the two hemispheres. This means different structural regions of the brain are being compared and rely on the user defining the mid-line in a repeatable manner. It may be more appropriate to adjust the quantification method to compare similar sized regions of the brain rather than two halves.

The fluorescence quantification method is very sensitive to artefacts. Artefacts can occur from tissue folds, OCT (used to embed the brain tissue) on the sections and inherent autofluorescence from brain regions such as the cerebellum. By altering the methodology so that only specific regions of interest are considered, there could be a reduction in the number of artefacts skewing the quantification. Alternatively, brain slices with dextran delivery could be compared to control brains without dextran in similarly placed brain slices. However, this may give rise to other issues including different levels of background fluorescence.

Alternative fluorescence quantification methods could also be explored. For example, the brain tissue could be separated upon extraction into anatomical parts e.g. brain stem, cerebellum, hippocampus, and fluorescence quantified using fluorometry. Whilst this technique would provide a more robust quantitative analysis, there would be a lack of spatial resolution of tracer delivery.

Tissue effects have not been examined here as the focus was BBBD. Other studies have reported a positive correlation between burst length, PRP and tissue damage (Hynynen et al., 2001, Choi et al., 2011a, Baseri et al., 2010, Liu et al., 2008b, Liu et al., 2009, Choi et al., 2010b, McDannold et al., 2007). Longer burst lengths and higher PRP result in greater microbubble

stimulation which could result in microbubble collapse and associated tissue effects such as cell necrosis and erythrocyte extravasation (Fan et al., 2014b, Hynynen et al., 2006, Chen and Konofagou, 2014, Wu et al., 2017). Future studies investigating the effect of ultrasound parameters, and drug delivery should incorporate an assessment of tissue effects to determine the safety and efficacy trade-off. Methods of assessing tissue effects are discussed in section **§1.6**.

Lastly, the control mice in this chapter are dosed with microbubbles and model drug but received no ultrasound exposure. It would be constructive to include a control group that is exposed to ultrasound and is dosed with model drug but does not receive microbubbles.

3.6 Conclusion

The aim of this chapter was to establish a set of parameters for BBBD in the pons region using ultrasound emitted in a rapid short pulse sequence. BBBD was indicated by an increase in brain fluorescence of a model drug or presence of a dye which cannot normally enter the brain parenchyma. Previous work has shown that ultrasound emitted in a rapid short pulse sequence can safely and effectively disrupt the BBB in the hippocampus at a centre frequency of 1 MHz. Here, the centre frequency (300 kHz) and pulse length (1 cycle) were adjusted to those more likely to be used in the clinic in the hope that the results more closely represent drug delivery. BBBD was achievable at a centre frequency of 300 kHz but was inconsistent. Burst length, peak-rarefactional acoustic pressure and microbubble type were explored but there was a lot of variation between mice in BBBD. Further work must be carried out at 300 kHz to establish a parameter set and ultrasound regimen for repeatable BBBD. This may involve exploring and understanding microbubble behaviour and dynamics at 300 kHz *in vitro* before success is achieved *in vivo*. The aim of the work described in this thesis is the delivery of therapeutics to the pons region for the treatment of DIPG. Morse et al. (2019) had less inter-subject variability at 1 MHz and so is explored for BBBD in the pons in the next chapter.

4 Blood-brain barrier disruption in the pons at 1.00 and 1.05 MHz

4.1 Background

The studies described in the previous chapter (**chapter 3**) aimed to examine the ability of short pulse ultrasound to improve drug delivery to the normal tissue of the pons, at a centre frequency suitable for human transcranial transmission (300 kHz). BBB disruption (BBBD) was achieved but was unpredictable, and thus not suitable for examining drug delivery for DIPG. Therefore, extravasation of model drugs at a centre frequency similar to that used by Morse et al. (2019) was explored here.

4.1.1 Centre frequency

The choice of ultrasound exposure parameters largely dictates the microbubble behaviour and thus their effect on drug dose and distribution (McDannold et al., 2008, Choi et al., 2011a, Choi et al., 2010b). Published work in non-tumour bearing mice and xenograft models targeting the pons have used centre frequencies ranging between 1.5 – 1.68 MHz (with acoustic pressures of 0.4-0.61 MPa) (Zhang et al., 2020, Alli et al., 2018, Englander et al., 2021, Ye et al., 2018, Haumann et al., 2022). These studies all used long pulses (~10 ms) of ultrasound and so the ultrasound exposure parameters used may not be optimal for the rapid short pulses used here. The transducers (both H117, Sonic Concepts, WA, USA) used in the studies were different to the transducer used by Morse et al. (2019). To best match the pulse shape of Morse et al. (2019) ultrasound was emitted at a frequency of 1.05 MHz at Imperial College London (ICL) and 1 MHz at the Institute of Cancer Research (ICR).

4.1.2 Beam size change and targeting

The change from 300 kHz to 1.05 MHz (calibration data found in **§2.3.1 & 2.4.1**) altered the size of the focus and its position, which had moved 5 mm in the axial plane further away from the transducer. At 300 kHz, the focal region is at the opening of the cone so the distance between the mouse head and cone opening was kept to a minimum. (**§2.1.1**). The separation of the coupling cone and mouse head required for BBBD in the pons at 1.05 MHz required experimental verification.

4.1.3 Acoustic pressure

Peak negative pressure (PRP) is a key ultrasound parameter that influences microbubble behaviour, affecting drug delivery (Hosseinkhah et al., 2015, McDannold et al., 2015, McMahon et al., 2020, Hynynen et al., 2003b, McMahon and Hynynen, 2017). It is widely reported that a pressure threshold for BBBD exists and that this changes with frequency (Konofagou et al., 2014). Morse et al. (2019) found the pressure threshold for BBBD using short pulse ultrasound in the hippocampus to be 0.4 MPa (free field) at a centre frequency of 1 MHz. Whilst a similar frequency was used here, the pons lies ~4 mm deeper in the brain than the hippocampus.

There are also differences in vasculature, thickness and shape of the skull covering between the two brain regions which can affect microbubble behaviour and BBBD threshold (**§1.5.2**). The blood flow velocity will affect local microbubble concentration (Sassaroli and Hynynen, 2006) and compliance, stiffness and vessel size will affect bubble interaction with the vessels (Sassaroli and Hynynen, 2006, Qin and Ferrara, 2006). Skull thickness and radius of curvature impact ultrasound attenuation and inversely correlate with *in situ* acoustic pressure (Zhang et al., 2021). The thickness of the parietal bone (covering the hippocampus) is ~0.15 mm and the interparietal bone (covering the pons) is ~0.28 mm and so in situ acoustic pressure might be lower in the pons than the hippocampus for the same transducer drive settings (Copes et al., 2018).

4.1.4 Tissue effects

As well as a threshold for BBBD, acoustic pressure is associated with unwanted tissue damage (**§1.6**). Tissue damage can vary, depending on acoustic pressure amplitude (Hynynen et al., 2005, Alonso et al., 2010, Baseri et al., 2010). In mice, (Tsai et al., 2018b) saw microhaemorrhages with higher PRPs (0.9 MPa; frequency 400 kHz) and detected the least tissue damage at 0.2 - 0.3 MPa PRP. In rats, (Shin et al., 2018b) found optimal safety and drug delivery at PRP 0.3 MPa using 500 kHz. Overall, in pre-clinical studies, successful BBBD (assessed by extravasation of MRI contrast agents, tracer molecules and quantification of therapeutic agents) with minimal tissue damage has been achieved with PRPs of 0.2 – 0.5 MPa using 0.2-1.5 MHz (Gandhi et al., 2022).

Tissue damage is commonly assessed using haematoxylin and eosin (H&E) staining, allowing the identification of extravasated erythrocytes and morphological tissue changes such as microvacuolations (**§1.6**). Published studies have found tissue effects observed using H&E staining to depend on the ultrasound parameters used (Liu et al., 2008a, Chen and Konofagou, 2014, Baseri et al., 2010, Kinoshita et al., 2006b, Weng et al., 2011, Fan et al., 2012, Tsai et al., 2018b, McDannold et al., 2012).

4.1.5 ICR sonication system

The overall aim of the work in this thesis is to examine drug delivery into a DIPG tumour in a mouse model of human cancer. As the Institute of Cancer Research (ICR) has expertise in DIPG mouse models and therapeutics, an ultrasound system was assembled in the ICR to use this knowledge (**§2.2**). To match the waveform used at ICL, ultrasound was emitted at a centre frequency of 1.05 MHz. All other exposure conditions established at ICL for BBBD in the pons were adopted to assess the efficacy of the novel system.

4.2 Aims and objectives

The aim of the work in this chapter was to establish repeatable BBBD in the pons with minimal tissue damage using FUS, emitted in a rapid short pulse sequence, and intravenous microbubbles. The first objective was to establish BBBD in the pons using the existing ICL ultrasound system at a frequency of 1.05 MHz. The optimal vertical position of the transducer above the mouse scalp covering the pons was established. The next objective was to investigate (i) the efficacy of BBBD, (ii) safety by the avoidance of tissue damage as a function of PRP in the pons and (iii) whether acoustic emissions recorded during sonication could predict BBBD. The final objective was to assess whether a newly assembled ultrasound system at the ICR could use the ultrasound sequence established at ICL to increase model drug in the pons with little tissue damage.

4.3 Materials and methods

This was the first study to use rapid short pulses of ultrasound for BBBD in the pons at 1.05 MHz and so it was initially necessary to identify the optimum targeting position as defined by model drug extravasation throughout the pons region after one exposure. Once the pons could be accurately targeted, the probability of BBBD at three PRPs was assessed to determine the best acoustic pressure for drug delivery in the pons at 1.05 MHz. Safety of BBBD at each acoustic pressure was assessed by H&E staining. Next, the newly assembled sonication system that was built at the ICR during the earlier experiments at ICL was tested with two model drugs (Evans Blue and Dextran) and immediate tissue effects evaluated by H&E staining. Common methods, described in **chapter 2,** are referenced where appropriate.

4.3.1 Pons sonications at ICL

Mice (strain, gender, weight are described in **§2.1**) were prepared for exposure (**§2.2**) to 1.05 MHz ultrasound delivered in a rapid short-pulse sequence (PRP: 0.400 ± 0.004 MPa; pulse length: 5 cycles; pulse repetition frequency (PRF): 1.25 kHz; burst length: 38 pulses; burst repetition frequency (BRF): 0.5 Hz; number of bursts: 125; total time: 250s; shown in **table 2.3.1**). As sonication started, SonoVue® microbubbles followed by the model drug dextran (3 kDa) were administered intravenously through a tail vein cannula (**§2.5**). Immediately after sonication, mice were perfused transcardially, fixed and the brain extracted (**§2.6**). The brain tissue was cryoprotected and sectioned sagittally into 30 μm slices (**§2.6**). Brain slices were imaged using a microscope and assessed for BBBD by dextran observation (**§2.8**).

4.3.2 Targeting the pons

In the first exposures, dextran extravasation was not seen in the pons but occurred in the dorsal region of the brain. A pilot study was therefore conducted to establish the optimum targeting position for BBBD in the pons at 1.05 MHz (**figure 4.3.1**). The coupling cone attached to the transducer was positioned vertically in contact with the mouse head and raised in 1 mm increments from 0-8 mm (n=1 at each height, excluding 4 mm) away from the head. Mice were sonicated and tissue processed as described above in **§4.3.1**. Each height was assessed by qualitative observation of dextran extravasation in sagittal brain slices. The optimum

targeting position contained the greatest amount of dextran in the axial plane, covering the pons region.

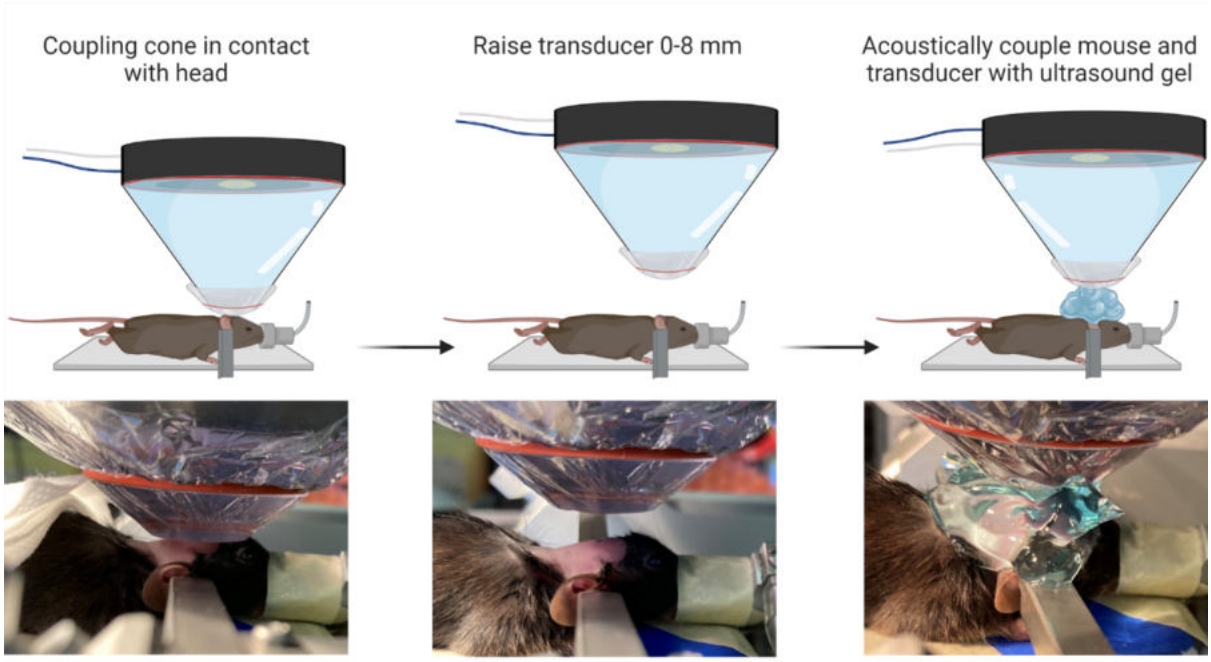

Figure 4.3.1 Schematic and photographs of height study. *The transducer was located using a 3D positioning system. The opening of the coupling cone was positioned in contact with the mouse head then raised 0-8 mm. Ultrasound gel was used to acoustically couple the mouse and transducer.*

4.3.3 Acoustic pressure optimisation

Similarly, to the previous section, mice were exposed to 1.05 MHz rapid short-pulse ultrasound at a peak rarefactional pressure of either 0.200 ± 0.004 MPa, 0.400 ± 0.004 MPa or 0.600 ± 0.004 MPa (n=5 each pressure) and sham controls were exposed to 0 MPa (n=3). BBBD was assessed based on dextran extravasation in the targeted region and then quantified in five brain slices per mouse brain using the method described in **§2.9** as a proxy for dose delivered. The mean fluorescence pixel intensity and standard deviation was calculated at each acoustic pressure.

Additional mice (n=4 per PRP and n=3 sham control) were sonicated to allow histological damage assessment using H&E staining. Additional mice were sonicated as brain tissue for dextran assessment and H&E staining must be processed differently. For this study, brains were halved sagittally and embedded in paraffin blocks. Five 4 µm sagittal slices were

collected at 100 µm intervals throughout the brain Since the brain was halved, each slide contained both the targeted and untargeted brain hemisphere. Six brain slices spanning 360-500 µm of brain tissue were H&E stained (**§2.7**). Extravasated erythrocytes and microvacuolations in the parenchyma were identified by morphological features and counted in each brain slice stained with H&E.

Six sections across the targeted hemisphere from each brain were analysed and compared to their contralateral section in the untargeted hemisphere which acted as a control, as well as to un-sonicated control mice (n=3). The number of sites with microvacuolations and extravasated erythrocytes were counted in each brain slice.

4.3.3.1 Statistical analysis

GraphPad Prism v9.01 was used for all statistical analysis. A two-way ANOVA test was performed to examine the statistical significance of any effect of acoustic pressure on model drug delivery. A post-hoc Tukey's multiple comparison test was performed on any significant interaction. A students t-test was used to assess the difference between the number of microvacuolations and extravasated erythrocytes for the three acoustic pressures and sham control mice. Welch ANOVA test was performed to examine the difference between acoustic emissions calculated at each pressure, Dunnett's T3 multiple comparisons test was performed on any significant interaction. The Pearson correlation coefficient was calculated to assess correlation between accumulated acoustic emission energy and fluorescence pixel intensity of dextran calculated in **§4.3.3**. Presence of outliers was examined using the robust regression followed by outlier elimination (ROUT) method.

4.3.4 Sonications with the novel system at the ICR

The objective of the ultrasound exposures at the ICR were to establish whether the system could disrupt the BBB in the pons and if any immediate tissue effects occurred that enabled drug delivery in a DIPG mouse model. Therefore, these were pilot studies yielding qualitative data.

Twenty- two mice (strain, gender, weight as described in **§2.1**) were exposed to 1.00 MHz ultrasound at a PRP of 0.4 MPa (determined by the pressure study at ICL). Ultrasound was

emitted in a rapid short-pulse sequence, as shown in **table 2.3.1**, alongside the intravenous injection of microbubbles and a model drug (**§2.3.3**). Either Evans Blue dye (2%) or the fluorescently tagged dextran (3 kDa) were used as model drugs to assess BBBD (**§2.5**). Evans Blue was used initially to provide a BBBD readout on the macroscopic scale as the brain is extracted. Dextran enabled the assessment of distribution of drug delivery on a more localised scale after more lengthy histological processing.

Immediately after sonication, mice were perfused transcardially (**§2.6**). Where Evans Blue was used as the model drug, brains were fixed and sectioned as described in **§2.6**. The brains of mice receiving dextran were fixed, cryoprotected and cryosectioned (**§2.6**). Brain slices (30 µm thick) were imaged and qualitatively assessed for BBBD (**§2.9**).

4.3.4.1 Targeting assessment

To assess the targeting accuracy of the ICR system, the location of dextran delivery in non-tumour-bearing mice was compared to the tumour location in a mouse model (**figure 4.3.2**). Sagittal T2-weighted MRI scans of a syngeneic DIPG mouse model (n=3: d072, d077 and d088 after tumour inoculation) were provided by a member of the preclinical MRI team at the ICR (Dr Jessica Boult). The height and width of the tumour was measured in one section of each mouse brain containing the tumour mass using RadiAnt DICOM viewer 2022.1.1. For comparison, the width of dextran delivery as well as the approximate distance from the central tumour location to central dextran delivery (height and width) was measured on fluorescent images from **§4.3.4** with ImageJ 1.53t. Measurements were made in two slides per mouse brain (n=5). Examples of measurements are shown in **figure 4.3.2**.

4.3.4.2 Tissue effects with the ICR system

Histological staining was used to assess immediate tissue effects of sonication. Mice (n=3) were sonicated as described in **§4.3.4** with the model drug dextran given. Immediately after sonication, mice were perfused transcardially, brains fixed (described in **§2.6**) and embedded in paraffin. The brains were sectioned using a microtome then H&E stained and imaged (described in **§2.7**). Sonicated regions were compared to the un-targeted region in the same brain section and their un-sonicated contralateral hemisphere acting as an internal control.

Differences in tissue morphology and the presence of extravasated erythrocytes and microvacuolations were assessed.

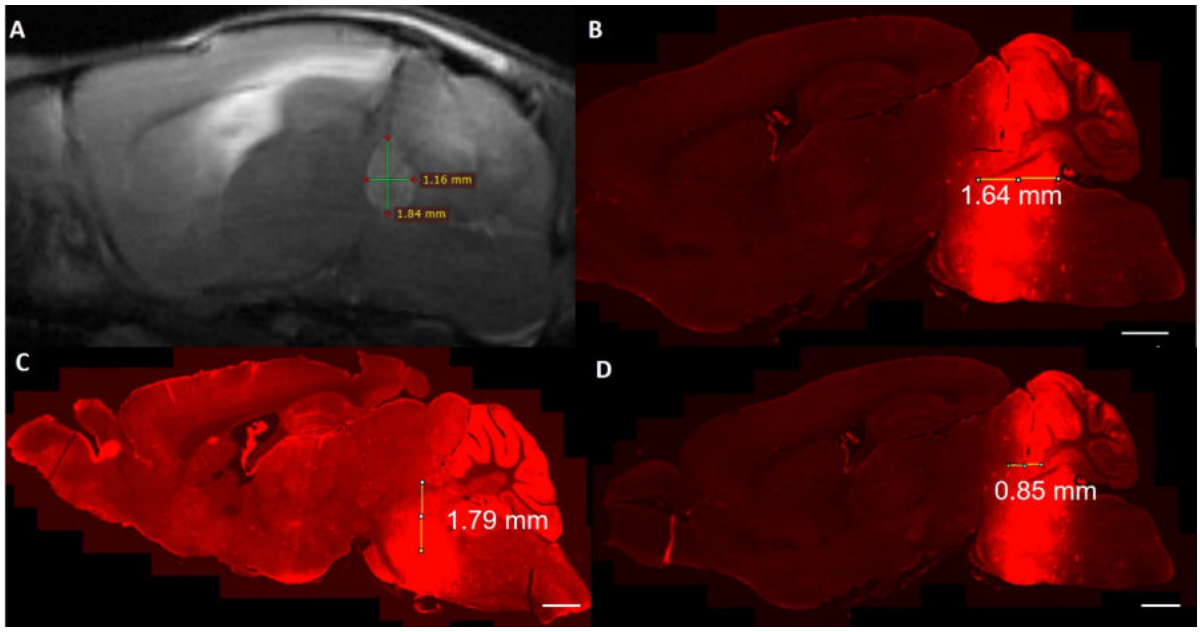

Figure 4.3.2 ICR system targeting assessment. *(A) T2-weighted MRI scan of a syngeneic DIPG mouse model and example 2D height and width measurements of tumour mass. OB-3 (nestin-Tv-a/p53fl/fl, RCAS-ACVR1R206H + RCAS-H3.1K27M) murine cell line was injected intracranially into C57BL/6J mice (B) Sagittal section showing measurement of the width of dextran delivery and the (C) the height and (D) width from central tumour location of central dextran extravasation. Scale bars represent 1 mm.*

4.4 Results

Repeatable BBBD was achieved in the pons region at both ICL and ICR, indicated by dextran extravasation, using the same FUS parameters.

4.4.1 Targeting the pons at 1.05 MHz (ICL)

In the first six exposures of rapid-short pulses of ultrasound at 1.05 MHz at ICL, no dextran delivery occurred (**figure 4.4.1A**). Then, by chance dextran delivery was observed in the dorsal pons region, approximately 0.5 mm in height from the skull base (**figure 4.4.1B**).

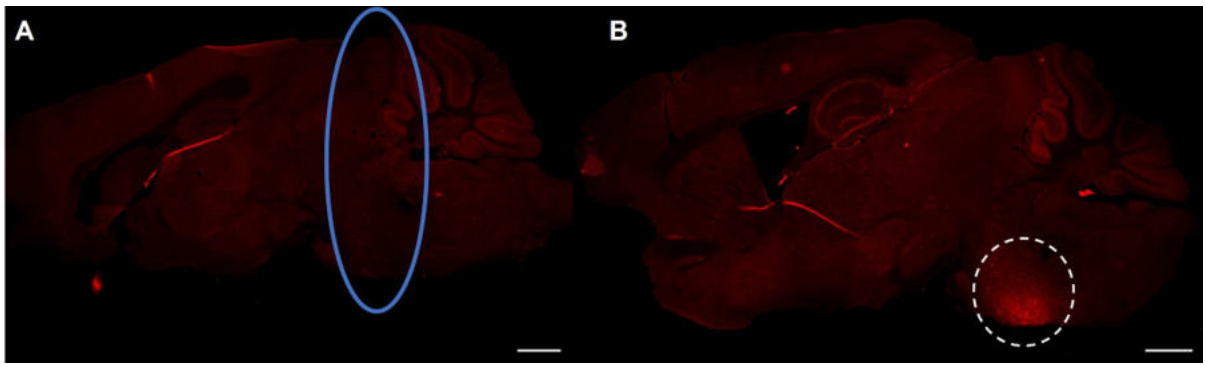

Figure 4.4.1 Blood-brain barrier disruption in the pons at 1.05 MHz. *Example fluorescent images (10x) from two mice exposed to ultrasound at a frequency of 1.05 MHz in the presence of SonoVue(R) microbubbles and fluorescently tagged dextran (3 kDa). The approximate targeted region based on the acoustic focal volume is represented by the blue ellipsoid. (A) Initially, no blood-brain barrier disruption (BBBD) was observed, indicated by lack of dextran in the brain slice. (B) Dextran was observed in the dorsal pons region, near the skull base shown by the dashed circle. Bright regions outside of the pons region are tissue folds/ tears.*

The separation between the transducer and mouse head was investigated to determine at what separation dextran delivery was present throughout the whole height of the brain (~7 mm), including the pons region (**figure 4.3.1**). No dextran was seen at 1 mm or 6 mm, so the data is not shown, and dextran extravasation varies laterally due to errors in targeting. At a separation of 0-3 mm between the front opening of coupling cone and the mouse head, dextran delivery was seen in the bottom half of the mouse brain (~3.5 mm; **figure 4.4.2A-C**).

Dextran was seen throughout the height of the mouse brain (~7 mm) at a separation of 5 mm (**figure 4.4.2.D**).

At a separation of 7 and 8 mm the dextran extravasation moves higher up the brain and does not reach the skull base. At 7 mm, dextran is seen in ~5 mm of the top half of the brain and ~3.5 mm at a separation of 8 mm (**figure 4.4.2E&F**).

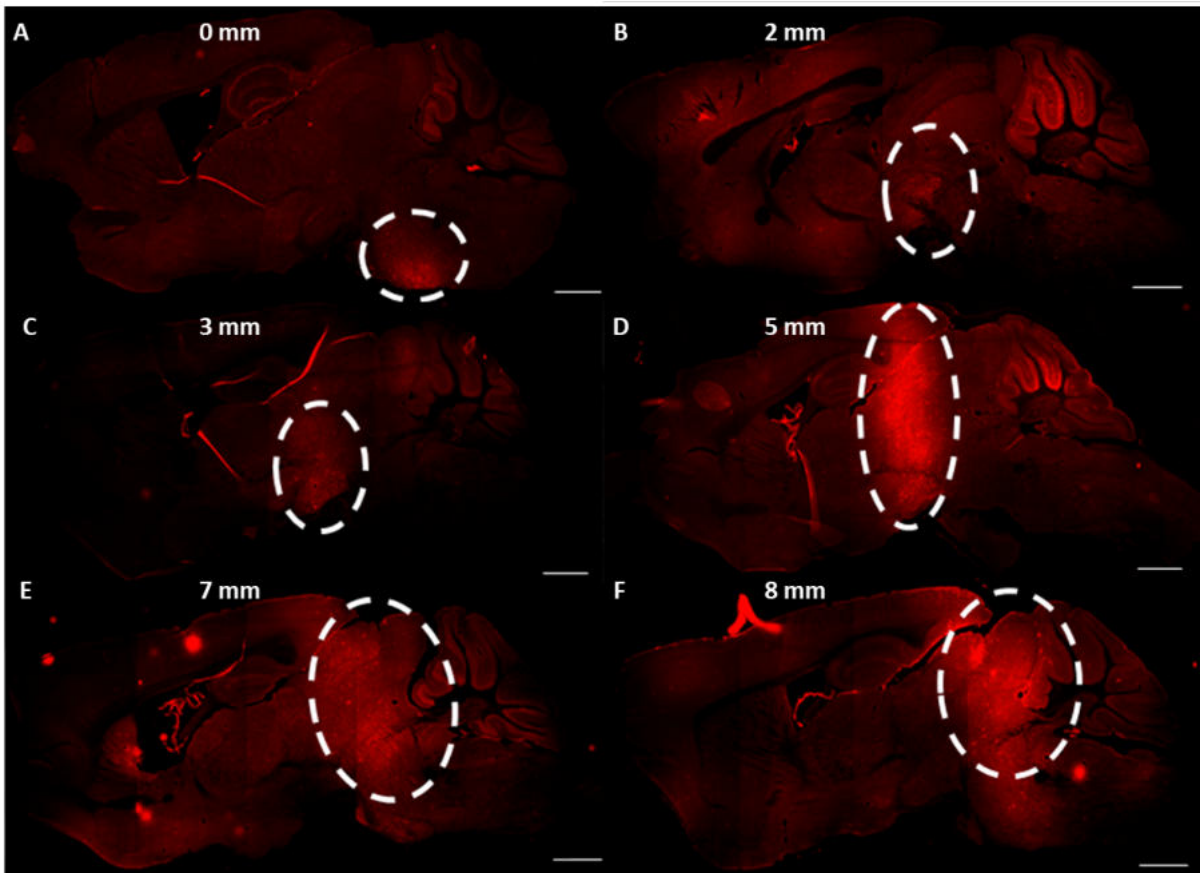

Figure 4.4.2 Targeting the pons at 1.05 MHz. *Sagittal fluorescence microscopy images (10x) of dextran extravasated in the mouse brain after exposure to focused ultrasound and intravenous microbubbles. Each image represents a different mouse where the separation between the mouse scalp and front of the coupling cone was (A) 0 mm, (B) 2mm, (C) 3 mm, (D) 5 mm, (E) 7 mm and (F) 8mm. Scale bars represent 1 mm.*

4.4.2 Acoustic pressure optimisation

Dextran delivery at three acoustic pressures was assessed using optimal separation between the mouse head and transducer cone established above (**§4.4.1**). The aim was to

establish the acoustic pressures that result in repeatable BBBD and minimal tissue damage using the short pulse ultrasound sequence.

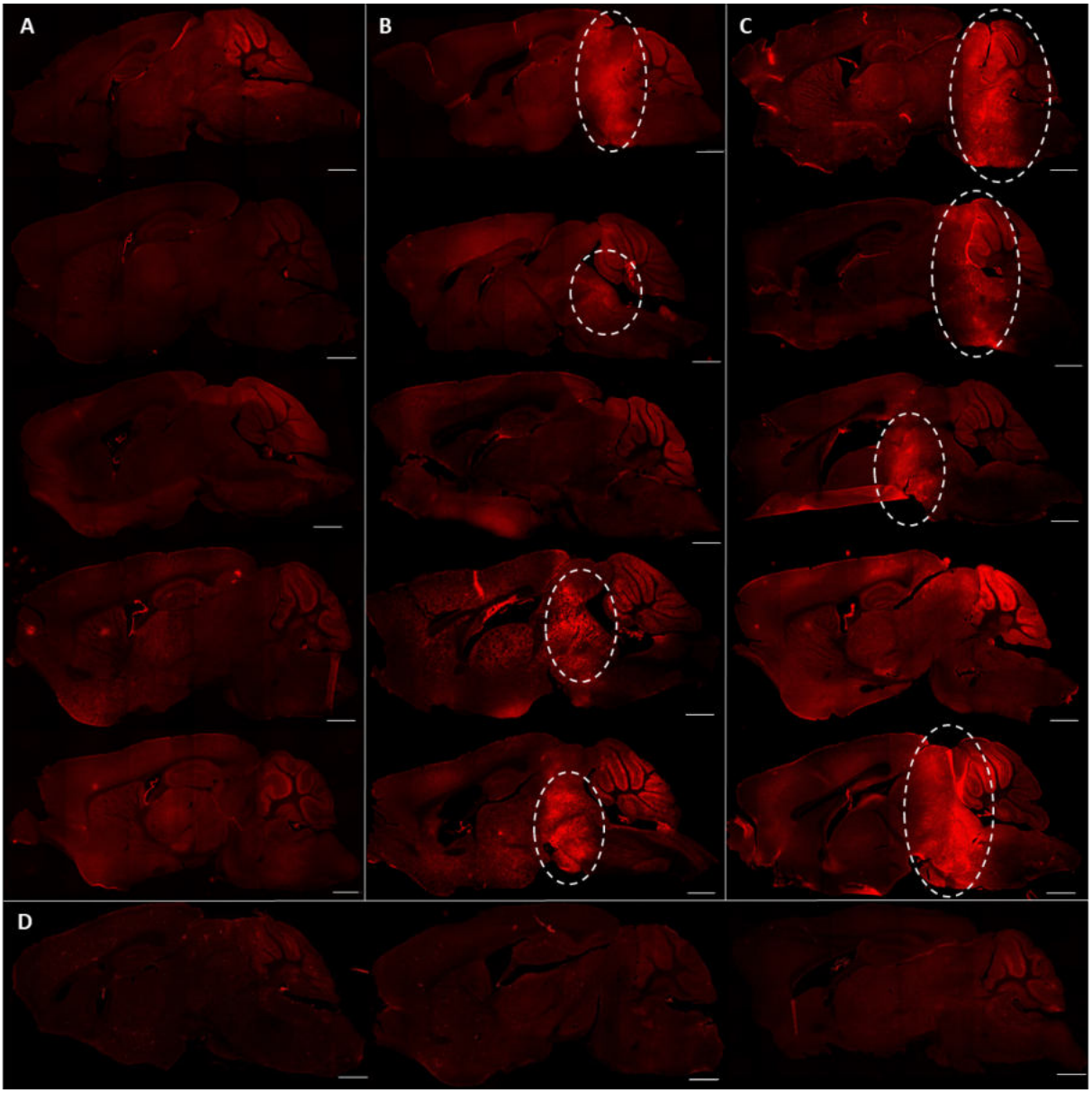

Figure 4.4.3 Drug delivery at three acoustic pressures and sham control. *The results of exposing mice to rapid short pulses of ultrasound at peak rarefactional pressures of (A) 0.2, (B) 0.4 or (C) 0.6 MPa (n=5 per pressure). Successful blood-brain barrier disruption (BBBD) is represented by the extravasation of the model drug as indicated by the dashed ellipsoid, compared to (D) sham controls (dosed with microbubbles, no ultrasound). Bright regions outside the marked ellipsoids are imaging artefacts from tissue folds and tears, tissue processing or autofluorescence of brain regions. Scale bars represent 1 mm.*

4.4.2.1 Pressure dependence for blood-brain barrier disruption

The dextran distribution was similar in all mice with successful (8/15) BBBD; dextran delivery was homogenously distributed throughout the pons and surrounding region (**figure 4.4.3**). There was no dextran observed in either the sham controls or those sonicated at 0.2 MPa. At 0.4 MPa and 0.6 MPa, dextran was seen in four of the five mice exposed to ultrasound (**figure 4.4.4A**). Some bright regions occurred outside the targeting region due to imaging artefacts from tissue folds and tears, tissue processing or autofluorescence of brain regions.

Quantification of dextran dose using fluorescence pixel intensity revealed little difference between the mean fluorescence pixel intensity at 0.4 MPa ($9.3x10^9 \pm 8.3x10^9$ A.U.) and 0.6 MPa ($1.0x10^{10} \pm 4.8x10^9$ A.U.) (**figure 4.4.4B**). There was considerable variation in the amount of dextran delivered within each acoustic pressure at 0.4 (range: $1.0x10^9$ - $1.9x10^{10}$ A.U.) and 0.6 MPa (range: 4.81 $x10^9$ - 1.71 $x10^{10}$ A.U.). The variation is greatest at 0.4 MPa where very little model drug was delivered in one mouse compared to in the three other mice with

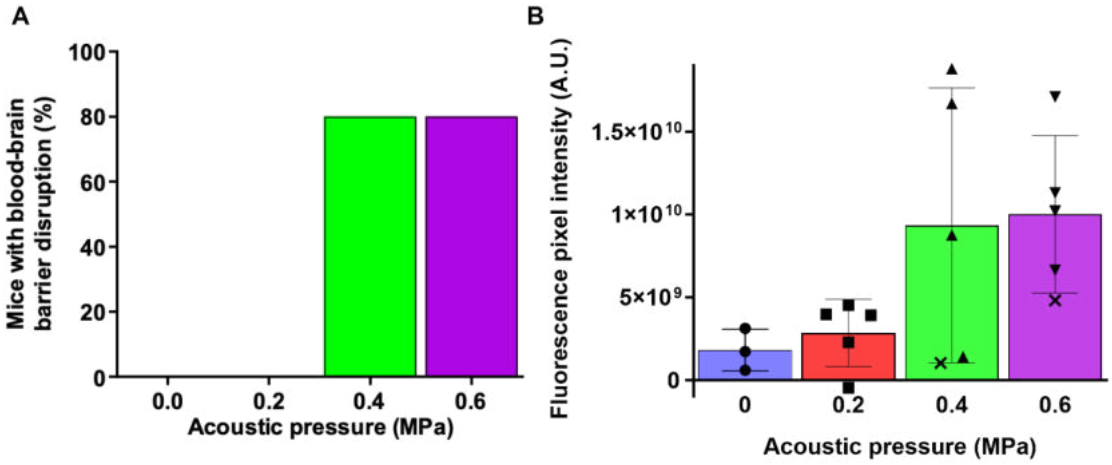

Figure 4.4.4 Pressure dependence for blood-brain barrier disruption. *(A) The percentage of mice (n=5) with observable dextran delivery assessed by fluorescence microscopy of brain slices was 0% in both the control and 0.2 MPa exposures and 80% in the 0.4 and 0.6 MPa exposures. (B) Quantification of fluorescence pixel intensity, an indication of the amount of model drug delivered, each symbol represents the mean of five slices from each mouse brain. There is no significant difference between the fluorescence pixel intensity at each acoustic pressure (p>0.05). The error bars represent standard deviation, and the 'X' symbol represents those mice without BBBD.*

observable successful dextran extravasation. One-way ANOVA confirmed there was no statistically significant difference in fluorescence pixel intensity at any of the acoustic pressures or control (p>0.05) and no outliers were identified.

4.4.2.2 Histological assessment

Mice (n=4) sonicated at 0, 0.2, 0.4 and 0.6 MPa were assessed for tissue damage by H&E staining for signs of extravasated erythrocytes and microvacuolations (**§1.6**); the number of each was counted in five brain slices per mouse (**figure 4.4.5**).

In the control (0 MPa) brains (n=3), one brain slice had five microvacuolations and no extravasated erythrocytes were present (**figure 4.4.6A&B**). Similar observations were seen at 0.2 MPa: 8% of brain slices had a damage site (across two mice of four), consisting of only microvacuolations and no extravasated erythrocytes (**figure 4.4.6C&D**). The total number of microvacuolations (6) across all mice was similar to the control (5) (**figure 4.4.5**).

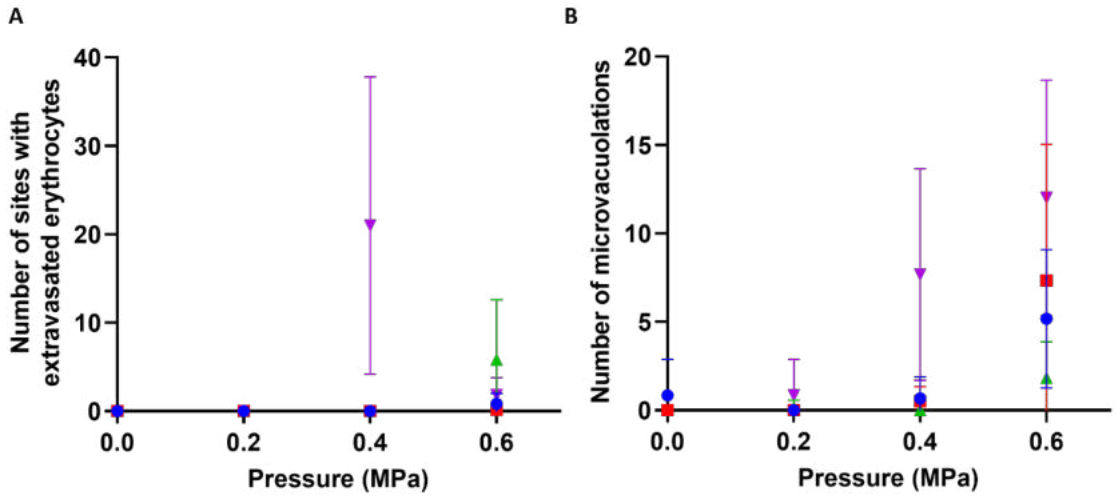

Figure 4.4.5 Quantification of tissue effects observed using H&E staining. *The number of (A) extravasated erythrocytes and (B) microvacuolations detected by H&E staining of brain slices (5 slices per brain) after exposure to ultrasound at peak-negative pressure of 0.2, 0.4, or 0.6 MPa (n=4 mice exposed each pressure) as well as sham controls not exposed to ultrasound (n=3). Each mouse within each pressure is shown in a different colour. Data is shown as mean ± standard deviation per mouse.*

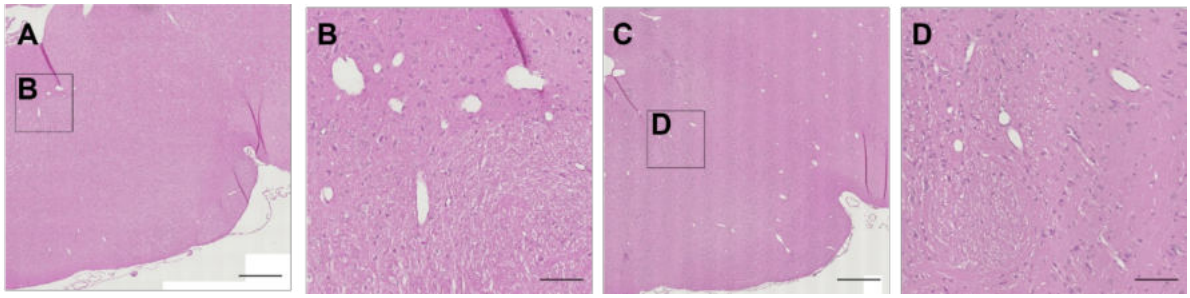

Figure 4.4.6 Histological assessment of brain slices from mice exposed to ultrasound with peak rarefactional pressure of 0 MPa (sham control) and 0.2 MPa. *Tissue effects in the pons region at 0 MPa (A&B) and 0.2 MPa (C&D) were comparable. Scale bars represent (A&C) 500 µm and (B&D) 100 µm.*

At 0.4 MPa, there was one brain with more tissue damage than the others. This brain had the most extravasated erythrocytes (126), 91 higher than the next largest value across all PRPs (**figure 4.4.7E-G**). The erythrocytes were confined to the targeted region; the contralateral brain slice, and untargeted regions showed normal tissue histology (**figure 4.4.7C&D**). Extravasated erythrocytes were associated with a range of vessel sizes throughout

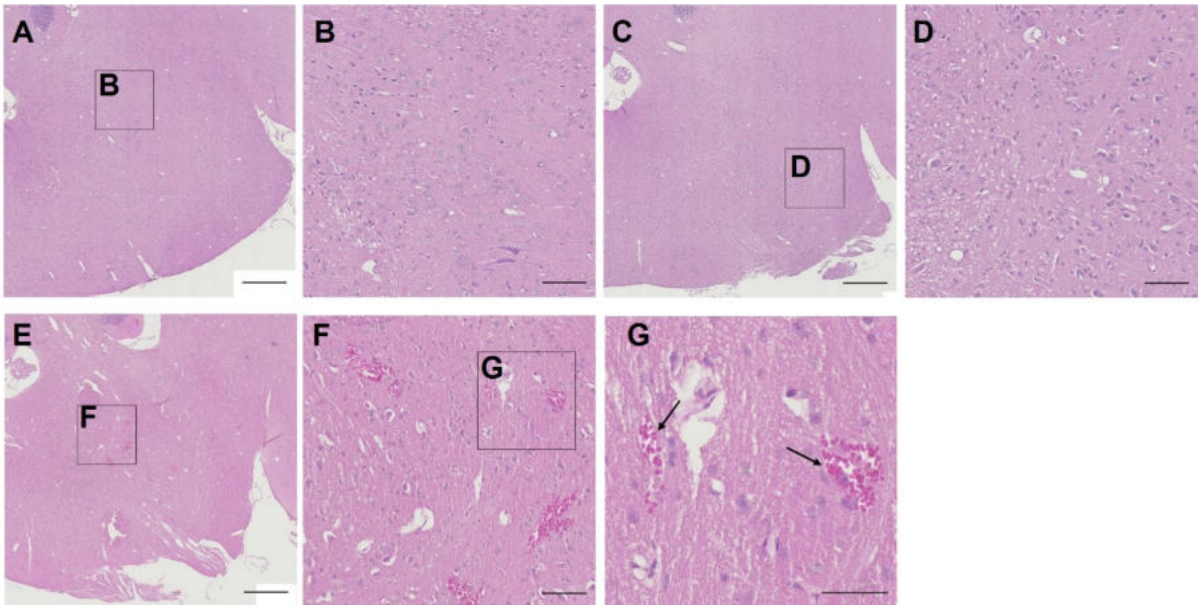

Figure 4.4.7 The pons region of H&E-stained brain slices from mice exposed to ultrasound at peak rarefactional pressure of 0.4 MPa. *(A&B) Three of four mice had comparable tissue effects to the (C&D) unexposed hemisphere. One mouse exposed to 0.4 MPa had large regions of erythrocyte extravasation (E-G) indicated by the arrows. Scale bars represent (A, C&E) 500 µm, (B, D & F) 100 µm and (G) 50 µm.*

the targeted region. There were some greater areas of haemorrhage around larger vessels near the skull base.

Two of the mice exposed to 0.6 MPa had gross haemorrhage damage, observed upon brain extraction, on the underside of the mouse brain in the pons region (**figure 4.4.8**).

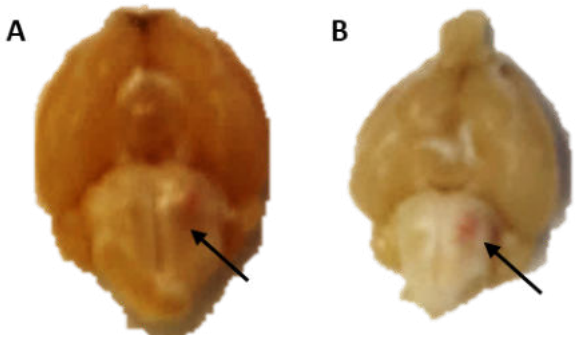

Figure 4.4.8 Gross histological damage seen in brains of two mice exposed to ultrasound at peak rarefactional pressure of 0.6 MPa. *Two brains had gross histological damage at the base of the brain shown by the arrows.*

H&E staining of brains exposed to 0.6 MPa showed at least one detected extravasated erythrocyte (range: 1-35) and microvacuolation in every brain (range: 11-72) (**figure 4.4.9A-C**). The untargeted contralateral hemisphere showed no microvacuolations or erythrocyte extravasation (**figure 4.4.9D&E**).

Statistical analysis was performed on the number of extravasated erythrocytes and microvacuolations counted at each pressure. One-way ANOVA and Tukey multiple comparisons revealed there to be significantly more extravasated erythrocytes at 0.4 MPa than 0.2 MPa ($p = 0.04$). Significantly more microvacuolations were present at 0.6 MPa than at each of the other pressure levels (0.6 MPa vs. control, $p< 0.0001$; 0.6 MPa vs. 0.2 MPa, $p<0.0001$; 0.6 MPa vs 0.4 MPa, $p=0.002$).

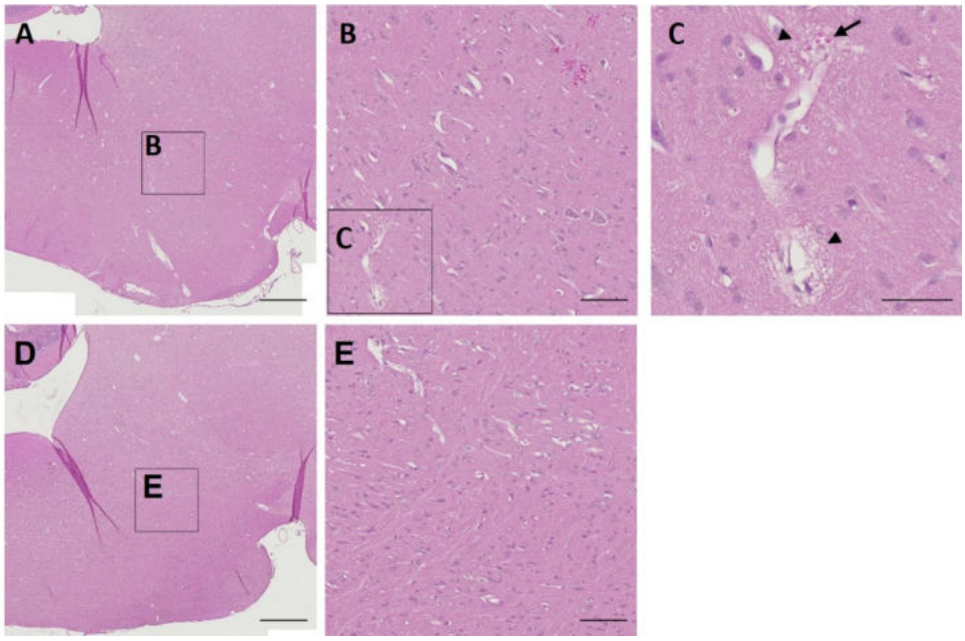

Figure 4.4.9 Histological assessment of brain slices from mice exposed to ultrasound at peak rarefactional pressure of 0.6 MPa, pons region shown. *(A-C) Erythrocyte extravasation (solid arrows) and microvacuolations (arrow heads) were observed in all mice (n=4). The tissue damage was confined to the targeted region and the contralateral brain slice showed no tissue damage (D&E). Scale bars represent (A&D) 500 µm, (B&E) 100 µm and (C) 50 µm.*

4.4.2.3 Acoustic emissions analysis

Acoustic emissions generated by the microbubbles were recorded during exposure and processed to give a value for total acoustic emissions energy, summed over the entire sonication (250 s). The mean total emissions energy was lowest at 0.2 MPa ($3.0 \times 10^5 \pm 3.3 \times 10^5$ A.U.) and similar at 0.4 MPa ($2.1 \times 10^6 \pm 2.1 \times 10^6$ A.U.) and 0.6 MPa ($1.4 \times 10^6 \pm 1.4 \times 10^6$ A.U.; **figure 4.4.10A**). The mouse with the highest emissions energy (5.1×10^6 A.U.) was exposed to 0.4 MPa, this value was almost double the next largest at 0.4 MPa (2.8×10^6 A.U.) but was not statistically deemed to be an outlier by ROUT method. Welch ANOVA and Dunnett's T3 multiple comparisons revealed no statistically significant difference between the total energy at each acoustic pressure.

In brains in which fluorescence pixel intensity was assessed, the dose delivered was plotted against total energy (**figure 4.4.10B**). There was a cluster of data points where no drug delivery occurred, and low total energy was recorded (grey box in **figure 4.4.10B**). There

was one data point in this cluster for which drug delivery was observed (solid arrow in **figure 4.4.10B**). Overall, there was weak correlation between total energy and fluorescence pixel intensity (r^2 = 0.41).

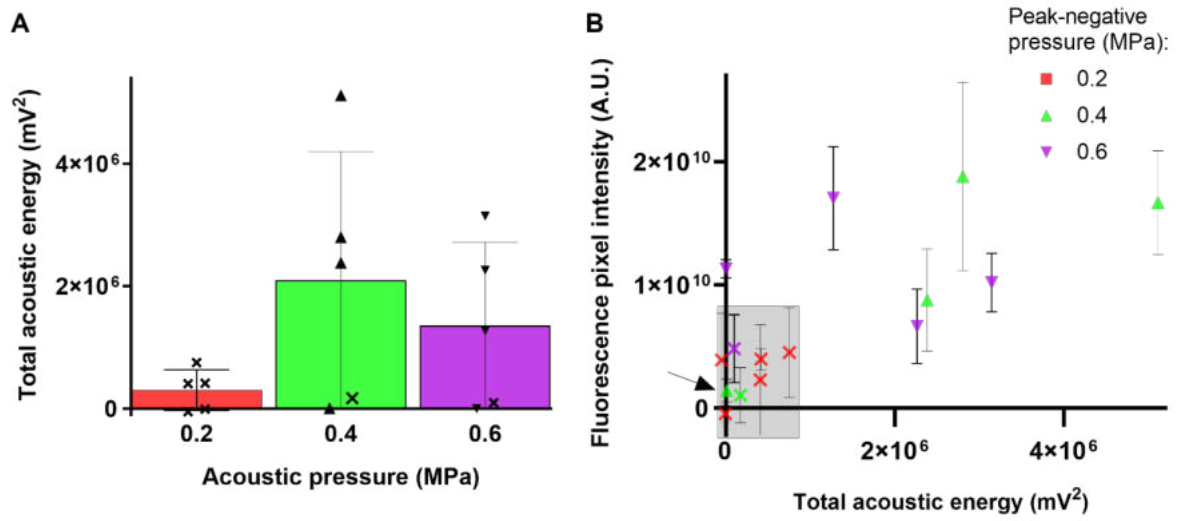

Figure 4.4.10 Total acoustic emission energy as a function of acoustic pressure and the corresponding fluorescence pixel intensity. *The total acoustic energy summed over the entire sonication (250 s) and fluorescent pixel intensity calculated for mice exposed to PRP of 0.2, 0.4 and 0.6 MPa (n=5). (A) There was no significant difference between the total acoustic energy by Welch ANOVA (p>0.05). (B) In those experiments where fluorescence pixel intensity was calculated (n=5 per pressure), the value (mean of five brain slices per mouse ± standard deviation) was plotted against the accumulated emission energy. The grey box represents the brains where no dextran delivery was observed, except for one brain where dextran delivery was observed which is indicated by the arrow. There was weak positive correlation between total energy and fluorescence pixel intensity across all data sets (r^2 = 0.41). The 'X' symbol represents those mice without BBBD.*

4.4.3 Targeting the pons at 1 MHz (ICR)

Once the ICR system had been assembled (**chapter 2**), 22 mice were sonicated with microbubbles and Evans Blue to assess the ability of the system to produce BBBD in the pons. Targeting adjustments were made to establish repeatable BBBD in the pons ahead of future drug delivery studies. Evans Blue delivery could be seen throughout the targeted region in images of the whole brain, and 1 mm coronal sections (**figure 4.4.11**).

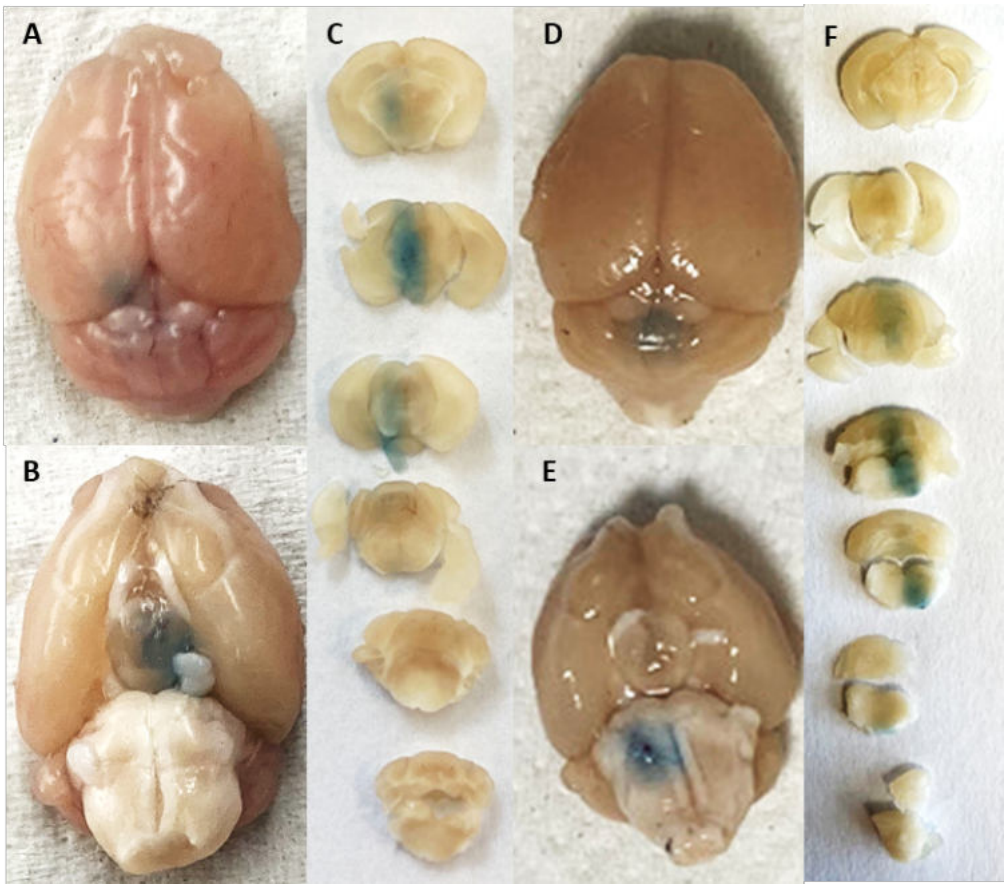

Figure 4.4.11 ICR system Evans Blue tests. *Mice were exposed to ultrasound, microbubbles, and Evans Blue dye to test the in vivo efficacy of the newly assembled ICR sonication system (frequency: 1.05 MHz, peak-negative pressure: 0.4 MPa). Extravasation of the dye can be seen from photographs of the (A&D) superior and (B&E) inferior view of the whole brain after extraction, as well as in 1 mm coronal slices (C&F).*

4.4.3.1 Dextran delivery

Dextran was repeatably delivered across the BBB to the pons region (**figure 4.4.12A&B**). The dextran delivery was homogenously distributed, and intensity maintained with distance from blood vessels, as seen on the ICL system (**figure 4.4.3**). Morphological patterns suggest neuronal uptake of the dextran (**figure 4.4.12D-F**).

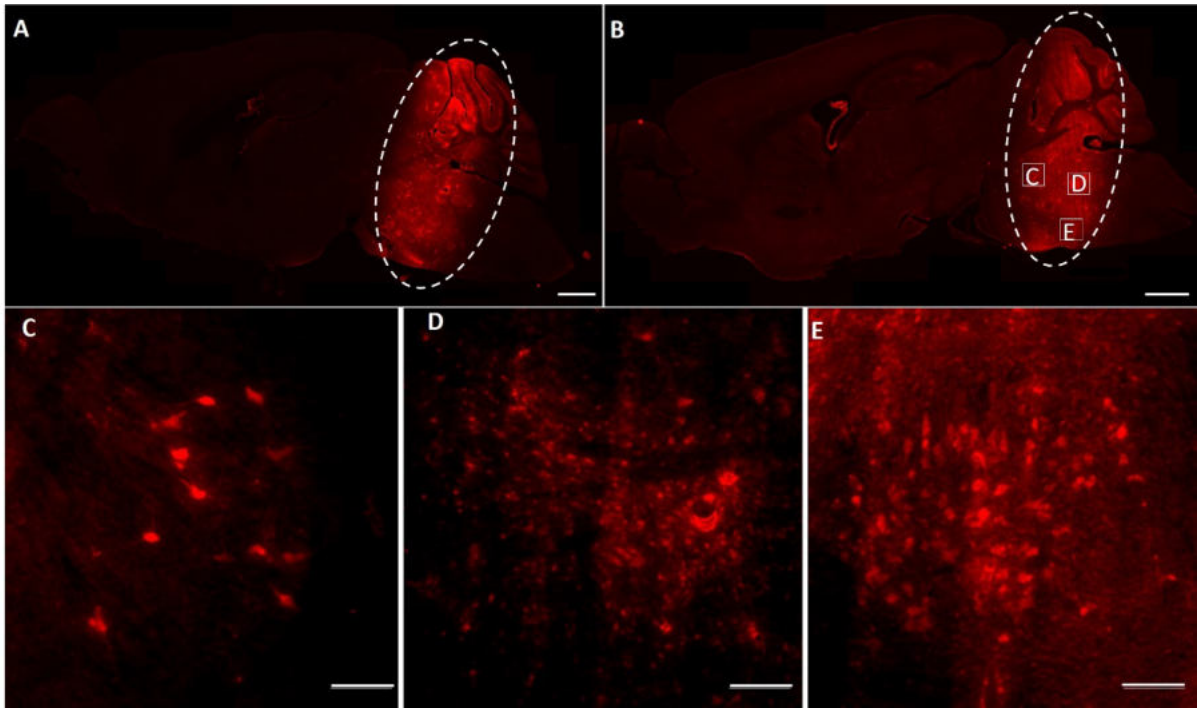

Figure 4.4.12 ICR system dextran delivery. *Sagittal brain slices of mice exposed to ultrasound whilst receiving an intravenous injection of microbubbles and a fluorescently tagged tracer (Dextran, 3kDa). (A&B) Examples from two mice showing dextran extravasation in the targeted pons region, shown by the dashed ellipsoids. (C-E) Morphological patterns indicating neuronal uptake seen throughout the targeted region. Scale bars are (A&B) 1 mm and (C-E) 100 µm.*

4.4.3.2 Targeting assessment

The aim of the work described in this chapter was to establish BBBD in the pons in preparation for drug delivery to a DIPG mouse model and so the accuracy of targeting was assessed. MR images of a syngeneic DIPG mouse model (nestin-Tv-a/p53fl/fl, RCAS-ACVR1R206H + RCAS-H3.1K27M murine cell line in C57BL/6J mice) were provided by a member of the preclinical MRI team and the mean tumour size (2D) measured as 1.3 ± 0.1 mm (width) x 2.0 ± 0.3 mm (height) (**figure 4.4.13**).

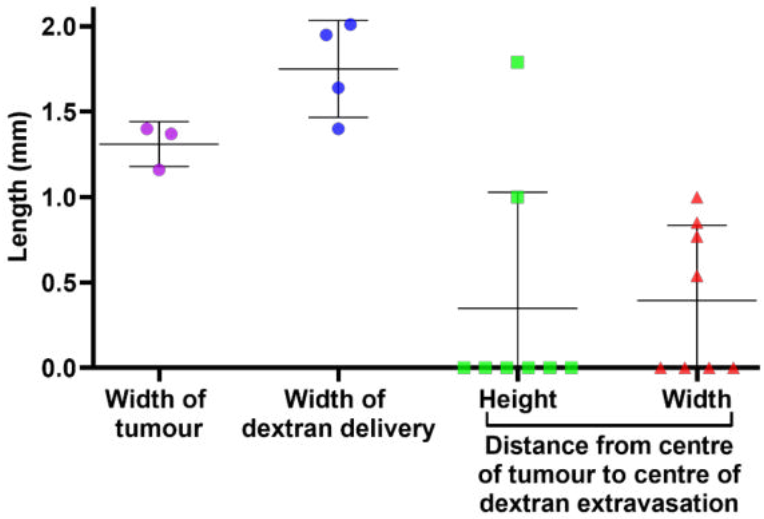

Figure 4.4.14 ICR targeting assessment: comparison of model drug (dextran) extravasation in non-tumour-bearing mice with tumour growth in a mouse model. *Measurements of tumour width measured from a T2-weigthed MRI of a syngeneic DIPG tumour model. Approximate width of dextran delivery and distance from the centre of the tumour to centre of dextran extravasation. Data are mean and standard deviation.*

Comparison of the location of dextran delivery in non-tumour-bearing brain slices from five mice from **§4.3.5.2**, showed some co-localisation with the expected tumour growth location (example shown in **figure 4.4.14**). The mean width of dextran delivery was 1.8 ± 0.3 mm, this is larger than the measured width of the tumours (1.33 ± 0.1 mm; **figure 4.4.13**). The distance from centre of tumour to centre of dextran extravasation was measured as 0.4 ± 0.7 mm (height) and 0.4 ± 0.4 mm.

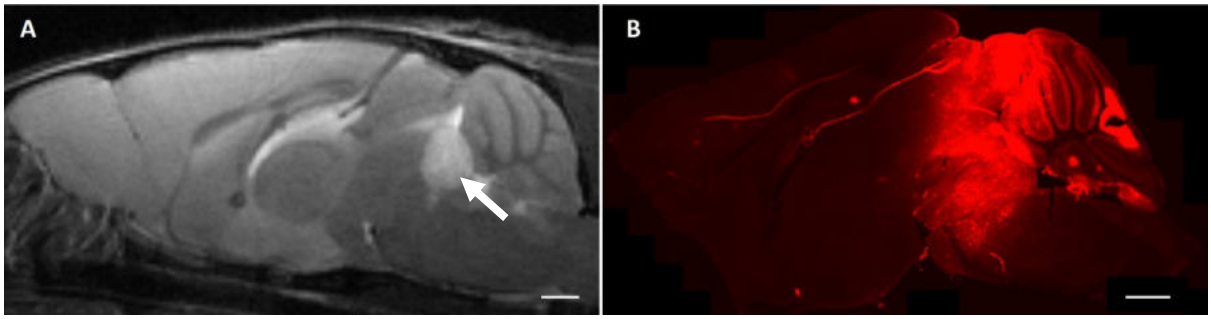

Figure 4.4.13 Co-localisation of tumour growth and dextran extravasation. *Examples images showing (A) tumour growth (indicated by the arrow) in a syngeneic DIPG mouse model on a T2-weighted MRI scan and (B) fluorescence microscopy of dextran extravasation after ultrasound-mediated blood-brain barrier disruption. Scale bar is 1 mm.*

4.4.3.3 Histological assessment of mice exposed to ultrasound at the ICR

The mice (n=3) sonicated for histological assessment of unwanted tissue damage (by H&E staining) showed no haemorrhage, erythrocyte extravasation or microvacuolations. Tissue histology in the targeted regions was the same the un-targeted regions throughout the targeted pons region (**figure 4.4.15**).

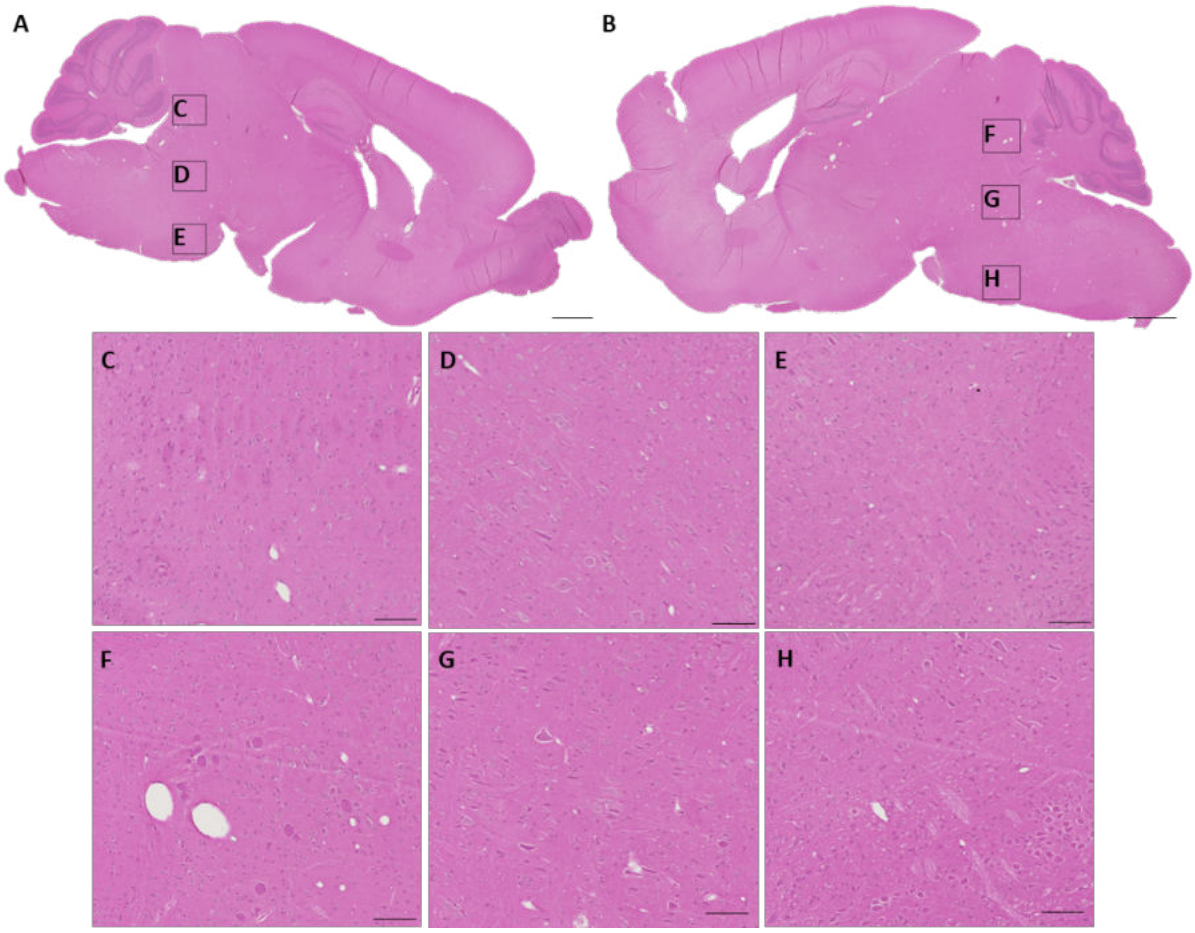

Figure 4.4.15 Histological assessment after ultrasound exposure (peak rarefactional pressure: 0.4 MPa) on the ICR system. *Sagittal brain slices were stained with haematoxylin and eosin (H&E) to assess for tissue damage. No sign of tissue damage e.g. extravasated erythrocytes and microvacuolations was observed in the (A) targeted left hemisphere compared to the (B) untargeted right hemisphere from the same mouse. Scale bars are (A&B) 1 mm and (C-H) 100 µm.*

4.5 Discussion

This chapter has described rapid short pulses of ultrasound in combination with intravenous microbubbles that can disrupt the BBB, enabling the extravasation of a model drug (dextran) at both ICL and the ICR. At ICL, a pressure window for dextran delivery was established between 0.2 and 0.4 MPa. At the ICR, dextran extravasation co-localised with tumour growth location of a syngeneic DIPG mouse model and no observable tissue damage was detected using H&E staining at a PRP of 0.4 MPa.

4.5.1 Targeting the pons (ICL)

Extravasation of the model drug dextran indicated BBBD in the pons region with a diffuse and homogenous distribution of dextran (**figure 4.4.3**), typical of short pulse ultrasound (Morse et al., 2019). The ultrasound sequence was designed to gently stimulate microbubbles at multiple locations, spreading their cavitation activity and resultant drug delivery, more diffusely throughout the targeted region (**§1.5.4**). The uniform distribution of dextran in the pons region indicates that a similar drug dose could reach targeted brain cells. This will also depend on drug pH, size, and lipophilicity. This is advantageous when treating diseases such as DIPG, thus that ensuring regions are not under treated.

4.5.2 Pressure window for blood-brain barrier disruption (ICL)

Once BBBD in the pons region had been established at 1.05 MHz, the acoustic pressure was varied. The results showed (**figure 4.4.4**) that between peak negative pressure amplitude between 0.2 and 0.4 MPa are necessary for BBBD and extravasation of dextran in the pons; no mice exposed to 0.2 MPa had BBBD yet 80% of mice exposed to 0.4 MPa did. Further work could investigate an intermediate range of pressures to define a smaller window for drug delivery.

The pressure threshold for drug delivery will vary with characteristics of the drug/ model drug such as size and lipophilicity (**§1.5.7**). It has been shown that a greater acoustic pressure is required to deliver larger compounds across the BBB e.g. 0.6 MPa to deliver a 500 kDa dextran with long pulses of ultrasound (Gandhi et al., 2022, Chen and Konofagou, 2014, Pandit et al., 2020). The studies reported in this chapter have used 3 kDa dextran to assess BBBD,

yet many approved cancer drugs are smaller than 1 kDa e.g. carboplatin (371 Da) and panobinostat (349 Day). Overall, the evidence from this study suggests that ultrasound exposures using the parameters (**§4.3.1**) used here and an acoustic pressure of 0.4 MPa should be able to deliver a range of potential drugs to the pons region for the treatment of DIPG.

The probability of BBBD (80%) was the same at 0.4 MPa and 0.6 MPa, and no statistical difference was found in the amount of dextran delivered as quantified by fluorescence pixel intensity. This contradicts previously published studies that have shown that the delivered dose of a model drug increases with acoustic pressure (Choi et al., 2011a, Valdez et al., 2020, Shen et al., 2016, McDannold et al., 2008, Chopra et al., 2010, Morse et al., 2022). It may be that with the ultrasound exposure conditions used in this study, at an acoustic pressure of 0.4 MPa the amount of dextran that can enter the brain parenchyma is saturated and no benefit is gained from increasing the pressure to 0.6 MPa.

4.5.3 Histological assessment of tissue damage (ICL)

Assessing tissue damage, in terms of the presence of extravasated erythrocytes and microvacuolations, at different acoustic pressures showed the greatest tissue damage at 0.6 MPa (**figure 4.4.7-9**). Although tissue damage was only assessed immediately, microvacuolations are expected to occur immediately due to mechanical forces from the microbubbles on the tissue but resolve with time (Morse, 2020). More microvacuolations were detected at 0.6 MPa than for the other acoustic pressures examined. This could be explained by more violent microbubble behaviour (inertial cavitation) and associated activities that are associated with mechanical damage to the tissue e.g. rapid expansion, violent collapse, and liquid jets, occurring at this acoustic pressure (**§1.6**).

More extravasated erythrocytes were seen at 0.6 MPa than at the other exposure conditions. The gross haemorrhage seen at 0.6 MPa (n=2/4) is likely to be due to acoustic reflections from the skull base (**§1.5.2.**) This is an important consideration when targeting the pons which lies deeper (~5 mm) in the brain than other, previously targeted, regions, such as the hippocampus. Whilst haemorrhage is undesirable, the location of the pons in mice and

humans is different, and therefore this should not hinder the pre-clinical development and clinical translation of the technique.

Haemorrhage was seen in one mouse at 0.4 MPa (**figure 4.4.7**). Acoustic emissions analysis showed that the total energy in this mouse was greater than in all other mice in this study by 59.5 A.U. (**figure 4.4.10**). Published studies have reported that higher acoustic energy results in greater microbubble oscillation and greater vascular effects (Fan et al., 2014a, Baseri et al., 2010). This suggests that the microbubbles underwent violent microbubble behaviour e.g. unstable inertial cavitation, associated with greater tissue damage compared to stable cavitation (**§1.5.2**). The ultrasound parameters were the same for all exposures at 0.4 MPa, so it is not clear why this occurred. An increase in sample size would reveal whether this was an outlier.

The PCD used to record microbubble activity during ultrasound exposures in this study could be used to create a real-time feedback system, allowing monitoring of the level of bubble activity (**§1.7**). This could inform on excessive microbubble behaviour allowing the user to halt exposure, thus preventing unwanted tissue damage as described.

Published studies have also successfully used acoustic emissions recorded during exposures to successfully predict BBBD (O'Reilly et al., 2017b). Analysis of the acoustic emissions emitted during the experiments reported in this chapter suggest that the total energy has a moderate positive correlation (r=0.6) with drug delivery. Another method of processing acoustic emissions recorded during exposure might provide a stronger correlation with drug delivery.

4.5.4 Efficacy of the ICR BBBD system

The newly assembled ultrasound system at the ICR was assessed for its ability to disrupt the BBB in the pons region using the pulse sequence, and the pressure threshold window established at ICL (0.4 MPa). BBBD in the targeted region was first confirmed with the model drug Evans Blue, and then dextran was used to examine the resultant drug distribution (**figure 4.4.11&12**). The distribution of dextran was typical of rapid short pulse ultrasound seen by Morse et al. (2019) and in the studies presented in this chapter using the ICL ultrasound system (**fig 4.4.3**).

Uptake of dextran by neurons was suggested on fluorescence images (**figure 4.4.12**). Dextran has previously been used as a neuronal marker and neuronal uptake of dextran after FUS exposure has been previously reported (Morse, 2020, Choi et al., 2011a). This suggests that the drug could enter cells rather than remaining in the extracellular matrix, although cellular penetration will depend on the properties of the drug including size and lipophilicity as well as on cellular properties.

4.5.5 Histological assessment at ICR

After it had been confirmed that the new ICR FUS system was able to disrupt the BBB in regions including the pons, tissue damage after ultrasound exposure was assessed using H&E staining. There were no observable differences in tissue morphology between ultrasound targeted and un-targeted regions (**figure 4.4.15**). Specifically, microvacuolations and extravasated erythrocytes, observed after sonication using the ICL system, were absent under the almost identical exposure conditions with the ICR system. The main difference between these two systems is the targeting method and acoustic coupling. At the ICR, the mouse head sits in the water of the coupling cone whilst at ICL ultrasound gel is required for acoustic coupling. H&E staining was chosen to provide information on general tissue morphology and common effects from ultrasound exposure. Other histological changes to be considered in future work include cell death and activation of inflammatory cells and pathways (**§1.6.2**).

4.5.6 Limitations and future work

One limitation with this study, and of any *in vivo* study, is likely to be the amount of biological variation between mice. This is most evident in the data at 0.4 MPa as seen in the model drug delivery quantification (**figure 4.4.4**), histological analysis (**figure 4.4.7**) and acoustic emissions data (**figure 4.4.10**).

The large variation (standard deviation) in fluorescence pixel intensity between animals given the same exposure may arise from errors in the quantification method as discussed in **§3.5.6**. The method is sensitive to artefacts which are common in cryosectioned brain slices, whilst artefacts are removed during quantification, some may remain.

More quantitative assays for assessing BBBD might aid the reduction in error. For example, the use of whole brain fluorometry would provide a quantitative measure of fluorescence in the brain. However, this technique would not provide any spatial resolution and so could be combined with fluorescence microscopy, as used in this thesis. Brain tissue could be separated into brain sections to compare drug, or model drug, delivery. Fluorescence spectroscopy is another option that provides both quantitative measure of intensity as well as spatial distribution of the marker and could be investigated.

The variation in total energy measured from of acoustic emissions reported here, including an overlap between the three acoustic pressures (**figure 4.4.10**), may be due to differences in microbubble behaviour between experiments, possibly because of anatomical and vasculature differences between mice. The skull attenuates the ultrasound beam and will contribute to differences in the *in-situ* pressure, and thus in the amplitude of microbubble oscillation, which will vary for each mouse brain. Vasculature and perfusion differences within the mouse brain can affect bubble distribution and concentration within the focus and resulting microbubble behaviour (**§1.5.2**). These vasculature parameters will also vary over time throughout the exposure.

The aim of the studies described in this chapter was achieved, with no significant barrier being found to progressing to exposing orthotopic DIPG tumours with the aim of studying anti-cancer efficacy. Further work could be performed to inform future drug studies, beyond those explored in the next chapter. Such studies include investigating time taken for BBB permeability to return to pre-FUS levels, size threshold of drugs that can be delivered, effect of altering ultrasound parameters on drug delivery and tissue effects after FUS exposure over a range of time points.

A size threshold study would indicate which therapeutics could potentially be delivered using FUS/microbubble mediated BBBD. Successful extravasation of 3 kDa dextran shown here indicates that drugs smaller than this could be successfully delivered into the brain parenchyma (although hydrophobicity should be considered). A 3 kDa dextran was chosen here as many drugs are smaller than this, however, some therapeutics are larger e.g. antibody fragments and antisense oligonucleotides (small pieces of DNA or RNA). Published studies using long pulse ultrasound have reported successful delivery up to, and including, 500 kDa

dextran (Pandit et al., 2020). It has also been reported that the size threshold depends on ultrasound parameters e.g. acoustic pressure and pulse length, and should be investigated for specific exposure conditions (Choi et al., 2011a, Valdez et al., 2020, Nhan et al., 2013, Shen et al., 2016, McDannold et al., 2008, Chopra et al., 2010, Lapin et al., 2020).

Whilst no correlation has been made between model drug delivery and therapeutic efficacy, distribution of a model drug within a wild type or disease mouse model provides an indication of drug distribution. Model drug extravasation in a disease mouse model would confirm if (i) the BBB is intact prior to FUS exposure by examining model drug extravasation in non-FUS exposed regions and (ii) whether FUS can disrupt the BBB in the disease model. A pilot study investigating these points would prevent wastage of animals if a drug delivery study were to be started where (i) and (ii) are not true, and so their investigation is described in the next chapter (**chapter 5**).

4.6 Conclusion

This chapter has described preliminary evidence that repeatable BBBD can be achieved in the pons region of mice using rapid short-pulse ultrasound with two setups, demonstrating that a centre frequency of 1 and 1.05 MHz is superior to 300 kHz in mice. FUS and microbubble mediated BBBD can be achieved, facilitating the delivery of a model drug (dextran) at 1.05 MHz, using an ultrasound setup and exposure sequence established previously by the ICL non-invasive surgery and biopsy (NSB) laboratory. A pressure window for BBBD was identified between 0.2 and 0.4 MPa. Above 0.4 MPa, no more model drug is delivered yet more tissue damage occurs.

These ultrasound parameters (PRP: 0.4 MPa, pulse length: 5 cycles, PRF: 1.25 kHz, burst length: 38 pulses, BRF: 0.5 Hz, number of bursts: 125, total time: 250s) established at ICL were used to examine the efficacy of the ICR system. Overall, the results in this chapter have shown that in mice the ICR FUS system is able to disrupt the BBB in the pons with no observable tissue damage, enabling the progression to investigation of drug delivery in a DIPG tumour grown in a mouse model.

5 Assessment of ultrasound-mediated panobinostat delivery to the pons

5.1 Background

Diffuse intrinsic pontine glioma (DIPG), a type of diffuse midline glioma, is a highly aggressive childhood brain tumour with a 9-month median survival (**§1.3**) (Zhou et al., 2017). Poor treatment options are largely attributed to the presence of an intact blood-brain barrier (BBB) which prevents drugs from reaching tumour tissue. Focused ultrasound (FUS) and intravenous (IV) microbubbles can transiently increase the permeability of the BBB and could improve drug delivery for the treatment of DIPG.

The results described in the previous chapter (**chapter 4**) showed that BBBD can be achieved in the pons (where DIPG arises) with an acceptable drug delivery and safety profile using short pulses of ultrasound. The studies described in this chapter investigate the use of FUS to increase concentration of a drug in a DIPG tumour model.

5.1.1 Panobinostat *in vitro*

DIPG arises in the pons and the majority of cases (~80%) exhibit the H3 histone mutation H3K27M (Mackay et al., 2017). This mutation results in the substitution of the amino acid lysine with methionine, resulting in global epigenetic changes. These are hypomethylation, resulting in expression of oncogenes, and the suppression of tumour suppressor genes by histone deacetylasation, both of which drive tumorigenesis (El-Hashash, 2021).

The significant role of H3K27M in DIPG tumorigenesis makes it a key therapeutic target. Panobinostat is a pan-histone deacetylase (HDAC) inhibitor with therapeutic potential for the treatment of DIPG. This drug has been shown to be effective *in vitro* against human and murine DIPG cell lines, resulting in inhibition of cell proliferation, viability and clonogenicity, and induce apoptosis (Hennika et al., 2017). For example, Hennika et al. (2017) significantly reduced cell proliferation from a 10 nM concentration in mouse brainstem glioma cells driven by PDGF-B, H3.3-K27M, and Cre-induced p53 loss cells. Moreover, in drug screens panobinostat has shown the most potential, regardless of H3 histone status, of approved and investigational drugs (Grasso et al., 2015b, Lin et al., 2019). As a non-selective HDAC,

panobinostat is advantageous for clinical translation as it increases the number of patients eligible to receive the drug (**§1.3.4**).

5.1.2 Panobinostat *in vivo*

However, studies reported in published literature have not managed to achieve a therapeutic effect at a tolerable dose of panobinostat. Hennika et al. (2017) reported significant toxicity after daily treatments of 10 or 20 mg/kg in a genetically engineered and patient-derived mouse model. However, reduced, well-tolerated panobinostat doses did not prolong overall survival (OS). It was hypothesised this was due to lack of brain penetration, with this also being seen in larger animal models. In a non-human primate pharmacokinetic study, panobinostat cerebrospinal fluid (CSF) concentration was low, and detectable levels were only present in two of three primates dosed with 1.0 mg/kg, 1.8 mg/kg and 3.0 mg/kg (Rodgers et al., 2020).

5.1.3 Panobinostat in the clinic

Panobinostat (Farydak) is currently approved for the treatment of multiple myeloma in the UK (NICE, 2016). However, a phase I study of panobinostat in DIPG patients showed no significant improvement in progression-free survival (PFS) or OS (Monje et al., 2022). The molecular weight (349 Da) and lipophilicity (2.643 logP) of panobinostat suggests that the drug should cross the BBB. However, *in vivo* studies have struggled to achieve a therapeutic effect at a tolerable dose, and pharmacokinetic studies in the clinic suggests that CNS penetration is poor. Improved delivery of panobinostat could have great significance for the treatment of DIPG.

5.1.4 Panobinostat delivery using focused ultrasound

The use of focused ultrasound (FUS) and microbubbles could noninvasively and transiently increase the permeability of the BBB, increasing the concentration of panobinostat in the brain to a therapeutic level at a tolerable systemic dose. As well as increasing drug concentration, there is evidence that FUS treatment can suppress the P-glycoprotein (P-gp) efflux pump, for which panobinostat is a substrate (Aryal et al., 2017).

Overall, the use of FUS to increase the concentration of a drug with great therapeutic potential could expand treatment options for patients with DIPG.

5.1.5 Study design

In this chapter, the effect of FUS and microbubbles on panobinostat concentration in the brain is assessed, first in non-tumour bearing mice, then in a syngeneic DIPG model, using the optimised protocol and parameters described in the previous chapter (**§chapter 4**). The protocol was designed to closely mirror studies published in the literature to enable comparisons. In FUS studies, such as those described earlier in this thesis, the (model) drug is commonly administered intravenously via tail vein injection. However, only one published study has administered panobinostat in this manner, whilst the drug was administered by intraperitoneal (IP) injection in other studies (Homan et al., 2021). Therefore, in this study, panobinostat was administered by IP injection.

To maximise the potential for drug delivery, FUS treatment should be performed at peak blood drug concentration (Cmax). Following IP injection, the drug concentration in the blood takes time to reach its maximum as the drug is absorbed through the peritoneal cavity. A pharmacokinetic study was therefore performed to examine the time course of C_{max} in the blood following IP injection, to establish the ideal timepoint for the ultrasound treatment to maximise drug delivery. Across the literature, a panobinostat dose of 10 mg/kg has been reported as being well tolerated, whilst 20 mg/kg was not (Grasso et al., 2015b, Hennika et al., 2017). 10 mg/kg was therefore used in the studies reported here.

5.2 Aims and objectives

The overall aim of the work described in this chapter was to assess whether short-pulse ultrasound and microbubbles can increase the concentration of panobinostat in the parenchyma of a DIPG tumour model. Firstly, a pharmacokinetic study assessed the concentration of the drug in the plasma and brain over time following intraperitoneal injection to determine peak blood concentration and enable optimal timing of the FUS procedure. Next, using non-tumour-bearing mice, concentration of panobinostat was compared for mice that received drug only, and mice which received drug and ultrasound, at several time points after treatment. Finally, a DIPG tumour model was established. The tolerability of FUS exposure was assessed using a model drug (dextran), and then the effect on panobinostat concentration in the brain measured.

5.3 Materials and methods

The work described in this chapter builds towards the overall aim of drug delivery to a DIPG mouse model. First, the *in vitro* efficacy of panobinostat against DIPG cell lines was assessed. Then, *in vivo* studies in non-tumour-bearing mice evaluated the pharmacokinetic profile of the drug, and tolerability and efficacy of FUS-mediated drug delivery. Meanwhile, mice were inoculated with DIPG cells, and monitored for tumour growth using MRI. The tolerability of the FUS procedure was assessed using a model drug (dextran). Lastly, the concentration of panobinostat in the mouse brain was assessed with and without FUS and microbubble exposure.

5.3.1 Cell culture

The cytotoxicity of panobinostat was assessed in four cell lines (**table 5.3.1**). All cell lines were cultured under neurosphere conditions and incubated at 37^{o}C with 5% CO_2. The three DIPG patient-derived cell lines were cultured in tumour stem cell medium consisting of neurobasal-A medium, Dulbecco's Modified Eagle Medium/Nutrient Mixture F-12 (D-MEM/F-12 1X), HEPES Buffer Solution (1 M), MEM Sodium Pyruvate Solution (100 mM), MEM Non-Essential Amino Acids Solution (10 mM), GlutaMAX-I Supplement (Invitrogen, Paisley, UK) supplemented with B-27 (Invitrogen), heparin (2 µg/mL; Stem Cell Technologies, Vancouver, Canada) and the growth factors: human epidermal growth factor (EGF, 20 ng/mL); human basic fibroblast growth factor (FGF, 20 ng/mL); human platelet derived growth factor (PDGF)-AA (10 ng/mL), and human PDGF-BB (10 ng/mL; all Shenandoah Biotech, Warwick, PA, USA).

The mouse cell line, OB-3, was cultured in Dulbecco's Modified Eagle Medium (DMEM; Life Technologies) supplemented with neurocult proliferation supplement (10%; Stem Cell Technologies), human basic FGF (20 ng/mL; Invitrogen), human EGF (10 ng/mL; Invitrogen), and heparin solution (2 µg/mL; Stem Cell Technologies).

For passaging, cells were centrifuged at 1000 revolutions per minute (RPM) for 10 min then incubated (37^{o}C with 5% CO_2) with 500 µL Accutase® (Merck Life Sciences, Gillingham, UK) for 5 min. Culture medium was added to neutralise the Accutase® and cells centrifuged at 1300 rpm for 3 min. Neurospheres were resuspended in 200 µL culture medium and titrated to form a single cell suspension. Finally, cells were passaged in appropriate dilutions.

Table 5.1 The cell lines tested in vitro. *p. refers to the location of the mutation.*

		Genetic status			
Cell line	Origin	Histone status	ACVR1	TP53	Other genes
BIOMEDE-169	Patient derived	*H3F3A* p.K27M	Wild-type	*TP53* p.C176Y	*BRAF* p.G469V
BIOMEDE-184	Patient derived	HIST1H3C p.K27M	Wild-type	*TP53* p.C275Y	*PIK3CA* p.E542K, *NF1* p.Glu76fs, *NF1* p.I1824S
HSJD-DIPG-007	Patient derived	*H3F3A* p.K27M	*ACVR1* p.R206H	Wild-type	*PIK3CA* p.H1047R & PPM1D p.P428fs
OB-3	Mouse	*H3.1* p.K27M	*ACVR1*-R206H-FLAG	TP53 loss	PDGFA

5.3.2 *In vitro* panobinostat cytotoxicity assay

CellTiter-Glo® (CTG®), an adenosine triphosphate (ATP) based viability assay, was used here to determine cell survival after drug treatment. First, cells were seeded in their culture media at appropriate densities (**table 5.3.2**) in 96-well plates. After 3 days, cells were treated with LBH-589 (panobinostat; Selleckchem, TX, USA) in serial concentrations (1.00 to 1.91×10^{-6} µM, halving the concentration each time) and vehicle only control. Eight days post drug treatment, the cells were incubated with CTG reagent (Promega, Southampton, UK) for 25 min, before the luminescence was read on a plate reader (BMG Labtech, Ortenberg, Germany; **figure 5.3.1**). Data was normalised to the vehicle control and analysed with a non-linear regression using Prism v9.5.1 to give a growth inhibition (GI_{50}) value for each cell line. The GI_{50} corresponds to the concentration of panobinostat that inhibits cell proliferation by 50% (Catalano et al., 2011).

Table 5.2 Seeding density for in vitro panobinostat cytotoxicity assay.

Cell line	Seeding density (cells/mL)
BIOMEDE-169	5 x10^4
BIOMEDE-184	5 x10^4
HSJD-DIPG-007	5 x10^3
OB-3	1 x10^4

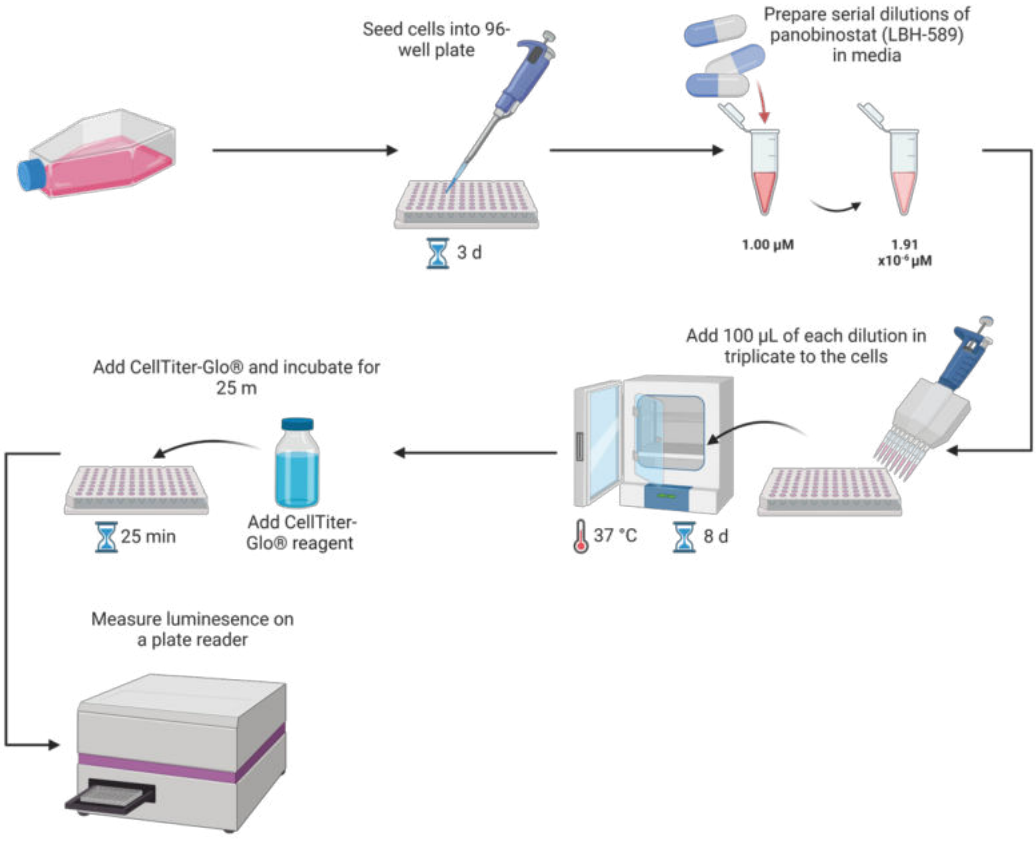

Figure 5.3.1 In vitro panobinostat cytotoxicity assay. *Cells from three human and one murine cell line were seeded at appropriate densities in their culture media. After three days, panobinostat was added in serial dilutions from 1.00 µm to 1.91 x 10^{-6} µm and incubated for 8 days. CellTiter-Glo® was added for 25 min then luminescence measured on a plate reader. Figure created with BioRender.com.*

5.3.3 Pharmacokinetic study

A pharmacokinetic study of panobinostat to determine blood and brain concentrations of the drug after intraperitoneal (IP) injection was performed in C57BL/6J mice. Mice were administered 10 mg/kg of panobinostat or vehicle [2% dimethyl sulfoxide (DMSO, Fisher Scientific, UK), 48% PEG300 (Merck Life Sciences), 2% Tween 80 (Merck Life Sciences), 48% ddH_2O (Merck Life Sciences)]. Mice were euthanised by overdose of the sedative pentobarbital, administered by IP injection. Plasma and brain samples were obtained 1 h, 6 h and 24 h (in the first study), and 5 min, 15 min and 1 h (in the second study), as described below.

5.3.4 Plasma and brain tissue collection for LC-MS/MS

Plasma samples were obtained by cardiac puncture and centrifuged at 13000 rpm for 2 min. Brain samples were extracted, and both samples were snap frozen and stored at -80°C.

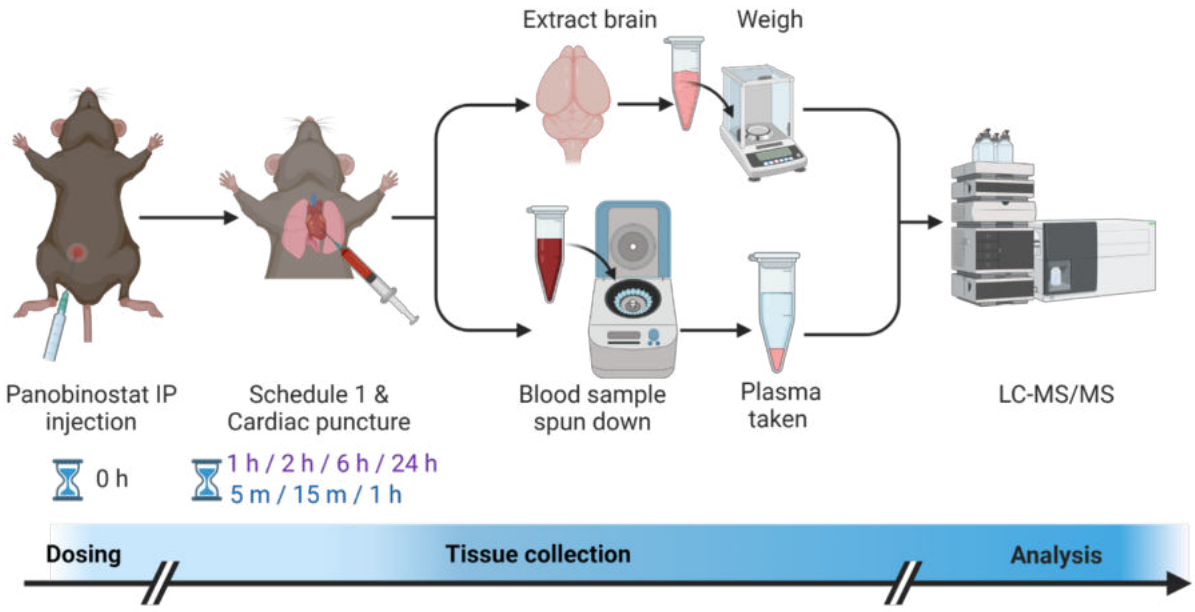

Figure 5.3.2 Pharmacokinetic study of panobinostat (LBH-589) in C57BL/6J mice. *Mice were administered 10 mg/kg panobinostat by intraperitoneal injection. Plasma and brain samples were taken 1 h, 2 h, 4 h and 24 h after dosing in the first study (purple) and 5 min, 15 min and 1 h in the second study (blue). Plasma samples were spun down at 13,000 rpm for two min and plasma was snap frozen along with brain tissue. Panobinostat concentration was measured using LC-MS/MS. Figure created with BioRender.com.*

Finally, the panobinostat concentration was obtained using Liquid Chromatography Triple Quadrupole Mass Spectrometry (LC-MS/MS) by Ruth Ruddle, an internal collaborator at the ICR.

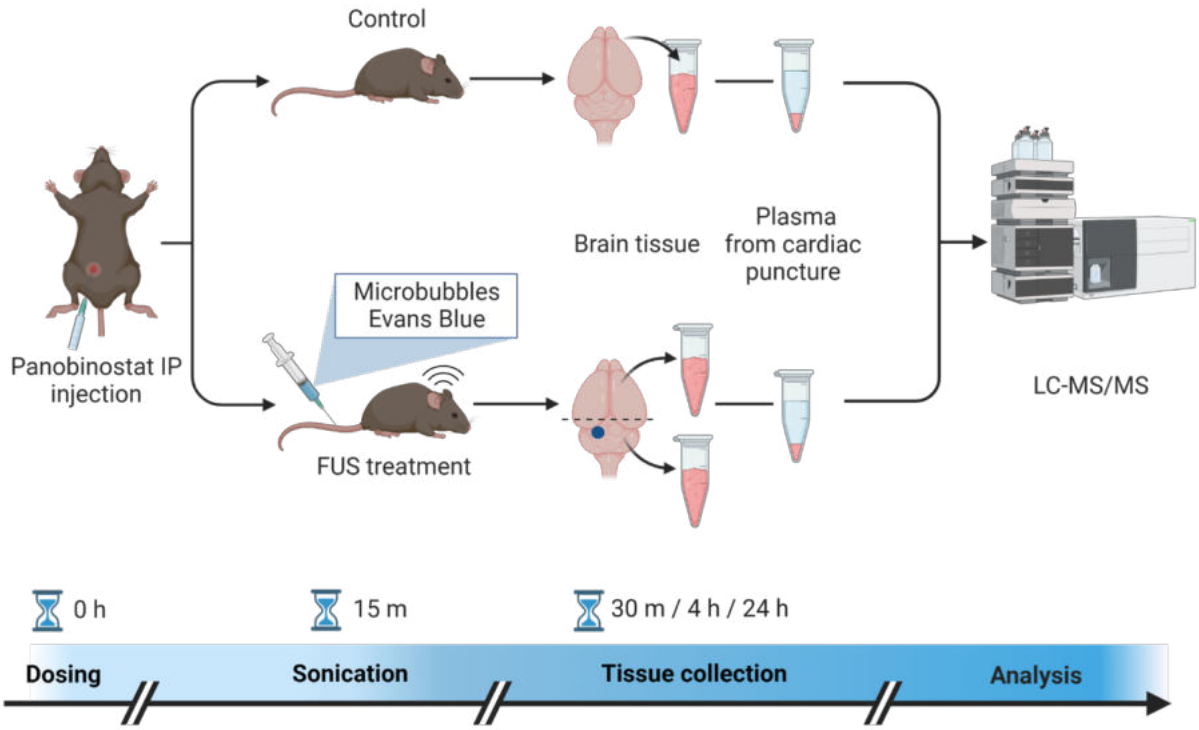

Figure 5.3.3 Tolerability and assessment of panobinostat delivered across the blood-brain barrier via focused ultrasound and microbubbles in non-tumour bearing mice. *Mice were administered 10 mg/kg panobinostat by intraperitoneal injection and were exposed to drug with or without focused ultrasound (FUS). Mice in the FUS treatment group received an intravenous injection SonoVue® microbubbles and Evans Blue (1%) to assess blood-brain barrier disruption. Plasma and brain samples were taken 30 min, 4 h and 24 h after injection (control group) or after sonication (FUS treatment group). Brain tissue in the FUS treatment group was split into 'front' and 'back' at lambda. Panobinostat concentration in both the brain and plasma were measured by LC-MS/MS. Figure created with BioRender.com.*

5.3.5 Tolerability and assessment of panobinostat delivery

When assessing panobinostat concentration in the brain, there would be no confirmation of BBB disruption. Therefore, it would not be known if a low panobinostat concentration was

due to poor drug delivery, or to unsuccessful BBBD. To overcome this, Evans Blue dye, which does not normally cross the BBB, was used to assess BBBD when the brain was extracted from the mouse after sonication. Evans Blue (2% in phosphate buffered saline (PBS)) has been used previously in this thesis work but on those occasions, the brain tissue was collected immediately. Here, the mice were recovered from the procedure for up to 24 h, and so toxicity from the dye had to be avoided. Published literature has reported that Evans Blue at 1% dilution is not toxic and was therefore used for these studies (Hamer et al., 2002).

Non-tumour bearing C57BL/6J mice were prepared for sonication (**§2.2)** and 10 mg/kg panobinostat was administered via IP injection, and then were exposed either to drug and FUS treatment, or to drug only (n=3 and n=1 vehicle control at each time point for each group). Those mice that received FUS treatment followed the targeting and sonication protocol described in **§2.4**. Only the FUS group received 100 μL SonoVue® microbubbles (Bracco) and 100 μL Evans Blue (1% w/v) via a tail vein cannula.

The pharmacokinetic study revealed that C_{max} of panobinostat in the plasma was achieved between 15- 30 min. Therefore, the target was to sonicate mice 15 min after IP injection with panobinostat, but this ranged from 15-25 min due to the difficulty of inserting a tail vein cannula.

Sonication started at the same time as microbubble injection and mice in the FUS group were exposed to ultrasound (Centre frequency: 1 MHz, peak-negative pressure: 0.4 MPa, pulse length: 5 cycles, pulse repetition frequency: 1.25 kHz, burst length: 38 pulses, burst repetition frequency: 0.5 Hz, number of bursts: 125, total time: 250s, shown in **table 2.2.1**). All mice were monitored as they recovered from the procedure on a heat mat. Plasma and brain tissue were collected as described in **§5.3.4** at 30 min, 4 h and 24 h post-treatment. The treatment time was measured either from the IP injection (in the control group) or from the start of the sonication (FUS treatment group). The brains from mice in the FUS treatment group were divided into 'front' and 'back' at approximately lambda using a razor blade and brain matrix. Plasma and brain tissue from three untreated mice were used as blank tissue for LC-MS/MS calibration (**figure 5.3.3**).

The drug delivery study described above was repeated with a revised protocol (**figure 5.3.4**). All mice (n=3 and n=1 vehicle control at each time point for each group) were placed

on the stereotactic frame and 100 µL SonoVue® microbubbles and 100 µL Evans Blue (1% w/v) were injected sequentially via a tail vein cannula. Mice in the control group remained on the frame for 250 s (the duration of the sonication). Plasma and brain tissue were collected as described in **§5.3.4,** 1 h, 2 h and 4 h post-treatment, measured from IP injection in both groups. The mice in this study were perfused transcardially with heparin (0.05 mg/ml w/v in PBS) before the brain was extracted. All brains, including the drug only group, were divided

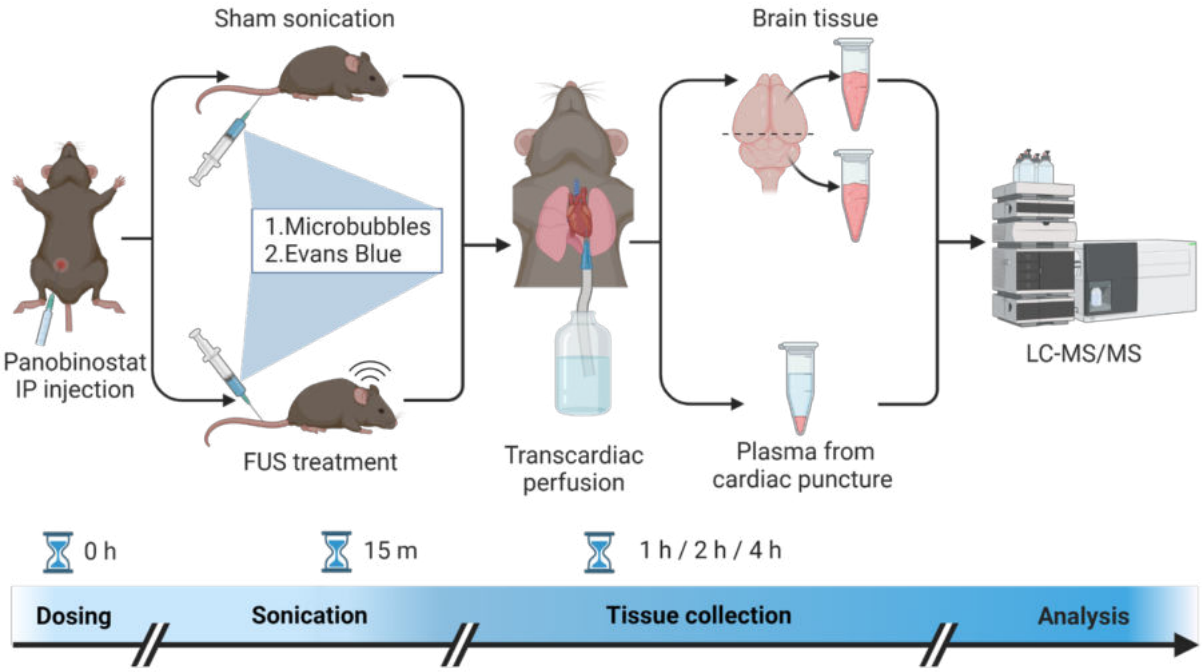

Figure 5.3.4 Tolerability and assessment of panobinostat delivered across the blood-brain barrier via focused ultrasound and microbubbles in non-tumour bearing mice: revised protocol. *In this revised protocol, all mice received an intravenous injection of SonoVue® microbubbles and Evans Blue (1%) to assess blood-brain barrier disruption. Plasma and brain samples were taken 1 h, 2 h & 4 h after injection in both groups. Mice were perfused transcardially with 0.05 mg/ml heparin in PBS then brain tissue split into 'front' and 'back' at lambda. Panobinostat concentration was measured using LC-MS/MS. Figure created with BioRender.com.*

into 'front' and 'back' at approximately lambda using a razor blade and brain matrix.

5.3.6 Tumour model selection

Mouse models are essential for evaluating the potential of new therapies, such as the use of FUS and microbubbles for drug delivery. There are several types of mouse model, each with its strengths and limitations. The mouse model selected must be relevant to the aims of the specific study. Here, the tumour growth needed to be monitorable, tumour margins needed to be within the constraints of the FUS focal volume, and tumour engraftment and growth rate in line needed to be within the time constraints of the thesis work. Lastly, since there is evidence that FUS and microbubble exposure have immunomodulatory effects, an immunocompetent model was desirable. As a result, the mouse-derived cell line (OB-3) examined in the *in vitro* cytotoxicity study, was chosen, and implanted in C57BL/6J mice (**§5.3.1**). This tumour model could be monitored using MRI, with a clear tumour mass visible lying within the ultrasound focal volume and had a reasonable growth time (within 5 months).

5.3.7 Tumour inoculation

The OB-3 (nestin-Tv-a/p53fl/fl, RCAS-ACVR1R206H + RCAS-H3.1K27M) murine cell line was injected intracranially into 28 C57BL/6J mice (**figure 5.3.5**). Mice were anaesthetised with 1.5-2.0% vaporised isoflurane (Zoetis, UK) carried in oxygen (2 L/min) and administered using an anaesthesia vaporizer (Harvard Apparatus, UK). The analgesic, buprenorphine 0.03 mg/kg (Vetergesic®, Ceva animal health inc., Ontario, Canada), was injected subcutaneously. Fur on the mouse head was removed with depilatory cream and topical analgesia (EMLA cream 5%) applied to the incision site. Viscotears (Bausch + Lomb, Ontario, Canada) were used to protect the eyes and iodinated povidone (10% w/w; Ecolab, Minnesota, USA) was used to disinfect the skin. An incision was made along the scalp, and cotton buds were used to clear the connective tissue from the skull and reveal the sutures. 2.5 x10^5 cells in 5 μL culture medium was injected at a rate of 2 μL / min through a drilled hole, located 1 mm left, 0.8 mm proximal of lambda and 4 mm inferior to the dura, as measured using a stereotactic frame. Surgical glue was used to close the skin, 5 mg/kg meloxicam (Metacam® injectable, Boehringer Ingelheim Vetmedica GmbH, Ingelheim, Germany) was injected subcutaneously for pain relief and mice were monitored for recovery.

24 h later, mice were given another dose of analgesia (0.03 mg/kg Vetergesic®), and the surgical site was re-glued where necessary. Mice were monitored daily for behavioural changes (altered response to handling, impairment of consciousness, circling motion, stupor, or epileptic seizure) and weighed twice weekly to monitor for continuous weight loss.

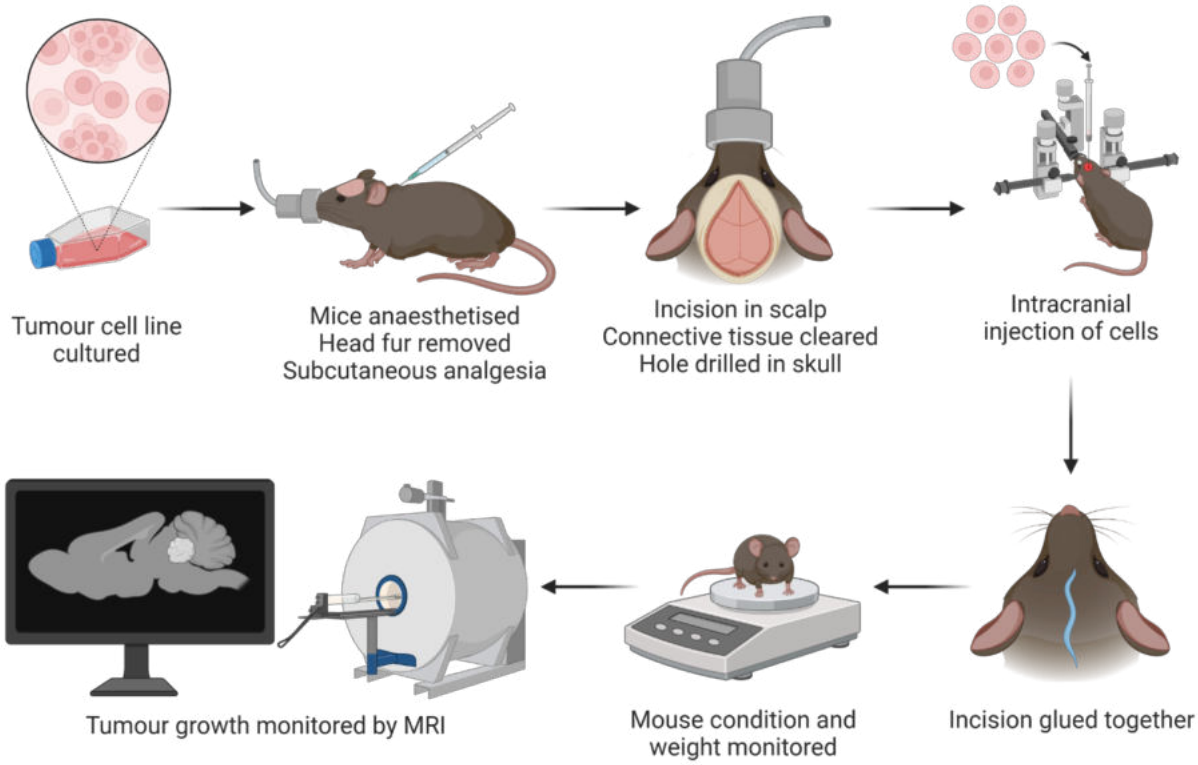

Figure 5.3.5 Tumour inoculation. *A nestin-Tv-a/p53fl/fl, RCAS-ACVR1R206H + RCAS-H3.1K27M murine cell line was cultured as spheroids and then injected intracranially into C57BL/6 mice. For the procedure, mice were anaesthetised and fur on the head removed. Mice were administered the analgesics buprenorphine (0.03 mg/kg) and meloxicam (5 mg/kg) subcutaneously and topical analgesia (ELMA cream 5%) at the incision site. An incision was made in the scalp, connective tissue cleared, and a hole drilled in the skull before intracranial injection of ~2.5 x105 cells in 5 µL culture media. Cells were injected 1 mm left, 0.8 mm proximal and 4 mm inferior of lambda using a stereotactic frame. The incision was glued, and mice recovered. Mice were monitored for behavioural and weight changes and tumour growth via MRI. Figure created with BioRender.com.*

5.3.8 Monitoring tumour growth

After tumour inoculation, mice were monitored for tumour growth using ^{1}H MRI. Mice were imaged monthly until there was indication of tumour presence, then fortnightly or sooner if appropriate. For imaging, mice were anaesthetised with 3% vaporised isoflurane (Zoetis, UK) carried in oxygen (1 L/min) and maintained at 1.5-2.0%, with vital signs being monitored using a physiological monitoring system (SA Instruments, Stony Brook, NY, USA). Body temperature was maintained using a water-heated blanket. Mice were scanned in a horizontal bore Bruker Biospec 70/20 (Ettlingen, Germany) using a 2cm x 2cm mouse brain array coil. First, the magnetic field homogeneity was optimised using a localised map shim over the whole brain. The tumours were then imaged with a rapid acquisition with refocused echoes (RARE) T2-weighted sequence [repetition time (TR) = 4500 ms, effective echo time (TEeff) = 36 ms, 1 or 2 averages, RARE factor = 8, in-plane resolution 98 µm x 98 µm, 1 mm thick slices] in the axial, coronal, and sagittal planes. T2-weighted sequences were chosen as water content appears bright in diseased tissue, making tumours easy to identify.

5.3.9 Focused ultrasound treatment tolerability in tumour-bearing mice

Before the effect of FUS and microbubbles on drug concentration could be assessed, the tolerability of the procedure by the mouse was evaluated. Tumour-bearing mice were monitored during, and after, FUS exposure for any physiological change such as breathing rate. After the procedure, mice were monitored for behavioural signs of distress. Brain slices were histologically stained to assess short-term tissue effects.

In parallel to tolerability, the efficacy of FUS-mediated BBBD in the DIPG mouse model was assessed using a fluorescently tagged model drug (dextran). Dextran, used previously in the studies reported in this thesis, does not normally cross the BBB. Therefore, it would provide information as to whether the BBB/BTB is compromised and whether FUS exposure can disrupt the BBB/BTB in this mouse model. If dextran was successfully delivered into the tumour, the spatial distribution of the model drug would provide insights into the expected drug distribution within the tumour.

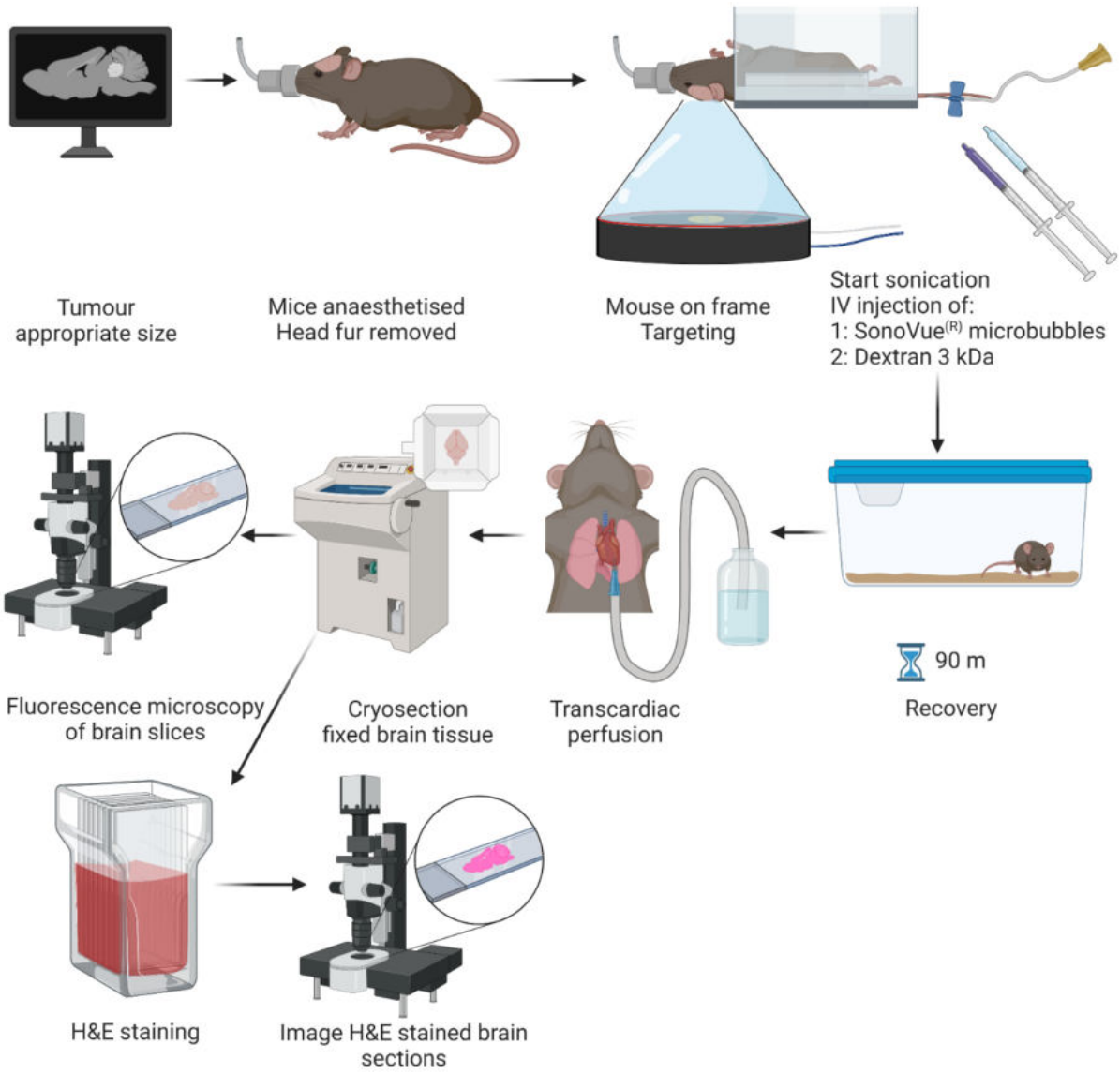

Figure 5.3.6 Tolerability and efficacy of ultrasound and microbubble mediated blood-brain barrier disruption in a DIPG tumour model. *C57BL/6 mice were implanted with a DIPG (murine) cell line and tumour growth was monitored using MRI. 40 d post tumour inoculation an intravenous injection of 100 µL SonoVue® microbubbles and 50 µL of fluorescently tagged tracer (Dextran 3kDa) was administered to two mice, which were then exposed to ultrasound. Mice recovered for 90 min then were perfused transcardially with 0.05 mg/ml heparin in PBS and 10% PFA. Brains were fixed overnight and cryosectioned. Slides were either fluorescently imaged to assess blood-brain barrier disruption or H&E stained to evaluate histological damage. Figure created with BioRender.com.*

The first four mice with appropriate (approximately 1 mm x 1.5 mm) tumours were used to establish tolerability of the procedure by assessing dextran (3kDa) extravasation (**figure 5.3.6**). Mice were exposed to ultrasound as described in **§2.2**, **§2.8-10**, and dextran was administered through an IV tail vein injection. Here, the mice were allowed to recover for 90 min after the procedure before the brain tissue was processed (**§2.11**). Brain tissue was cryosectioned into 30-µm-thick sections with every 5th and 6th brain slice being sectioned at 7 µm and 5 µm respectively. The 7-µm-thick and 5-µm- thick sections were stained with H&E to assess tissue histology (**§2.12**) and all sections were imaged as previously described in **§2.13**. Brain tissue was sectioned in two thicknesses since obtaining thin cryosections is difficult and so the chance of obtaining useful brain slices was maximised.

5.3.10 Panobinostat delivery in tumour-bearing mice

When tumours had reached approximately 1 mm x 1.5 mm, the mice were assigned alternately to the FUS treatment (n=7) and control (n=4) groups (**figure 5.3.7**). The protocol described in §**5.3.6** was followed, with all blood and plasma samples taken 2 h post sonication. Plasma and brain tissue from three untreated tumour-bearing mice were used as blanks for LC-MS/MS calibration.

5.3.11 Statistical analysis

All data was analysed using GraphPad Prism v9.5.1. Mean and standard deviation of panobinostat concentration in the plasma and brain tissue were plotted. Analysis of variance (ANOVA) test was performed to examine the difference between the groups at each time point within and between the non-tumour and tumour-bearing mice groups. A *post-hoc* Tukey's multiple comparison test was performed on any significant interaction. A simple linear regression was used to assess the correlation between: panobinostat concentration in the front and back of the brain; panobinostat concentration in the plasma and brain tissue; and brain mass and panobinostat concentration in the mouse model.

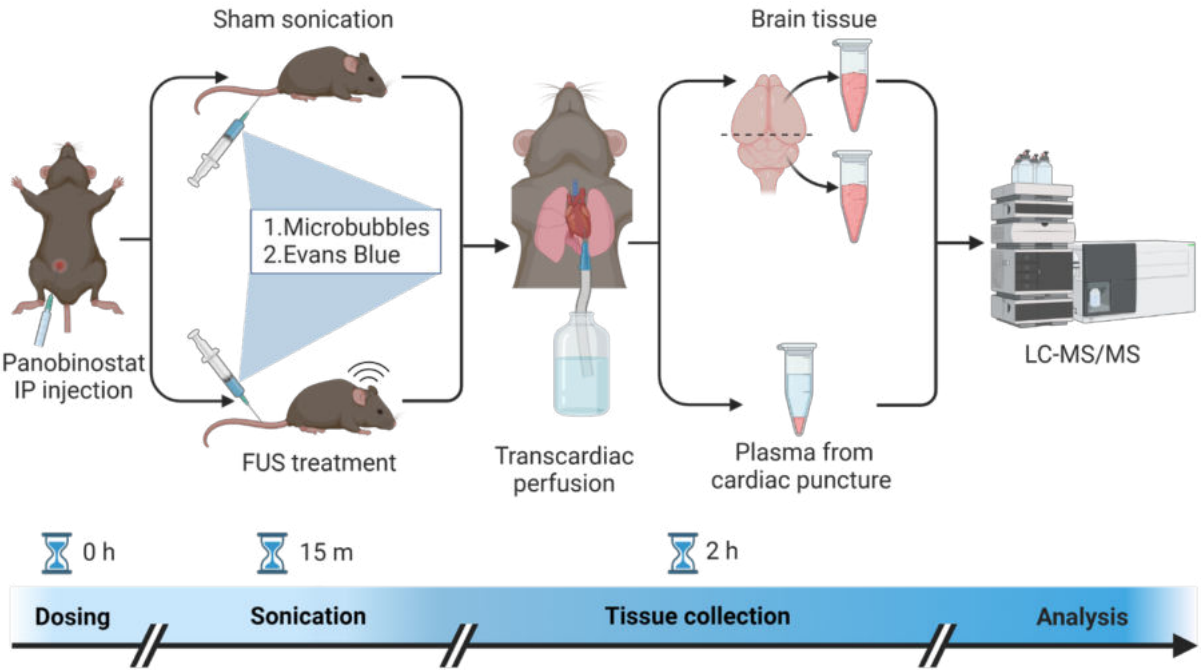

Figure 5.3.7 Assessment of panobinostat delivery across the blood-brain barrier using focused ultrasound and microbubbles in a DIPG mouse model. *C57BL/6 mice were implanted with a DIPG (murine) cell line and tumour growth was monitored using MRI. When tumours reached an appropriate size, 10 mg/kg panobinostat was administered via intraperitoneal injection and mice received either focused ultrasound (FUS) treatment or sham sonication. All mice received an intravenous injection of 100 µL SonoVue® microbubbles and 50 µL Evans Blue (1%) to assess blood-brain barrier disruption. Plasma and brain samples were taken 2 h after injection. Blood samples were obtained via cardiac puncture and spun down at 13,000 rpm for two min. Mice were perfused transcardially with 0.05 mg/ml heparin in PBS then brain tissue divided into 'front' and 'back' at lambda. Plasma and brain tissue were snap frozen and stored at -80°C before panobinostat concentration was measured via LC-MS/MS. Figure created with BioRender.com.*

5.4 Results

The work described in this chapter aimed to investigate the use of FUS and microbubbles for improving drug delivery to the brain in, first, non-tumour bearing mice, then a DIPG mouse model.

5.4.1 *In vitro* efficacy of panobinostat

Before assessing drug delivery, *in vitro* cytotoxicity of LBH-589 (panobinostat) was evaluated against three patient-derived (BIOMEDE-169, BIOMEDE-184, HSJD-DIPG-007) and one murine (OB-3) cell lines (**figure 5.4.1**). The GI_{50} was similar between cell lines, ranging from 11.07 – 23.71 nM (**table 5.4.1**). The murine (OB-3) cell line, which was selected for *in vivo* experiments, had the second lowest GI_{50}.

Table 5.3 The GI_{50} of LBH-589 (panobinostat) in four diffuse intrinsic pontine glioma (DIPG) cell lines. *Data are mean ± standard deviation.*

Cell line	GI_{50} (nM)
BIOMEDE-169	18.53 ± 3.14
HSJD-DIPG-007	11.07 ± 3.71
BIOMEDE-184	23.71 ± 10.06
OB-3	15.86 ± 0.51

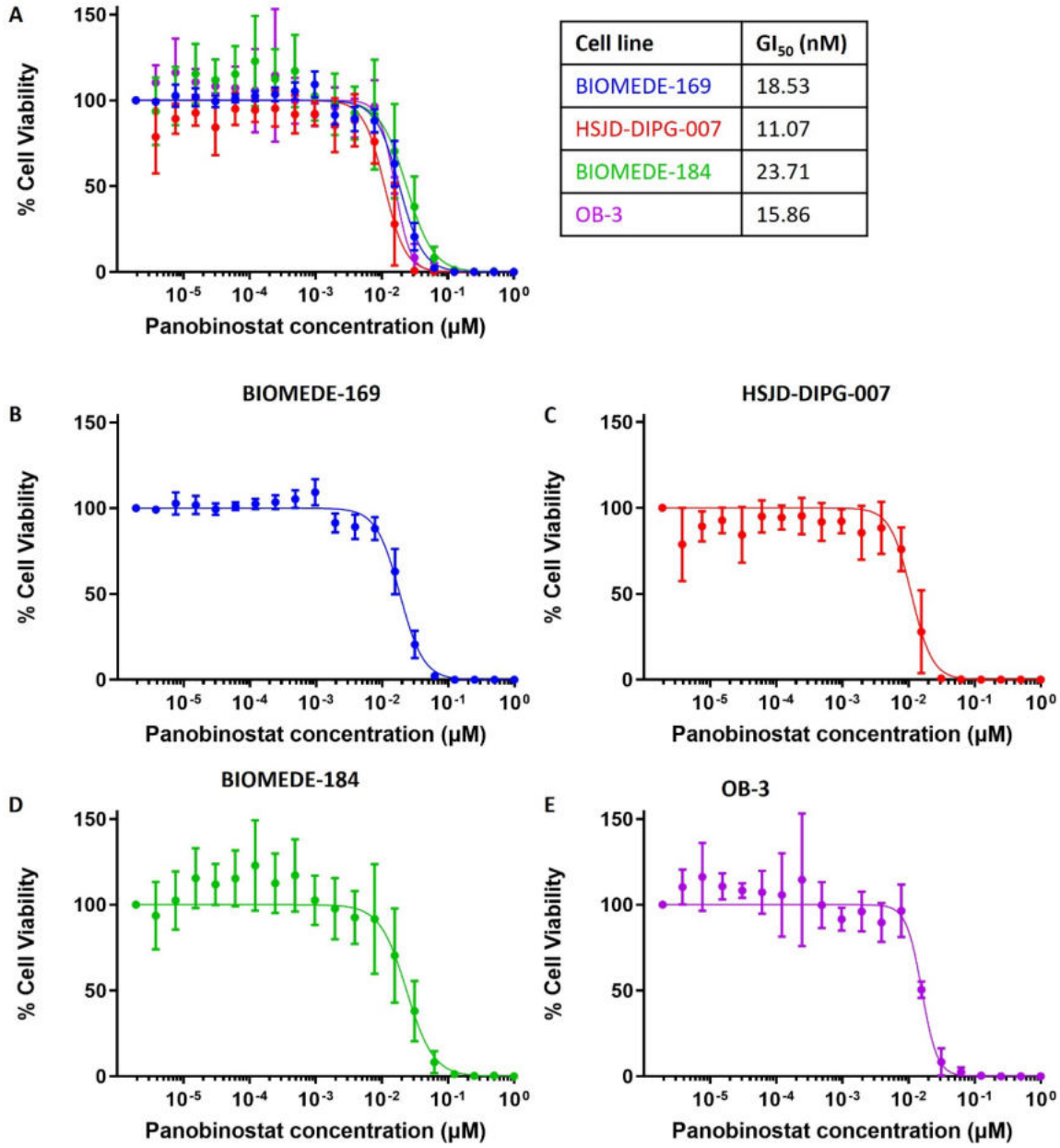

Cell line	GI_{50} (nM)
BIOMEDE-169	18.53
HSJD-DIPG-007	11.07
BIOMEDE-184	23.71
OB-3	15.86

Figure 5.4.1 In vitro cytotoxicity of panobinostat. *The cytotoxicity of panobinostat (LBH-589) assessed in four DIPG cell lines (A); three human (B-D) and one murine (E). Cells were incubated with serial dilutions of panobinostat for eight days then cell viability assessed using the CellTitre-Glo® assay. The resultant GI50 is shown in A. Data points are mean ± standard deviation.*

5.4.2 Pharmacokinetic study of panobinostat

A pharmacokinetic study was used to determine the C_{max} of panobinostat in the plasma after IP injection. A secondary aim was to determine whether panobinostat crosses the BBB, and to what extent. In the first pharmacokinetic study, blood and brain samples were taken 1 h, 2 h, 6 h and 24 h after drug injection. There was a steep decrease in plasma concentration (1 h: 17928 ± 7793 nM; 2 h: 587.7 ± 190 nM; 6 h: 50 ± 9 nM; and 24 h: 7 ± 3 nM), which followed a trend of exponential decay (**figure 5.4.2**). As a result, a second pharmacokinetic study was performed with the earlier time points of 5 min, 15 min and 1 h. These results showed an increase in panobinostat plasma concentration from 5 min (5826 ± 6305 nM) to 15 min (13642 ± 15808 nM), before subsequently decreasing, with the concentration at 1 h (1134 ± 1502 nM) falling below the concentration at 5 min.

Results from both pharmacokinetic studies show that panobinostat entered the brain and followed a similar trend to the plasma concentration. The peak brain concentration appeared 15 min post-injection (47 ± 20 nM), followed by a rapid decrease to a concentration below the detectable threshold (< 5 nM) at 24 h (**figure 5.4.2**).

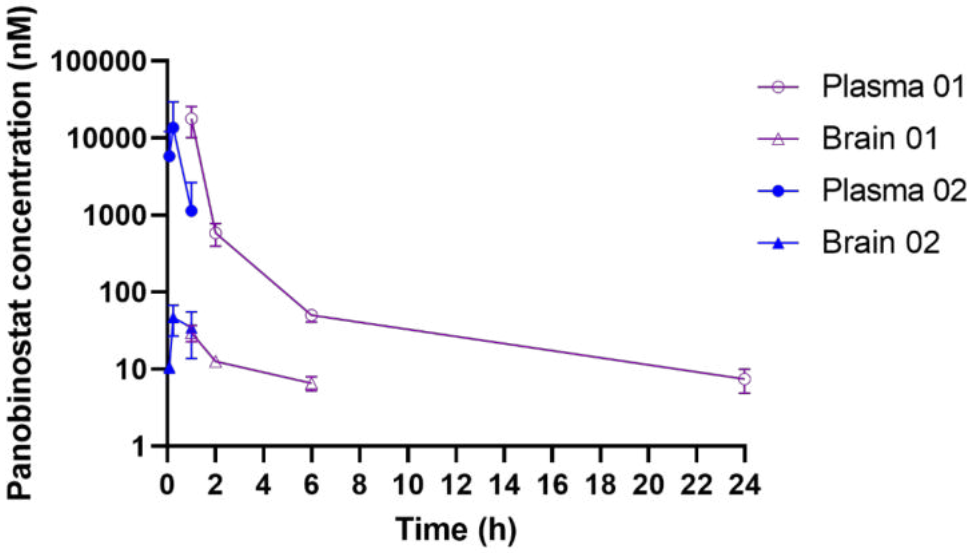

Figure 5.4.2 Pharmacokinetic study of panobinostat (LBH-589) in C57BL/J mice. *Concentration of panobinostat measured by LC-MS/MS after 10 mg/kg of panobinostat administered intraperitoneally with plasma and brain samples measured at 1 h, 2 h, 4 h & 24 h in the first study (purple) and at 5 min, 15 min and 1 h in the second study (blue), post injection. Brain concentration at 24 h was below the detectable threshold and therefore absent. Data points are mean ± standard deviation.*

The 1 h time point was included in both pharmacokinetic studies to assess the repeatability of the measurements. The concentrations of panobinostat in the brain at 1 h were very similar (30 ± 7 nM in the first study, 34 ± 20 nM in the second study), but the 1 h plasma concentration was higher in the first pharmacokinetic study ($1.8 \times 10^4 \pm 7.8 \times 10^4$ nM) than the second ($1.1 \times 10^3 \pm 1.5 \times 10^3$ nM) (**figure 5.4.2**).

5.4.3 Tolerability and efficacy of panobinostat delivered across the blood-brain barrier using focused ultrasound in non-tumour bearing mice

Before examining drug delivery in tumour-bearing mice, the tolerability and efficacy of the procedure was assessed in non-tumour-bearing (NTB) mice. The procedure was well-tolerated in all mice and Evans Blue extravasation in the targeted region (left pons) revealed successful BBB disruption in all FUS-exposed mice (**figure 5.4.3A-C**). The delivery distribution of Evans Blue was the same at all time points, although there were differences in the observable intensity of the dye. Visually, the most Evans Blue was present at 4 h, compared to 30 min and 24 h. A visibly higher concentration of Evans Blue was present at 30 min than at 24 h, where the dye was faint but still present.

Following FUS exposure, mice had their brain tissue divided into 'front' (FUS-F) and 'back' (FUS-B; containing the targeted pons region) to assess whether the drug (panobinostat) remained in the targeted region after sonication. In the FUS-B group, the LC-MS/MS data for panobinostat concentration reflected trends observed with Evans Blue, increasing from 30 min (43.9 ± 30.8 nM) to 4 h (52.5 ± 28.5 nM; **figure 5.4.3D**). The panobinostat concentration in the FUS-F and FUS-B groups at 24 h was below the detectable threshold.

In the FUS-F and control group (drug only, no ultrasound), the panobinostat concentration decreased between 30 min (31.6 ± 19.1 nM and 129 ± 43.8 nM) and 4 h (15.4 ± 4.9 nM and 37.1 ± 9.2 nM). In the control group, the panobinostat concentration decreased further at 24 h (12.4 nM; **figure 5.4.3D**).

At 30 min, the panobinostat brain concentration in the control group was higher than both the FUS-F and FUS-B groups. An unpaired Student's *t*-test revealed this difference to be significant between the control and FUS-F group (p=0.04).

At 30 min and 4 h, the panobinostat brain concentration was higher in the FUS-B than the FUS-F group. This difference was significant at 4 h (p=0.05). The panobinostat

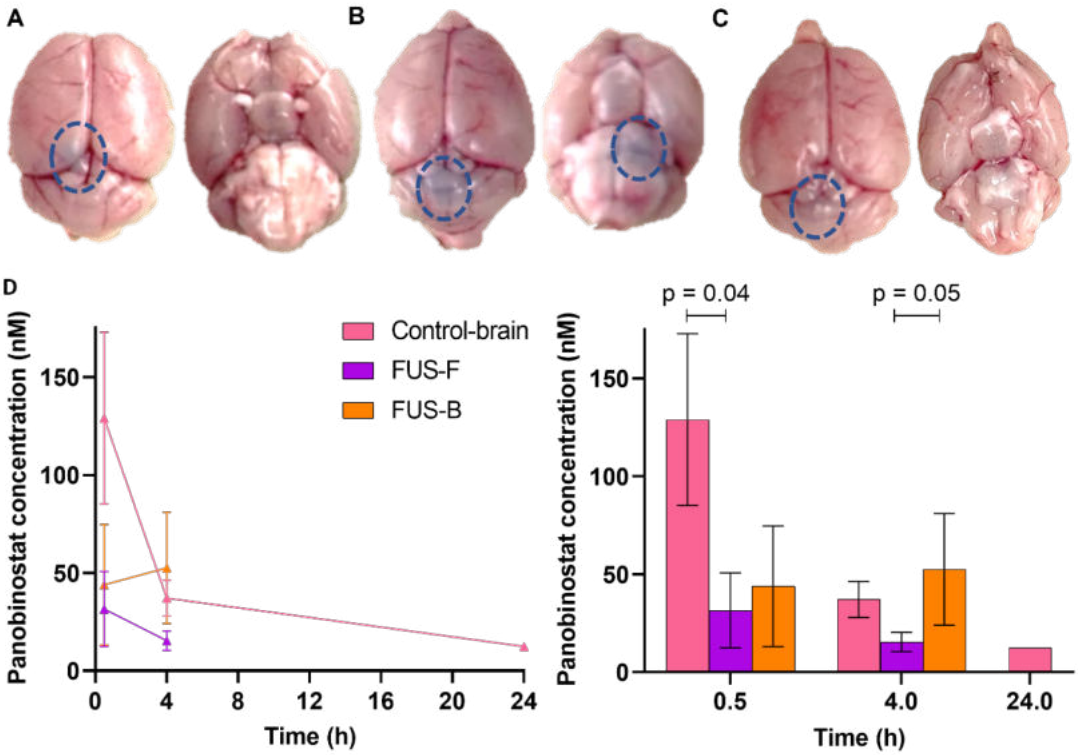

Figure 5.4.3 Tolerability and efficacy of panobinostat delivered across the blood-brain barrier via focused ultrasound in non-tumour bearing mice: study one. *A-C: Evans Blue (1%) was used to confirm blood-brain barrier disruption in the FUS treatment group with examples shown at each time point and Evans Blue extravasation indicated by the blue dashed oval; (A) 30 min, (B) 4 h & (C) 24 h. (D) Panobinostat concentration measured in the brain using LC-MS/MS after dosing of 10 mg/kg of panobinostat only (control) or panobinostat and ultrasound (FUS; n=3 at each time point). Brains exposed to ultrasound were separated into 'front' (FUS-F) and 'back' (FUS-B) containing the targeted region. Data points are mean ± standard deviation.*

concentration in the FUS-B group was also higher than the control group at 4 h, although this difference was not statistically significant (**figure 5.4.3D**).

The panobinostat concentration in the plasma of both FUS and control groups (drug, no ultrasound) followed a similar trend of rapid decline (**figure 5.4.4**). The plasma levels in the control group ($1.0 \times 10^4 \pm 1.6 \times 10^4$ nM) were higher at 30 min than in the FUS group (1.1×10^3

± 8.0 x10^2 nM). However, at 4 h (68.0 ± 29.7 nM and 78.9 ± 16.7 nM) and 24 h (4.7 ± 2.2 nM and 4.8 ± 1.5 nM) the plasma levels of both groups were similar. There was no significant

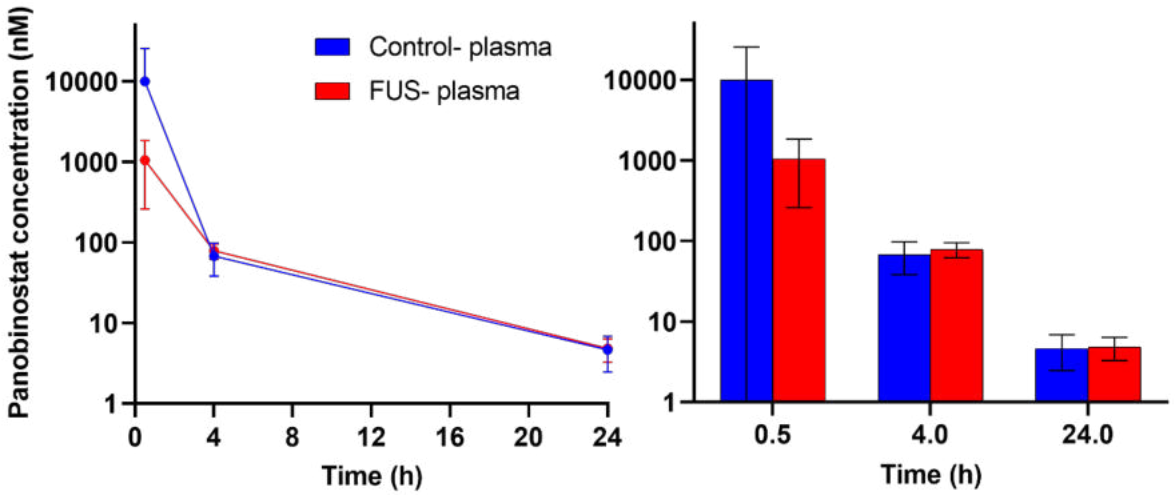

Figure 5.4.4 Tolerability and efficacy of panobinostat delivered across the blood-brain barrier via focused ultrasound in non-tumour bearing mice: study one. *Plasma concentration of mice 0.5 h, 4 h and 24 h after 10 mg/kg panobinostat only (control) or with focused ultrasound (FUS) exposure. Data points are mean ± standard deviation.*

difference between the FUS treated and drug only groups (p>0.05) at any time point.

5.4.3.1 Refined protocol

The results described above indicated that the early time points were important. The protocol was therefore refined to improve the control group and the study repeated with 1 h, 2 h and 4 h timepoints after drug dosing. No Evans blue delivery was seen in the brains of the drug-only control group, but IV injections were successful as the mouse vasculature became blue, typical of Evans Blue. As in the first study, Evans Blue extravasation was more obvious in the FUS group at later time points and was most evident at 4 h (**figure 5.4.5 A-C**).

In the FUS-B group, the drug concentration decreased between 1 h (97.7 ± 17.1 nM) and 2 h (69.7 ± 12.7 nM) and increased at 4 h (98.7 ± 45.0 nM; **figure 5.4.5D**). At 4 h, the panobinostat concentration was similar in the FUS-B group (98.7 ± 26.0 nM) and plasma (111.1 ± 20.0 nM).

In the FUS-F group, the panobinostat concentration decreased between 1 h (87.7 ± 12.2 nM) and 2 h (57.2 ± 9.5 nM), before plateauing (64.5 ± 30.1 nM at 4 h; **figure 5.4.5D**).

Similarly, to the FUS groups, the brain tissue of the control group (drug, no ultrasound) was separated into 'front' (control-F) and 'back' (control-B). The panobinostat concentration, measured by LC-MS/MS, in both the control-F and control-B decreased with time after

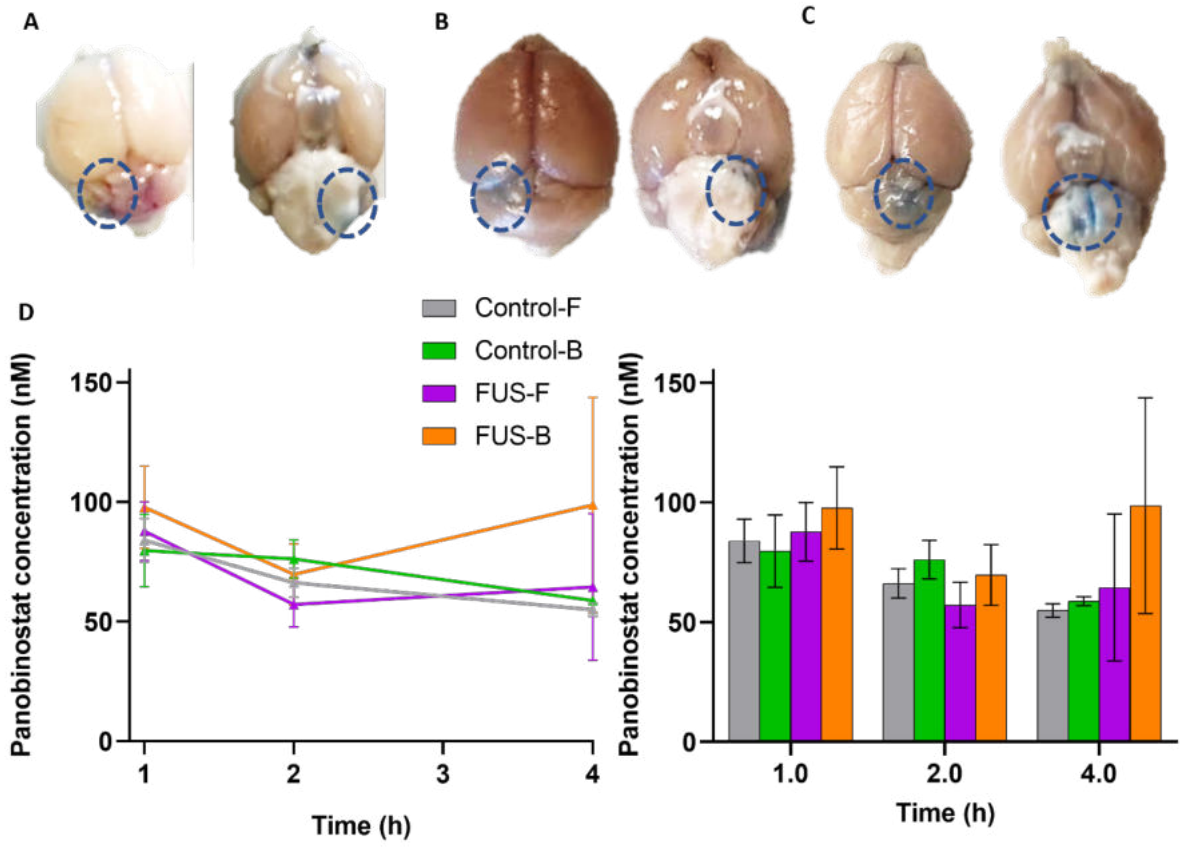

Figure 5.4.5 Tolerability and efficacy of panobinostat delivered across the blood-brain barrier via focused ultrasound in non-tumour bearing mice: study two. *Mice were administered 10 mg/kg of panobinostat intraperitoneally and either received a sham (control; microbubble injection but no exposure to ultrasound) or focused ultrasound (FUS) exposure. A-C: Examples of Evans Blue extravasation (indicated by the blue dashed oval) shown for each timepoint for the FUS treatment group; (A) 1 h, (B) 2 h & (C) 4 h. D Panobinostat concentration measured in the 'front' (-F) and 'back' (B-) of the brain using LC-MS/MS. Data points are mean ± standard deviation.*

treatment (**figure 5.4.5D**). The drug concentration in the control-F group was similar to the control-B group at all time points.

At 1 h and 4 h, the panobinostat concentration in the brain was higher in the FUS groups than in their corresponding control group. At 2 h, this trend is reversed and the drug concentration in the control group was higher than the corresponding FUS groups. At 1 h and 2 h, the panobinostat concentration in all four groups were very similar. However, at 4 h, the drug concentration in the FUS-B group was higher than in the other three groups (98.7 ± 45 nM vs. 54.9 ± 2.8 nM, 58.8 ± 1.8 nM and 64.5 ± 30.7 nM).

Two-way ANOVA and Tukey's multiple comparison test showed no significant difference between any of the time points or groups in this FUS-mediated panobinostat delivery study (p<0.05).

The LC-MS/MS results showed that panobinostat plasma concentration in the control and FUS group were similar at 1 h (642 ± 149 nM and 681 ± 158 nM) and 4 h (103 ± 14 nM and 111 ± 34 nM; **figure 5.4.6**). At 2 h, the plasma concentration was higher in the control group (197 ± 48 nM) than the FUS group (127 ± 10 nM). There was no significant difference in the

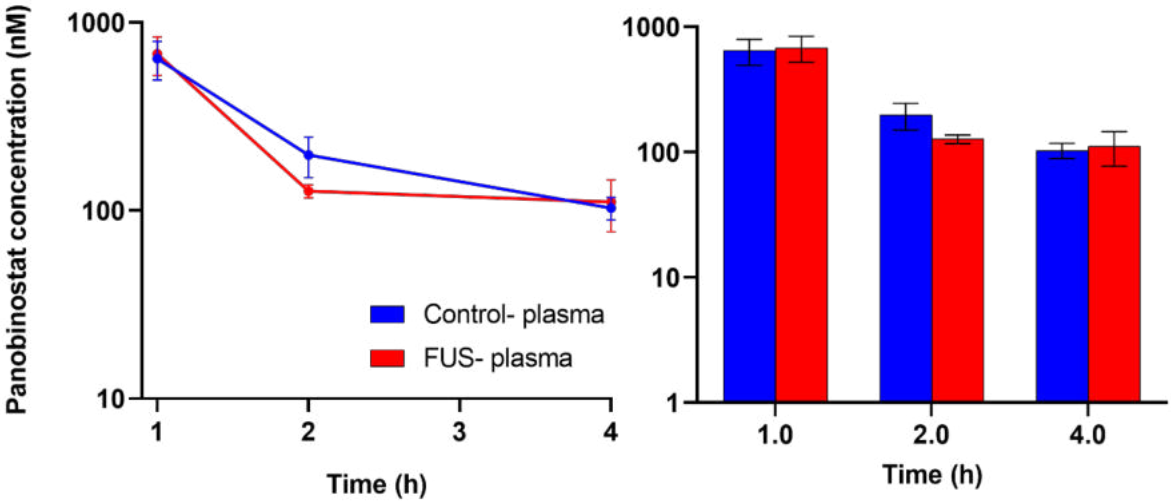

Figure 5.4.6 Tolerability and efficacy of panobinostat delivered across the blood-brain barrier via focused ultrasound in non-tumour bearing mice: study two. *Plasma concentration of mice 1 h, 2 h and 4 h after 10 mg/kg panobinostat only (control) or panobinostat with focused ultrasound (FUS) exposure. Data points are mean ± standard deviation.*

plasma concentrations of the drug-only and FUS-exposed group at any of the time points (p>0.05).

The panobinostat concentration in the brain was higher in the second study than in the first (**figure 5.4.3 & 5**). This is most evident in the FUS-treated group as the brains were split into front and back for both studies and the time point of 4 h was common to both studies and, thus, directly comparable. The drug concentration in the front and back of the brain was higher in the second study than in the first, despite the brains being perfused transcardially in the second study. The same trend was seen in the drug only groups at 4 h. The panobinostat concentration was higher in the front and back brain of the second study compared to the total brain of the first study.

Linear regression analysis showed that there was a positive correlation between the concentration of panobinostat in the front vs. the back of the brain (**figure 5.4.7A**). The control group showed a stronger correlation compared to the FUS group and both were statistically significant (r^2 = 0.79, p = 0.01 vs. r^2 = 0.67, p = 0.005).

Linear regression analysis was performed to determine whether there was a relationship between brain and plasma concentrations. The FUS groups across both drug delivery studies showed no significant correlation between plasma and brain panobinostat concentration (p>0.05; **figure 5.4.7B**). There was strong positive correlation between brain and plasma panobinostat concentration in the control group of the first study (r^2=0.9808, p=0.0032) and in the control-F group of the second study (r^2=0.7636, p=0.0274; **figure 5.4.7B**). There was weak correlation in the control-B group (r^2=0.2745, p=0.5105).

It is hypothesised that in the FUS group, the concentration of panobinostat in the brain would be higher in the back vs. the front, as the back of the brain encompasses the area of tissue over which the FUS beam is targeted. A pairwise comparison showed that in the first study, the drug concentration in the FUS-B of the brain was lower than the FUS-F in two of seven samples; both samples were taken at the 30 min time point (**figure 5.4.7C**). In the second drug delivery study, panobinostat concentration is higher in FUS-B than the corresponding FUS-F, but similar between the control-F and control-B groups.

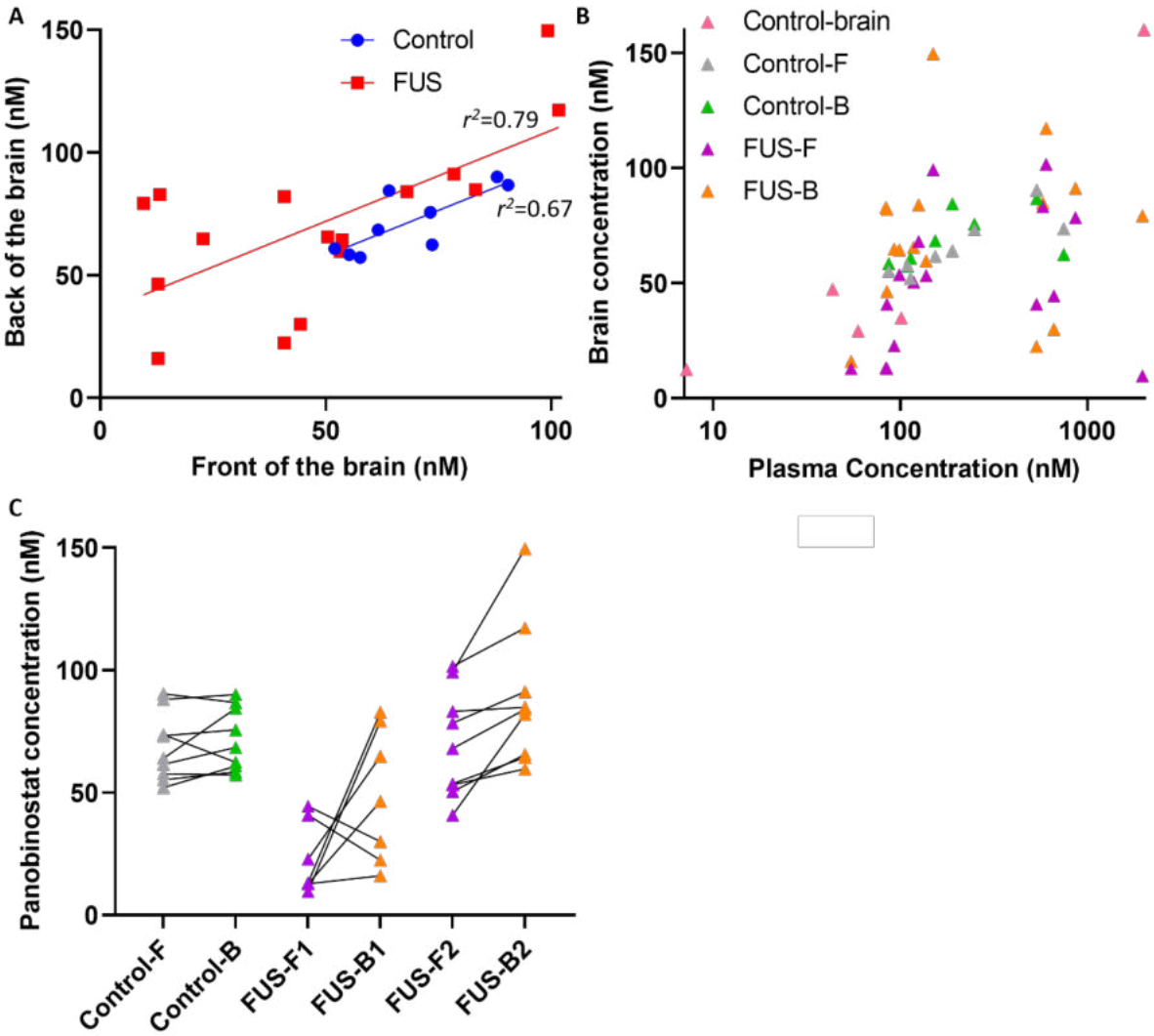

Figure 5.4.7 Tolerability of panobinostat delivered across the blood-brain barrier using focused ultrasound in non-tumour bearing mice. *Mice were administered 10 mg/kg of panobinostat intraperitoneally and either received a sham ultrasound (control) or focused ultrasound (FUS) treatment. (A) Correlation between panobinostat concentration in the front and the back of the brain was significant in both the FUS treated group (r^2=0.79, p=0.01) and control group (r^2=0.67, p=0.005). (B) There was no correlation between panobinostat concentration in the brain and plasma in the FUS group (p>0.05). In the control group of the first drug delivery study, there was strong positive correlation between brain and plasma panobinostat concentration (r^2=0.98, p=0.003). In the second drug delivery study there was strong positive correlation between brain and plasma panobinostat concentration in the front (control-F) of the brain (r^2=0.76, p=0.03) and weak correlation in the back (control-B) of the brain (r^2=0.27, p=0.51). (C) A pairwise comparison showing the difference between panobinostat concentration in the front (-F) and back (-B) of the brain in the control group of the second study and FUS groups of both studies.*

5.4.4 Tolerability, safety, and efficacy of blood-brain barrier disruption in a DIPG mouse model

Once panobinostat delivery in a non-tumour bearing mouse had been established, drug delivery to a DIPG mouse model was assessed. The mouse model chosen was a murine cell line (Nestin-Tv-a/p53fl/fl, RCAS-ACVR1R206H + RCAS-H3.1K27M) implanted into 28 C57BL/6J mice. The median time from tumour inoculation to sonication or euthanasia was 113 d with a range of 40-162 d. Of those mice suitable for experimentation in either the dextran tolerability or drug delivery study, the median was 132 d with the same range of 40-162 d. There was some variation in the tumour growth location, but most tumours grew above the pons (in front of the cerebellum (**figure 5.4.8A**). Three mice grew tumours in the front of the brain. These tumours grew rapidly and appeared as large, necrotic tumours, indicated by dark regions on the MR images (**figure 5.4.8B**). These tumours appeared at 49 d, 56 d and 78 d post implantation.

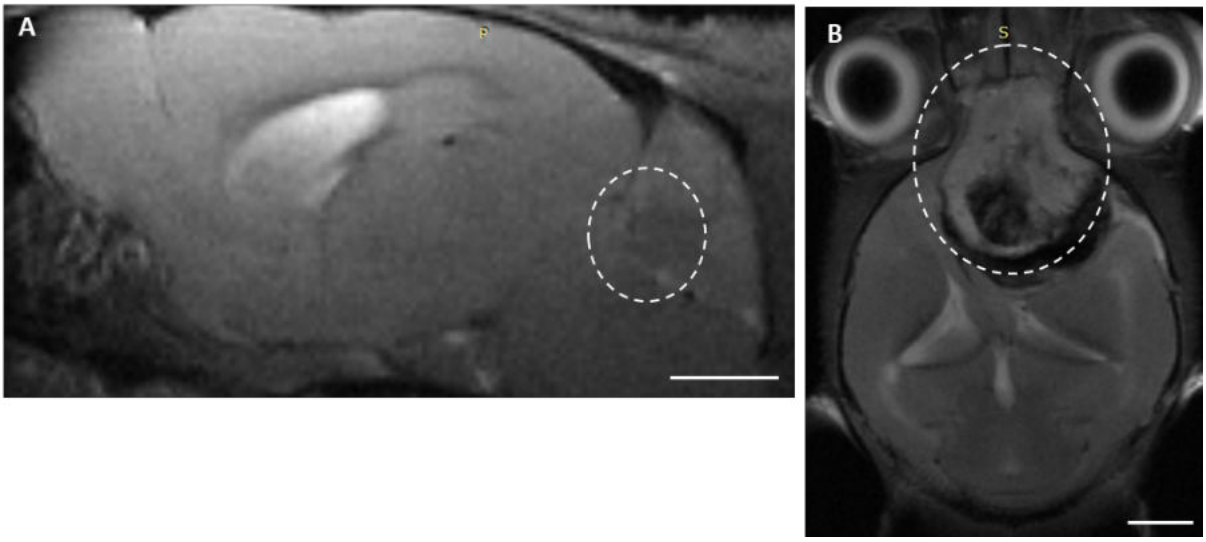

Figure 5.4.8 T2-weighted MRI of tumour growth of a DIPG cell line. *C57BL/6J mice were implanted with a murine DIPG cell line in the pons region. (A) Most tumours grew in the expected region, but four mice showed tumour growth in the front of the brain, an example of which is shown in (B). Tumours are indicated by the dashed oval. Scale bars are 2 mm.*

Firstly, it was assessed whether the tumour-bearing mice could tolerate the procedure and whether FUS could increase the permeability of the BBB in the tumour. To achieve this, two mice were exposed to FUS and microbubbles 40 d post tumour injection and the fluorescently tagged tracer (3 kDa dextran) was used to evaluate BBBD. The procedure was well-tolerated, and mice recovered as expected. Upon brain extraction, no obvious histological damage was present in either mouse (**figure 5.4.9A**). The tumour mass could be clearly seen by MRI and during cryosectioning (**5.4.9B&C**).

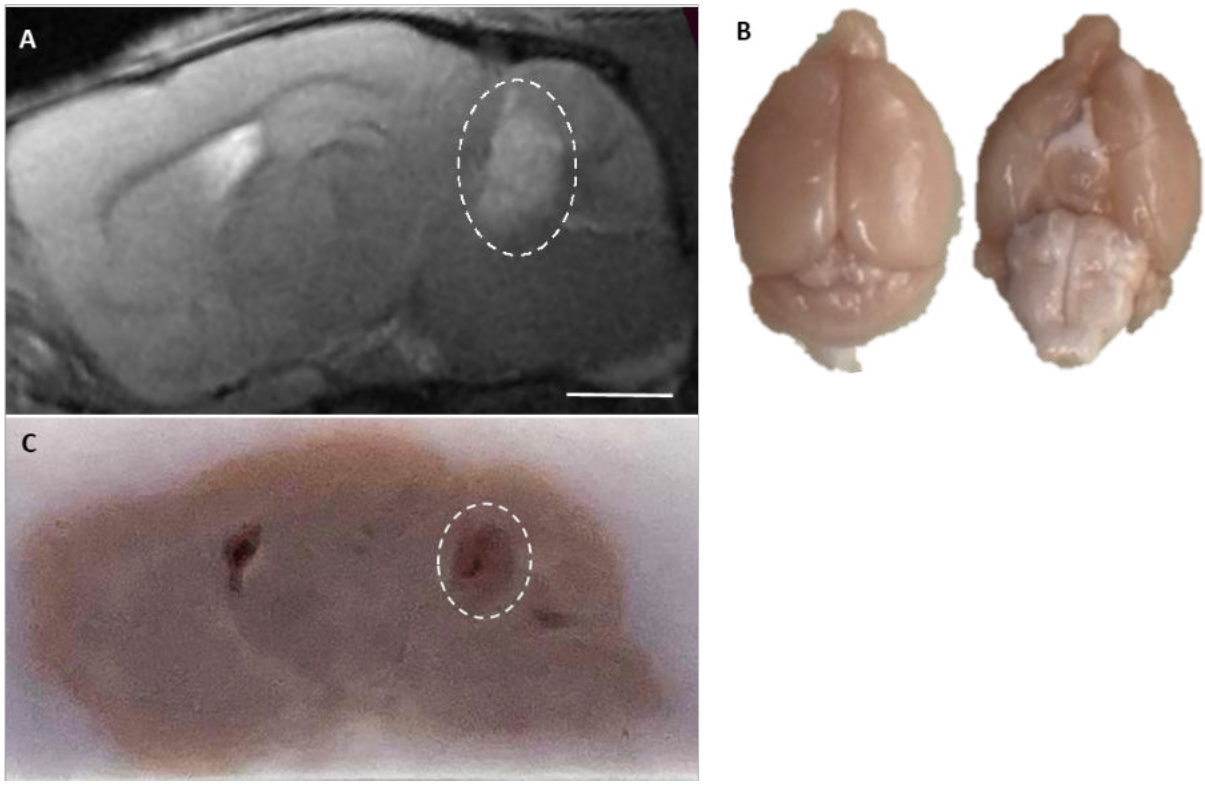

Figure 5.4.9 Tolerability of blood-brain barrier disruption in a DIPG mouse model. *A murine DIPG cell line was implanted into the pons of C57BL/6J mice and tumour growth (indicated by the dashed oval) monitored using T2-weighted MRI. (A) Tumour growth 39 d after inoculation. (B) Whole brain images after ultrasound exposure with intravenous SonoVue® microbubbles showed no gross histological damage. (C) The tumour could be seen during cryosectioning.*

Dextran delivery was seen in both mice throughout the targeted region, including the tumour (**figure 5.4.10A&B, figure 5.4.11B**). The distribution was similar to that seen in non-tumour mice- a homogenous distribution with spot-like neuronal uptake. Higher resolution images showed spot-like dextran present throughout the tumour, with this distribution also seen in non-tumour tissue (**figure 5.4.10C&D**). In the tumour, there appeared to be increased dextran uptake in the proximity of blood vessels, although no immunohistological staining for blood vessels was performed (**figure 5.4.10D**).

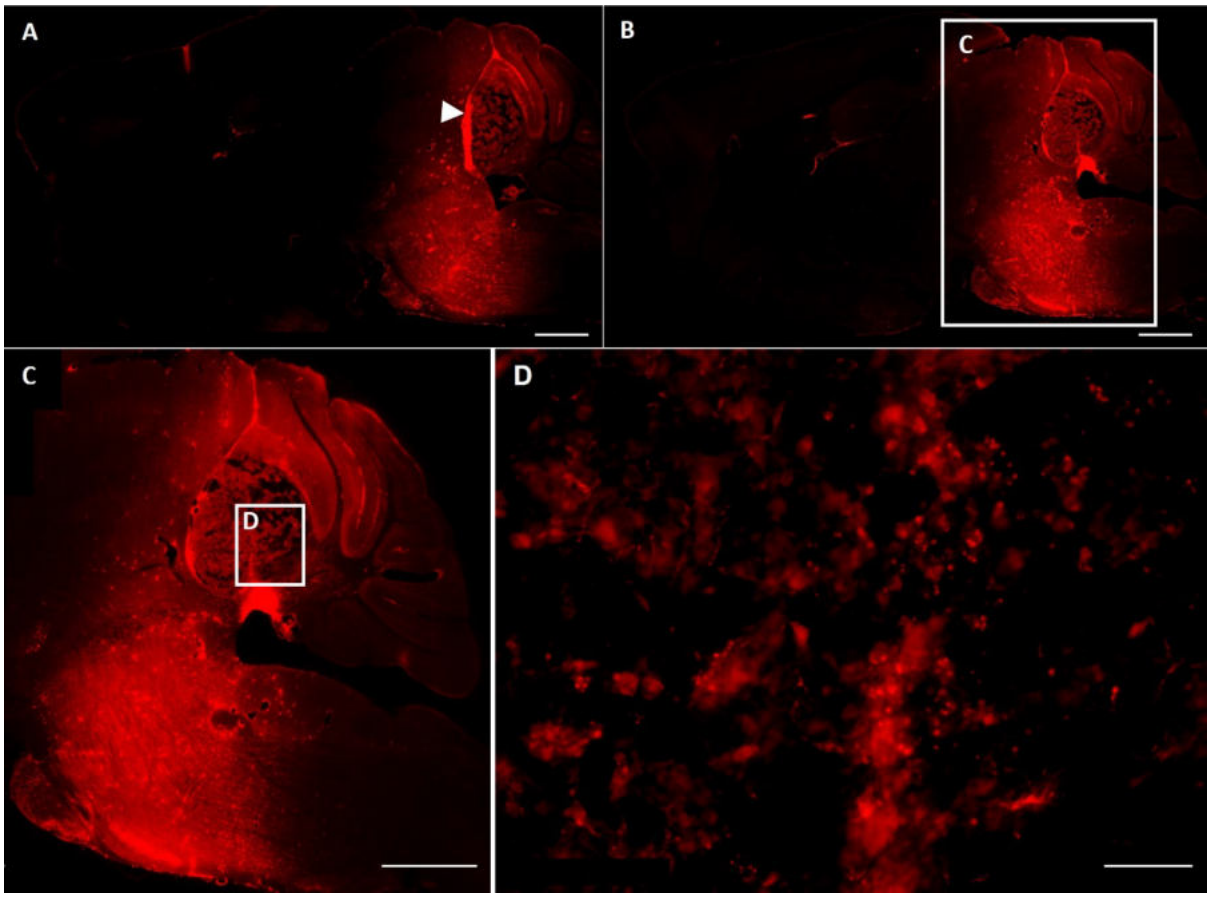

Figure 5.4.10 Blood-brain barrier disruption in a DIPG mouse model. *(A&B) Fluorescence microscopy (20 X) of sagittal brain slices (30 µm thick) showing successful blood-brain barrier disruption and fluorescently tagged dextran extravasation in a DIPG mouse model. (C) The pons and (D) tumour region (40 X). Scale bars are 1 mm (A-C) and 100 µM (D). Arrowhead indicates tissue folds.*

One mouse had a fluid-filled region, apparent on MRI, that was located within the path of the ultrasound focal region (**figure 5.4.11A**). In this mouse, the spot-like pattern was more conspicuous throughout the tumour (**figure 5.4.11B-D**). There was an intense region of dextran uptake directly below this fluid-filled region.

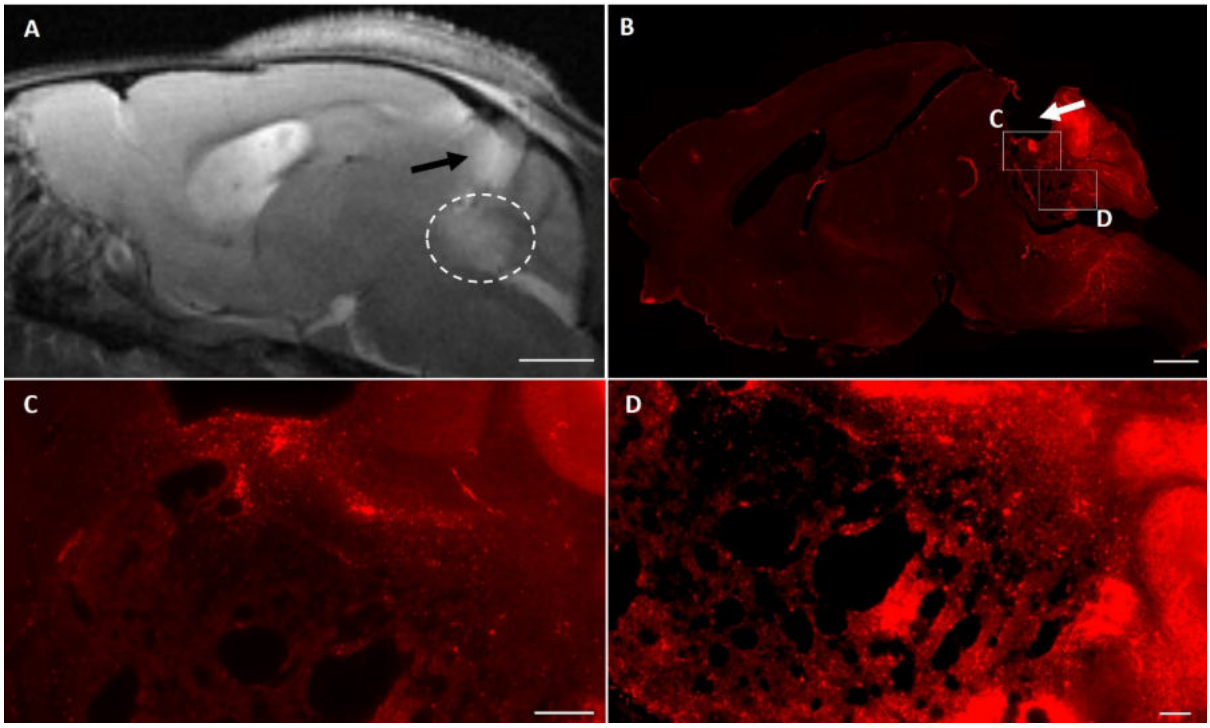

Figure 5.4.11 Blood-brain barrier disruption in a DIPG mouse model, despite a fluid-filled region. *(A) T2-weighted MRI showing tumour growth (dashed oval) and a fluid-filled region (arrow). (B) Fluorescence microscopy (20 X) of a sagittal brain slice (30 µM thick) showing successful blood-brain barrier disruption through extravasation of fluorescently tagged dextran. (C&D) Tumour regions (40 X). Scale bars are 1 mm (B) and 200 µM (C&D).*

A preliminary evaluation of safety was made by H&E staining brain sections from the mice assessed for dextran delivery, as described above. There was no observable histological damage outside the tumour region (**figure 5.4.12**). Inside the tumour, there was some erythrocyte extravasation which occasionally co-localised with dextran delivery (**figure 5.4.12B&C**). The H&E staining and dextran imaging showed regions of cysts within the tumour. This was seen as the gaps between the tissue in the H&E-stained sections and dark regions in the dextran images (**figure 5.4.12B&C**).

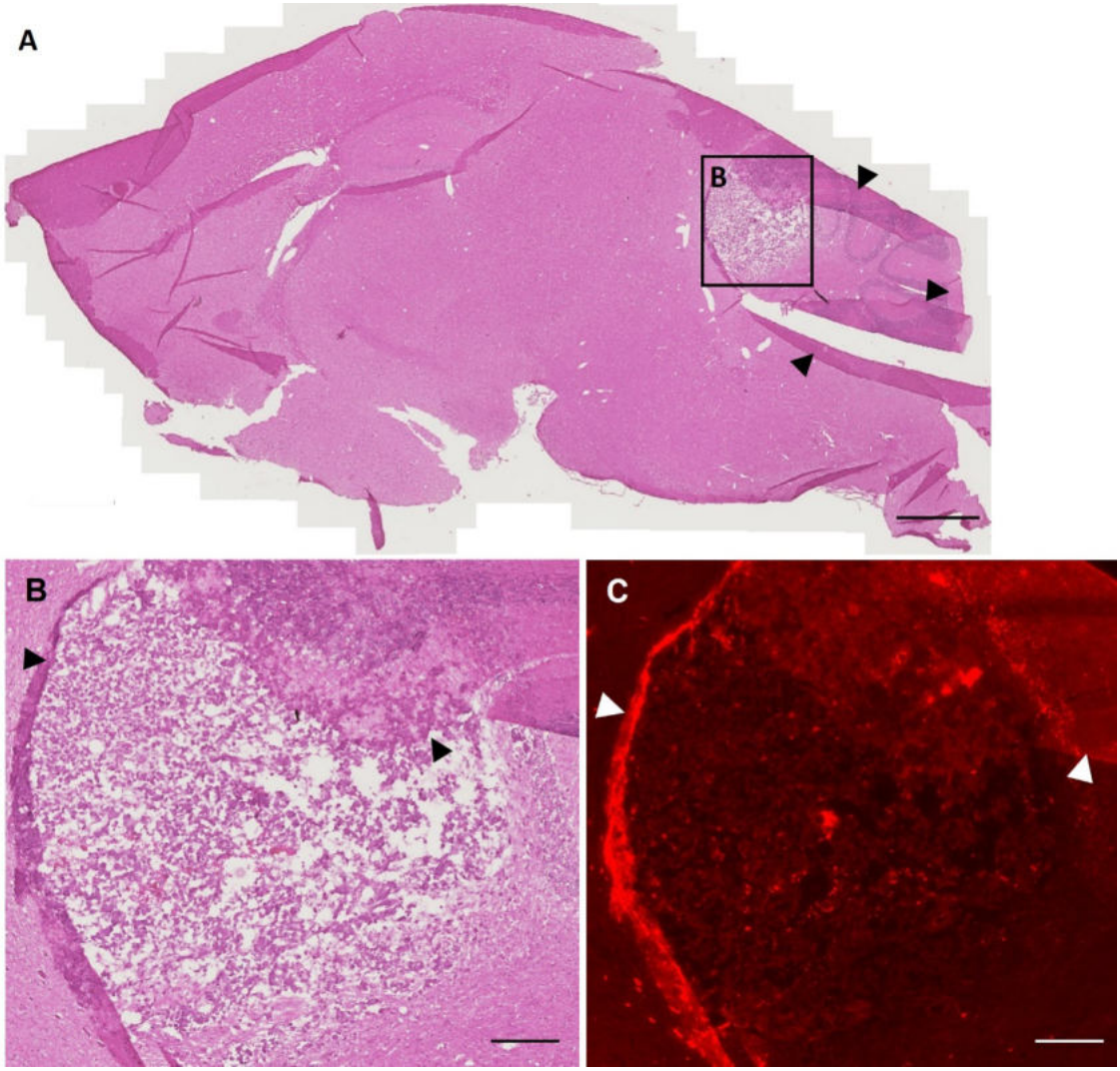

Figure 5.4.12 Tissue effects of blood-brain barrier disruption in a DIPG mouse model. *Cryosectioned brain slices were stained with H&E after focused ultrasound and microbubble exposure shown as (A) the whole sagittal brain slice and (B) tumour region. (C) Fluorescence microscopy (20 X) of dextran extravasation in the same tumour region. Scale bars are 1 mm (A) and 200 µM (B&C). Arrowheads indicate tissue folding.*

5.4.5 Delivery of panobinostat across the blood-brain barrier using focused ultrasound in a DIPG mouse model

Once it had been established that the sonication was well tolerated by the DIPG mouse model and that no obvious histological damage occurred, panobinostat delivery was assessed. Evans Blue dye was administered via tail vein cannulation in both the FUS-exposure and control groups. As the dye does not normally cross the BBB, Evans Blue in the control group enabled the assessment of BBB integrity in the tumour and of whether BBBD was successfully achieved in the treatment group. Evans Blue delivery was seen in all mice in the FUS-exposed group, throughout the tumour and surrounding targeted pons region in a

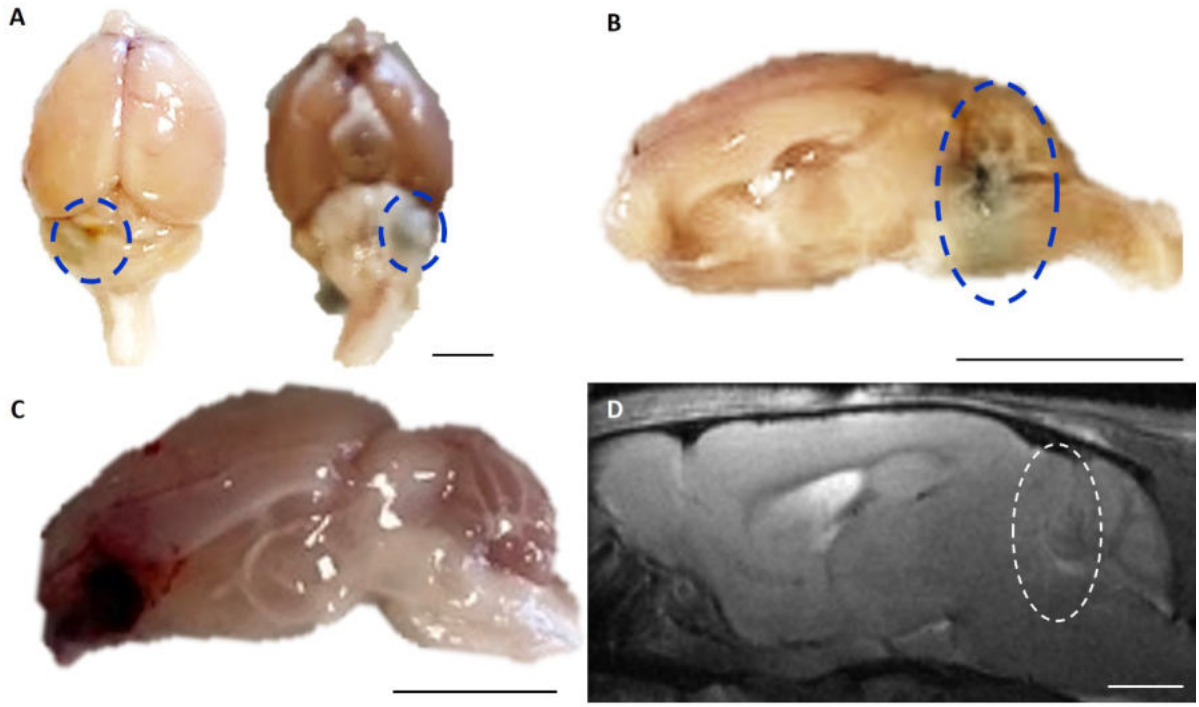

Figure 5.4.13 Ultrasound-mediated panobinostat delivery in a DIPG tumour model. C57BL/6J mice were implanted with a murine DIPG cell line in the pons region. *(A) Example photograph of Evans Blue extravasation (indicated by the dash oval) 2 h after FUS exposure seen in the whole brain (A) and (B) throughout the targeted tumour region. (C) None of the mice in the control group (no ultrasound exposure) showed Evans Blue extravasation in the tumour. (D) One mouse showed tumour growth on MRI in the expected pons region 132 d post tumour inoculation but (C) tumour growth in the front of the brain upon brain extraction at 150 d. Scale bars are (A-C) 5 mm (D) 2 mm.*

diffuse, homogenous, manner (**figure 5.4.13A-B**). No Evans Blue extravasation was seen in any of the control group mice, including in the tumour region (**figure 5.4.13C**). One mouse showed tumour growth in the expected pons region at 132 d and, when treated at 150 d, a large tumour in the front of the brain, was visible upon extraction (**figure 5.4.13C&D**).

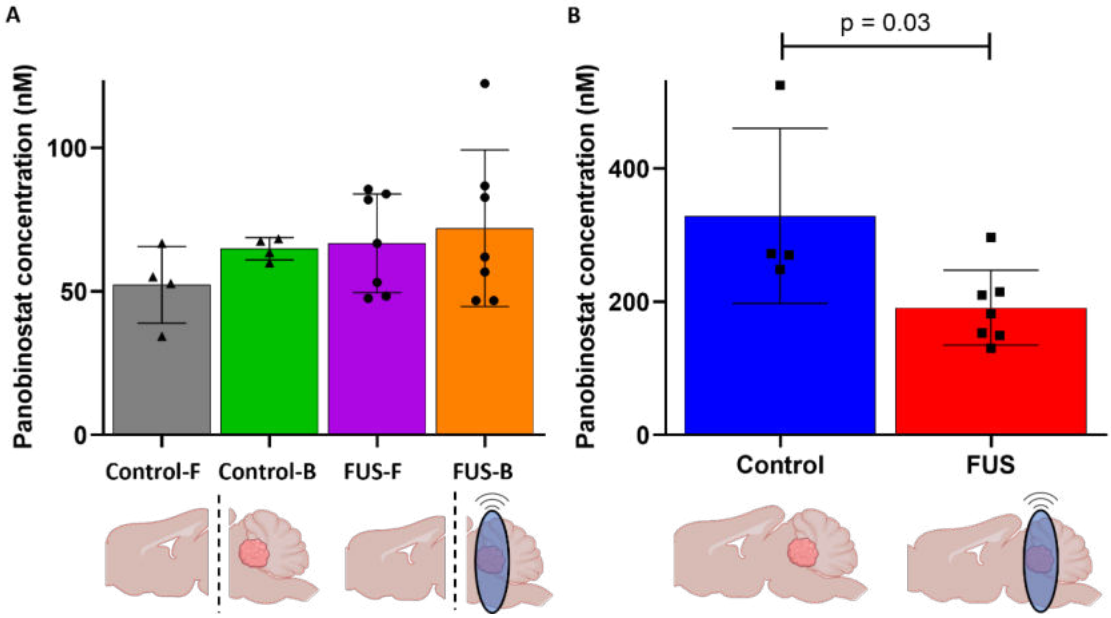

Figure 5.4.14 Ultrasound-mediated panobinostat delivery in a DIPG tumour model. *Panobinostat concentration measured by LC-MS/MS in the (A) brain and (B) plasma in a syngeneic DIPG mouse model 2 h after focused ultrasound (FUS; n=7) or sham control (microbubble injection but no ultrasound exposure; n=4). Brain tissue was split into 'front' (-F) and 'back' (-B). A t-test revealed a significant difference in the panobinostat concentration of the plasma between the control and FUS treatment groups (p=0.03) but no significant difference in the brain (p>0.05). Bars represent mean ± standard deviation.*

Panobinostat concentration was assessed in both the plasma and brain using LC-MS/MS. In the brain, the mean panobinostat concentration was higher in both the FUS-F (66.8 ± 17.1 nM) and FUS-B (72.1 ± 27.3 nM) groups than in the corresponding drug-only control group (control-F: 52.3 ± 13.4 nM and control-B: 66.8 ± 3.9 nM; **figure 5.4.14A**). Whilst the mean drug concentration was highest in the FUS-B group (containing the tumour region), there was no significant difference between any of the groups (p>0.05). The variation (standard

deviation) in the FUS-exposed groups was larger than in the control groups, despite the sample size being greater in the FUS treated group.

Drug concentration in the plasma was significantly higher in the control group (329.0 ± 131.2 nM) than the FUS group (191 nM ± 56.3; p=0.04; **figure 5.4.14B**).

It was hypothesised that mice exposed to FUS would have higher panobinostat concentration in the region targeted by the ultrasound (FUS-B) than the untargeted region (FUS-F). In a pairwise comparison, this was true for three of seven samples (**figure 5.4.15A**). Two brains had very similar drug concentration in FUS-F and FUS-B and the final two had a higher drug concentration in FUS-F than FUS-B. This is different from the NTB mice at 4 h where the panobinostat concentration was higher in the FUS-B than FUS-F for all FUS treated animals (**figure 5.4.7C**). In the control group of the tumour-bearing mice, 3 of 4 brains had a higher drug concentration in control-B than control-F (**figure 5.4.15A**), whilst in the equivalent NTB mice, the drug concentrations were similar in the front and back of the brain (**figure 5.4.7C**).

A simple linear regression analysis was performed to determine whether there was any correlation between panobinostat concentration in the brain and plasma, and between the front and back of the brain. There was no correlation between plasma and brain concentration in any of the four groups (r^2<0.31, p>0.05; **figure 5.4.15B**). In contrast, there was strong positive correlation between panobinostat concentration in the FUS-F and FUS-B groups (r^2=0.87, p=0.01; **figure 5.4.15C**). In the control group, there was no significant correlation between the front and back of the brain (r^2=-0.38, p=0.62; **figure 5.4.15C**).

A third linear regression analysis was performed to examine if there was a correlation between brain mass and panobinostat concentration. There was a strong negative correlation between brain mass and panobinostat concentration in the control group (r^2=-0.80, p=0.02; **figure 5.4.15D**). There was no correlation between drug concentration and brain mass in the FUS-exposed group (r^2=-0.10, p=0.07; **figure 5.4.15D**). When both groups were combined there was no correlation between brain mass and panobinostat concentration (r^2=-0.23, p=0.30).

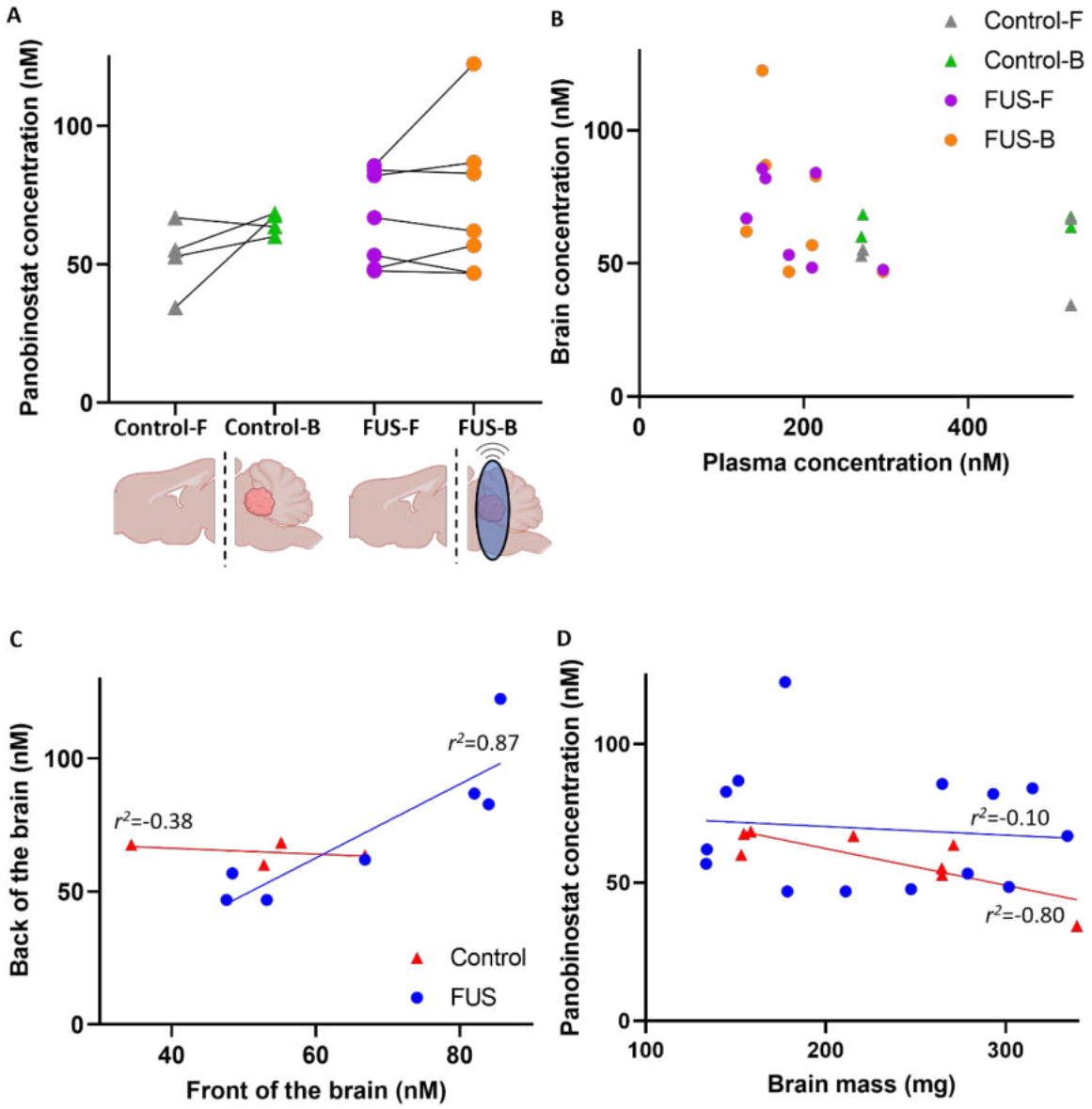

Figure 5.4.15 Ultrasound-mediated panobinostat delivery in a DIPG tumour model. *Panobinostat concentration measured by LC-MS/MS in the brain and plasma of mice after receiving drug + focused ultrasound (FUS) or drug only (control). A: A pairwise comparison of panobinostat concentration in the 'front' (-F) and 'back' (-B) of the brain in both control and FUS treatment groups. B: A simple linear regression showed no correlation between plasma and brain concentration in any of the four groups (r^2<0.31, p>0.05). C: In the FUS treated group, there was strong positive correlation between the panobinostat concentration in the front and back of the brain (r^2=0.87, p=0.01). No such correlation was seen in the control group (r^2=-0.38, p=0.62). D: There was no correlation between brain mass and panobinostat concentration in the FUS treatment group (r^2=-0.10, p=0.07) but strong negative correlation in the control group (r^2=-0.80, p=0.02).*

5.4.5.1 Comparison of panobinostat concentration in non-tumour and tumour bearing mice

2 h after sonication, the mean panobinostat concentration in the control groups was lower in the tumour-bearing (TB) than non-tumour bearing (NTB) mice (**figure 5.4.16A**). This was reversed in the FUS group, in which the mean panobinostat concentration was higher in the TB mice than the NTB mice in both the front and back of the brain. When comparing the panobinostat concentration in the TB mice at 2 h with the NTB mice at 4 h, the mean drug concentration was found to be highest in the NTB FUS-B group (**figure 5.4.16B**). The panobinostat concentration in the other groups (FUS-F, control-F, and control-B) were similar

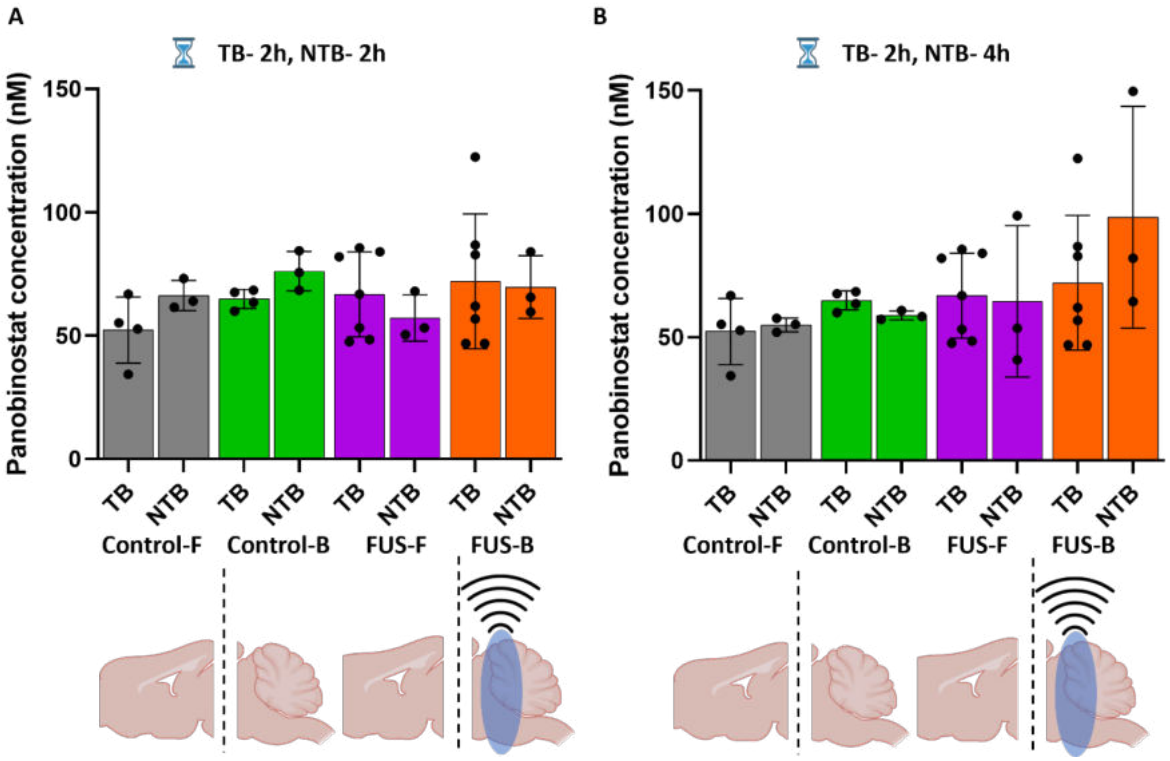

Figure 5.4.16 Ultrasound-mediated panobinostat delivery in tumour bearing (TB) and non-tumour bearing (NTB) mice. *A comparison of panobinostat concentration in C57BL/6J mice with or without a DIPG tumour after 10 mg/kg of panobinostat administered intraperitoneally and exposed to focused ultrasound (FUS) or control. All TB data are at 2 h, and NTB data is at 2 h (A) or 4 h (B) after drug dosing. Panobinostat concentration was measured via LC-MS/MS in the 'front' (-F) and the 'back' (-B) of the brain. Bars represent mean ± standard deviation. T-tests revealed no significant difference between the panobinostat concentration in TB and NTB mice (p>0.05).*

between NTB and TB mice. There was no significant difference between the panobinostat concentration in NTB mice at 2 h and TB mice at 4 h (p>0.05).

5.5 Discussion

The aim of the work described in this chapter was to determine the effects of FUS and microbubble exposure on the concentration of a promising therapeutic (panobinostat) within the tumour region of a DIPG mouse model. Previous published studies have been unable to attain therapeutic efficacy with the drug administered at a tolerable systemic dose. It was hypothesised that FUS could increase the concentration of panobinostat in a targeted manner, resulting in a therapeutic effect at a tolerable systemic dose.

5.5.1 *In vitro* cytotoxicity and pharmacokinetics of panobinostat

Firstly, the therapeutic efficacy of panobinostat was assessed in four cell lines that were considered for the mouse model in this work. The GI_{50} ranged from 11.07 – 23.71 nM, indicating strong cytotoxicity of the drug against these cell lines. Next, the *in vivo* dynamics of the drug were assessed. In alignment with published literature, panobinostat was administered by intraperitoneal injection. A pharmacokinetic study was performed to determine the peak blood concentration (C_{max}) of the drug and synchronise this with the time of sonication. The data suggested that C_{max} occurs between 15minand 30 min, which is similar to published data (Chopra et al., 2016). The pharmacokinetic study also revealed that panobinostat does enter the brain, but as discussed, previously published data suggests this may not be at a sufficient concentration to elicit a therapeutic effect (Hennika et al., 2017, Grasso et al., 2015b).

5.5.2 Panobinostat delivery in non-tumour bearing mice

Panobinostat delivery using FUS, and microbubbles was first assessed in NTB mice, across two studies (where the second was a refinement of the protocol carried out in the first). Overall, the procedure was well-tolerated, and successful BBBD (as indicated by Evans Blue extravasation) was achieved in all mice in the FUS-exposed group. The drug concentration decreased or remained stable over time in the brain regions not exposed to ultrasound. This was expected and in line with the results of the pharmacokinetic study.

There was insignificant difference in the concentration of panobinostat between the brain tissue of mice receiving FUS exposure or drug only. At the 30mintime point, the drug concentration was higher in the drug-only group than the FUS group. This may be explained by the timing of sample extractions. In this study, the time point of the FUS group was measured from sonication, approximately 15 minutes after injection, whilst the control group was measured from injection. Therefore, it may be more appropriate to shift the FUS treatment group times by 15 minutes to compensate. This 15-minute shift appears to be crucial at the 30 min time point, likely due to the rapid clearance of panobinostat, as seen in the pharmacokinetic study. Moreover, the brain tissue for the FUS-exposed group was split into two whilst the drug only group were left whole. The differences in the sizes and masses of brain tissue extracts and 15-minute time shift may explain the panobinostat concentration being higher in the drug-only group than the FUS treatment group at 30 min.

The drug delivery study was repeated, and the time points of both groups were then measured from the panobinostat dosing. Other changes were made to the study design to align the control and FUS groups: all time points were measured from panobinostat dosing, the drug only group underwent the same sonication protocol, without the ultrasound emitted. Despite the protocol changes, the differences in drug concentration between the control and FUS-treated groups were not significant. Whilst the sample size was small (n=3 for each group) and results not statistically significant, the same trend observed in both studies suggests the observations are accurate and representative of actual trends. In the second study, the panobinostat concentration in the FUS-F and FUS-B groups at 2 h were lower than in control groups. The 2 h sonications were performed on the same day, so there might have been an issue with the equipment.

The greatest difference in panobinostat concentration between the FUS and control group was at 4 h. At this time point, the drug concentration was significantly higher in the FUS-B than the FUS-F group, suggesting that the drug remains in the targeted region. This is beneficial when treating DIPG as it reduces the exposure of non-tumour cells to the cytotoxic drug and reduces the chance of neurological deficits - a priority when treating children.

5.5.3 Blood-brain barrier disruption in a DIPG mouse model

A syngeneic mouse model was chosen over a human patient-derived model so that the same mouse strain (C57BL/6J), as used in previous experiments, could be used in this study, providing confidence in the suitability of the protocol and ultrasound parameters. Moreover, there is evidence that FUS and microbubble mediated BBBD has immunomodulatory effects. It was therefore important to use a mouse strain with an intact immune system so that this preliminary work could inform future survival studies. Human tumour derived models must be implanted into immunocompromised mouse strains. This cell line had only previously been implanted into five C57BL/6J mice at the ICR. Growth dynamics in a large cohort were therefore unknown.

The cell line was implanted via intracranial injection, which involves drilling a hole through the mouse skull to expose the brain. The hole in the skull and scar tissue could distort the ultrasound beam (**§1.5.1**), potentially affecting drug delivery profiles. However, its effects, if any, appear to have been negligible in this study. Moreover, one tumour-bearing mouse had typical dextran delivery directly under a fluid region (**figure 5.4.11**), indicating there was no effect.

The dextran distribution and uptake in the DIPG mouse model was similar to NTB mice, both within and outside the tumour. The morphology of the spot-like pattern throughout the tumour indicates cellular, and possibly neuronal, uptake of dextran. A z-stack movie of the tumour also showed typical dextran uptake throughout the tumour region. Tumour regions outside the targeted region did not show dextran uptake, further confirming the hypothesis that the dextran was entering the tumour tissue.

Prior limited evidence suggested that this tumour model has a slightly permeable BTB. Here, no Evans Blue extravasation was present in the tumour bearing mice in the drug-only control group, demonstrating that the BBB/BTB remains impermeable to Evans Blue. When comparing panobinostat concentration in TB and NTB mice, the mean brain concentration was lower in the TB mice, further supporting the hypothesis that the BTB permeability remains intact in this mouse model. However, histological staining showed co-localisation of dextran and erythrocyte extravasation inside the tumour, which could indicate leaky vessels

or damage to the blood vessels after sonication. Histological staining of tumour tissue not exposed to ultrasound could help differentiate between the two.

5.5.4 Panobinostat delivery in a DIPG mouse model

In the tumour-bearing mice, localised Evans Blue extravasation confirmed BBBD in the FUS-treated group. It was hypothesised that the panobinostat concentration would follow the same trend and would therefore be higher in all FUS-exposed mice, compared to the control group. However, this was not the case and panobinostat concentration was similar between the FUS and control groups.

One explanation could be the size difference between Evans Blue and panobinostat. Panobinostat is 345 Da whilst Evans Blue has a known tendency to bind to albumin in the blood, forming a 70 kDa complex. The blood vessels in the tumour could be permeable to panobinostat and not Evans Blue, but as previously discussed, the drug concentration was lower in the TB than the NTB mice, making this unlikely.

Efflux transporters which are responsible for removing substances from the brain parenchyma are present in endothelial cells (Bernardo-Castro et al., 2020). It could be that the Evans Blue is not effluxed as rapidly as panobinostat. At this 2 h time point, panobinostat may have entered the brain parenchyma and then been passively or actively cleared. There is, however, evidence that FUS mediated BBBD suppresses P-gp efflux pumps, for which panobinostat is a substrate (Rodgers et al., 2020).

In contrast, the panobinostat concentration in NTB mice was highest at 4 h suggesting that panobinostat is not rapidly cleared and the concentration in the brain increases over time. A 2 h time point was selected to align with other FUS drug delivery studies. Upon reflection, it would have been preferable to obtain samples at 4 h after sonication as this time point had the greatest difference in brain drug concentration between the FUS and control groups in the NTB mice. In future, it would be constructive to study more time points to fully understand the pharmacokinetics of panobinostat after FUS-mediated delivery in tumour-bearing mice.

5.5.5 Vascular differences between mice

In drug delivery studies with NTB mice, there was a correlation between panobinostat concentrations in the front and back of the brain, within both the control and FUS groups. This trend was also seen in the tumour-bearing mice, but only in the FUS group. This is likely due to vascular differences between brain regions within each mouse. Similarly, two thirds of brains in the control group had a higher drug concentration in the back of the brain than the front of the brain, which may be due to differences in BBB permeability across the brain.

The presence of the tumour could affect BBB permeability and resultant panobinostat concentration in the brain, with and without FUS treatment. Differences could lie in the permeability of the blood vessels in the tumour or response to FUS and microbubbles immediately and post-sonication. The results here show similar drug concentration in the targeted area 2 h after treatment suggesting that the blood vessels in TB and NTB mice respond similarly to FUS treatment.

5.5.6 Blood-brain barrier closing time and drug diffusion

Previous work with rapid short pulses showed that the BBB in the hippocampal region returned to pre-FUS permeability within 10 minutes when delivering a 3 kDa dextran molecule (Morse et al., 2019). The results from this study suggest that the BBB is permeable to panobinostat longer. The quantitative LC-MS/MS data showed a higher panobinostat concentration at 4 h than at 30 min or 1 h. Qualitative observations of Evans Blue delivery at these time points also revealed more intense Evans Blue extravasation in the targeted region at the later time point. The more intense Evans Blue at the later time points could be due to the dynamics of the dye staining the tissue, but the Evans Blue was least intense at 24 h suggesting this is not the case.

The difference in BBB closing time seen in this study compared with that found by Morse et al. (2019) could be explained by the size difference of the tracers and drug. Morse et al. (2019) used the 3 kDa dextran and panobinostat is smaller at 345 Da. It is likely the process of the BBB reverting to 'normal' permeability after FUS treatment is analogous to a closing door; therefore, smaller molecules will be able to enter the brain parenchyma for a longer period than larger ones. It would be beneficial to assess the time for BBB permeability to

drugs of different sizes to return to its pre-FUS state in the DIPG mouse model to inform future studies regarding dosing times and FUS regimens.

The potential longer closing time means a second dose of the drug could be administered before the BBB is completely closed. Tolerability tests are necessary to confirm whether mice are able to tolerate another dose of the drug, providing another avenue for exploring treatment options for DIPG.

Another explanation is that between 30m / 1h and 4h, panobinostat and Evans Blue diffuses further into the brain and away from blood vessels, and then is cleared by 24h.

5.5.7 Variation and sample size

There is a lot of variation (indicated by standard deviation values) in the panobinostat concentration in the brain tissue between mice. The variation in the FUS group was larger than in the control group, indicating a higher variation could arise from the FUS. This is highlighted in the 4 h NTB time points and the TB mice, where the variation in the back of the brain (targeted region) is higher than in the front. Differences in skull thickness and vasculature, and tumour heterogeneity in the DIPG mouse model could affect microbubble behaviour and resultant drug delivery.

Variation could also come from the microbubble size. SonoVue® microbubbles range in diameter from 0.5-11 mM and their resultant behaviour in response to ultrasound is size-dependent (Kovacs et al., 2018). As the microbubble behaviour directly affects the induced BBB permeability, the bubble size could influence the amount of panobinostat that crosses the BBB and, therefore, concentration in the brain.

The sample size in these studies was low (n=3 each group) and increasing the sample size will provide more evidence of actual trends and may decrease variation. A power calculation suggests that 20 mice are needed in each group for the NTB study at the 4 h time point for a power of 80%. In the tumour-bearing study, a power calculation suggests that 229 mice are needed in each group; this number is large due to the high variation and small difference between the control and treated groups.

5.5.8 Future prospects

The proof-of-concept study described in this chapter has shown that FUS and microbubbles could increase drug delivery in a DIPG mouse model. As discussed, the sample sizes were small and results preliminary, especially in the tumour model. As the procedure was well-tolerated by the mice, future studies can build on this initial work. Firstly, concentration of the drug in the brain should be measured at further time points to improve understanding of the pharmacokinetics of the drug after FUS exposure. As well as measuring drug concentration by LC-MS/MS, drug efficacy could be measured. Panobinostat is a deacetylase inhibitor, so acetylation of the histone H3 can be measured by Western Blot and spatial distribution assessed by immunohistochemistry of H3 acetylation on brain tissue sections. Another method of assessing drug distribution and concentration after FUS exposure is matrix-assisted laser desorption ionisation (MALDI) mass spectrometry imaging.

It has also been discussed that FUS suppresses expression of the efflux pump, for which panobinostat is a substrate (Rodgers et al., 2020). It would be instructive to compare P-gp expression with and without FUS using immunohistochemistry. The evidence that FUS can suppress P-gp expression is from studies using long pulses of ultrasound. So, it might be interesting to compare P-gp expression after FUS treatment with long pulses and rapid short pulses of ultrasound.

Repeat treatments will be needed in the clinic for therapeutic effect. The current National Institute for Heath and Care Excellence (NICE) panobinostat dosing regimen for patients with multiple myeloma is six days (1, 3, 5, 8, 10 &12) of a 21-day cycle for 8 cycles (NICE, 2016). Repeat treatments for FUS-mediated delivery of panobinostat should be approached with caution to avoid neurological toxicity. When repeat treatment regimens have been previously assessed with panobinostat, systemic toxicity has been a limiting factor. Grasso et al. (2015) found reduced tumour growth in mice after four weeks of receiving 20 mg/kg once per week. In the group receiving 10 mg/kg three times per week, a reduction of tumour growth was only seen at one week, not at four, highlighting the importance of dosing and timing for optimum tumour response. Published data suggests the half-life of panobinostat in the brain of

C57BL/6J mice, at a dose of 10 mg/kg, is 15 h. An appropriate starting point would be twice-weekly treatments (Chopra et al., 2016).

Grasso et al. (2015) also found resistance in DIPG cells that survived chronic exposure, highlighting the need for combination therapies. This is not surprising as multiple myeloma patients receive panobinostat in combination with dexamethasone and bortezomib (NICE, 2016). *In vitro* studies have shown synergy between panobinostat and BGB324 (AXL inhibitor)(Meel et al., 2020), GSK-J4 (histone demethylase inhibitor)(Grasso et al., 2015b), CBL0137 (facilitates chromatin transcription)(Ehteda et al., 2021). Panobinostat has also been shown to enhance tumour secreted form of necrosis factor-related apoptosis-inducing ligand (sTRAIL) gene therapy against DIPG, although the ability of FUS to deliver gene therapy across the BBB will depend on the size of the therapeutic agent (Choi et al., 2019). It is likely that FUS disrupts the BBB enough to allow the agents in combination therapies to enter the brain parenchyma, with 98-nm-diameter liposomes delivered by rapid short-pulses at a higher pressure (Morse et al., 2022). However, the resultant pharmacodynamics, drug interaction and toxicity of combination therapies towards DIPG are as-of-yet unknown.

Other drug targets, in combination with that of panobinostat, could be explored, such as the mutant *ACVR1* gene encoding ALK2, a driver of tumorigenesis in >30% of DIPGs (Carvalho et al., 2019). It has been shown that ALK2 inhibition improved survival in orthotopic xenograft mice with the *ACVR1* mutation compared to those without the mutation. The combination of panobinostat and an ALK2 inhibitor in mice harbouring both *H3K27M* and *ACVR1* mutations could be investigated.

Another avenue to explore would be the use of a radiolabelled panobinostat, enabling PET guided delivery. (Kommidi et al., 2018) found that [^{18}F]-panobinostat selectively inhibited the growth of DIPG *in vitro*. The advantage of using a radiolabelled drug is that BBBD, distribution and clearance of the drug can be assessed *in vivo*. This information would be especially informative during the early trials in the clinic to understand the mechanisms in patients. However, the addition of PET imaging would increase the costs, complexity, and risks of the treatment – in particular, its repeated use - and may require additional general anaesthesia for children.

It has been reported that with long pulses of ultrasound, it takes 4-48 h for the BBB permeability to return to pre-exposure levels (Sheikov et al., 2008, Samiotaki and Konofagou,

2013). Morse et al. (2019) showed that with rapid short pulses of ultrasound (used here), the BBB 'closes' in 10 minutes. However, the hippocampus was targeted in this study and closing time might be different in the pons. This information would be useful if long-circulating drugs or drugs that require a high dose to enter the brain are being considered. Conversely, if a drug is rapidly cleared from the blood stream, a second dose could be administered within the known time frame of BBBD.

This thesis has focused solely on *in vivo* work. *In vitro* models offer a controlled approach to investigate BBBD, enabling the investigation of specific aspects with increased reproducibility. Co-culture systems and the inclusion of relevant cell types enable the exploration of intricate interactions and signalling pathways involved in BBB modulation, providing insights into cellular and molecular mechanisms. Improvements have been made to traditional transwell models and microfluidic models. Spheroids and organoids enable the ability to examine cell-cell interactions with the possessing 3D architecture with extracellular components. Lastly, *in vitro* models address ethical concerns of animal use and reduce associated expenses.

However, there are limitations of *in vitro* models to consider. The main drawback is the lack of complexity compared to the *in vivo* BBB. Although advancements have been made in developing co-culture systems and microfluidic devices, these models may not completely capture the complexities of the *in vivo* scenario such as intact neuronal networks and the influence of blood flow. Moreover, the acoustic emissions produced during *in vitro* exposure will not represent those occurring in tissue. Therefore, *in vitro* models are unable to fully predict clinical outcomes. Another challenge is the establishment of consistent protocols and validation standards for *in vitro* models of BBBD. Standardisation is crucial to ensure reproducibility across different laboratories and facilitate the comparison of results.

Integrating *in vitro* studies with *in vivo* experiments could provide a comprehensive understanding of FUS-induced BBBD and its translation into drug delivery for the treatment of DIPG.

5.5.9 Clinical relevance

Currently, the only treatment option for patients with DIPG is palliative radiotherapy. Therapeutic radiotherapy and surgery are not viable treatment options due to the critical anatomical location of the pons. Moreover, the BBB remains intact meaning many therapeutics are unable to reach the tumour. Therefore, there is a strong motivation for improved drug delivery for DIPG and this underpins the importance of this work. The use of FUS and microbubbles to locally and temporarily increase the permeability of the BBB has strong potential to expand treatment options.

Clinical trials using FUS for BBBD began in 2015 for the treatment of a range of pathologies including Alzheimer's disease and glioblastoma, and there is an ongoing clinical trial in DIPG patients (Lipsman et al., 2018, Carpentier et al., 2016)(clinical trial: NCT04804709). Whilst clinical trials have been promising, there is still a need to improve performance and safety of the procedure. Pre-clinical work, such as that presented here using rapid short pulses of ultrasound, can inform clinical practice as the technique progresses.

Whilst the clinical link and need is very clear, limitations lie in the use of mouse models including interspecies variation in the BBB, potential breakdown of the BBB in tumour models, and brain size. It is thought that the BBB remains largely intact in DIPG, indicated by lack of efficacy with chemotherapy and minimal contrast enhancement on MRI. Other limitations of mouse models that should be considered are dissimilar brain organisation, BBB physiology and metabolism to human brains, resulting in different panobinostat pharmacokinetics. A pharmacokinetic study has been performed in non-human primates and this will better inform clinical design (Rodgers et al., 2020). A phase I dose-escalation study in DIPG patients is also ongoing to inform dosing limits and regimens (NCT04804709).

5.6 Conclusion

This chapter describes preliminary work aiming to improve treatment options for DIPG by increasing BBB/BTB permeability using the combination of FUS with intravenous microbubbles. Whilst the results have not been uniformly significant, mice treated with ultrasound showed a non-significant increase in panobinostat concentration in the brain compared to mice that received panobinostat only. It has been shown that immunocompetent mice bearing DIPG-like tumours can tolerate FUS treatment, and BBB disruption is possible in this tumour model. The ultrasound system and a suitable mouse model for DIPG have now been established and verified at the ICR. Further resources at the ICR can be exploited to rapidly develop the drug delivery system for DIPG, as well as for other brain disease pathologies.

6 Thesis conclusions

Treatment for patients with diffuse intrinsic pontine glioma (DIPG) is currently restricted to palliative radiotherapy. This, combined with the 9-month median survival from diagnosis, highlights the fact that improved treatment options are necessary. Multiple drug targets have been effective *in vitro,* but have failed *in vivo,* which has been attributed to the presence of an intact blood-brain barrier (BBB). There is thus strong motivation for improved drug delivery for the treatment of DIPG.

Focused ultrasound (FUS) and microbubbles can transiently increase the permeability of the BBB, in a targeted and non-invasive manner, allowing drugs in the bloodstream to enter the brain parenchyma and reach tumour cells.

Current clinical systems use ultrasound emitted in long pulses (~10 ms) that are associated with limitations such as uneven drug distribution (Nhan et al., 2013, Choi et al., 2011b, Choi et al., 2007a, Choi et al., 2011a, Stieger et al., 2007) and tissue damage (Shin et al., 2018b, Baseri et al., 2010, Kinoshita et al., 2006a). Recent work has shown that short pulses (<5 µs) of ultrasound emitted in a rapid sequence can overcome these limitations (Morse et al., 2019). This work was conducted at a frequency of 1 MHz which cannot easily traverse the human skull.

The studies described in this thesis investigated whether the benefits of short pulse ultrasound could be achieved in the pons at 300 kHz, a frequency more suitable for human transcranial transmission. BBB disruption (BBBD) was achieved, but was variable, at this frequency. Next, BBBD was examined at a frequency similar to that used by Morse et al. (2019) at both Imperial College London (ICL) and on a modified FUS system at The Institute of Cancer Research (ICR). Lastly, the effect of FUS exposure on drug concentration in the brains of a mouse DIPG tumour model was examined.

In chapter 3, the ability of a rapid short pulse ultrasound sequence, emitted at 300 kHz, to increase the permeability of the BBB was assessed by examining the extravasation of a model drug in the brain parenchyma. It was shown that BBBD was achievable at this frequency but was unpredictable. The effect of burst length, acoustic pressure and microbubble type on model drug delivery were assessed, but variable results were found

when mice were exposed to identical conditions. Future work should examine BBBD at 300 kHz in a larger animal model which may be more suitable for this frequency.

Chapter 4 describes work designed to achieve reliable BBBD in the pons. As the we were unable to achieve this at 300 kHz, this work reverted to the frequency used by Morse et al. (2019). BBBD in the pons was established and the pressure threshold deemed to be between 0.2 to 0.4 MPa for a 3 kDa model drug. The drug delivery and safety profile were typical of short pulse ultrasound. Work described thus far was performed at ICL. A similar FUS, but modified, system was developed at the ICR. The two systems produced similar drug delivery under the same ultrasound exposure parameters. Histological analysis revealed no detectable tissue damage, indicating that the system was suitable for investigating drug delivery in a DIPG mouse model. Future work could expand on the initial knowledge to provide insight into drug delivery studies. For example, examination of the time taken for the BBB permeability to return to pre-exposure levels and the size of therapeutics that could be delivered across the BBB under certain exposure conditions, would be helpful.

In chapter 5, the ability of rapid short pulse ultrasound to increase the concentration of a promising DIPG drug (panobinostat) in the brain is described. This was done first in non-tumour bearing mice and was well tolerated. Next, it was shown that immunocompetent mice bearing DIPG-like tumours can tolerate FUS exposure and the permeability of the BBB/ blood tumour barrier can be increased, resulting in the extravasation of a model drug that does not normally penetrate the brain. FUS increased the concentration of panobinostat in both the non-tumour bearing and tumour mice in the targeted region compared to mice receiving the drug alone, however this result was not statistically significant. Future work should increase the sample size to elucidate real trends, investigate further time points to understand the pharmacokinetics of the drug after FUS exposure, and examine the efficacy of the drug using immunohistological staining and survival studies.

In conclusion, the preliminary work described in this thesis has shown that FUS-mediated drug delivery is effective in a DIPG tumour model, providing a platform for rapidly expanding treatment options for DIPG and other pathologies.

7 Appendix

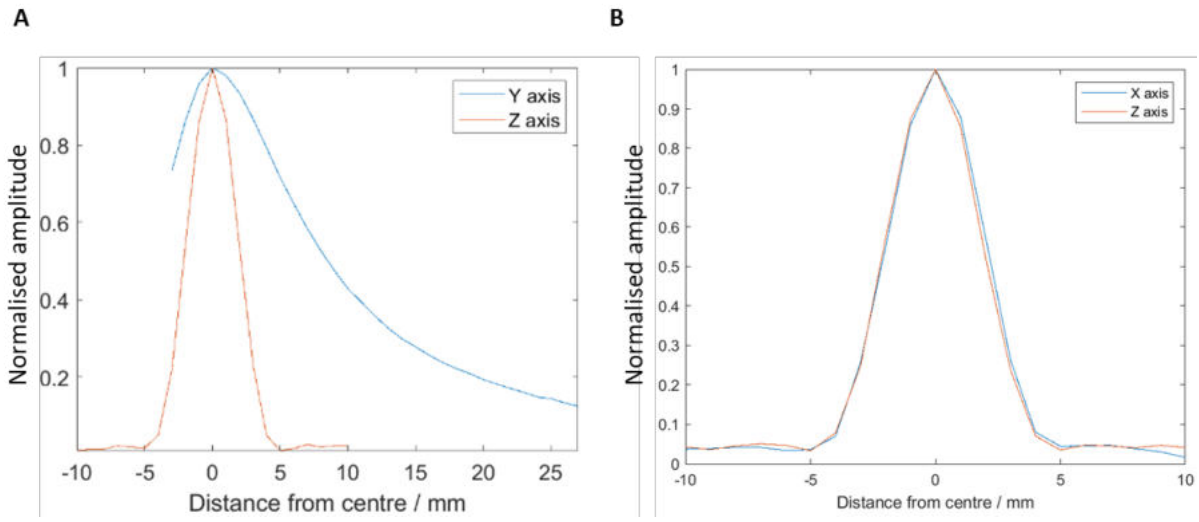

Figure 7.1 Beam profiles at 300 kHz (ICL). *Beam profiles of the H-117 transducer (Sonic Concepts, WA, USA) along the (A) axial (YZ plane) and (B) lateral (XZ plane) dimensions at centre frequency of 300 kHz, 335° phase, 1 cycle pulse length. All beam profiles were obtained using a 0.2 mm needle PVDF hydrophone in a degassed, deionised water tank. The hydrophone was calibrated by the national physical laboratory (NPL) with a ± 9 % uncertainty. 0.3 mm step size was achieved using a 3D-positioning system and the plot shown is peak negative pressure. The measured dimensions at pressure full-width half-maximum (FWHM) were 5 x 5 x 18 mm. Figures obtained from Dr Matthew Copping.*

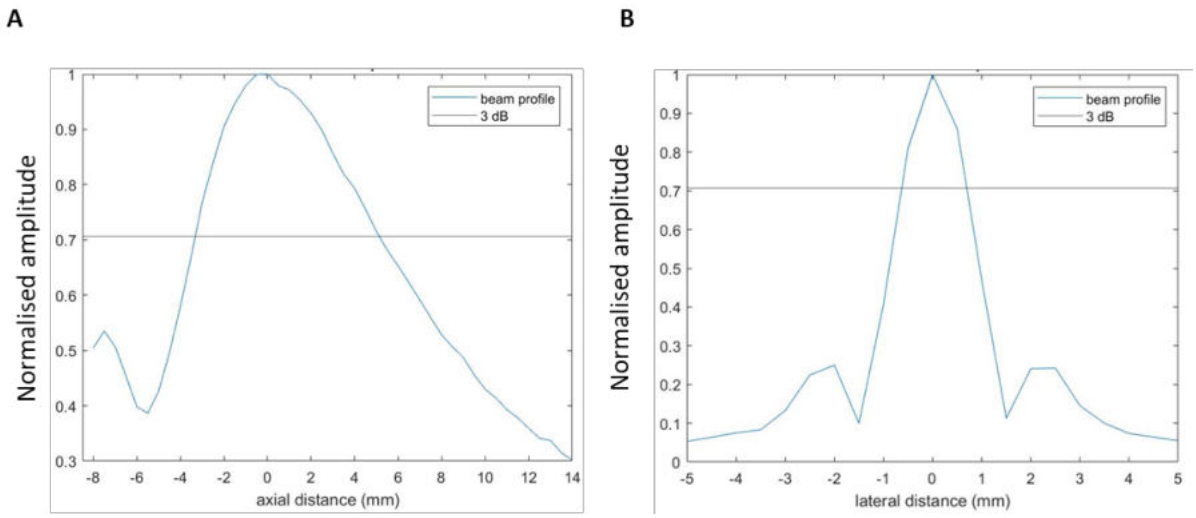

Figure 7.5.6.1 Beam profiles at 1.05 MHz (ICL). *Beam profiles of the H-117 transducer (Sonic Concepts, WA, USA) along the (A) axial and (B) lateral dimensions at centre frequency of 1.05 MHz, 340^{o} phase, 5 cycle pulse length. All beam profiles were obtained using a 0.2 mm needle PVDF hydrophone in a degassed, deionised water tank. The hydrophone was calibrated by the national physical laboratory (NPL) with a ± 9 % uncertainty. 0.3 mm step size was achieved using a 3D-positioning system and the plot shown is peak negative pressure. The measured dimensions at pressure full-width half-maximum (FWHM) were 1.8 x 1.8 x 12.8 mm.*

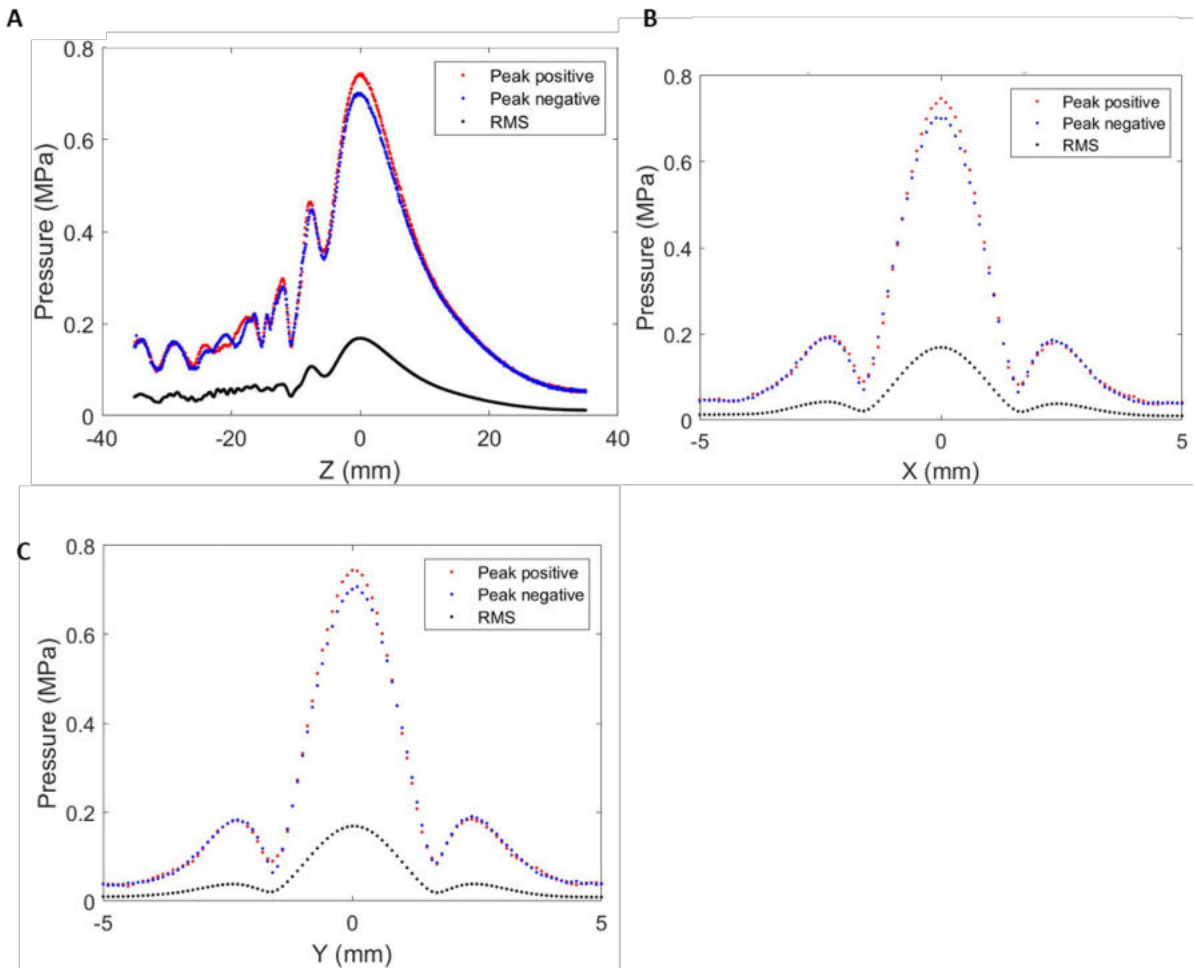

Figure 7.5.6.2 Beam profiles at a centre frequency of 1 MHz (ICR). *Beam profiles at a centre frequency of 1 MHz (ICR). Beam profiles of H-117 transducer (Sonic Concepts, WA, USA) along the (A) axial, (B) lateral and (C) elevational dimensions obtained using an HNA-0400 needle hydrophone (ONDA Corp., USA, CA) in a degassed, deionised water tank. The hydrophone was calibrated in-house with ± 10% uncertainty. 0.1 mm step size was achieved using a 3D-positioning system and ultrasound emitted at 80 mV, 5 cycle pulse length, 60º phase. The measured dimensions at pressure full-width half-maximum (FWHM) were 2.0 x 2.0 x 14.5 mm.*

8 References

ABDELHAKAM, D., YOUNG, P. R., JAIN, M. K., NASSAR, A., COPLAND, J. A. & TAN, W. 2020. Complete remission with immunotherapy: Case report of a patient with metastatic bladder cancer to the humerus. *Urol Case Rep,* 30**,** 101130.

ALLEN, B. D. & LIMOLI, C. L. 2022. Breaking barriers: Neurodegenerative repercussions of radiotherapy induced damage on the blood-brain and blood-tumor barrier. *Free Radical Biology and Medicine,* 178**,** 189-201.

ALLI, S., FIGUEIREDO, C. A., GOLBOURN, B., SABHA, N., WU, M. Y., BONDOC, A., LUCK, A., COLUCCIA, D., MASLINK, C., SMITH, C., WURDAK, H., HYNYNEN, K., O'REILLY, M. & RUTKA, J. T. 2018. Brainstem blood brain barrier disruption using focused ultrasound: A demonstration of feasibility and enhanced doxorubicin delivery. *J Control Release,* 281**,** 29-41.

ALONSO, A., REINZ, E., FATAR, M., JENNE, J., HENNERICI, M. G. & MEAIRS, S. 2010. Neurons but not glial cells overexpress ubiquitin in the rat brain following focused ultrasound-induced opening of the blood-brain barrier. *Neuroscience,* 169**,** 116-24.

APFEL, R. E. 1997. *Sonic effervescence: a tutorial on acoustic cavitation.*

ARSIWALA, T. A., SPROWLS, S. A., BLETHEN, K. E., FLADELAND, R. A., WOLFORD, C. P., KIELKOWSKI, B. N., GLASS, M. J., WANG, P., WILSON, O., CARPENTER, J. S., RANJAN, M., FINOMORE, V., REZAI, A. & LOCKMAN, P. R. 2022. Characterization of passive permeability after low intensity focused ultrasound mediated blood-brain barrier disruption in a preclinical model. *Fluids Barriers CNS,* 19**,** 72.

ARVANITIS, C. D., ASKOXYLAKIS, V., GUO, Y., DATTA, M., KLOEPPER, J., FERRARO, G. B., BERNABEU, M. O., FUKUMURA, D., MCDANNOLD, N. & JAIN, R. K. 2018. Mechanisms of enhanced drug delivery in brain metastases with focused ultrasound-induced blood-tumor barrier disruption. *Proc Natl Acad Sci U S A,* 115**,** E8717-e8726.

ARYAL, M., FISCHER, K., GENTILE, C., GITTO, S., ZHANG, Y. Z. & MCDANNOLD, N. 2017. Effects on P-Glycoprotein Expression after Blood-Brain Barrier Disruption Using Focused Ultrasound and Microbubbles. *PLoS One,* 12**,** e0166061.

AZIZ-BOSE, R. & MONJE, M. 2019. Diffuse intrinsic pontine glioma: molecular landscape and emerging therapeutic targets. *Current Opinion in Oncology,* 31**,** 522-530.

BAGCCHI, S. 2015. Panobinostat active against diffuse intrinsic pontine glioma. *The Lancet Oncology,* 16**,** e267.

BAILEY, S., HOWMAN, A., WHEATLEY, K., WHERTON, D., BOOTA, N., PIZER, B., FISHER, D., KEARNS, P., PICTON, S., SARAN, F., GIBSON, M., GLASER, A., CONNOLLY, D. J. & HARGRAVE, D. 2013. Diffuse intrinsic pontine glioma treated with prolonged temozolomide and radiotherapy--results of a United Kingdom phase II trial (CNS 2007 04). *Eur J Cancer,* 49**,** 3856-62.

BARZEGAR-FALLAH, A., GANDHI, K., RIZWAN, S. B., SLATTER, T. L. & REYNOLDS, J. N. 2022. Harnessing Ultrasound for Targeting Drug Delivery to the Brain and Breaching the Blood–Brain Tumour Barrier. *Pharmaceutics,* 14**,** 2231.

BASERI, B., CHOI, J. J., TUNG, Y. S. & KONOFAGOU, E. E. 2010. Multi-modality safety assessment of blood-brain barrier opening using focused ultrasound and definity microbubbles: a short-term study. *Ultrasound Med Biol,* 36**,** 1445-59.

BATTS, A. J., JI, R., NOEL, R. L., KLINE-SCHODER, A. R., BAE, S., KWON, N. & KONOFAGOU, E. E. 2023. Using a novel rapid alternating steering angles pulse sequence to evaluate the impact of theranostic ultrasound-mediated ultra-short pulse length on blood-brain barrier opening volume and closure, cavitation mapping, drug delivery feasibility, and safety. *Theranostics,* 13**,** 1180-1197.

BEDNAR, J., HOROWITZ, R. A., GRIGORYEV, S. A., CARRUTHERS, L. M., HANSEN, J. C., KOSTER, A. J. & WOODCOCK, C. L. 1998. Nucleosomes, linker DNA, and linker histone form a unique structural motif that directs the higher-order folding and compaction of chromatin. *Proc Natl Acad Sci U S A,* 95**,** 14173-8.

BERNARDO-CASTRO, S., SOUSA, J. A., BRÁS, A., CECÍLIA, C., RODRIGUES, B., ALMENDRA, L., MACHADO, C., SANTO, G., SILVA, F., FERREIRA, L., SANTANA, I. & SARGENTO-FREITAS, J. 2020. Pathophysiology of Blood-Brain Barrier Permeability Throughout the Different Stages of Ischemic Stroke and Its Implication on Hemorrhagic Transformation and Recovery. *Front Neurol,* 11**,** 594672.

BING, C., HONG, Y., HERNANDEZ, C., RICH, M., CHENG, B., MUNAWEERA, I., SZCZEPANSKI, D., XI, Y., BOLDING, M., EXNER, A. & CHOPRA, R. 2018. Characterization of different bubble formulations for blood-brain barrier opening using a focused ultrasound system with acoustic feedback control. *Sci Rep,* 8**,** 7986.

BORDEN, M. A., KRUSE, D. E., CASKEY, C. F., ZHAO, S., DAYTON, P. A. & FERRARA, K. W. 2005. Influence of lipid shell physicochemical properties on ultrasound-induced microbubble destruction. *IEEE Trans Ultrason Ferroelectr Freq Control,* 52**,** 1992-2002.

BRIGHI, C., REID, L., WHITE, A. L., GENOVESI, L. A., KOJIC, M., MILLAR, A., BRUCE, Z., DAY, B. W., ROSE, S., WHITTAKER, A. K. & PUTTICK, S. 2020. MR-guided focused ultrasound increases antibody delivery to nonenhancing high-grade glioma. *Neuro-Oncology Advances,* 2.

CARETTI, V., BUGIANI, M., FRERET, M., SCHELLEN, P., JANSEN, M., VAN VUURDEN, D., KASPERS, G., FISHER, P. G., HULLEMAN, E., WESSELING, P., VOGEL, H. & MONJE, M. 2014. Subventricular spread of diffuse intrinsic pontine glioma. *Acta Neuropathol,* 128**,** 605-7.

CARPENTIER, A., CANNEY, M., VIGNOT, A., REINA, V., BECCARIA, K., HORODYCKID, C., KARACHI, C., LECLERCQ, D., LAFON, C., CHAPELON, J. Y., CAPELLE, L., CORNU, P., SANSON, M., HOANG-XUAN, K., DELATTRE, J. Y. & IDBAIH, A. 2016. Clinical trial of blood-brain barrier disruption by pulsed ultrasound. *Sci Transl Med,* 8**,** 343re2.

CARVALHO, D., TAYLOR, K. R., OLACIREGUI, N. G., MOLINARI, V., CLARKE, M., MACKAY, A., RUDDLE, R., HENLEY, A., VALENTI, M. & HAYES, A. 2019. ALK2 inhibitors display beneficial effects in preclinical models of ACVR1 mutant diffuse intrinsic pontine glioma. *Communications biology,* 2**,** 156.

CASKEY, C., KRUSE, D., DAYTON, P., KITANO, T. & FERRARA, K. 2006. Microbubble oscillation in tubes with diameters of 12, 25, and 195 microns. *Applied Physics Letters,* 88**,** 033902-033902.

CATALANO, M. G., PUGLIESE, M., GARGANTINI, E., GRANGE, C., BUSSOLATI, B., ASIOLI, S., BOSCO, O., POLI, R., COMPAGNONE, A. & BANDINO, A. 2011. Cytotoxic activity of the histone deacetylase inhibitor panobinostat (LBH589) in anaplastic thyroid cancer. Vitro.

CERRONI, B., CICCONI, R., ODDO, L., SCIMECA, M., BONFIGLIO, R., BERNARDINI, R., PALMIERI, G., DOMENICI, F., BONANNO, E., MATTEI, M. & PARADOSSI, G. 2018. In vivo biological fate of poly(vinylalcohol) microbubbles in mice. *Heliyon,* 4**,** e00770.

CHAN, K.-M., FANG, D., GAN, H., HASHIZUME, R., YU, C., SCHROEDER, M., GUPTA, N., MUELLER, S., JAMES, C. D. & JENKINS, R. 2013. The histone H3. 3K27M mutation in pediatric glioma reprograms H3K27 methylation and gene expression. *Genes & development,* 27**,** 985-990.

CHANG, W. L. K., CHAN, T. G., RAGUSEO, F., MISHRA, A., CHATTENTON, D., DE ROSALES, R. T. M., LONG, N. J. & MORSE, S. V. 2023. Rapid Short-Pulses of Focused Ultrasound and Microbubbles Deliver a Range of Agent Sizes to the Brain.

CHEN, H. & KONOFAGOU, E. E. 2014. The size of blood-brain barrier opening induced by focused ultrasound is dictated by the acoustic pressure. *J Cereb Blood Flow Metab,* 34**,** 1197-204.

CHEN, K.-T., CHAI, W.-Y., LIN, Y.-J., LIN, C.-J., CHEN, P.-Y., TSAI, H.-C., HUANG, C.-Y., KUO, J. S., LIU, H.-L. & WEI, K.-C. 2021. Neuronavigation-guided focused ultrasound for transcranial blood-brain barrier opening and immunostimulation in brain tumors. *Science Advances,* 7**,** eabd0772.

CHEN, P. Y., HSIEH, H. Y., HUANG, C. Y., LIN, C. Y., WEI, K. C. & LIU, H. L. 2015. Focused ultrasound-induced blood-brain barrier opening to enhance interleukin-12 delivery for brain tumor immunotherapy: a preclinical feasibility study. *J Transl Med,* 13**,** 93.

CHENG, M., LI, F., HAN, T., YU, A. C. H. & QIN, P. 2019. Effects of ultrasound pulse parameters on cavitation properties of flowing microbubbles under physiologically relevant conditions. *Ultrasonics Sonochemistry,* 52**,** 512-521.

CHIEN, C.-Y., XU, L., PACIA, C. P., YUE, Y. & CHEN, H. 2022. Blood–brain barrier opening in a large animal model using closed-loop microbubble cavitation-based feedback control of focused ultrasound sonication. *Scientific Reports,* 12**,** 16147.

CHO, H., LEE, H.-Y., HAN, M., CHOI, J.-R., AHN, S., LEE, T., CHANG, Y. & PARK, J. 2016. Localized down-regulation of P-glycoprotein by focused ultrasound and microbubbles induced blood-brain barrier disruption in rat brain. *Scientific reports,* 6**,** 31201.

CHOI, H., LEE, E.-H., HAN, M., AN, S.-H. & PARK, J. 2019. Diminished expression of P-glycoprotein using focused ultrasound is associated with JNK-dependent signaling pathway in cerebral blood vessels. *Frontiers in Neuroscience,* 13**,** 1350.

CHOI, J. J., FESHITAN, J. A., BASERI, B., WANG, S., TUNG, Y. S., BORDEN, M. A. & KONOFAGOU, E. E. 2010a. Microbubble-size dependence of focused ultrasound-induced blood-brain barrier opening in mice in vivo. *IEEE Trans Biomed Eng,* 57**,** 145-54.

CHOI, J. J., PERNOT, M., BROWN, T. R., SMALL, S. A. & KONOFAGOU, E. E. 2007a. Spatio-temporal analysis of molecular delivery through the blood-brain barrier using focused ultrasound. *Phys Med Biol,* 52**,** 5509-30.

CHOI, J. J., PERNOT, M., SMALL, S. A. & KONOFAGOU, E. E. 2007b. Noninvasive, transcranial and localized opening of the blood-brain barrier using focused ultrasound in mice. *Ultrasound Med Biol,* 33**,** 95-104.

CHOI, J. J., SELERT, K., GAO, Z., SAMIOTAKI, G., BASERI, B. & KONOFAGOU, E. E. 2011a. Noninvasive and localized blood-brain barrier disruption using focused ultrasound can be achieved at short pulse lengths and low pulse repetition frequencies. *J Cereb Blood Flow Metab,* 31**,** 725-37.

CHOI, J. J., SELERT, K., VLACHOS, F., WONG, A. & KONOFAGOU, E. E. 2011b. Noninvasive and localized neuronal delivery using short ultrasonic pulses and microbubbles. *Proc Natl Acad Sci U S A,* 108**,** 16539-44.

CHOI, J. J., WANG, S., TUNG, Y. S., MORRISON, B., 3RD & KONOFAGOU, E. E. 2010b. Molecules of various pharmacologically-relevant sizes can cross the ultrasound-induced blood-brain barrier opening in vivo. *Ultrasound Med Biol,* 36**,** 58-67.

CHOMAS, J. E., DAYTON, P., ALLEN, J., MORGAN, K. & FERRARA, K. W. 2001a. Mechanisms of contrast agent destruction. *IEEE Trans Ultrason Ferroelectr Freq Control,* 48**,** 232-48.

CHOMAS, J. E., DAYTON, P., MAY, D. & FERRARA, K. 2001b. Threshold of fragmentation for ultrasonic contrast agents. *J Biomed Opt,* 6**,** 141-50.

CHOPRA, R., VYKHODTSEVA, N. & HYNYNEN, K. 2010. Influence of exposure time and pressure amplitude on blood-brain-barrier opening using transcranial ultrasound exposures. *ACS Chem Neurosci,* 1**,** 391-398.

CHOPRA, V., QUINTI, L., KHANNA, P., PAGANETTI, P., KUHN, R., YOUNG, A. B., KAZANTSEV, A. G. & HERSCH, S. 2016. LBH589, a hydroxamic acid-derived HDAC inhibitor, is neuroprotective in mouse models of Huntington's disease. *Journal of Huntington's Disease,* 5**,** 347-355.

CHUNG, C., SWEHA, S. R., PRATT, D., TAMRAZI, B., PANWALKAR, P., BANDA, A., BAYLISS, J., HAWES, D., YANG, F. & LEE, H.-J. 2020. Integrated metabolic and epigenomic reprograming by H3K27M mutations in diffuse intrinsic pontine gliomas. *Cancer Cell,* 38**,** 334-349. e9.

CHURCH, C. C. & CARSTENSEN, E. L. 2001. "Stable" inertial cavitation. *Ultrasound Med Biol,* 27**,** 1435-7.

CHURCH, C. C. & MILLER, D. L. 2016. A Two-Criterion Model for Microvascular Bio-Effects Induced In Vivo by Contrast Microbubbles Exposed to Medical Ultrasound. *Ultrasound Med Biol,* 42**,** 1385-98.

CIPOLLA, M. J., CRETE, R., VITULLO, L. & RIX, R. D. 2004. Transcellular transport as a mechanism of blood-brain barrier disruption during stroke. *Frontiers in bioscience : a journal and virtual library* [Online], 9. Available: http://europepmc.org/abstract/MED/14766407 https://doi.org/10.2741/1282 [Accessed 2004/01//].

COPES, L. E., SCHUTZ, H., DLUGSOZ, E. M., JUDEX, S. & GARLAND, T., JR. 2018. Locomotor activity, growth hormones, and systemic robusticity: An investigation of cranial vault thickness in mouse lines bred for high endurance running. *Am J Phys Anthropol,* 166**,** 442-458.

COUSSIOS, C. C. & ROY, R. A. 2008. Applications of Acoustics and Cavitation to Noninvasive Therapy and Drug Delivery. *Annual Review of Fluid Mechanics,* 40**,** 395-420.

CRUK. No date. *Brain, other CNS and intracranial tumours mortality statistics* [Online]. Available: https://www.cancerresearchuk.org/health-professional/cancer-statistics/statistics-by-cancer-type/brain-other-cns-and-intracranial-tumours/mortality [Accessed 18/03/2023 2023].

CURLEY, C. T., MEAD, B. P., NEGRON, K., KIM, N., GARRISON, W. J., MILLER, G. W., KINGSMORE, K. M., THIM, E. A., SONG, J. & MUNSON, J. M. 2020. Augmentation of brain tumor interstitial flow via focused ultrasound promotes brain-penetrating nanoparticle dispersion and transfection. *Science advances,* 6**,** eaay1344.

CZARNOTA, G. J., KARSHAFIAN, R., BURNS, P. N., WONG, S., AL MAHROUKI, A., LEE, J. W., CAISSIE, A., TRAN, W., KIM, C., FURUKAWA, M., WONG, E. & GILES, A. 2012. Tumor radiation response enhancement by acoustical stimulation of the vasculature. *Proceedings of the National Academy of Sciences of the United States of America,* 109**,** E2033-E2041.

DALLE ORE, C., COLEMAN-ABADI, C., GUPTA, N. & MUELLER, S. 2023. Advances and Clinical Trials Update in the Treatment of Diffuse Intrinsic Pontine Gliomas. *Pediatr Neurosurg*.

DAVIS, M. E. 2016. Glioblastoma: Overview of Disease and Treatment. *Clin J Oncol Nurs,* 20**,** S2-8.

DI, K., LLOYD, G. K., ABRAHAM, V., MACLAREN, A., BURROWS, F. J., DESJARDINS, A., TRIKHA, M. & BOTA, D. A. 2016. Marizomib activity as a single agent in malignant gliomas: ability to cross the blood-brain barrier. *Neuro Oncol,* 18**,** 840-8.

DONG, X. 2018. Current Strategies for Brain Drug Delivery. *Theranostics,* 8**,** 1481-1493.

DOOLITTLE, N. D., MINER, M. E., HALL, W. A., SIEGAL, T., JEROME, E., OSZTIE, E., MCALLISTER, L. D., BUBALO, J. S., KRAEMER, D. F., FORTIN, D., NIXON, R., MULDOON, L. L. & NEUWELT, E. A. 2000. Safety and efficacy of a multicenter study using intraarterial chemotherapy in conjunction with osmotic opening of the blood-brain barrier for the treatment of patients with malignant brain tumors. *Cancer,* 88**,** 637-47.

DOWNS, M. E., BUCH, A., KARAKATSANI, M. E., KONOFAGOU, E. E. & FERRERA, V. P. 2015a. Blood-Brain Barrier Opening in Behaving Non-Human Primates via Focused Ultrasound with Systemically Administered Microbubbles. *Sci Rep,* 5**,** 15076.

DOWNS, M. E., BUCH, A., SIERRA, C., KARAKATSANI, M. E., TEICHERT, T., CHEN, S., KONOFAGOU, E. E. & FERRERA, V. P. 2015b. Long-Term Safety of Repeated Blood-Brain Barrier Opening via Focused Ultrasound with Microbubbles in Non-Human Primates Performing a Cognitive Task. *PLoS One,* 10**,** e0125911.

DRAGO, J. Z., MODI, S. & CHANDARLAPATY, S. 2021. Unlocking the potential of antibody–drug conjugates for cancer therapy. *Nature Reviews Clinical Oncology,* 18**,** 327-344.

EHTEDA, A., SIMON, S., FRANSHAW, L., GIORGI, F. M., LIU, J., JOSHI, S., ROUAEN, J. R., PANG, C. N. I., PANDHER, R. & MAYOH, C. 2021. Dual targeting of the epigenome via FACT complex and histone deacetylase is a potent treatment strategy for DIPG. *Cell reports,* 35**,** 108994.

EL-HASHASH, A. H. 2021. Histone H3K27M mutation in brain tumors. *Histone Mutations and Cancer***,** 43-52.

ENGLANDER, Z. K., WEI, H. J., POULIOPOULOS, A. N., BENDAU, E., UPADHYAYULA, P., JAN, C. I., SPINAZZI, E. F., YOH, N., TAZHIBI, M., MCQUILLAN, N. M., WANG, T. J. C., BRUCE, J. N., CANOLL, P., FELDSTEIN, N. A., ZACHAROULIS, S., KONOFAGOU, E. E. & WU, C. C. 2021. Focused ultrasound mediated blood-brain barrier opening is safe and feasible in a murine pontine glioma model. *Sci Rep,* 11**,** 6521.

FAN, C. H., LIN, W. H., TING, C. Y., CHAI, W. Y., YEN, T. C., LIU, H. L. & YEH, C. K. 2014a. Contrast-enhanced ultrasound imaging for the detection of focused ultrasound-induced blood-brain barrier opening. *Theranostics,* 4**,** 1014-25.

FAN, C. H., LIU, H. L., HUANG, C. Y., MA, Y. J., YEN, T. C. & YEH, C. K. 2012. Detection of intracerebral hemorrhage and transient blood-supply shortage in focused-ultrasound-induced blood-brain barrier disruption by ultrasound imaging. *Ultrasound Med Biol,* 38**,** 1372-82.

FAN, C. H., LIU, H. L., TING, C. Y., LEE, Y. H., HUANG, C. Y., MA, Y. J., WEI, K. C., YEN, T. C. & YEH, C. K. 2014b. Submicron-bubble-enhanced focused ultrasound for blood-brain barrier disruption and improved CNS drug delivery. *PLoS One,* 9**,** e96327.

FAN, C. H., TING, C. Y., CHANG, Y. C., WEI, K. C., LIU, H. L. & YEH, C. K. 2015. Drug-loaded bubbles with matched focused ultrasound excitation for concurrent blood-brain barrier opening and brain-tumor drug delivery. *Acta Biomater,* 15**,** 89-101.

FERRARA, K. W., BORDEN, M. A. & ZHANG, H. 2009. Lipid-Shelled Vehicles: Engineering for Ultrasound Molecular Imaging and Drug Delivery. *Accounts of Chemical Research,* 42**,** 881-892.

FLYNN, H. G. 1975. Cavitation dynamics. I. A mathematical formulation. *The Journal of the Acoustical Society of America,* 57**,** 1379-1396.

FRAZIER, J. L., LEE, J., THOMALE, U. W., NOGGLE, J. C., COHEN, K. J. & JALLO, G. I. 2009. Treatment of diffuse intrinsic brainstem gliomas: failed approaches and future strategies. *J Neurosurg Pediatr,* 3**,** 259-69.

FRY, F. 1977. Transkull transmission of an intense focused ultrasonic beam. *Ultrasound in medicine & biology,* 3**,** 179-184.

GANDHI, K., BARZEGAR-FALLAH, A., BANSTOLA, A., RIZWAN, S. B. & REYNOLDS, J. N. J. 2022. Ultrasound-Mediated Blood–Brain Barrier Disruption for Drug Delivery: A Systematic Review of Protocols, Efficacy, and Safety Outcomes from Preclinical and Clinical Studies. *Pharmaceutics,* 14**,** 833.

GASPARIAN, A. V., BURKHART, C. A., PURMAL, A. A., BRODSKY, L., PAL, M., SARANADASA, M., BOSYKH, D. A., COMMANE, M., GURYANOVA, O. A. & PAL, S. 2011. Curaxins: anticancer compounds that simultaneously suppress NF-κB and activate p53 by targeting FACT. *Science translational medicine,* 3**,** 95ra74-95ra74.

GILL, S. K., WILSON, M., DAVIES, N. P., MACPHERSON, L., ENGLISH, M., ARVANITIS, T. N. & PEET, A. C. 2014. Diagnosing relapse in children's brain tumors using metabolite profiles. *Neuro Oncol,* 16**,** 156-64.

GRASSO, C. S., TANG, Y., TRUFFAUX, N., BERLOW, N. E., LIU, L., DEBILY, M.-A., QUIST, M. J., DAVIS, L. E., HUANG, E. C. & WOO, P. J. 2015a. Functionally defined therapeutic targets in diffuse intrinsic pontine glioma. *Nature medicine,* 21**,** 555-559.

GRASSO, C. S., TANG, Y., TRUFFAUX, N., BERLOW, N. E., LIU, L., DEBILY, M.-A., QUIST, M. J., DAVIS, L. E., HUANG, E. C., WOO, P. J., PONNUSWAMI, A., CHEN, S., JOHUNG, T. B., SUN, W., KOGISO, M., DU, Y., QI, L., HUANG, Y., HÜTT-CABEZAS, M., WARREN, K. E., LE DRET, L., MELTZER, P. S., MAO, H., QUEZADO, M., VAN VUURDEN, D. G., ABRAHAM, J., FOULADI, M., SVALINA, M. N., WANG, N., HAWKINS, C., NAZARIAN, J., ALONSO, M. M., RAABE, E. H., HULLEMAN, E., SPELLMAN, P. T., LI, X.-N., KELLER, C., PAL, R., GRILL, J. & MONJE, M. 2015b. Functionally defined therapeutic targets in diffuse intrinsic pontine glioma. *Nature Medicine,* 21**,** 555.

GRIMM, S. A. & CHAMBERLAIN, M. C. 2013. Brainstem glioma: a review. *Curr Neurol Neurosci Rep,* 13**,** 346.

GUO, J., SONG, X., CHEN, X., XU, M. & MING, D. 2021. Mathematical Model of Ultrasound Attenuation With Skull Thickness for Transcranial-Focused Ultrasound. *Front Neurosci,* 15**,** 778616.

HAMER, P., MCGEACHIE, J. I., DAVIES, M. & GROUNDS, M. 2002. Evans Blue Dye as an in vivo marker of myofibre damage: optimising parameters for detecting initial myofibre membrane permeability. *Journal of anatomy,* 200**,** 69-79.

HAMILL, O. 2006. Twenty odd years of stretch-sensitive channels. *Pflügers Archiv,* 453**,** 333-351.

HARUTYUNYAN, A. S., KRUG, B., CHEN, H., PAPILLON-CAVANAGH, S., ZEINIEH, M., DE JAY, N., DESHMUKH, S., CHEN, C. C. L., BELLE, J., MIKAEL, L. G., MARCHIONE, D. M., LI, R., NIKBAKHT, H., HU, B., CAGNONE, G., CHEUNG, W. A., MOHAMMADNIA, A., BECHET, D., FAURY, D., MCCONECHY, M. K., PATHANIA, M., JAIN, S. U., ELLEZAM, B., WEIL, A. G., MONTPETIT, A., SALOMONI, P., PASTINEN, T., LU, C., LEWIS, P. W., GARCIA, B. A., KLEINMAN, C. L., JABADO, N. & MAJEWSKI, J. 2019. H3K27M induces defective chromatin spread of PRC2-

mediated repressive H3K27me2/me3 and is essential for glioma tumorigenesis. *Nat Commun,* 10**,** 1262.

HASHIZUME, R. 2017. Epigenetic targeted therapy for diffuse intrinsic pontine glioma. *Neurologia medico-chirurgica,* 57**,** 331-342.

HAUMANN, R., BIANCO, J. I., WARANECKI, P. M., GAILLARD, P. J., STORM, G., RIES, M., VAN VUURDEN, D. G., KASPERS, G. J. L. & HULLEMAN, E. 2022. Imaged-guided focused ultrasound in combination with various formulations of doxorubicin for the treatment of diffuse intrinsic pontine glioma. *Translational Medicine Communications,* 7**,** 8.

HAYDEN, E., HOLLIDAY, H., LEHMANN, R., KHAN, A., TSOLI, M., RAYNER, B. S. & ZIEGLER, D. S. 2021. Therapeutic Targets in Diffuse Midline Gliomas—An Emerging Landscape. *Cancers,* 13**,** 6251.

HENNIKA, T., HU, G., OLACIREGUI, N. G., BARTON, K. L., EHTEDA, A., CHITRANJAN, A., CHANG, C., GIFFORD, A. J., TSOLI, M., ZIEGLER, D. S., CARCABOSO, A. M. & BECHER, O. J. 2017. Pre-Clinical Study of Panobinostat in Xenograft and Genetically Engineered Murine Diffuse Intrinsic Pontine Glioma Models. *PLoS One,* 12**,** e0169485.

HIMES, B. T., ZHANG, L. & DANIELS, D. J. 2022. Deploying Kinase Inhibitors to Study Pediatric Gliomas. *Methods Mol Biol,* 2415**,** 167-173.

HOFFMAN, L. M., VAN ZANTEN, S., COLDITZ, N., BAUGH, J., CHANEY, B., LANE, A., FULLER, C., MILES, L., HAWKINS, C., BARTELS, U., BOUFFET, E., GOLDMAN, S., LEARY, S., FOREMAN, N. K., PACKER, R., WARREN, K. E., BRONISCER, A., KIERAN, M. W., MINTURN, J., COMITO, M., BROXON, E., SHIH, C. S., KHATUA, S., CHINTAGUMPALA, M., CARRET, A. S., HASSALL, T., ZIEGLER, D., GOTTARDO, N., DHOLARIA, H., LERME, B., KIRKENDALL, J., DOUGHMAN, R., HOFFMANN, M., WOLLMAN, M., O'KEEFE, R., BENESCH, M., GERBER, N., BAILEY, S., SOLANKI, G., MASSIMINO, M., BIASSONI, V., CVRLJE, F. J., HULLEMAN, E., DRISSI, R., NAZARIAN, J., JABADO, N., VON BUEREN, A. O., PIETSCH, T., GIELEN, G. H., STURM, D., JONES, D. T., PFISTER, S., JONES, C., HARGRAVE, D., SANCHEZ, E., BISON, B., WARMUTH-METZ, M., LEACH, J., JONES, B., VAN VUURDEN, D. G., KRAMM, C. M. & FOULADI, M. 2016. HG-75: CLINICAL, RADIOLOGICAL, AND HISTO-GENETIC CHARACTERISTICS OF LONG-TERM SURVIVORS OF DIFFUSE INTRINSIC PONTINE GLIOMA: A COLLABORATIVE REPORT FROM THE INTERNATIONAL AND SIOP-E DIPG REGISTRIES. *Neuro Oncol,* 18**,** iii65-6.

HOMAN, M. J., FRANSON, A., RAVI, K., ROBERTS, H., PAI, M. P., LIU, C., HE, M., MATVEKAS, A., KOSCHMANN, C. & MARINI, B. L. 2021. Panobinostat penetrates the blood-brain barrier and achieves effective brain concentrations in a murine model. *Cancer Chemother Pharmacol,* 88**,** 555-562.

HORODYCKID, C., CANNEY, M., VIGNOT, A., BOISGARD, R., DRIER, A., HUBERFELD, G., FRANCOIS, C., PRIGENT, A., SANTIN, M. D., ADAM, C., WILLER, J. C., LAFON, C., CHAPELON, J. Y. & CARPENTIER, A. 2017. Safe long-term repeated disruption of the blood-brain barrier using an implantable ultrasound device: a multiparametric study in a primate model. *J Neurosurg,* 126**,** 1351-1361.

HOSSEINKHAH, N., CHEN, H., MATULA, T. J., BURNS, P. N. & HYNYNEN, K. 2013. Mechanisms of microbubble–vessel interactions and induced stresses: A numerical study. *The Journal of the Acoustical Society of America,* 134**,** 1875-1885.

HOSSEINKHAH, N., GOERTZ, D. E. & HYNYNEN, K. 2015. Microbubbles and blood-brain barrier opening: a numerical study on acoustic emissions and wall stress predictions. *IEEE Trans Biomed Eng,* 62**,** 1293-304.

HUANG, X., SHI, S., WANG, H., ZHAO, T., WANG, Y., HUANG, S., SU, Y., ZHAO, C. & YANG, M. 2023. Advances in antibody-based drugs and their delivery through the blood-brain barrier for targeted therapy and immunotherapy of gliomas. *International Immunopharmacology,* 117**,** 109990.

HUNT, J. W., ARDITI, M. & FOSTER, F. S. 1983. Ultrasound transducers for pulse-echo medical imaging. *IEEE Transactions on Biomedical Engineering***,** 453-481.

HWANG, J. H., TU, J., BRAYMAN, A. A., MATULA, T. J. & CRUM, L. A. 2006. Correlation between inertial cavitation dose and endothelial cell damage in vivo. *Ultrasound in Medicine & Biology,* 32**,** 1611-1619.

HYNYNEN, K. & JOLESZ, F. A. 1998. Demonstration of potential noninvasive ultrasound brain therapy through an intact skull. *Ultrasound Med Biol,* 24**,** 275-83.

HYNYNEN, K., MCDANNOLD, N., MARTIN, H., JOLESZ, F. A. & VYKHODTSEVA, N. 2003a. The threshold for brain damage in rabbits induced by bursts of ultrasound in the presence of an ultrasound contrast agent (Optison). *Ultrasound Med Biol,* 29**,** 473-81.

HYNYNEN, K., MCDANNOLD, N., SHEIKOV, N. A., JOLESZ, F. A. & VYKHODTSEVA, N. 2005. Local and reversible blood-brain barrier disruption by noninvasive focused ultrasound at frequencies suitable for trans-skull sonications. *Neuroimage,* 24**,** 12-20.

HYNYNEN, K., MCDANNOLD, N., VYKHODTSEVA, N. & JOLESZ, F. A. 2001. Noninvasive MR imaging-guided focal opening of the blood-brain barrier in rabbits. *Radiology,* 220**,** 640-6.

HYNYNEN, K., MCDANNOLD, N., VYKHODTSEVA, N. & JOLESZ, F. A. 2003b. Non-invasive opening of BBB by focused ultrasound. *Acta Neurochir Suppl,* 86**,** 555-8.

HYNYNEN, K., MCDANNOLD, N., VYKHODTSEVA, N., RAYMOND, S., WEISSLEDER, R., JOLESZ, F. A. & SHEIKOV, N. 2006. Focal disruption of the blood-brain barrier due to 260-kHz ultrasound bursts: a method for molecular imaging and targeted drug delivery. *J Neurosurg,* 105**,** 445-54.

IDBAIH, A., CANNEY, M., BELIN, L., DESSEAUX, C., VIGNOT, A., BOUCHOUX, G., ASQUIER, N., LAW-YE, B., LECLERCQ, D., BISSERY, A., DE RYCKE, Y., TROSCH, C., CAPELLE, L., SANSON, M., HOANG-XUAN, K., DEHAIS, C., HOUILLIER, C., LAIGLE-DONADEY, F., MATHON, B., ANDRÉ, A., LAFON, C., CHAPELON, J. Y., DELATTRE, J. Y. & CARPENTIER, A. 2019. Safety and Feasibility of Repeated and Transient Blood-Brain Barrier Disruption by Pulsed Ultrasound in Patients with Recurrent Glioblastoma. *Clin Cancer Res,* 25**,** 3793-3801.

ILOVITSH, T., ILOVITSH, A., FOIRET, J., CASKEY, C. F., KUSUNOSE, J., FITE, B. Z., ZHANG, H., MAHAKIAN, L. M., TAM, S. & BUTTS-PAULY, K. 2018. Enhanced microbubble contrast agent oscillation following 250 kHz insonation. *Scientific reports,* 8**,** 1-15.

ISHIDA, J., ALLI, S., BONDOC, A., GOLBOURN, B., SABHA, N., MIKLOSKA, K., KRUMHOLTZ, S., SRIKANTHAN, D., FUJITA, N., LUCK, A., MASLINK, C., SMITH, C., HYNYNEN, K. & RUTKA, J. 2021. MRI-guided focused ultrasound enhances drug delivery in experimental diffuse intrinsic pontine glioma. *J Control Release,* 330**,** 1034-1045.

JONES, C., KARAJANNIS, M. A., JONES, D. T. W., KIERAN, M. W., MONJE, M., BAKER, S. J., BECHER, O. J., CHO, Y.-J., GUPTA, N., HAWKINS, C., HARGRAVE, D., HAAS-KOGAN, D. A., JABADO, N., LI, X.-N., MUELLER, S., NICOLAIDES, T., PACKER, R. J., PERSSON, A. I., PHILLIPS, J. J., SIMONDS, E. F., STAFFORD, J. M., TANG, Y., PFISTER, S. M. & WEISS, W. A. 2017. Pediatric high-grade glioma: biologically and clinically in need of new thinking. *Neuro-oncology,* 19**,** 153-161.

KAMIMURA, H. A., FLAMENT, J., VALETTE, J., CAFARELLI, A., ARON BADIN, R., HANTRAYE, P. & LARRAT, B. 2018. Feedback control of microbubble cavitation for ultrasound-mediated blood-brain barrier disruption in non-human primates under magnetic resonance guidance. *J Cereb Blood Flow Metab***,** 271678x17753514.

KHAN, A., GAMBLE, L. D., UPTON, D. H., UNG, C., YU, D. M., EHTEDA, A., PANDHER, R., MAYOH, C., HÉBERT, S. & JABADO, N. 2021. Dual targeting of polyamine synthesis and uptake in diffuse intrinsic pontine gliomas. *Nature communications,* 12**,** 971.

KINOSHITA, M., MCDANNOLD, N., JOLESZ, F. A. & HYNYNEN, K. 2006a. Noninvasive localized delivery of Herceptin to the mouse brain by MRI-guided focused ultrasound-induced blood-brain barrier disruption. *Proc Natl Acad Sci U S A,* 103**,** 11719-23.

KINOSHITA, M., MCDANNOLD, N., JOLESZ, F. A. & HYNYNEN, K. 2006b. Targeted delivery of antibodies through the blood-brain barrier by MRI-guided focused ultrasound. *Biochem Biophys Res Commun,* 340**,** 1085-90.

KIRBY, J., WALSHAW, E. G., YESUDIAN, G. & DEERY, C. 2020. Repeat paediatric dental general anaesthesia at Sheffield Children's NHS Foundation Trust: a service evaluation. *British Dental Journal,* 228**,** 255-258.

KIRCHNER, G. I., MEIER-WIEDENBACH, I. & MANNS, M. P. 2004. Clinical pharmacokinetics of everolimus. *Clin Pharmacokinet,* 43**,** 83-95.

KLUIVER, T. A., ALIEVA, M., VAN VUURDEN, D. G., WEHRENS, E. J. & RIOS, A. C. 2020. Invaders Exposed: Understanding and Targeting Tumor Cell Invasion in Diffuse Intrinsic Pontine Glioma. *Front Oncol,* 10**,** 92.

KNOX, E. G., ABURTO, M. R., CLARKE, G., CRYAN, J. F. & O'DRISCOLL, C. M. 2022. The blood-brain barrier in aging and neurodegeneration. *Molecular Psychiatry,* 27**,** 2659-2673.

KNUDSEN, E. S. & WITKIEWICZ, A. K. 2017. The strange case of CDK4/6 inhibitors: mechanisms, resistance, and combination strategies. *Trends in cancer,* 3**,** 39-55.

KOBUS, T., ZERVANTONAKIS, I. K., ZHANG, Y. & MCDANNOLD, N. J. 2016. Growth inhibition in a brain metastasis model by antibody delivery using focused ultrasound-mediated blood-brain barrier disruption. *J Control Release,* 238**,** 281-288.

KOMMIDI, H., GUO, H., NURILI, F., VEDVYAS, Y., JIN, M. M., MCCLURE, T. D., EHDAIE, B., SAYMAN, H. B., AKIN, O. & ARAS, O. 2018. 18F-positron emitting/trimethine cyanine-

fluorescent contrast for image-guided prostate cancer management. *Journal of medicinal chemistry,* 61**,** 4256-4262.

KONOFAGOU, E., CHEN, C., CHEN, H., DOWNS, M., FERRERA, V., OLUMOLADE, O., SAMIOTAKI, G., SUN, T., WANG, S. & WU, S.-Y. 2014. Drug delivery through the opened blood-brain barrier in mice and non-human primates. *The Journal of the Acoustical Society of America,* 135**,** 2210-2210.

KOVACS, Z. I., BURKS, S. R. & FRANK, J. A. 2018. Focused ultrasound with microbubbles induces sterile inflammatory response proportional to the blood brain barrier opening: Attention to experimental conditions. *Theranostics,* 8**,** 2245-2248.

KOVACS, Z. I., KIM, S., JIKARIA, N., QURESHI, F., MILO, B., LEWIS, B. K., BRESLER, M., BURKS, S. R. & FRANK, J. A. 2017. Disrupting the blood-brain barrier by focused ultrasound induces sterile inflammation. *Proc Natl Acad Sci U S A,* 114**,** E75-e84.

KUROKAWA, R., KUROKAWA, M., BABA, A., OTA, Y., PINARBASI, E., CAMELO-PIRAGUA, S., CAPIZZANO, A. A., LIAO, E., SRINIVASAN, A. & MORITANI, T. 2022. Major Changes in 2021 World Health Organization Classification of Central Nervous System Tumors. *Radiographics,* 42**,** 1474-1493.

LAPIN, N. A., GILL, K., SHAH, B. R. & CHOPRA, R. 2020. Consistent opening of the blood brain barrier using focused ultrasound with constant intravenous infusion of microbubble agent. *Scientific reports,* 10**,** 16546.

LEIGHTON, T. G. & APFEL, R. E. 1994. The Acoustic Bubble. *The Journal of the Acoustical Society of America,* 96**,** 2616-2616.

LIN, C. Y., HSIEH, H. Y., CHEN, C. M., WU, S. R., TSAI, C. H., HUANG, C. Y., HUA, M. Y., WEI, K. C., YEH, C. K. & LIU, H. L. 2016. Non-invasive, neuron-specific gene therapy by focused ultrasound-induced blood-brain barrier opening in Parkinson's disease mouse model. *J Control Release,* 235**,** 72-81.

LIN, G. L., NAGARAJA, S., FILBIN, M. G., SUVÀ, M. L., VOGEL, H. & MONJE, M. 2018. Non-inflammatory tumor microenvironment of diffuse intrinsic pontine glioma. *Acta neuropathologica communications,* 6**,** 51-51.

LIN, G. L., WILSON, K. M., CERIBELLI, M., STANTON, B. Z., WOO, P. J., KREIMER, S., QIN, E. Y., ZHANG, X., LENNON, J., NAGARAJA, S., MORRIS, P. J., QUEZADA, M., GILLESPIE, S. M., DUVEAU, D. Y., MICHALOWSKI, A. M., SHINN, P., GUHA, R., FERRER, M., KLUMPP-THOMAS,

C., MICHAEL, S., MCKNIGHT, C., MINHAS, P., ITKIN, Z., RAABE, E. H., CHEN, L., GHANEM, R., GERAGHTY, A. C., NI, L., ANDREASSON, K. I., VITANZA, N. A., WARREN, K. E., THOMAS, C. J. & MONJE, M. 2019. Therapeutic strategies for diffuse midline glioma from high-throughput combination drug screening. *Sci Transl Med,* 11.

LINDNER, J. R. 2004. Microbubbles in medical imaging: current applications and future directions. *Nature Reviews Drug Discovery,* 3**,** 527-533.

LIPSMAN, N., MENG, Y., BETHUNE, A. J., HUANG, Y., LAM, B., MASELLIS, M., HERRMANN, N., HEYN, C., AUBERT, I., BOUTET, A., SMITH, G. S., HYNYNEN, K. & BLACK, S. E. 2018. Blood-brain barrier opening in Alzheimer's disease using MR-guided focused ultrasound. *Nat Commun,* 9**,** 2336.

LIU, H.-L., HSU, P.-H., LIN, C.-Y., HUANG, C.-W., CHAI, W.-Y., CHU, P.-C., HUANG, C.-Y., CHEN, P.-Y., YANG, L.-Y., KUO, J. S. & WEI, K.-C. 2016. Focused Ultrasound Enhances Central Nervous System Delivery of Bevacizumab for Malignant Glioma Treatment. *Radiology,* 281**,** 99-108.

LIU, H. L., CHEN, H. W., KUO, Z. H. & HUANG, W. C. 2008a. Design and experimental evaluations of a low-frequency hemispherical ultrasound phased-array system for transcranial blood-brain barrier disruption. *IEEE Trans Biomed Eng,* 55**,** 2407-16.

LIU, H. L., HSU, P. H., CHU, P. C., WAI, Y. Y., CHEN, J. C., SHEN, C. R., YEN, T. C. & WANG, J. J. 2009. Magnetic resonance imaging enhanced by superparamagnetic iron oxide particles: usefulness for distinguishing between focused ultrasound-induced blood-brain barrier disruption and brain hemorrhage. *J Magn Reson Imaging,* 29**,** 31-8.

LIU, H. L., PAN, C. H., TING, C. Y. & HSIAO, M. J. 2010. Opening of the blood-brain barrier by low-frequency (28-kHz) ultrasound: a novel pinhole-assisted mechanical scanning device. *Ultrasound Med Biol,* 36**,** 325-35.

LIU, H. L., WAI, Y. Y., CHEN, W. S., CHEN, J. C., HSU, P. H., WU, X. Y., HUANG, W. C., YEN, T. C. & WANG, J. J. 2008b. Hemorrhage detection during focused-ultrasound induced blood-brain-barrier opening by using susceptibility-weighted magnetic resonance imaging. *Ultrasound Med Biol,* 34**,** 598-606.

LONG, W., YI, Y., CHEN, S., CAO, Q., ZHAO, W. & LIU, Q. 2017. Potential New Therapies for Pediatric Diffuse Intrinsic Pontine Glioma. *Front Pharmacol,* 8**,** 495.

LOUIS, D. N., PERRY, A., REIFENBERGER, G., VON DEIMLING, A., FIGARELLA-BRANGER, D., CAVENEE, W. K., OHGAKI, H., WIESTLER, O. D., KLEIHUES, P. & ELLISON, D. W. 2016. The 2016 World Health Organization Classification of Tumors of the Central Nervous System: a summary. *Acta Neuropathol,* 131**,** 803-20.

LOVÉN, J., HOKE, H. A., LIN, C. Y., LAU, A., ORLANDO, D. A., VAKOC, C. R., BRADNER, J. E., LEE, T. I. & YOUNG, R. A. 2013. Selective inhibition of tumor oncogenes by disruption of super-enhancers. *Cell,* 153**,** 320-334.

MACKAY, A., BURFORD, A., CARVALHO, D., IZQUIERDO, E., FAZAL-SALOM, J., TAYLOR, K. R., BJERKE, L., CLARKE, M., VINCI, M. & NANDHABALAN, M. 2017. Integrated molecular meta-analysis of 1,000 pediatric high-grade and diffuse intrinsic pontine glioma. *Cancer cell,* 32**,** 520-537. e5.

MARCHI, N., ANGELOV, L., MASARYK, T., FAZIO, V., GRANATA, T., HERNANDEZ, N., HALLENE, K., DIGLAW, T., FRANIC, L., NAJM, I. & JANIGRO, D. 2007. Seizure-promoting effect of blood-brain barrier disruption. *Epilepsia,* 48**,** 732-42.

MARQUET, F., TEICHERT, T., WU, S. Y., TUNG, Y. S., DOWNS, M., WANG, S., CHEN, C., FERRERA, V. & KONOFAGOU, E. E. 2014. Real-time, transcranial monitoring of safe blood-brain barrier opening in non-human primates. *PLoS One,* 9**,** e84310.

MARTY, B., LARRAT, B., VAN LANDEGHEM, M., ROBIC, C., ROBERT, P., PORT, M., LE BIHAN, D., PERNOT, M., TANTER, M., LETHIMONNIER, F. & MERIAUX, S. 2012. Dynamic study of blood-brain barrier closure after its disruption using ultrasound: a quantitative analysis. *J Cereb Blood Flow Metab,* 32**,** 1948-58.

MARTYNOV, S., STRIDE, E. & SAFFARI, N. 2009. The natural frequencies of microbubble oscillation in elastic vessels. *The Journal of the Acoustical Society of America,* 126**,** 2963-2972.

MCDANNOLD, N., ARVANITIS, C. D., VYKHODTSEVA, N. & LIVINGSTONE, M. S. 2012. Temporary disruption of the blood-brain barrier by use of ultrasound and microbubbles: safety and efficacy evaluation in rhesus macaques. *Cancer Res,* 72**,** 3652-63.

MCDANNOLD, N., VYKHODTSEVA, N. & HYNYNEN, K. 2006a. Targeted disruption of the blood-brain barrier with focused ultrasound: association with cavitation activity. *Phys Med Biol,* 51**,** 793-807.

MCDANNOLD, N., VYKHODTSEVA, N. & HYNYNEN, K. 2006b. Targeted disruption of the blood–brain barrier with focused ultrasound: association with cavitation activity. *Physics in Medicine & Biology,* 51**,** 793.

MCDANNOLD, N., VYKHODTSEVA, N. & HYNYNEN, K. 2007. Use of ultrasound pulses combined with Definity for targeted blood-brain barrier disruption: a feasibility study. *Ultrasound Med Biol,* 33**,** 584-90.

MCDANNOLD, N., VYKHODTSEVA, N. & HYNYNEN, K. 2008. Effects of acoustic parameters and ultrasound contrast agent dose on focused-ultrasound induced blood-brain barrier disruption. *Ultrasound Med Biol,* 34**,** 930-7.

MCDANNOLD, N., VYKHODTSEVA, N., RAYMOND, S., JOLESZ, F. A. & HYNYNEN, K. 2005. MRI-guided targeted blood-brain barrier disruption with focused ultrasound: histological findings in rabbits. *Ultrasound Med Biol,* 31**,** 1527-37.

MCDANNOLD, N., ZHANG, Y., POWER, C., ARVANITIS, C. D., VYKHODTSEVA, N. & LIVINGSTONE, M. 2015. Targeted, noninvasive blockade of cortical neuronal activity. *Sci Rep,* 5**,** 16253.

MCDANNOLD, N., ZHANG, Y. & VYKHODTSEVA, N. 2011. Blood-brain barrier disruption and vascular damage induced by ultrasound bursts combined with microbubbles can be influenced by choice of anesthesia protocol. *Ultrasound Med Biol,* 37**,** 1259-70.

MCMAHON, D., DENG, L. & HYNYNEN, K. 2021. Comparing rapid short-pulse to tone burst sonication sequences for focused ultrasound and microbubble-mediated blood-brain barrier permeability enhancement. *Journal of Controlled Release,* 329**,** 696-705.

MCMAHON, D. & HYNYNEN, K. 2017. Acute Inflammatory Response Following Increased Blood-Brain Barrier Permeability Induced by Focused Ultrasound is Dependent on Microbubble Dose. *Theranostics,* 7**,** 3989-4000.

MCMAHON, D., LASSUS, A., GAUD, E., JEANNOT, V. & HYNYNEN, K. 2020. Microbubble formulation influences inflammatory response to focused ultrasound exposure in the brain. *Sci Rep,* 10**,** 21534.

MEEL, M. H., DE GOOIJER, M. C., METSELAAR, D. S., SEWING, A. C. P., ZWAAN, K., WARANECKI, P., BREUR, M., BUIL, L. C., LAGERWEIJ, T. & WEDEKIND, L. E. 2020. Combined therapy of AXL and HDAC inhibition reverses mesenchymal transition in diffuse intrinsic pontine glioma. *Clinical Cancer Research,* 26**,** 3319-3332.

MENG, Y., REILLY, R. M., PEZO, R. C., TRUDEAU, M., SAHGAL, A., SINGNURKAR, A., PERRY, J., MYREHAUG, S., POPLE, C. B., DAVIDSON, B., LLINAS, M., HYEN, C., HUANG, Y., HAMANI, C., SUPPIAH, S., HYNYNEN, K. & LIPSMAN, N. 2021. MR-guided focused ultrasound enhances delivery of trastuzumab to Her2-positive brain metastases. *Sci Transl Med,* 13**,** eabj4011.

MILLER, D. L., SMITH, N. B., BAILEY, M. R., CZARNOTA, G. J., HYNYNEN, K. & MAKIN, I. R. 2012. Overview of therapeutic ultrasound applications and safety considerations. *J Ultrasound Med,* 31**,** 623-34.

MOHAMMAD, F., WEISSMANN, S., LEBLANC, B., PANDEY, D. P., HØJFELDT, J. W., COMET, I., ZHENG, C., JOHANSEN, J. V., RAPIN, N. & PORSE, B. T. 2017. EZH2 is a potential therapeutic target for H3K27M-mutant pediatric gliomas. *Nature medicine,* 23**,** 483-492.

MONJE, M., COONEY, T., GLOD, J., HUANG, J., BAXTER, P., VINITSKY, A., KILBURN, L., ROBISON, N. J., PEER, C. J. & FIGG, W. D. 2022. DIPG-10. A Phase I trial of panobinostat following radiation therapy in children with diffuse intrinsic pontine glioma (DIPG) or H3K27M-mutated thalamic diffuse midline glioma (DMG): Report from the Pediatric Brain Tumor Consortium (PBTC-047). *Neuro-Oncology,* 24**,** i19-i20.

MOORE, D. 2016. Panobinostat (Farydak): A Novel Option for the Treatment of Relapsed Or Relapsed and Refractory Multiple Myeloma. *P t,* 41**,** 296-300.

MORISHITA, K., KARASUNO, H., YOKOI, Y., MOROZUMI, K., OGIHARA, H., ITO, T., HANAOKA, M., FUJIWARA, T., FUJIMOTO, T. & ABE, K. 2014. Effects of therapeutic ultrasound on range of motion and stretch pain. *J Phys Ther Sci,* 26**,** 711-5.

MORSE, S. V. 2020. *In vivo evaluation of the efficacy and safety of rapid short-pulse sequences for ultrasound-medicated delivery of agents to the brain.* Doctor of Philosphy (PhD), Imperial College London.

MORSE, S. V., MISHRA, A., CHAN, T. G., R, T. M. D. R. & CHOI, J. J. 2022. Liposome delivery to the brain with rapid short-pulses of focused ultrasound and microbubbles. *J Control Release,* 341**,** 605-615.

MORSE, S. V., POULIOPOULOS, A. N., CHAN, T. G., COPPING, M. J., LIN, J., LONG, N. J. & CHOI, J. J. 2019. Rapid Short-pulse Ultrasound Delivers Drugs Uniformly across the Murine Blood-Brain Barrier with Negligible Disruption. *Radiology,* 291**,** 459-466.

MOUNT, C. W., MAJZNER, R. G., SUNDARESH, S., ARNOLD, E. P., KADAPAKKAM, M., HAILE, S., LABANIEH, L., HULLEMAN, E., WOO, P. J., RIETBERG, S. P., VOGEL, H., MONJE, M. &

MACKALL, C. L. 2018. Potent antitumor efficacy of anti-GD2 CAR T cells in H3-K27M+ diffuse midline gliomas. *Nature Medicine,* 24**,** 572-579.

MULLARD, A. 2021. FDA approves 100th monoclonal antibody product. *Nature reviews. Drug discovery,* 20**,** 491-495.

NHAN, T., BURGESS, A., CHO, E. E., STEFANOVIC, B., LILGE, L. & HYNYNEN, K. 2013. Drug delivery to the brain by focused ultrasound induced blood-brain barrier disruption: quantitative evaluation of enhanced permeability of cerebral vasculature using two-photon microscopy. *J Control Release,* 172**,** 274-280.

NICE. 2016. *Panobinostat for treating multiple myeloma after at least 2 previous treatments* [Online]. National Institute for Health and Care Excellence. Available: https://www.nice.org.uk/guidance/ta380/chapter/6-Review-of-guidance [Accessed 22/03/2023 2023].

NOLSØE, C. P., X000E, LLSON & LORENTZEN, T. 2016. International guidelines for contrast-enhanced ultrasonography: ultrasound imaging in the new millennium. *Ultrasonography,* 35**,** 89-103.

NOROOZIAN, Z., XHIMA, K., HUANG, Y., KASPAR, B. K., KÜGLER, S., HYNYNEN, K. & AUBERT, I. 2019. MRI-Guided Focused Ultrasound for Targeted Delivery of rAAV to the Brain. *Methods Mol Biol,* 1950**,** 177-197.

O'REILLY, M. A., HOUGH, O. & HYNYNEN, K. 2017a. Blood-Brain Barrier Closure Time After Controlled Ultrasound-Induced Opening Is Independent of Opening Volume. *J Ultrasound Med,* 36**,** 475-483.

O'REILLY, M. A., HUANG, Y. & HYNYNEN, K. 2010. The impact of standing wave effects on transcranial focused ultrasound disruption of the blood-brain barrier in a rat model. *Phys Med Biol,* 55**,** 5251-67.

O'REILLY, M. A., JONES, R. M., BARRETT, E., SCHWAB, A., HEAD, E. & HYNYNEN, K. 2017b. Investigation of the Safety of Focused Ultrasound-Induced Blood-Brain Barrier Opening in a Natural Canine Model of Aging. *Theranostics,* 7**,** 3573-3584.

OMATA, D., MARUYAMA, T., UNGA, J., HAGIWARA, F., MUNAKATA, L., KAGEYAMA, S., SHIMA, T., SUZUKI, Y., MARUYAMA, K. & SUZUKI, R. 2019. Effects of encapsulated gas on stability of lipid-based microbubbles and ultrasound-triggered drug delivery. *Journal of Controlled Release,* 311**,** 65-73.

PANDIT, R., KOH, W. K., SULLIVAN, R. K., PALLIYAGURU, T., PARTON, R. G. & GÖTZ, J. 2020. Role for caveolin-mediated transcytosis in facilitating transport of large cargoes into the brain via ultrasound. *Journal of Controlled Release,* 327**,** 667-675.

PARK, E. J., ZHANG, Y. Z., VYKHODTSEVA, N. & MCDANNOLD, N. 2012. Ultrasound-mediated blood-brain/blood-tumor barrier disruption improves outcomes with trastuzumab in a breast cancer brain metastasis model. *J Control Release,* 163**,** 277-84.

PARK, S. H., KIM, M. J., JUNG, H. H., CHANG, W. S., CHOI, H. S., RACHMILEVITCH, I., ZADICARIO, E. & CHANG, J. W. 2020. Safety and feasibility of multiple blood-brain barrier disruptions for the treatment of glioblastoma in patients undergoing standard adjuvant chemotherapy. *J Neurosurg***,** 1-9.

PELEKANOS, M., LEINENGA, G., ODABAEE, M., ODABAEE, M., SAIFZADEH, S., STECK, R. & GOTZ, J. 2018. Establishing sheep as an experimental species to validate ultrasound-mediated blood-brain barrier opening for potential therapeutic interventions. *Theranostics,* 8**,** 2583-2602.

PIUNTI, A., HASHIZUME, R., MORGAN, M. A., BARTOM, E. T., HORBINSKI, C. M., MARSHALL, S. A., RENDLEMAN, E. J., MA, Q., TAKAHASHI, Y.-H. & WOODFIN, A. R. 2017. Therapeutic targeting of polycomb and BET bromodomain proteins in diffuse intrinsic pontine gliomas. *Nature medicine,* 23**,** 493-500.

POULIOPOULOS, A. N., BONACCORSI, S. & CHOI, J. J. 2014. Exploiting flow to control thein vitrospatiotemporal distribution of microbubble-seeded acoustic cavitation activity in ultrasound therapy. *Physics in Medicine and Biology,* 59**,** 6941-6957.

POULIOPOULOS, A. N., LI, C., TINGUELY, M., GARBIN, V., TANG, M.-X. & CHOI, J. J. 2016. Rapid short-pulse sequences enhance the spatiotemporal uniformity of acoustically driven microbubble activity during flow conditions. *The Journal of the Acoustical Society of America,* 140**,** 2469-2480.

POULIOPOULOS, A. N., WU, S.-Y., BURGESS, M. T., KARAKATSANI, M. E., KAMIMURA, H. A. & KONOFAGOU, E. E. 2020. A clinical system for non-invasive blood–brain barrier opening using a neuronavigation-guided single-element focused ultrasound transducer. *Ultrasound in medicine & biology,* 46**,** 73-89.

QI, D., LI, J., QUARLES, C. C., FONKEM, E. & WU, E. 2022. Assessment and prediction of glioblastoma therapy response: challenges and opportunities. *Brain*.

QIN, E. Y., COOPER, D. D., ABBOTT, K. L., LENNON, J., NAGARAJA, S., MACKAY, A., JONES, C., VOGEL, H., JACKSON, P. K. & MONJE, M. 2017. Neural Precursor-Derived Pleiotrophin Mediates Subventricular Zone Invasion by Glioma. *Cell,* 170**,** 845-859.e19.

QIN, S. & FERRARA, K. W. 2006. Acoustic response of compliable microvessels containing ultrasound contrast agents. *Physics in Medicine & Biology,* 51**,** 5065.

QUADER, S., KATAOKA, K. & CABRAL, H. 2022. Nanomedicine for brain cancer. *Advanced Drug Delivery Reviews,* 182**,** 114115.

RAGGI, A. & LEONARDI, M. 2020. Burden of brain disorders in Europe in 2017 and comparison with other non-communicable disease groups. *J Neurol Neurosurg Psychiatry,* 91**,** 104-105.

RALFF, M. D., LULLA, A. R., WAGNER, J. & EL-DEIRY, W. S. 2017. ONC201: a new treatment option being tested clinically for recurrent glioblastoma. *Translational Cancer Research***,** S1239-S1243.

RINCON-TORROELLA, J., KHELA, H., BETTEGOWDA, A. & BETTEGOWDA, C. 2022. Biomarkers and focused ultrasound: the future of liquid biopsy for brain tumor patients. *Journal of neuro-oncology***,** 1-16.

RODGERS, L. T., LESTER MCCULLY, C. M., ODABAS, A., CRUZ, R., PEER, C. J., FIGG, W. D. & WARREN, K. E. 2020. Characterizing the pharmacokinetics of panobinostat in a non-human primate model for the treatment of diffuse intrinsic pontine glioma. *Cancer chemotherapy and pharmacology,* 85**,** 827-830.

ROSS, J. L., CHEN, Z., HERTING, C. J., GRABOVSKA, Y., SZULZEWSKY, F., PUIGDELLOSES, M., MONTERROZA, L., SWITCHENKO, J., WADHWANI, N. R. & CIMINO, P. J. 2021. Platelet-derived growth factor beta is a potent inflammatory driver in paediatric high-grade glioma. *Brain,* 144**,** 53-69.

ROUJEAU, T., MACHADO, G., GARNETT, M. R., MIQUEL, C., PUGET, S., GEOERGER, B., GRILL, J., BODDAERT, N., DI ROCCO, F., ZERAH, M. & SAINTE-ROSE, C. 2007. Stereotactic biopsy of diffuse pontine lesions in children. *J Neurosurg,* 107**,** 1-4.

SABBAGH, A., BECCARIA, K., LING, X., MARISETTY, A., OTT, M., CARUSO, H., BARTON, E., KONG, L.-Y., FANG, D., LATHA, K., ZHANG, D. Y., WEI, J., DEGROOT, J., CURRAN, M. A., RAO, G., HU, J., DESSEAUX, C., BOUCHOUX, G., CANNEY, M., CARPENTIER, A. & HEIMBERGER, A. B. 2021. Opening of the Blood–Brain Barrier Using Low-Intensity Pulsed Ultrasound Enhances

Responses to Immunotherapy in Preclinical Glioma Models. *Clinical Cancer Research,* 27**,** 4325-4337.

SAMIOTAKI, G., KARAKATSANI, M. E., BUCH, A., PAPADOPOULOS, S., WU, S. Y., JAMBAWALIKAR, S. & KONOFAGOU, E. E. 2017. Pharmacokinetic analysis and drug delivery efficiency of the focused ultrasound-induced blood-brain barrier opening in non-human primates. *Magn Reson Imaging,* 37**,** 273-281.

SAMIOTAKI, G. & KONOFAGOU, E. E. 2013. Dependence of the reversibility of focused-ultrasound-induced blood-brain barrier opening on pressure and pulse length in vivo. *IEEE Trans Ultrason Ferroelectr Freq Control,* 60**,** 2257-65.

SAMIOTAKI, G., VLACHOS, F., TUNG, Y. S. & KONOFAGOU, E. E. 2012. A quantitative pressure and microbubble-size dependence study of focused ultrasound-induced blood-brain barrier opening reversibility in vivo using MRI. *Magn Reson Med,* 67**,** 769-77.

SAMUEL, S., COOPER, M. A., BULL, J. L., FOWLKES, J. B. & MILLER, D. L. 2009. An ex vivo study of the correlation between acoustic emission and microvascular damage. *Ultrasound Med Biol,* 35**,** 1574-86.

SASSAROLI, E. & HYNYNEN, K. 2005. Resonance frequency of microbubbles in small blood vessels: a numerical study. *Physics in Medicine and Biology,* 50**,** 5293-5305.

SASSAROLI, E. & HYNYNEN, K. 2006. On the impact of vessel size on the threshold of bubble collapse. *Applied Physics Letters,* 89**,** 123901.

SCHOEN, S., KILINC, M. S., LEE, H., GUO, Y., DEGERTEKIN, F. L., WOODWORTH, G. F. & ARVANITIS, C. 2022. Towards controlled drug delivery in brain tumors with microbubble-enhanced focused ultrasound. *Advanced Drug Delivery Reviews,* 180**,** 114043.

SCHROEDER, K. M., HOEMAN, C. M. & BECHER, O. J. 2014. Children are not just little adults: recent advances in understanding of diffuse intrinsic pontine glioma biology. *Pediatr Res,* 75**,** 205-9.

SHEIKOV, N., MCDANNOLD, N., JOLESZ, F., ZHANG, Y. Z., TAM, K. & HYNYNEN, K. 2006. Brain arterioles show more active vesicular transport of blood-borne tracer molecules than capillaries and venules after focused ultrasound-evoked opening of the blood-brain barrier. *Ultrasound Med Biol,* 32**,** 1399-409.

SHEIKOV, N., MCDANNOLD, N., SHARMA, S. & HYNYNEN, K. 2008. Effect of focused ultrasound applied with an ultrasound contrast agent on the tight junctional integrity of the brain microvascular endothelium. *Ultrasound Med Biol,* 34**,** 1093-104.

SHEIKOV, N., MCDANNOLD, N., VYKHODTSEVA, N., JOLESZ, F. & HYNYNEN, K. 2004. Cellular mechanisms of the blood-brain barrier opening induced by ultrasound in presence of microbubbles. *Ultrasound Med Biol,* 30**,** 979-89.

SHEN, Y., GUO, J., CHEN, G., CHIN, C. T., CHEN, X., CHEN, J., WANG, F., CHEN, S. & DAN, G. 2016. Delivery of Liposomes with Different Sizes to Mice Brain after Sonication by Focused Ultrasound in the Presence of Microbubbles. *Ultrasound Med Biol,* 42**,** 1499-511.

SHEYBANI, N. D., BREZA, V. R., PAUL, S., MCCAULEY, K. S., BERR, S. S., MILLER, G. W., NEUMANN, K. D. & PRICE, R. J. 2021. ImmunoPET-informed sequence for focused ultrasound-targeted mCD47 blockade controls glioma. *Journal of Controlled Release,* 331**,** 19-29.

SHIN, J., KONG, C., CHO, J. S., LEE, J., KOH, C. S., YOON, M.-S., NA, Y. C., CHANG, W. S. & CHANG, J. W. 2018a. Focused ultrasound–mediated noninvasive blood-brain barrier modulation: preclinical examination of efficacy and safety in various sonication parameters. *Neurosurgical Focus,* 44**,** E15.

SHIN, J., KONG, C., CHO, J. S., LEE, J., KOH, C. S., YOON, M. S., NA, Y. C., CHANG, W. S. & CHANG, J. W. 2018b. Focused ultrasound-mediated noninvasive blood-brain barrier modulation: preclinical examination of efficacy and safety in various sonication parameters. *Neurosurg Focus,* 44**,** E15.

SHRIKI, J. 2014. Ultrasound Physics. *Critical Care Clinics,* 30**,** 1-24.

SIERRA, C., ACOSTA, C., CHEN, C., WU, S. Y., KARAKATSANI, M. E., BERNAL, M. & KONOFAGOU, E. E. 2017. Lipid microbubbles as a vehicle for targeted drug delivery using focused ultrasound-induced blood-brain barrier opening. *J Cereb Blood Flow Metab,* 37**,** 1236-1250.

SIM, H.-W., GALANIS, E. & KHASRAW, M. 2022. PARP inhibitors in glioma: a review of therapeutic opportunities. *Cancers,* 14**,** 1003.

SIRSI, S. & BORDEN, M. 2009. Microbubble Compositions, Properties and Biomedical Applications. *Bubble Sci Eng Technol,* 1**,** 3-17.

SONG, K. H., FAN, A. C., HINKLE, J. J., NEWMAN, J., BORDEN, M. A. & HARVEY, B. K. 2017. Microbubble gas volume: A unifying dose parameter in blood-brain barrier opening by focused ultrasound. *Theranostics,* 7**,** 144-152.

SRIKANTHAN, D., TACCONE, M. S., VAN OMMEREN, R., ISHIDA, J., KRUMHOLTZ, S. L. & RUTKA, J. T. 2021. Diffuse intrinsic pontine glioma: current insights and future directions. *Chin Neurosurg J,* 7**,** 6.

STAMATOVIC, S. M., JOHNSON, A. M., KEEP, R. F. & ANDJELKOVIC, A. V. 2016. Junctional proteins of the blood-brain barrier: New insights into function and dysfunction. *Tissue Barriers,* 4**,** e1154641.

STAVARACHE, M. A., PETERSEN, N., JURGENS, E. M., MILSTEIN, E. R., ROSENFELD, Z. B., BALLON, D. J. & KAPLITT, M. G. 2018. Safe and stable noninvasive focal gene delivery to the mammalian brain following focused ultrasound. *J Neurosurg***,** 1-10.

STEEG, P. S. 2021. The blood–tumour barrier in cancer biology and therapy. *Nature Reviews Clinical Oncology,* 18**,** 696-714.

STIEGER, S. M., CASKEY, C. F., ADAMSON, R. H., QIN, S., CURRY, F.-R. E., WISNER, E. R. & FERRARA, K. W. 2007. Enhancement of vascular permeability with low-frequency contrast-enhanced ultrasound in the chorioallantoic membrane model. *Radiology,* 243**,** 112-121.

STINE, C. A. & MUNSON, J. M. 2019. Convection-Enhanced Delivery: Connection to and Impact of Interstitial Fluid Flow. *Frontiers in Oncology,* 9.

TAYLOR, I. C., HÜTT-CABEZAS, M., BRANDT, W. D., KAMBHAMPATI, M., NAZARIAN, J., CHANG, H. T., WARREN, K. E., EBERHART, C. G. & RAABE, E. H. 2015. Disrupting NOTCH slows diffuse intrinsic pontine glioma growth, enhances radiation sensitivity, and shows combinatorial efficacy with bromodomain inhibition. *Journal of Neuropathology & Experimental Neurology,* 74**,** 778-790.

TRAN, V. L., NOVELL, A., TOURNIER, N., GERSTENMAYER, M., SCHWEITZER-CHAPUT, A., MATEOS, C., JEGO, B., BOULEAU, A., NOZACH, H. & WINKELER, A. 2020. Impact of blood-brain barrier permeabilization induced by ultrasound associated to microbubbles on the brain delivery and kinetics of cetuximab: An immunoPET study using 89Zr-cetuximab. *Journal of Controlled Release,* 328**,** 304-312.

TSAI, H.-C., TSAI, C.-H., CHEN, W.-S., INSERRA, C., WEI, K.-C. & LIU, H.-L. 2018a. Safety evaluation of frequent application of microbubble-enhanced focused ultrasound blood-brain-barrier opening. *Scientific Reports,* 8**,** 17720.

TSAI, H. C., TSAI, C. H., CHEN, W. S., INSERRA, C., WEI, K. C. & LIU, H. L. 2018b. Safety evaluation of frequent application of microbubble-enhanced focused ultrasound blood-brain-barrier opening. *Sci Rep,* 8**,** 17720.

TSAI, M. T., ZHANG, J. W., WEI, K. C., YEH, C. K. & LIU, H. L. 2018c. Assessment of temporary cerebral effects induced by focused ultrasound with optical coherence tomography angiography. *Biomed Opt Express,* 9**,** 507-517.

TSOLI, M., LIU, J., FRANSHAW, L., SHEN, H., CHENG, C., JUNG, M., JOSHI, S., EHTEDA, A., KHAN, A. & MONTERO-CARCABOSSO, A. 2018. Dual targeting of mitochondrial function and mTOR pathway as a therapeutic strategy for diffuse intrinsic pontine glioma. *Oncotarget,* 9**,** 7541.

TU, J., MATULA, T. J., BRAYMAN, A. A. & CRUM, L. A. 2006. Inertial cavitation dose produced in ex vivo rabbit ear arteries with Optison by 1-MHz pulsed ultrasound. *Ultrasound in medicine & biology,* 32 2**,** 281-8.

VALDEZ, M. A., FERNANDEZ, E., MATSUNAGA, T., ERICKSON, R. P. & TROUARD, T. P. 2020. Distribution and diffusion of macromolecule delivery to the brain via focused ultrasound using magnetic resonance and multispectral fluorescence imaging. *Ultrasound in medicine & biology,* 46**,** 122-136.

VANAN, M. I. & EISENSTAT, D. D. 2015. DIPG in Children - What Can We Learn from the Past?

VERINGA, S. J., BIESMANS, D., VAN VUURDEN, D. G., JANSEN, M. H., WEDEKIND, L. E., HORSMAN, I., WESSELING, P., VANDERTOP, W. P., NOSKE, D. P., KASPERS, G. J. & HULLEMAN, E. 2013. In vitro drug response and efflux transporters associated with drug resistance in pediatric high grade glioma and diffuse intrinsic pontine glioma. *PLoS One,* 8**,** e61512.

VLACHOS, F., TUNG, Y. S. & KONOFAGOU, E. 2011. Permeability dependence study of the focused ultrasound-induced blood-brain barrier opening at distinct pressures and microbubble diameters using DCE-MRI. *Magn Reson Med,* 66**,** 821-30.

WANG, S., SAMIOTAKI, G., OLUMOLADE, O., FESHITAN, J. A. & KONOFAGOU, E. E. 2014. Microbubble type and distribution dependence of focused ultrasound-induced blood-brain barrier opening. *Ultrasound Med Biol,* 40**,** 130-7.

WARREN, K. E. 2018. Beyond the Blood:Brain Barrier: The Importance of Central Nervous System (CNS) Pharmacokinetics for the Treatment of CNS Tumors, Including Diffuse Intrinsic Pontine Glioma. *Front Oncol,* 8**,** 239.

WEINHOLD, B. 2006. Epigenetics: the science of change. *Environ Health Perspect,* 114**,** A160-7.

WENG, J. C., WU, S. K., LIN, W. L. & TSENG, W. Y. 2011. Detecting blood-brain barrier disruption within minimal hemorrhage following transcranial focused ultrasound: a correlation study with contrast-enhanced MRI. *Magn Reson Med,* 65**,** 802-11.

WERBROUCK, C., EVANGELISTA, C. C. S., LOBÓN-IGLESIAS, M.-J., BARRET, E., LE TEUFF, G., MERLEVEDE, J., BRUSINI, R., KERGROHEN, T., MONDINI, M., BOLLE, S., VARLET, P., BECCARIA, K., BODDAERT, N., PUGET, S., GRILL, J., DEBILY, M.-A. & CASTEL, D. 2019. TP53 Pathway Alterations Drive Radioresistance in Diffuse Intrinsic Pontine Gliomas (DIPG). *Clinical Cancer Research,* 25**,** 6788-6800.

WILLIAMS, J. R., YOUNG, C. C., VITANZA, N. A., MCGRATH, M., FEROZE, A. H., BROWD, S. R. & HAUPTMAN, J. S. 2020. Progress in diffuse intrinsic pontine glioma: advocating for stereotactic biopsy in the standard of care. *Neurosurgical Focus FOC,* 48**,** E4.

WU, S. K., CHU, P. C., CHAI, W. Y., KANG, S. T., TSAI, C. H., FAN, C. H., YEH, C. K. & LIU, H. L. 2017. Characterization of Different Microbubbles in Assisting Focused Ultrasound-Induced Blood-Brain Barrier Opening. *Sci Rep,* 7**,** 46689.

WU, S. Y., CHEN, C. C., TUNG, Y. S., OLUMOLADE, O. O. & KONOFAGOU, E. E. 2015. Effects of the microbubble shell physicochemical properties on ultrasound-mediated drug delivery to the brain. *J Control Release,* 212**,** 30-40.

YANG, F. Y. & LEE, P. Y. 2012. Efficiency of drug delivery enhanced by acoustic pressure during blood-brain barrier disruption induced by focused ultrasound. *Int J Nanomedicine,* 7**,** 2573-82.

YANG, Y., PACIA, C. P., YE, D., YUE, Y., CHIEN, C.-Y. & CHEN, H. 2021. Static Magnetic Fields Dampen Focused Ultrasound–mediated Blood-Brain Barrier Opening. *Radiology,* 300**,** 681-689.

YASUI, K., TUZIUTI, T., LEE, J., KOZUKA, T., TOWATA, A. & IIDA, Y. 2008. The range of ambient radius for an active bubble in sonoluminescence and sonochemical reactions. *The Journal of Chemical Physics,* 128**,** 184705.

YE, D., SULTAN, D., ZHANG, X., YUE, Y., HEO, G. S., KOTHAPALLI, S., LUEHMANN, H., TAI, Y. C., RUBIN, J. B., LIU, Y. & CHEN, H. 2018. Focused ultrasound-enabled delivery of radiolabeled nanoclusters to the pons. *J Control Release,* 283**,** 143-150.

YIN, X. & HYNYNEN, K. 2005. A numerical study of transcranial focused ultrasound beam propagation at low frequency. *Phys Med Biol,* 50**,** 1821-36.

YOSHIMURA, J., ONDA, K., TANAKA, R. & TAKAHASHI, H. 2003. Clinicopathological study of diffuse type brainstem gliomas: analysis of 40 autopsy cases. *Neurol Med Chir (Tokyo),* 43**,** 375-82; discussion 382.

ZAKI GHALI, M. G., SRINIVASAN, V. M. & KAN, P. 2019. Focused Ultrasonography-Mediated Blood-Brain Barrier Disruption in the Enhancement of Delivery of Brain Tumor Therapies. *World Neurosurg,* 131**,** 65-75.

ZARAGOZA, R. 2020. Transport of Amino Acids Across the Blood-Brain Barrier. *Front Physiol,* 11**,** 973.

ZHANG, H., ZHANG, Y., XU, M., SONG, X., CHEN, S., JIAN, X. & MING, D. 2021. The Effects of the Structural and Acoustic Parameters of the Skull Model on Transcranial Focused Ultrasound. *Sensors (Basel),* 21.

ZHANG, X., YE, D., YANG, L., YUE, Y., SULTAN, D., PACIA, C. P., PANG, H., DETERING, L., HEO, G. S., LUEHMANN, H., CHOKSI, A., SETHI, A., LIMBRICK, D. D., BECHER, O. J., TAI, Y.-C., RUBIN, J. B., CHEN, H. & LIU, Y. 2020. Magnetic Resonance Imaging-Guided Focused Ultrasound-Based Delivery of Radiolabeled Copper Nanoclusters to Diffuse Intrinsic Pontine Glioma. *ACS Applied Nano Materials,* 3**,** 11129-11134.

ZHAO, B., CHEN, Y., LIU, J., ZHANG, L., WANG, J., YANG, Y., LV, Q. & XIE, M. 2018. Blood-brain barrier disruption induced by diagnostic ultrasound combined with microbubbles in mice. *Oncotarget,* 9**,** 4897-4914.

ZHAO, Y., YUE, P., PENG, Y., SUN, Y., CHEN, X., ZHAO, Z. & HAN, B. 2023. Recent advances in drug delivery systems for targeting brain tumors. *Drug Deliv,* 30**,** 1-18.

ZHENG, H., DAYTON, P. A., CASKEY, C., ZHAO, S., QIN, S. & FERRARA, K. W. 2007. Ultrasound-Driven Microbubble Oscillation and Translation Within Small Phantom Vessels. *Ultrasound in Medicine & Biology,* 33**,** 1978-1987.

ZHOU, H., LIU, Y., LONG, X., QIAO, Y., LEE, J., LIU, X., ZHENG, H. & ZOU, C. 2021. MR-guided blood-brain barrier opening induced by rapid short-pulse ultrasound in non-human primates. *Quant Imaging Med Surg,* 11**,** 2415-2427.

ZHOU, Z., SINGH, R. & SOUWEIDANE, M. M. 2017. Convection-Enhanced Delivery for Diffuse Intrinsic Pontine Glioma Treatment. *Current neuropharmacology,* 15**,** 116-128.

ZLOKOVIC, B. V. 2008. The blood-brain barrier in health and chronic neurodegenerative disorders.